THEORETICAL STUDIES ON MOLECULAR INTERACTIONS WITH FREE CLUSTERS AND CLUSTERS ON SURFACE

by

CHINAGANDHAM RAJESH

CHEM012008040024

BHABHA ATOMIC RESEARCH CENTRE

A thesis submitted to the

Board of Studies in Chemical Science Discipline

In partial fulfillment of requirements

For the Degree of

DOCTOR OF PHILOSOPHY

of

HOMI BHABHA NATIONAL INSTITUTE

October 2014

HOMI BHABHA NATIONAL INSTITUTE

Recommendations of the Viva Voce Board

As members of the Viva Voce Board, we certify that we have read the dissertation prepared by **Chinagandham Rajesh** entitled **“Theoretical Studies on Molecular Interactions with Free Clusters and Clusters on Surface”** and recommend that it may be accepted as fulfilling the dissertation requirement for the Degree of Doctor of Philosophy.

Prof. Swapan K. Ghosh
Chairman Date:

Extermal Examiner Date

Prof. Tapan K. Ghanty
Member 1 Date

Prof. Dilip K. Maity
Member 2 Date

Dr. Chiranjib Majumder
Guide and Convener Date

Final approval and acceptance of this dissertation is contingent upon the candidate’s submission of the final copies of the dissertation to HBNI.

I hereby certify that I have read this dissertation prepared under my direction and recommend that it may be accepted as fulfilling the dissertation requirement.

Date:
Place: Mumbai Guide - Dr. Chiranjib Majumder

STATEMENT BY AUTHOR

This dissertation has been submitted in partial fulfillment of requirement for an advanced degree at Homi Bhabha National Institute (HBNI) and is deposited in the Library to be made available to borrowers under rules of the HBNI.

Brief quotations from this dissertation are allowable without special permission, provided that accurate acknowledgement of source is made. Requests for permission for extended quotation from or reproduction of this manuscript in whole or in part may be granted by the Competent Authority of HBNI when in his or her judgment the proposed use of the material is in the interests of scholarship. In all other instances, however, permission must be obtained from the author.

Chinagandham Rajesh

DECLARATION

I, hereby declare that the investigation presented in the thesis has been carried out by me. The work is original and has not been submitted earlier as a whole or in part for a degree/diploma at this or any other Institution/University.

Chinagandham Rajesh

ACKNOWLEDGEMENTS

On the penultimate day of this thesis going to print when I sat down to write this page, I feel very nostalgic. On a chilly winter evening in Mumbai, when Kaustav introduced me to Chiranjib Majumder Sir, a chord struck well with a fine bonding. Thank you, Kaustav for introducing me to this wonderful man. The transition of mine from acquaintance to being his PhD student was smooth and I am indeed thankful to him for giving me a chance to work with him on several challenging projects in a very nice and stimulating environment and his continuous support and advice. He was always there for me to help and taught me how science and life really works. "*Stand on the shoulders of giants"* is an old saying and I had one to stand on. I could not have asked a better advisor and mentor for my PhD. A special thanks goes to Sandeep, my good friend, colleague and crisis man for being there always to sort out all the small and big issues (scientific and non scientific) that appeared on my way and sharing his knowledge and experiences with me. I wish the association continues for a long time in future.

It gives me immense pleasure to acknowledge and thank the members of my doctoral committee: Prof. S.K. Ghosh (Chairman), Dr. T. K. Ghanty and Dr. D. K. Maity for their valuable guidance, encouragement and suggestions throughout the years. Behind a successful computational scientist, there is strong HPC group. At this juncture, I would like to acknowledge the HPC group, BARC for the computing resources and especially Vaibhav, for making me better at using the resources efficiently. Last, not least, the biggest thanks goes to Sailaja for her support, endless patience and for forgiving me spending so much time in front of a computer screen and Rakshit, my little stress buster.

TABLE OF CONTENTS

SYNOPSIS

Clusters are building blocks of nano-structured materials and constitute an intermediate state of matter between atoms (or molecules) and solids[1]. They are aggregates of atoms (or molecules) and show properties between those of individual atoms (with discrete energy states) and bulk matter (characterized by bands of states). The size of nanoclusters ranges from sub-nanometer to about 10 nanometers in diameter and are of technological importance in numerous areas of applied science (*e.g.*, materials science, catalysis, (opto) electronics). The properties of nano-clusters gradually approach to those of bulk materials or extended surfaces, which are scalable with size. Nanoclusters, however, have properties and structures which are very sensitive to their composition and size (i.e. "every atom counts"), can lead to new and interesting properties which are not realized in the corresponding bulk material[2].

Bimetallic clusters composed of elements with different atoms have gained considerable attention[3] because by controlling the composition one can tune the electronic, optical, and chemical properties. Moreover, binary clusters are challenging for (i) better understanding of the characteristic properties of impurities or defects in solids (ii) the elucidation of the role of heterogeneous bonding in mixed clusters which provides understanding of fundamental effects responsible for the stability of covalent or metallic clusters and (iii) the effect of mixing on the electronic shell structure.

Understanding the electronic structure of metal clusters supported on solid substrates is of fundamental to the heterogeneous catalysis. Much effort is devoted to understand this phenomenon and to create a tailor-made catalyst with high efficiency and selectivity[4,5]. The size dependent electronic structure of these clusters is of great importance in the catalytic properties of these systems[6]. The unique size-dependent properties of these supported clusters are only one part of a more complex problem. The oxide supports on which the metal clusters are chemically active suggests that careful understanding is required to separate the effects of cluster and support. Charge transfer between support and cluster and diffusion of reactant molecules from support to cluster are some of the important and complex roles of the support materials in these catalytic systems. In addition, metal clusters exhibit dynamic structural transformations, during a chemical reaction to optimize the catalytic pathway. Moreover, selective doping changes their electronic structure, their relationship to the oxide support, and their catalytic activity.

The goal of the present thesis is to gain fundamental understanding on isolated and supported metallic clusters and their interactions with gas molecules. These studies have implications towards designing new materials for heterogeneous catalysis. Throughout the work standard codes of density functional theory, within the plane-wave based pseudo-potential framework were used as a tool to illustrate the physico-chemical behavior of all systems in this study. The first part of this thesis involves understanding the quantum size effect on the equilibrium geometries and energetics of small lead clusters in the neutral and charged states. In addition, the effect of an impurity dopant on the geometric and electronic structure of lead clusters was investigated. The second part dealt with the interactions of O_2 with Al doped Au clusters. This work was further extended to study the O_2 interaction with $Al-Au$ nano-composites. The primary objective of these works was to investigate the influence of an electro-positive element like Al on the bonding characteristics of electro-negative Au atoms. The results showed an improved oxidation behavior of Au in presence of Al atoms, be it inside the core for core-shell type structure or at the sub-surface layer for periodic slabs. As a natural continuation of the O_2 adsorption, the CO oxidation mechanism on the $Au-Al$ nano-composites was also investigated. In the third part of the thesis, the role of support on the structure and reactivity of metal clusters was investigated. This was carried out by studying the interaction of Au_n clusters on Al_2O_3 surface and subsequent molecular

O_2interactions over them

Chapter 1:

The work described in this thesis is theoretical and its main objective is to look into the fundamental understanding of three important aspects of different types of clusters, namely the atomic structure, bonding and electronic properties. In this introductory chapter, the subject of cluster science is introduced, followed by a brief description on driving force for cluster science and some aspects of the evolution of size dependent properties of clusters so as to provide the necessary background for this thesis. This chapter also covers few experimental methods used for the generation and detection of clusters. In addition, role of theoretical calculations in understanding the experimental results and to predict the geometry and electronic properties of clusters has been described. In this chapter we have also described how theoretical data can be useful for the elucidation of the cluster structure and to interpret the experimental results. At the end of this chapter, a brief outline of the thesis is presented.

Chapter 2:

This chapter describes the general theoretical approach used throughout this thesis. Firstly, an overview is given of the underlying DFT quantum-mechanical approach and the computational details of the level of theory employed for the calculations. Technical aspects of the calculations *viz*. initial guess wave function or basis set, pseudo-potentials, simulation cell, geometry optimization techniques, utilized computer systems configuration *etc*. are discussed. Emphasis has been laid on the philosophy behind the methods rather than the concrete mathematical basis of different methods.

Chapter 3:

The structural and physicochemical properties of the Group IV elemental clusters have been the subjects of intense research because of the fundamental interest to understand their bonding and growth patterns and the possibility of applications in nanotechnology. Their growth behavior and the nature of bonding differ considerably as one goes down from C to Pb. In this chapter we elucidate the evolution of geometric and electronic structure of Pb_n and Pb_n^+ clusters ($n = 2- 15$) and compared it with other Group IV elemental clusters. The results suggest that unlike Si, Ge, and Sn clusters, which favour less compact prolate shape in the small size range, Pb clusters favour compact spherical structures consisting of fivefold or six fold symmetries. The difference in the growth motif can be attributed to their bulk crystal structure, which is diamond-like for Si,Ge, and Sn but *fcc* for Pb. The relative stability of Pb_n clusters analyzed based on the calculated binding energies and second difference in energy suggests that $n = 4, 7, 10$ and 13 clusters are more stable than their respective neighbours. This is in good agreement with experimental observations[7]. Charged Pb_n^+ clusters also showed compact growth pattern as those observed for neutrals with small local distortions. Based on the fragmentation pattern it is seen that small clusters up to $n = 12$ favour monomer evaporation, larger ones fragment into two stable daughter products. The experimental observation of a large abundance for $n = 7$ and lowest abundance of $n = 14$ have been demonstrated from their fragmentation pattern. The chemical stability of these clusters was analyzed by evaluating their energy gap between the highest occupied and lowest unoccupied molecular orbitals and adiabatic ionization potentials. Albeit higher binding energy of Pb_{13}, the lower ionization potential was explained based on its electronic structure through the density of states and electron shell filling model of spherical clusters. A good agreement of our theoretical results with that of the experimental findings reported earlier implied accurate predictions of the ground state geometries of these clusters.

Chapter 4:

Introduction of an impurity atom can play a very important role in the modification of electronic and geometrical properties of homoatomic clusters[3]. However, these studies are relatively few due to difficulties in the experimental arrangements and more number of isomeric structures that needs to be evaluated from theoretical side. In this chapter we report the structural and electronic properties of Pb_nM ($M = C, Al, In, Mg, Sr, Ba$, and Pb; $n = 8, 10, 12$ and 14) clusters. Extensive search based on large number of initial configurations has been carried out to locate the stable isomers of Pb_nM clusters. The results revealed that the location of the impurity atom depends on the nature of interaction between the impurity atom and the host cluster and the size of the impurity atom. While the impurity atoms smaller than Pb, favor to occupy the endohedral position, the larger atoms form exohedral capping of the host cluster. The stability of these clusters has been analyzed based on the average binding energy, interaction energy of the impurity atoms and the energy gap between the highest occupied and lowest unoccupied energy levels (HLG). Based on the interaction energy of the M atoms with Pb_n clusters, it is found that $p - p$ interaction dominates over the $s - p$ interaction and smaller size atoms interact more strongly. The stability analysis of these clusters suggests that while the substitution of Pb by C or Al enhances the stability of the Pb_n clusters, Mg lowers the stability. Apart from geometrical effects, it is found that the stability of these clusters can be tuned by the ordering of their energy levels. The energy gap analysis revealed that while the substitution of Mg atom widens the HLG, all other elements reduce the gap of the Pb_nM clusters. The unusual increase in the interaction energy of Mg with Pb_{12} and the largest HOMO–LUMO gap of $MgPb_{12}$ cluster has been explained based on the 50 electrons rule for icosahedral structures. Further investigations of the stability of Pb_nM clusters revealed that the interplay between the atomic and electronic structure is crucial to understand the stability of these clusters.

Further in this chapter, fragmentation behavior of the bimetallic cluster ions Sn_nPb^+ and Pb_nSn^+ has been investigated. A systematic theoretical study of the structure and electronic properties of $Sn_{n-1}Pb$ and $Pb_{n-1}Sn$ ($n = 2 - 13$) clusters and comparison with pure Sn_n and Pb_n to understand the influence of the dopant elements was presented. Fragmentation studies have revealed that, for Sn_nPb^+ first the single lead atom is split off; in contrast the Pb_nSn^+ clusters dissociate mainly in fragments retaining the single tin atom, which is in full accordance with the low-energy surface-induced dissociation patterns of Sn_nPb^+ and Pb_nSn^+ clusters. For larger collision energies the complete set of smaller tin fragment ions Sn_{n-m}^+ with $m < n$ is found for Sn_nPb^+, whereas the Pb_nSn^+ clusters decay into two series of $Pb_{n-m}Sn^+$ and Pb_{n-m}^+ fragments with $m < n$.

Chapter 5:

Gold, which is inert in the bulk, is found to be highly active in its nano form. Their potential as active catalysts for a large number of reactions (*e.g.,* CO oxidation) has been elucidated earlier[8]. Moreover the chemical reactivity of the Au clusters can be tuned by the incorporating a dopant in it. In this chapter, we have presented the atomic and electronic structure of $Au_{n-1}Al$ clusters ($n = 2 - 7$) and elucidated the results with a view to understand how chemical bonding influences the stability and structure of small size Au clusters. This work is divided into two parts: (i) the equilibrium structures and stability of Al doped Au_{n-1} clusters ($n = 2\text{–}7{,}21$) and (ii) the interaction of O_2 with stable clusters. The optimized geometries of $Au_{n-1}Al$ clusters indicate that the substitution of Au by Al results an early onset of three-dimensional structures from tetramer onwards. The stability of $Au_{n-1}Al$ clusters has been analyzed based on the binding energy, second difference in energy, and the energy gaps between the highest occupied and lowest unoccupied molecular orbital energy levels. Based on the energetics, Au_3Al and Au_5Al clusters are found to be extraordinary stable. The oxidation of $Au_{n-1}Al$ clusters undergoes *via* dissociative mechanism, albeit significant charge transfer from Al to Au. Moreover, the O_2 molecule prefers to attach at the Al site rather than at the Au site.

On the basis of the above results it is envisaged that it will be of interest to investigate the CO oxidation behavior of $Au-Al$ nano-composites. $Al-Au$ nano-composites in three different size ranges; (*i*) a small cluster Al_6Au_8, (*ii*) a mid-sized cluster $Al_{13}Au_{42}$, and (*iii*) a periodic slab of $Au(111)$ surface, where the Au atoms in the second layer is substituted by Al atoms have been modelled. While the Al_6Au_8 forms a cage like structure with both the Au and Al atoms on the surface of the cage, $Al_{13}Au_{42}$ forms core-shell type symmetric icosahedral structure. For the Al substituted $Au(111)$ surface, the ionic relaxation results in compression between the interlayer separations. The charge distribution analysis suggests that in all cases Al atoms donate electronic charges to the Au atoms. This has been corroborated by the red shift in the density of states spectrum, a signature of more negative charge state whence a higher chemical reactivity. The CO oxidation on these nano-composite systems was investigated through both Eley -Rideal (E-R) and Langmuir Hinshelwood (L-H) mechanism. The interaction of O_2 molecule with these systems occurs non-dissociative way with elongation of the $O-O$ bond. Further interaction with CO molecule leads to the formation of CO_2 spontaneously. On contrary, the CO_2 evolution by co-adsorption of O_2 and CO molecules undergoes through an intermediate complex of higher energy. On the basis of the results it is inferred that the efficient CO oxidation of the $Al-Au$ nanocomposite is due to negatively charged surface Au atoms.

Chapter 6:

The pioneering work of Haruta *et al.*[8a,9,10] which showed low temperature CO oxidation of supported Au clusters has resulted in the surge of theoretical and experimental studies to understand the mechanism of CO oxidation on these deposited clusters. Motivated by these studies, we have carried out a systematic study on the adsorption of $Au_n(n=1-6)$ clusters on a regular $\alpha-Al_2O_3(0001)$ surface. The results have been divided into four major sections (*i*) Ground state geometries of the adsorbed Au_n clusters (*ii*) Energetics of adsorption as a function of cluster size (*iii*) Charge transfer analysis and the resultant electronic structure changes of the adsorbed Au_n clusters and (iv) interaction of Au_2 cluster adsorbed on Al_2O_3 with O_2. The above results are compared with neutral and anionic Au_n clusters at the appropriate context. The results reveal a considerable resemblance of the deposited Au_n with their gas phase anionic counter parts. The adsorption energies of Au_n clusters showed strong odd-even variations on Al_2O_3 surface, with local maxima at $n = 2, 4, 6$ which are established to be stable by both experiment and theory. A qualitative understanding of the nature of the bonding characteristics was obtained by the charge difference analysis. Further, a red shift of the Fermi energy levels of the deposited Au/Al_2O_3 surface when compared to the Au_n was observed. Upon adsorption, O_2 is observed to strongly interact with deposited Au_2 cluster molecularly with an elongated $O - O$ bond. This activated O_2 molecule is expected to facilitate the oxidation of CO.

Chapter 7:

This chapter consists of conclusions and future directions. This gives a brief outline about the possible outcomes and future directions that can be charted out from the present studies on designing new materials for catalysis applications, which have been discussed in the present work.

References:

1. de Heer, W., *Rev. Mod. Phys.* 1993**,** *65* (3), 611-676.

2. (a) Brack, M., *Rev. Mod. Phys.* 1993**,** *65* (3), 677-732; (b) Kumar, V.; Esfarjani, K.; Kawazoe, Y., *Springer Series in Cluster Physics* 2002, 9.

3. (a) Knight, W. D.; Deheer, W. A.; Clemenger, K.; Saunders, W. A., *Solid State Commun.* 1985**,** *53* (5), 445-446; (b) Kappes, M. M.; Radi, P.; Schar, M.; Schumacher, E., *Chem. Phys. Lett.* 1985**,** *119* (1), 11-16; (c) Martin, T. P., *Angewandte Chemie-International Edition in English* 1986**,** *25* (3), 197-211; (d) Brechignac, C.; Cahuzac, P.; Roux, J. P., *Chem. Phys. Lett.* 1986**,** *127* (5), 445-451; (e) Hoshino, K.; Watanabe, K.; Konishi, Y.; Taguwa, T.;

Nakajima, A.; Kaya, K., *Chem. Phys. Lett.* 1994**,** *231* (4-6), 499-503.

4. Ertl, G.; Freund, H. J., *Physics Today* 1999**,** *52* (1), 32-38.

5. Somorjai, G. A.; Contreras, A. M.; Montano, M.; Rioux, R. M., *Proceedings of the National Academy of Sciences of the United States of America* 2006**,** *103* (28), 10577-10583.

6. Hakkinen, H.; Abbet, W.; Sanchez, A.; Heiz, U.; Landman, U., *Angew. Chem. Int. Ed.* 2003**,** *42* (11), 1297-1300.

7. (a) Mühlbach, J.; Sattler, K.; Pfau, P.; Recknagel, E., *Phys. Lett. A* 1982**,** *87* (8), 415-417; (b) Sattler, K.; Mühlbach, J.; Echt, O.; Pfau, P.; Recknagel, E., *Phys. Rev. Lett.* 1981**,** *47* (3), 160-163.

8. (a) Haruta, M., *Catal. Today* 1997**,** *36* (1), 153-166; (b) Valden, M.; Lai, X.; Goodman, D. W., *Science* 1998**,** *281* (5383), 1647-1650; (c) Bond, G. C.; Thompson, D. T., *Catal. Rev.* 1999**,** *41* (3-4), 319-388; (d) Sanchez, A.; Abbet, S.; Heiz, U.; Schneider, W. D.; Hakkinen, H.; Barnett, R. N.; Landman, U., *J. Phys. Chem. A* 1999**,** *103* (48), 9573-9578.

9. (a) Haruta, M.; Kobayashi, T.; Sano, H.; Yamada, N., *Chem. Lett.* 1987**,** (2), 405-408; (b) Hutchings, G. J.; Haruta, M., *Appl. Catal., A* 2005**,** *291* (1-2), 2-5.

10. (a) Bond, G. C., *Catal. Today* 2002**,** *72* (1-2), 5-9; (b) Haruta, M.; Date, M., *Appl. Catal., A* 2001**,** *222* (1-2), 427-437.

LIST OF FIGURES

LIST OF TABLES

1. Introduction

1.1 The Evolution of Cluster Science

There has been a continuous surge in the efforts directed towards the study of gas phase and surface deposited clusters, for various reasons. The foremost being, the intermediary nature of clusters accommodating as models fill the gap between the atoms/molecules having discrete energy states and bulk, whose states form continuous bands. An insight into the above progression is very important. They invoke a great interest among researchers, since the finite size effects lead to some unique electronic, magnetic, optical *etc*., properties which cannot be observed in the extreme size regimes. Secondly, clusters with high surface to bulk atomic ratio serve as representatives for the bulk surface. This has accelerated investigations on the reactivity and catalytic action of clusters and supported clusters. And finally, utilization of clusters as segments of nano-devices is additionally drawing in much attention. Nanoclusters are no more the strange morsels of matter as pointed by R. Pool a few decades back [1].

Research on colloids dating back to more than a century, laid the foundations for the contemporary cluster science. Faraday in his lecture on “Experimental Relation of (Colloidal) Gold to Light” way back in 1857 [2], predicted the present day research on metal clusters and their optical properties. Experiments carried out on cloud physics and aerosol science by Coulier and by Aitken in the nineteenth century, laid the road for present day studies on nucleation [3,4]. The famous cloud chamber experiments of Wilson, in which gaseous ions acted as condensation nuclei formed the basis of the current studies on cluster ions [5]. Langmuir, during 1930-1950 did extensive work on developing methods to form smokes and fogs and nucleation (seeding) of clouds [6], which had also directed the cluster research. Kush from his magnetic resonance studies on alkali halide beams gave a conclusive evidence of cluster formation in beams [7]. However, it was Ramsey who in his earlier experiments on molecular beams suspected the presence of clusters in molecular beams [8]. Advent of supersonic expansion nozzles [9,10] had a profound impact on the nature and pace of cluster research. Becker and Henkes, in 1956 observed large scale condensation in supersonic jets from small nozzles and demonstrated their possible use as sources for intense cluster beams [11]. The experiments of Bentley [12] and Henkes [13] around 1961, who have individually observed clusters of CO_2 using mass spectrometers, are the starting points for the present era of cluster science. Since then, the fusion of cluster beams and mass spectrometers has been a fruitful tool in cluster science.

Numerous original and primary studies pursued over the past few decades using a range of approaches shaped the cluster field [14-36]. With the gradual evolution of instrumentation in lasers and flow reactors by early 1970's, augmenting the beam sources and bettered mass spectrometers, cluster research was in a direction to get recognized as a zone of research in its own merit. Cluster science which was an integral area of physical chemistry and molecular physics till then emerged as Cluster Physics. Simultaneously, as the stride of computer developments accelerated, theoretical and computational chemists began to play a major role in investigating the nature of complex systems containing large numbers of atomic or molecular species. Further, the seminal work of Knight *et al.* [37] on the abundance distribution of Na clusters which reflected the formation of electronic shells in clusters similar to electrons in atoms and the discovery of C_{60} by Kroto *et al.* [38] and its subsequent structure elucidation have added strong impetus for the development of cluster science. From this genesis, cluster research blossomed, and an increasing number of mature experimental and theoretical accounts on cluster research have been appearing in literature.

The work described in this thesis is theoretical and its main objective is to look into the fundamental understanding of three important aspects of different types of clusters, namely the atomic structure, bonding and electronic properties. In this introductory chapter, the subject of cluster science is introduced, followed by a brief description on driving force for cluster science and some aspects of the evolution of size dependent properties of clusters so as to provide the necessary background for this thesis. This chapter also covers few experimental methods used for the generation and detection of clusters. In addition, role of theoretical calculations in understanding the experimental results and predict the geometry and electronic properties of clusters has been described.

1.2 Motivation for cluster research

Clusters, as described above provide a bridge between the extremes of independent atoms/molecules and bulk matter. Exploring the size effects on the structural, electronic, thermodynamic, magnetic, and chemical properties in these finite systems, whose size continuously varies motivates the area of cluster research. A better perspective of these systems will provide a better understanding of the behavior at more familiar limits. This thesis will touch upon some aspects of size evolution of cluster properties. Molecules, defined by a set of chemically bound atoms are constrained by stoichiometry and structure in

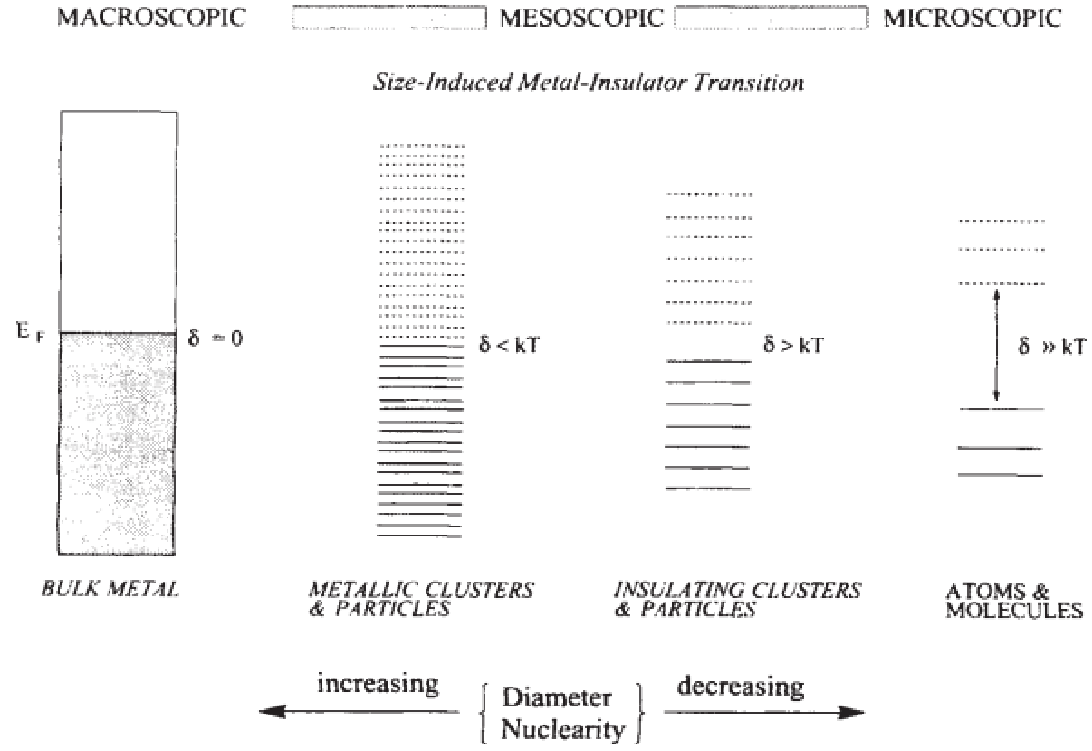

Figure 1.1: Variation of electronic structure of a metal with of decreasing particle size (nuclearity).

terms of symmetry. However, clusters with no such constraints, allow for a rich diversity in composition and proliferation of structural isomers. Cluster research is expected to shed light on some fundamental areas like the initial stages of the formation of matter and the evolution of cluster properties towards bulk. It has been always fascinating to understand the changes in the cluster geometry as a function of size and seek answers on the crystal growth at the microscopic scale form cluster growth patterns. A central issue in cluster science is to figure out how quickly the properties of clusters approach to that of bulk as a function of size. For example, in case of metallic clusters, at what size does the discrete energy levels evolve into continuous energy bands and metallic conductivity is observed? The issue becomes more intriguing since different properties of a specific cluster might converge at different point. Further, knowledge on the progression of the properties like the structure, ionization potential, electron affinity *etc.,* as the cluster grows atom by atom is also important.

Clusters provide a microscopic approach to macroscopic phenomena, such as nucleation, adsorption, desorption and catalysis. An assortment of applications like photography, aerosols, small particle sintering *etc*., rest on the physics and chemistry of clusters. Apart from this, understanding some phenomena in astrophysics like formation mechanism and properties of cosmic dust, infrared interstellar emission bands *etc*., also rely on understanding clusters better [39,40]. Studies on the thermodynamics of phase transformation also drove cluster research since the initial nuclei for any phase formation are in the cluster regime [41-43]. Current research on clusters is directed not considering clusters just as a model of nucleus but as an environment from where growth occurs at fast time scales [44,45]. Much work on clusters is driven by the hope that a fundamental understanding of the chemical reactivity of clusters might provide crucial insights for unique catalytic properties. Clusters, for example supported, by a zeolite will provide a large surface area to volume ratio and properties, such as activity and selectivity, can be tuned to catalyze specific reactions [46,47].

The possibility of building a new class of materials with tailored properties assembled from these highly stable clusters as building blocks made the study of clusters the most promising [48]. The synthesis of highly stable and symmetric clusters with varying size and compositions, which can be viewed as super-atoms belonging to a 3D periodic table, can mimic the chemistry of an atom in the periodic table. The synthesis of fullerite solid from self assembling of C_{60} clusters is a proven example to this end [49]. It is envisaged that cluster assembled materials might foster new outlooks in medicine, engineering and understand environment at an atomic scale [50].

These questions have motivated the development of experimental techniques for producing small clusters, as well as a series of experimental and theoretical studies of their structure and properties. But, for all this to happen, the fundamental issues concerning clusters have to be understood first.

1.3 Classification of Clusters

The classification of clusters can be approached from different perspectives. Standard classifications are based on number of constituent elements, size and bonding. The constituent species may be identical, referred as homo-atomic/homo-molecular clusters, X_n or composed of two or more different types of atoms or molecules leading to hetero-atomic/hetero-molecular clusters, $X_p Y_q$.

Based on their size regimes, clusters can be classified as: small clusters (<100 atoms), medium-sized clusters (100–10,000 atoms) and large clusters (>10,000 atoms). Considering the Spherical Cluster Approximation, the diameter of a cluster of n atoms is given as $d = 2R_{ws}n^{1/3}$ where R_{ws} is the Wigner-Seitz radius of the element under consideration. For example, the ranges of the three size regimes of Na clusters (R_{ws}~0.2 nm) is ~1.9 nm, 1.9-8.6 nm , > 8.6 nm respectively. From the fraction of atoms on the surface of the cluster, it is evident for clusters with ~10,000 atoms still have nearly 20% of their atoms on the surface.

A major classification of clusters is based on the nature of the forces that hold them together-the chemical bonding between the species forming the aggregate. In the absence of any bonding because of their closed shell configuration, the rare gas atoms interact *via* weak forces dominated by dispersion forces. The dynamic electron correlation effects *i.e.,* the fluctuations in the electron density, resulting in instantaneous dipoles, which in turn induce dipoles in the neighboring atoms gives rise to weak attractive non-covalent or van der Waals (VdW) interaction among the inert gas atoms. At low temperature, it is possible to form the clusters of rare gases like He, Ar, Ne, Kr and Rn whose average binding energy is about 0.3 eV/atom or less. Molecular clusters, formed as aggregates of closed shell molecules, like $(I_2)_n$,$(N_2)_n$,$(CO_2)_n$, $(SF_6)_n$ also belong to this class.

At the other extreme, we have the strongly bound clusters whose atoms are covalently bonded. They have high binding energy typically of the order of 1 eV/atom and 4 eV/atom. These clusters are composed of elements which are in general semiconductor like Si, Ge and other compounds like $GaAs$ and $CdTe$. The thin line between molecule and cluster disappears with some covalent clusters. Fullerenes with C_{60} as a classical example are more thought as molecules rather than clusters of C atoms. Another variety is the metal-carbohedrenes with the general formula $C_{20}M_{12}$. Metallic clusters, bound my strong metallic bonds though not as strong as covalent bonds make another class of clusters. The binding strength in metallic clusters ranges from 0.5 eV/atom to 3.0 eV/atom. The inter-atomic forces are partially directional leading to non closed pack structures for some metal clusters. Simple metals with valence electron of sp character (e.g., Na or Al) behave differently from transition metal clusters (Fe_n or Co_n), where the localized d electrons play an important role. Determining how and at what sizes such clusters become metal-like is a thrust area in cluster research. Metal clusters composed of more than one metal, gives rise to a subclass of intermetallic/nanoalloy clusters. Theories and models which have been developed to describe metal clusters will be discussed in the later sections. The hydrogen bonded clusters are another highly complex class of clusters and clusters of water molecules are by far the most studied in this class.

Ionic clusters, which, are derived from ionic solids fall in the class of heterogeneous clusters. They are composed of elements with a large difference in electronegativity, whose bonding is better described as electrostatic or ionic in nature. Hence ionic clusters are majorly derived from the halides and oxides of the alkali metals and alkaline earth elements, $e.g.$,$[Na_xCl_y]^{(x-y)+}$, $[Mg_xO_y]^{2(x-y)+}$.The average binding energy is ~2-4 eV/atom for ionic clusters.

1.4 Generation of Mass Selected Clusters

Two major approaches adopted in cluster generation include the big to small approach, where desorption and fragmentation of bulk matter by either bombardment of particles or lasers is used to produce clusters and the small to big approach, where nucleation and aggregation of atoms produces bigger clusters. The vaporization of atoms/molecules in the gas phase is followed by the condensation of atoms/molecules (nucleation), which act as nucleus for the further growth of the clusters. Further, small cluster might coalesce to form larger clusters or the growing clusters might fragment to form smaller clusters.

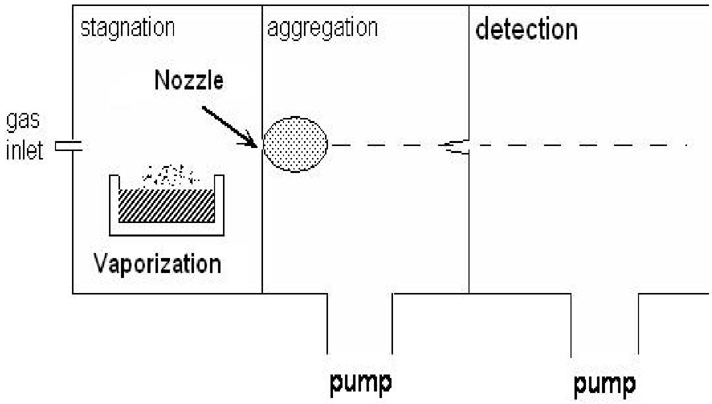

Figure 1.2: Schematic Diagram cluster generation and detection

In general, cluster sources are based on either supersonic expansion nozzle sources [51,52] or inert gas condensation sources [34]. Seeded supersonic nozzle sources are by far the most commonly used and the most intense cluster beam sources for low-boiling-point metals. Clusters with adequate abundance and up to several hundred atoms can be produced with a reasonably narrow speed distribution. In the gas aggregation sources metal atoms initially generated by evaporation or sputtering are introduced into a cold inert gas like He or Ar, where the vapour becomes supersaturated and cluster aggregation proceeds principally by sequential addition of single atoms. Clusters of sizes $n > 10000$ are efficiently produced by these sources and low cluster temperatures $(< 100K)$ can be achieved.

Several modifications of the nozzle expansion sources like specialized jet cluster sources [53], laser vaporization, pulsed beam sources [54], expansion jet/inert gas condensation combination cluster source [55,56] have been made. In laser vaporization sources, intense laser pulses are used to ablate the material of interest to produce vapours, which are introduced into a pulse of inert gas, which rapidly cools the vapour and initiates cluster formation. In Pulsed-arc cluster-ion sources intense electrical discharge rather than a laser is used to produce the clusters, resulting in intense cluster-ion beams [57]. Ion sputtering sources produce intense and continuous beam of small and singly ionized clusters of most metals by bombarding a target with high energy inert gas ions [58,59]. In Liquid metal ion sources, very high electric fields are generated at the tip of a needle which carries the metal of interest, heated above its melting point [60,61]. Hot and multiply charged clusters are generated in the process which undergo evaporative cooling and cluster fission, to generate smaller clusters. The size distribution of the generated clusters strongly depends on the particular cluster source being used, the vapour generation method, initial and final temperature, type of quenching gas, the dimensions and shape of aperture of the nozzle and whether supersonic expansion is carried out or not.

In general, cationic clusters can be generated by (i) electron impact where thermal electrons generated by thermionic emission from a heated wire knock off electrons from neutral clusters (*ii*) photo-ionization, where low energy UV photons can ionize the neutral clusters without fragmentation and (*iii*) electric discharge−positively charged clusters are generated in the stagnation chamber, before expansion by using a corona discharge. Two major ways of generating anionic clusters include (*i*) the electron transfer –where an electro-positive element (*e.g.*, Cs, Rh) introduced into the vapour phase transfers its valence electron to the clusters (*ii*) capture of low energy electrons which does not risk incorporation of unwanted atoms into the cluster.

In order to study the nature of clusters, cluster ions can be separated and selected, in general according to their masses by mass spectrometry. A couple of methods are introduced briefly here. In the Wien filter [62], when an electric field is applied perpendicular to a magnetic field and the charged clusters are injected perpendicular to two fields, ions with a velocity $v = E/B$, experience a zero net force, travel unperturbed through the crossed fields and get detected. Most commonly, homogeneous electric or magnetic field sectors are used to deflect charged clusters to an extent depending on their q/m ratio and their velocities. In a quadrupole mass filter, the trajectories of ions in a narrow mass range are stable in a two-dimensional quadrupole field if and only if the field has an ac component superimposed on a dc component with appropriate amplitudes and frequencies [63]**.** In the time-of-flight (TOF) mass spectrometer [64], when clusters with different m/z values are accelerated in multiple homogeneous electric fields before being introduced into a flight tube (no field zone), reach the detector at different time points. Ion cyclotron resonance mass spectrometry, is a type of mass analyzer in which the m/z of ions in determined based on the cyclotron frequency of the ions in a fixed magnetic field [65] and extremely accurate mass resolutions of 10^{-6} can be obtained. When neutral atomic or molecular clusters collide with a beam of rare gas atoms or ions, larger clusters are scattered by smaller angles than smaller clusters due to the conservation of momentum. Size-selected beams of neutral clusters can also be generated by re-neutralizing the positively or negatively charged clusters which have a priori undergone size selection.

1.5 Abundance Spectra

Abundance spectra obtained in the mass spectroscopy reflects the variation in the binding energy of the clusters as a function of their mass (or size). Though the absolute differences in the binding energy are very small, the Boltzmann factors involved in the mass spectra magnify the difference in their abundance *i.e.,* the relative cluster intensities are enhanced for clusters with larger stabilities. Hence, small changes in the binding energy highly influence the abundance intensities. Further, the intensities (I_n) in the mass spectrum are a function of various factors which is given as

$$I_n = (Production)_n\ (Transfer\ eff.)_n\ (Ionization\ eff.)_n\ (Detection\ eff.)_n \qquad \text{eq. 1.1}$$

and the actual contributing terms depend on the experimental conditions. Under the condition that the final cooling involves evaporation of atoms, cluster abundance can be determined by

$$\ln I_{n+1}/I_n = \Delta_2 F(n)/kT \qquad \text{eq. 1.2}$$

where $\Delta_2 F(n) = (F_{n+1} + F_{n-1} - 2 \times F_n)$, is the second difference in the Helmholtz free energies [66]. Alternatively, considering that the cluster abundances might reflect a quasi-equilibrium distribution in the nozzle, the relative abundance can be given by

$$ln\, I_n^2/I_{n+1}I_{n-1} = \Delta_2 BE(n)/kT \qquad \text{eq. 1.3}$$

where $BE(n)$ is the total binding energy of the cluster. The binding energy per atom (BE) for any neutral M_n is defined as

$$BE(M_n) = \big(E(M_n) - n \times E(M)\big)/n \qquad \text{eq. 1.4}$$

where $E(M_n)$ is the total energy of the cluster M_n and $E(M)$ is the energy of the M atom. The relative stability of the clusters can further be described by the dissociation energy (similar to the cohesive energy of a bulk solid), defined as the energy required to remove an atom from the cluster ($DE(M_n)$) and the first derivative of the total energy ($\Delta^2(E(M_n))$ of the clusters.

$$DE(M_n) = E(M_n) - E(M_{n-1}) - E(M) \qquad \text{eq. 1.5}$$

$$\Delta^2(E(M_n)) = 2 \times E(M_n) - E(M_{n+1}) - E(M_{n-1}) \qquad \text{eq. 1.6}$$

$\Delta^2(E(M_n)$ in particular is a measure of the relative stability of a cluster with respect to its left and right neighbours and helps in the interpretation of the mass abundance spectra obtained from experiments using hot cluster beams because the measured abundance spectra corresponds to clusters which have survived the fragmentation.

1.6 Shell Structure

The physical and chemical properties of a cluster or a cluster ion are closely related to its geometric and electronic structures, which are measured by optical absorption and photoelectron spectroscopy with the aid of theoretical calculations. Several works described below exemplify the relations [67,68].

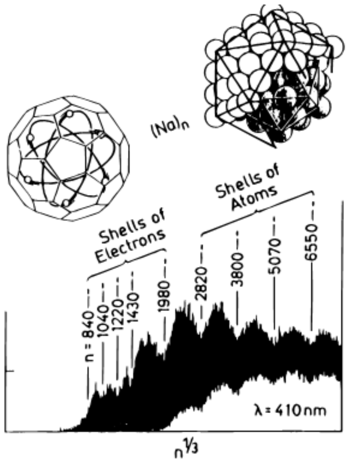

Figure 1.3: Mass spectra of Na_n clusters with electronic and structural shell sequence.

1.6.1 Electronic Shells

Knight *et al.* [37] in their seminal work on the abundance distribution of Na clusters observed a non-monotonic variation as a function of cluster size, with prominent maxima at $N = 8, 20, 40, 58$ and 92 cluster sizes whose valence electrons matched the shell closing numbers of a spherical potential well. Ekardt [69,70] has predicted a similar shell structure in his model for alkali clusters using the Jellium approach. Approximating small clusters with spheres can be only justified for closed-shell clusters. Clemenger [71] introduced a deformable potential well and assumed the effective single-particle

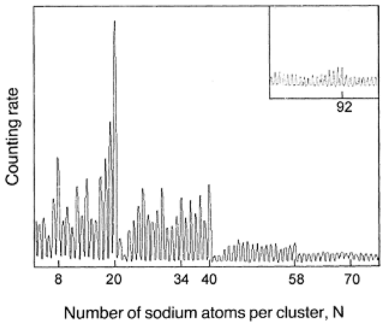

Figure 1.4: Mass spectrum of sodium clusters ($n < 120$)

potential is essentially that of a three-dimensional harmonic oscillator. The model predicts a sub-shell filling in the order of $1s, 1p, 1d, 2s, 1f, 2p, 1g, 2d, 1h, 3s, \ldots$ leading to 2, 8, 18, 20, 34, 40, 58, 68, 90, 92... sub-shell closures. This model reproduced most of the fine structure in the abundance spectrum observed by Knight *et al.* [37]. Ionization potential as a function of cluster size, indicate that the value of *IP* drops abruptly between n and $n+1$ precisely at the values $n =$ 8, 20, 40, 58 and 92 [68]. The disassociation energies obtained from fragmentation experiments [72] showed abrupt drops of the evaporation energy between Na_3^+ and Na_4^+, between Na_9^+ and Na_{10}^+, and between Na_{21}^+ and Na_{22}^+ which unambiguously associate the magic character with valence electron number in the cluster, and corroborate the magic numbers observed in the abundance spectra. The mass spectroscopy and the variation of the *IP* of noble metal clusters (Cu_n, Ag_n, Au_n) indicate the existence of shell effects, similar to those observed in the alkali clusters [73]. The measured detachment energies of Ag_n^- [74] and Cu_n^- [75,76] by photoelectron spectroscopy show drops between $n = 7$ and $n = 8$ and between $n = 19$ and $n = 20$, which again indicated major shell closing. Cha *et al.* [77] have qualitatively assigned the observed peaks in PES of Cu_n^- to the electronic shells of ellipsoid jellium model taking some additional effects like shake-up processes and multiplet splitting into account. Winter *et al.* [78] have ascribed the lack of reactivity of Cu_{20}, Cu_{34}, Cu_{40}, Cu_{58} and Cu_{92} towards O_2 to the closed electronic structure of these clusters. Since the gap between the

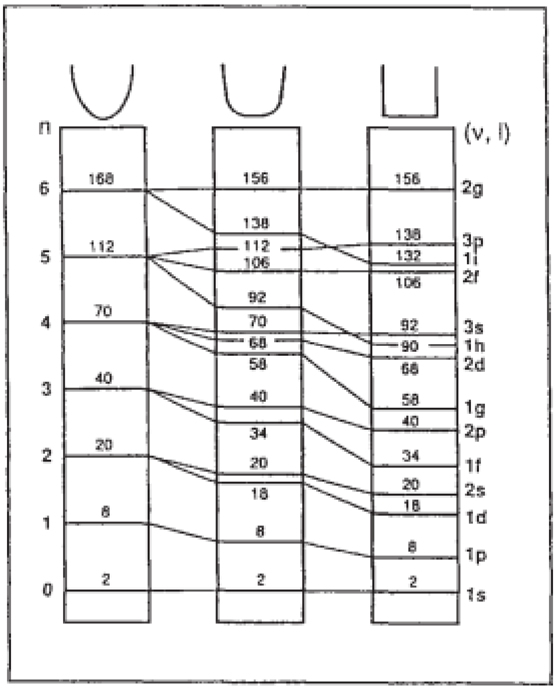

Figure 1.5: Energy level orderings and degeneracies for spherical 3-D, harmonic (left), intermediate (Woods-Saxon, centre), and square well (right) potentials.

electronic sub-shells becomes narrower with increasing occupied shell number, it is envisaged that the discrete energy levels evolve into a quasi-continuous energy bands of the solid. Experiments indicate that electronic shell effects remain important for clusters with a few thousand valence electrons [79-82].

1.6.2 Shells of Atoms

Echt *et al.* [83] in their mass abundance spectrum of Xenon clusters (Xe_n) observed that the abundance varies in a rather peculiar way as a function of size n, and main breaks at sizes $n = 13, 55$ and 147 are particularly noticeable. These, so called magic numbers, are elements of a series $n = 1 + \sum_{p=1}^{N}(10p^2 + 2)$, and this series [84] describes the packing of spheres in a family of closed icosahedral arrangements, and N gives the number of concentric atomic layers in the icosahedron. The electron diffraction patterns from argon clusters agreed with an icosahedral packing for a broad size range [85]. The mass abundance spectra have revealed that clusters with filled geometric shells, have increased stability by maximizing the average coordination number and reducing the cluster surface energy. The average binding energy per atom of icosahedral clusters calculated with the Lennard–Jones potential showed local maxima for sizes n corresponding to icosahedra with filled shells [86,87]. MD simulations of the evaporation of atoms from argon clusters confirmed that the magic cluster Ar_{13}

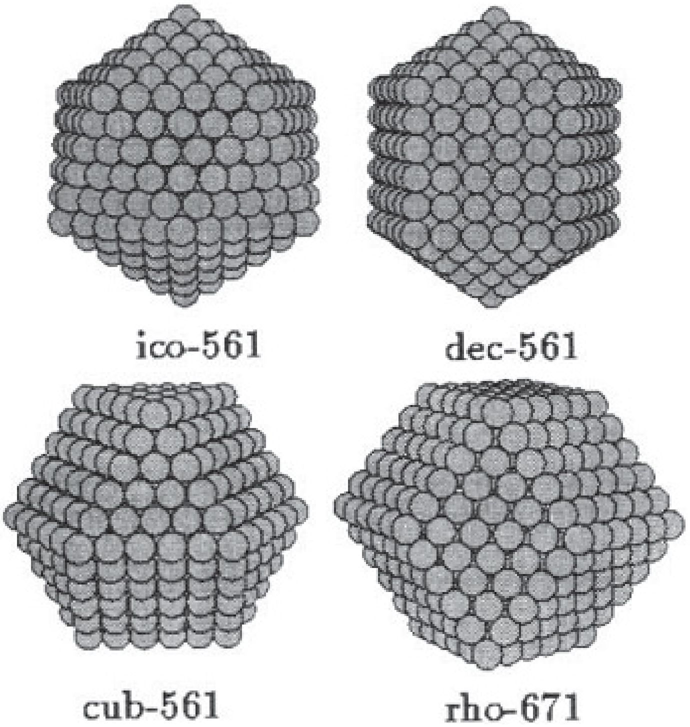

Figure 1.6: The outer shells of five-shell geometric shell metal clusters: ico=icosahedron; dec=(Ino)decahedron; cub=cuboctahedron; rho=rhombic dodecahedron.

evaporates less than clusters of neighboring sizes [88]. In summary, growth of van der Waals clusters by the packing of spheres occurs in stages; each stage terminates with the completion of a Mackay icosahedron. The magic numbers observed in the abundance spectrum of large Na clusters (~1500 atoms) suggests that as the clusters grow sufficiently large, they form a close-packed or nearly close-packed polyhedra with icosahedral or cuboctahedral (fcc) shapes [80,89] The total number of atoms in icosahedral or cuboctahedral clusters contains $n_K = \frac{10}{3}K^3 - 5K^2 + \frac{11}{3}K - 1$ atoms where K is the shell number [84,89]. However, the icosahedral, decahedral and cuboctahedral growth motifs can be distinguished by looking at the secondary magic numbers associated with the geometric sub-shells. Studies on alkaline earth metals clusters (Be, Mg, Ca and Ba) have revealed their preference to adopt icosahedral shell geometries [89-93]. Further, the structure in the mass spectra revealing the atomic shell structure reflected the size dependent variation in the ionization potential. Similar studies on large Al_n clusters revealed their preferential octahedral structures [94].

Magic number effects have been traditionally difficult to observe in the mass spectrum of transition metal clusters, although evidence of magic numbers in Fe, Ti, Zr, Nb and Ta clusters has been found [95]. All the elements listed above have in common the observation of the magic numbers $n = 7, 13$ and 15. In addition, $n = 19$ and 23 are seen for Fe, and $n = 19$ and 25 for Ti. The magic numbers $n = 7, 13, 19$ and 23 are interpreted as revealing icosahedral structure. For nickel clusters, a sharp increase in the abundance was observed at $n = 55, 147, 309$ and 561 [96]. Additional evidence for icosahedral, instead of cuboctahedral structures, came from the fact that, for $n > 200$, enhanced stability was observed every time that a face of an icosahedron was covered in the process of building the next icosahedron. The icosahedral structure of Ni_{13} is supported by DFT calculations [97]. The relatively low polarizability observed for $n = 19, 23, 26, 29, 32, 43$ and 55 by Knicklebein [98] can be correlated with the compact structure of Ni_n clusters with filled umbrellas. Studies on large clusters ($n \simeq 40{,}000$) of transition and noble metals [99,100] using Rossato potential [101], showed that icosahedral structures are favored at small sizes, decahedra at intermediate sizes, and truncated octahedra at large sizes. However, the crossover sizes are very sensitive to the particular metal: in Cu, the icosahedral structure is favored over large region, followed by a very wide decahedral window; in contrast, the icosahedral and the dodecahedral intervals are very narrow in gold. The other metals display intermediate behavior: Ag is similar to Cu and Pd and Pt are close to Au.

A considerable attention on the transition from electronic shell structure to geometrical shell structure has lead to a couple of factors which include the electronic density of states, atomic electron configuration, cluster-melting temperature and the temperature of the cluster. Martin *et al.* [80] rationalized that: since the atoms in small clusters are mobile, they take small spherical droplet morphology, while larger clusters, grow as small crystallites. When this occurs (~1500 atoms), the electronic shell effects become less intense and instead are replaced by patterns related to the growth of crystallites which are more difficult to change and further growth takes place by condensation of atoms onto the surface of a rigid core to form new shells of atoms. In brief, while hot liquid like clusters show electronic shell structure, geometric shell structure predominates in colder solid like clusters.

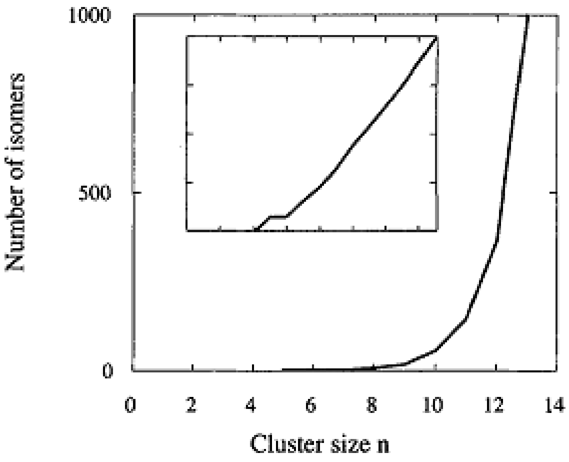

Figure 1.7: Number of possible geometric isomers for (L-J's bound) clusters: Number of isomers versus n. (logarithmic plot in insert).

1.7 Structure Determination

Unlike molecules which have fixed stoichiometry and structure, clusters can be formed of any number of components and exhibit a variety of structures for a specific number of component atoms or molecules. Identifying the lowest energy isomers has received a considerable attention and requires a considerable effort, since as a first approximation, the number of locally stable structures increases exponentially ($e^{n/3}$). Low lying isomers of some atomic clusters whose binding forces are well represented by pair wise interactions, such as *L-J* potentials can be modeled easily, however potentials are seldom pair-wise additive and more so for semiconductor and insulator species which require more complex models. Further, correlating cluster structures to their counterparts in bulk, for example the transition from polyhedral structures of rare gas clusters to the face-centered cubic (close packed lattice), is an interesting challenge.

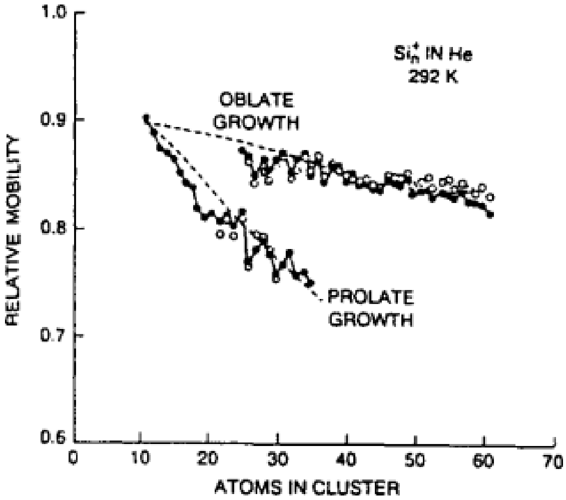

Figure 1.8: Relative mobilities (measured mobility divided by hard sphere mobility) of charged Si clusters in He. Predicted relative mobilities for prolate and oblate clusters are shown in hyphens.

Mobility of ionized clusters through a buffer gas (like He) is a measure of the collision cross-section of the clusters with the gas atoms and depends sensitively on the cluster shape. Compact spherical clusters have lower collision cross sections than prolate or oblate clusters i.e., their drift times are smaller [102-104]. In conjugation with theoretical simulations, mobility measurements provide information on cluster shapes. Hard spheres model [105] can be used to determine the collision cross sections starting with several isomeric structures obtained in theoretical calculations and compared with experimental cross section to determine the ground state structure. Results on carbon clusters showed that clusters of $29 \leq n \leq 45$ size show an isomeric progression from linear to rings to fullerenes and fullerenes first appear at C_{30}^+ and begin to dominate above C_{45}^+ [103]. Oger *et al.* [106] in their classical studies on B_n^+ clusters observed a good match between the experimental and computed nobilities and showed that the boron cluster cations undergo a transition between quasi-planar and tubular structures at B_{16}^{+}.

A great deal of data on the structure of clusters is obtained indirectly, by and large by investigating and modeling the results obtained from mass spectroscopic and ion-mobility experiments. However, recent advances achieved in the application of X-ray diffraction and electron microscopy gave an opportunity to investigate the structure of clusters directly. Microscopy is one of the best possible techniques to obtain direct information regarding the actual structure of clusters or at least significant information about the outer layers. However, conventional optical microscopy using UV-Vis light fails to obtain the atomic resolutions required. Instead, electron microscopy techniques, where electrons are accelerated to a sufficient energy to obtain appropriate wave lengths, have achieved the required atomic resolution to image atomic structure of clusters. Mapping of atoms has been obtained to an accuracy of 10^{-11} m *i.e.*, lesser than the width of an atom with these techniques. In Scanning electron microscopy and scanning tunneling microscopy, the topology of the clusters is mapped to the atomic resolution. The TEM and STM studies have revealed that while Pt and Pd colloids grow as fcc crystals, Au and Ag colloids have icosahedral and decahedral particles. Atomic force microscopy is a subtle variant, where the repulsive force between the tip and the substrate is measured to map the surface morphology. Diffraction techniques, like X-ray and electron diffraction from a beam of clusters, have proved to be a powerful method to study the crystal structure directly especially for larger particles [85,107-110]. Cluster models are generated and refined so as to maximize the simulated diffraction pattern with the experimentally observed diffraction results.

1.8 Physico-Chemical Properties of Clusters

1.8.1 Electronic and Optical Properties

The confinement of a metal to a small volume gives rise to significant deviations of

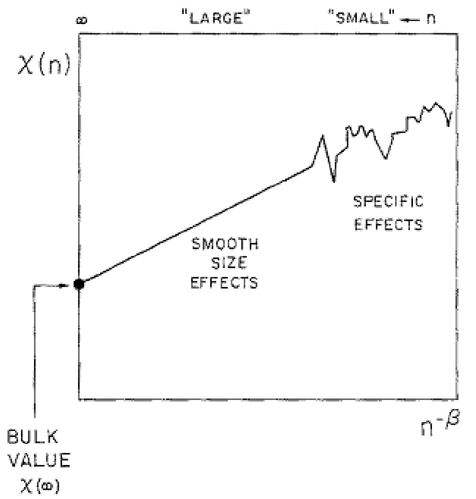

Figure 1.9: A schematic of dependence of cluster property on cluster size.

its physical and chemical properties from their respective bulk characteristics. In the case of alkali and alkali like clusters, the most pronounced confinement effects are: (i) a size dependence of observables such as ionization potential and electron affinity and (ii) pronounced shell effects in ionization and binding energies, especially at or near the so-called "magic numbers" of valence electrons. . In the large cluster regime, many generic cluster properties (G), such as ionization energy(IP), electron affinity(EA), melting temperature (T_m) and cohesive or binding energy (E_b) show a regular variation with cluster size. Spherical cluster model adopts an N-atom cluster as a sphere of radius R, expresses the smooth behavior by simple scaling laws: $G(R) = G(\infty) + aR^{-\alpha}$ or $G(N) = G(\infty) + bN^{-\beta}$ where $G(\infty)$ is the value of property G in the bulk limit.

1.8.1.1 Ionization Potential

Studies of ionization potentials as a function of cluster size have been especially important in tracking the evolution of cluster properties toward their bulk counterparts. IP defined as the smallest energy necessary to remove one electron from a neutral cluster X_n is given as $IP(X_n) = E(X_n^+) - E(X_n)$ and can be obtained from photo ionization measurements or electron impact ionization studies. A general finding is that the ionization energy of homogeneous systems tends to decrease with increasing cluster size, often with a linear dependence of the ionization energy on inverse

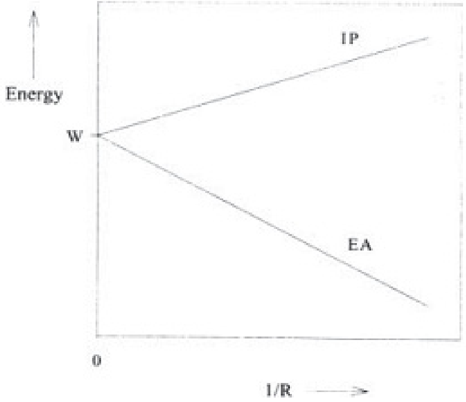

Figure 1.10: Schematic diagram of the variation in the Ionization energy (IE) and electron affinity (EA) of metal clusters as predicted by LDM

cluster size [111].

As discussed previously, experiments have revealed higher ionization potentials for stable closed jellium shell clusters and a sudden drop immediately after the shell closing. The enhanced stability associated with a magic number ($N_e = N$, for neutral clusters) of electrons, corresponding to complete filling of a set of jellium orbitals, leads to a high IP for M_N,while the IP of the cluster $N + 1$, with one extra electron, will be low. Further, the super-imposition of the jellium shell effects on the $N^{-1/3}\ or\ R^{-1}$ trend of the Liquid Drop Model (LDM), gives rise to an oscillatory pattern of IP(s) mentioned earlier. The odd-even alterations observed in several alkali metals (Figure 1.11) are due to the spin-pairing effects. Moreover, the photo ionization cross-sections which have significance in mass spectral measurements made using near threshold energies are found to be lower for jellium closed shells than for open or closed shell clusters. The transition from the non-metallic to metallic bonding possibly via semi-conducting clusters has been clearly demonstrated by the variation of variation of cluster ionization energies with size [112].

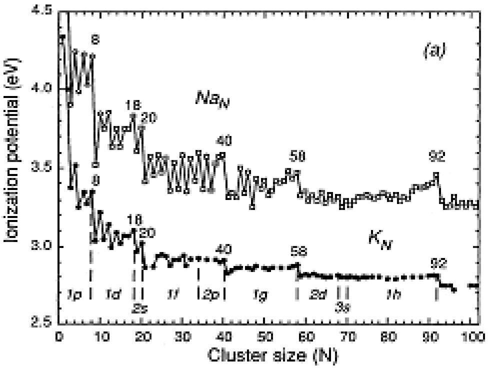

Figure 1.11: Ionization energies of K and Na clusters as a function of n with jellium shell closings indicated.

1.8.1.2 Electron Affinity

The correspondence between the photoelectron spectrum (PeS) and the density of electronic states involves the electronic and geometric structure of the final state. The PeS is plotted with the "electron binding energy" (defined as the difference between the energy of the incident photon and the emitted electron) as the abscissa. The electron affinity values of Al clusters [113] derived from the PeS experiments have a maxima at $6,13,19,27$ and 29 number of electrons which agree with electronic shell model with an ellipsoidal distortion.

Figure 1.12: a) Experimental electron affinities of Al_n clusters derived from photoelectron onset signals. The total electron numbers (3X) of the neutral clusters are listed for clusters which immediately precede a shell closing.(b)Vertical electron affinity of Cu_n clusters as a function of size n, and compared with the highest energy levels of the ellipsoidal shell model for $n + 1$ electrons

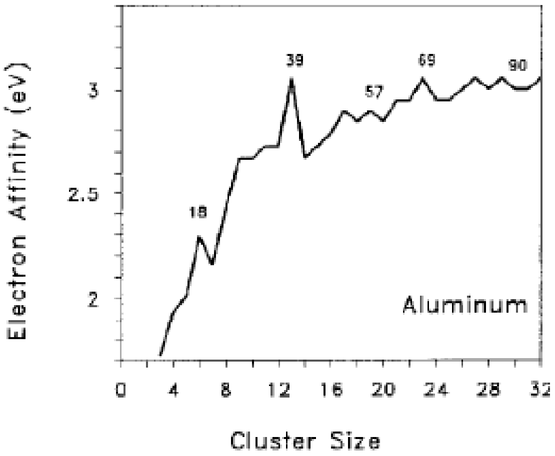

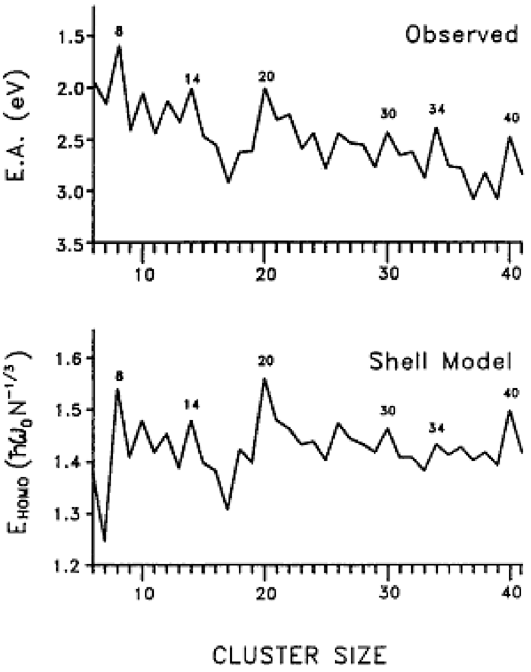

Pettiette *et al.* [76] in their photoelectron spectra of Cu_n^- cluster anions observed that the *EA*'s clearly exhibit shell structure where in the *EA* values of clusters with $7, 19$ and 39 atoms are greater than those of clusters with $8, 20$ and 40 atoms respectively, as expected from the shell model. The electron affinities computed from the ellipsoidal shell model agree qualitatively very well with the experimental results. The *EA*'s of silver clusters [114] and gold clusters [115] are qualitatively similar to copper clusters however with more pronounced odd-even alteration.

1.8.1.3 Odd–Even Effects

A subtle feature, in clusters of monovalent s electron metals is an odd–even effect in their *IP* and *EA* values arises from the interplay between cluster deformation and spin effect, which is also apparent in their mass spectrum. It was observed that the even clusters of the alkali metals Na_n and K_n with $n < 20$ have systematically larger IP's than their odd neighbors [116,117]. The fluctuation of IP is thus an electronic structure effect reflecting the shape of the cluster. The odd even oscillations in the ionization potentials of sodium clusters

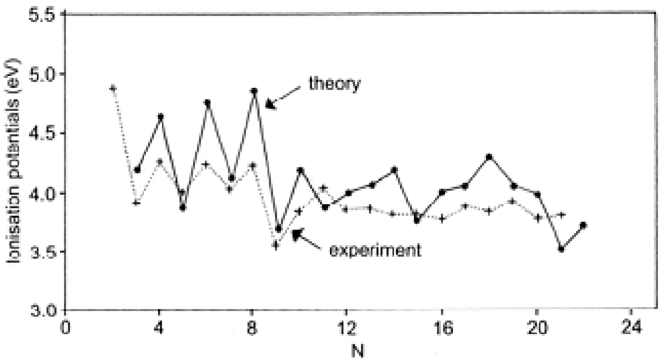

Figure 1.13: Comparison of the experimental and predicted IP with the spherical jellium model of Na_n

obtained with the spheroidal jellium model [118] compared well with the experiment [119]. An inverse trend is observed for *EA*'s of the noble metal clusters with the odd clusters having higher EA values *i.e.,* odd anion M_n^- clusters exhibit a higher photo-detachment thresholds [120]. Katakuse *et al.* have shown that the mass spectra of positively and negatively charged noble metal clusters obtained by ion bombardment show an odd–even alternation in the abundances, with even clusters being less abundant than their odd neighbors [73,121]. Odd-even alteration in the dissociation energies, which is defined as the smallest energy to fragment the cluster in two pieces was observed by Bréchignac *et al.* in small alkali clusters [72,122]. The odd-even staggering of free-electron metal clusters is studied using several simple models: Non-interacting electrons in a rectangular box, triaxial harmonic oscillator, and Hückel model [123]. All the models show qualitatively similar odd-even staggering. In a first of its kind result, Kruckeberg *et al.* have shown that the dissociation energies of Cu_n^+ and Cu_n^{2+} display odd–even effects where the dissociation energies of odd atom clusters are larger than the averaged values of their even-size neighbors [124]. DFT calculations by Martins *et al.* using the local spin density approximation (LSDA) under accurate pseudopotentials reproduced the odd–even effects in the ionization potentials and binding energies [125].

1.8.2 Melting and Fragmentation of Metal Clusters

1.8.2.1 Melting Transition

At low temperature, the cluster particles undergo small-amplitude vibrations and increase in temperature onsets diffusive motions leading to other minima getting populated, and finally as the temperature becomes high enough, the cluster undergoes fast rearrangements, thus behaving like a liquid droplet. A linear reduction of the melting temperature as a function of the inverse particle radius $1/R$ was observed [126,127] with a few known exceptions. The transitions are not sharp but happen smoothly over a finite temperature range [128,129]. The heat capacity can become negative in micro-canonical environments [130] and finally non equilibrium effects like the cluster structure and chemical ordering determine the melting transition. Cluster melting is followed by studying some physical property like photon or X-ray diffraction over the melting point or the internal energy of the cluster as a function of T. Computationally, melting of nanoclusters has largely been studied by molecular dynamics and Monte Carlo Simulations [131]. The simulated calorific curve (total E vs T curve) shows a smooth jump in the melting region corresponding to a peak in the heat capacity ($C(T) = \partial E/\partial T$) [132]. In general, the cluster melting point for a given material shows a monotonic decrease with decreasing size barring some irregular variations on a fine scale especially at small sizes, where the addition or the removal of a single atom can have dramatic effects [126,127]. Martin *et al.*[133] showed that the structure on mass spectra of large sodium clusters depends sensitively on the temperature and the disappearance of structure was attributed to melting. Schmidt *et al.*[136] have observed that the peaks in the calorific curves of Na clusters are not correlated to the stable clusters observed in the mass spectra but driven by the energetic separation of the global minimum from higher isomers. The variation of melting point in *L-J* clusters studied by Frantz [132] showed that $T_m(N)$ in general correlated with the energetic

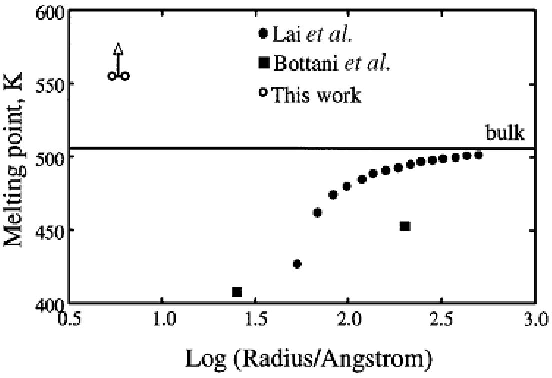

Figure 1.14: Melting points of Sn_n clusters as a function of the average cluster radius. Lai *et al.* [127] and Bottani *et al.* [134] for mesoscopic tin particles, and this work [135] for clusters with 19–31 atoms.

separation of the second isomer from the global minimum. Monte-Carlo simulations on Si clusters revealed dramatic changes in the melting point as the global-minimum structures changed from prolate to cage-like to atom-centered to nearly spherical morphology [137]. In case of gold it is observed that structural transformation from the low-T optimal structures to icosahedral structures takes place before the onset of melting process [138-140]. Shvartsburg *et al.* [135] gave a first experimental evidence of an exception showing the behavior of small Sn clusters whose melting temperature is higher than bulk tin and corroborated by Joshi *et al.* [141] by their molecular dynamics simulations. This was followed by reports on Ga clusters [142,143] and Al_{13} which showed similar exceptions [144].

1.8.2.2 Fragmentation of Clusters

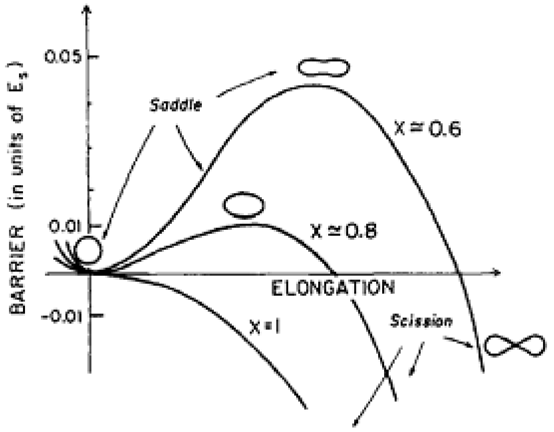

Figure 1.15: Fission of multiply charged clusters.

Clusters undergo fragmentation after collisions with other particle or after absorbing photons and this can proceed spontaneously if the free energy is greater than the binding energy of a constituent atom, ion, or possibly larger fragment. A single atom disassociation channel is normally referred to as evaporation. Since the fragmentation products are usually exited, successive evaporation/fragmentation events produce an ensemble of hot clusters ultimately giving rise to structured mass spectra. A critical size above which a cluster with charge $+q$ is observed is known as the as the effective appearance size, and this depends on the nature of the particle and the charge state [145]. Clusters around critical size seem to dissociate in two competing path ways: evaporation and fission. An unbalanced excess charge on the charged cluster deforms through elongated shapes keeping the volume constant. However, the increase in the surface energy does not match the increase in the surface area, leading to decrease in cohesion. This leads to a barrier for the fission irrespective of the fact that the total energy of the fission products is lower than the charged parent. On the contrary, small clusters undergo spontaneous fission, attributed zero barrier due to a strong columbic repulsion. Electronic shell effects are manifested in the fission products formed. Analysis of the fragmentation of silver clusters containing 12 to 22 atoms gave evidence for the preference of products with even number of electrons and especially species with 2 and 8 electrons are more prominent. Bergmann *et al.* [146,147] from their studies on the in-flight fragmentation of $Al, Cu, and\ Si$ clusters have reported the unimolecular decay of clusters in a molecular beam. Sodium cluster ions, Na_n^+ for $N < 37$, prefer a unimolecular decay, with the dissociation energies showing a saw-tooth like behaviour as a function of n [148,149]. Clusters of Li, Na and K showed a preferential emission of singly charged fragments with 2 and 8 electrons [150-152]. Core level excitation followed by inner-shell photo ionization and subsequent relaxation leads to the formation of multiply charged species. In case of Na_n^{+z} clusters the critical sizes for $z = 2, 3, 4, 5, 6$ and 7 are found to be approximately $27, 64, 123, 208, 321$ and 448 respectively [153]. The effective appearance sizes for doubly charged clusters is ~ 24 for Li_n^{2+} and Na_n^{2+}[150,154,155], 19 for K_n^{2+}[150,156], and 19 for Cs_n^{2+}[157]. In contrast to neutral and singly charged clusters, multiply charged clusters tend to disintegrate into two large charged fragments *i.e.,* undergo fission due to the Coulomb repulsion. For doubly charged Na_{27}^{+2} cluster dissociates to Na_{14}^+ and Na_{13}^+ and for larger clusters, evaporation dominates. This leads to a conclusion that for Na_{27}^{+2} the fission barrier approximately equals the dissociation energy for evaporating. An analysis of the fragmentation of Au_n^{+2} clusters revealed a strong odd-even alteration of the probability of fission to evaporation is larger for even clusters compared to neighboring odd clusters and, the probability of fission relative to evaporation increases strongly with decrease in size of the parent cluster [158]. Liquid-drop model adapted by Saunders [158,159] considered the cluster as a uniformly charged liquid drop whose shape is guided by a competition between the surface tension, which keeps it spherical and electrostatic energy, which prefers elongated shapes. The total energy as a function of shape shows an energy barrier to be overcome to undergo fission [158,159] and spontaneous fission occurs if the value of z^n/n exceeds the critical value $z^n/n = 10\frac{4\pi}{3}\frac{r_s^3\sigma}{e^2}$ where σ is the surface tension and r_s is the cluster radius [158]. Fragmentation of multiply charged Na clusters was explained well with this model. Symmetric and asymmetric fragmentation of doubly charge Ag_n clusters [160,161] and highly charged alkali metal clusters [162,163] are successfully explained by Strutinsky's shell correction method [164]. Molecular Dynamics and DFT formalism are successfully employed to obtain accurate results on fission of various systems [165-167].

1.8.3 Reactivity and Catalytic Activity of Clusters

Clusters are known to exhibit a unique, highly size-dependent reactivity and catalytic properties [168,169]. Studies on gas-phase clusters plays on important role in the evolution of approaches focused on a understanding the elementary steps, knowledge of which is important for the design of tailor-made catalysts Yang *et al.* have showed that small platinum anions Pt_n^- ($n = 3-7$) effectively catalyze the oxidation of CO with either molecular oxygen or N_2O under thermal conditions [170]. Further, typically important catalysis reactions like the reduction of nitrogen oxides by CO, the oxidation of hydrocarbons, or $C-C$ coupling reactions over metal/metal ion clusters are widely studied [171,172]. While, Bernhardt and coworkers have observed the CO oxidation over Au_2^- in a full thermal catalytic cycle [173], the complementary first-principle simulations by Landman and coworkers [173,174] have detailed the elementary reaction mechanisms involving charge transfer processes and the geometric structure and energetics of reaction intermediates. Cox, Kaldor, and coworkers in their studies on the reactivity of anionic and cationic gold clusters $Au_n^{+/-}$ ($n = 2-25$)

towards molecular oxygen, methane, and deuterium [175,176] have observed strong cluster size and charge state dependent reaction behavior. Joint experimental and theoretical investigations demonstrated the capability of the isolated cationic gold dimer Au_2^+ to catalytically activate methane and to subsequently mediate $C-C$ as well as $C-O$ bond formation [177,178].

The catalytic activity of the nanometer-sized clusters supported on thin surfaces depends strongly on the support properties in addition to the composition and size of the deposited clusters. Hence, progress in the designing of size selected cluster catalysts requires a proper insight of the support effects on the deposited clusters. Considering the experimental difficulties in getting direct data on their structural and electronic properties, theoretical information provides an intuitive description of the cluster-surface interactions. All-embracing, the support induced, kinetic and co-adsorption factors control the cluster catalysis on surfaces. Clusters as homogeneous catalysts, have an inherent tendency to decompose, or aggregate to form large colloids or metal particles. Hence, heterogeneous catalysts are more commonly fabricated by dispersing the metal clusters on a high surface area support like an oxide-surface. For a given mass of metal catalyst, this maximizes the total surface area available for catalysis resulting in higher catalytic activity and further, sticking to the support immobilizes them and stabilizes them against coalescence. Moreover, recovery of the catalyst and separation from reactant and product comes at ease.

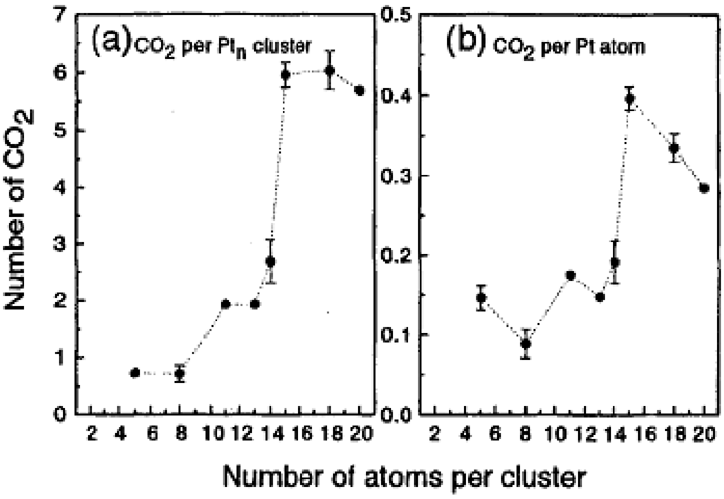

Figure 1.16: Reactivity of Pt_n clusters supported on MgO film

Oxides like MgO, silica (SiO_2), alumina (Al_2O_3) and Titania (TiO_2) have been the most preferred support materials in the heterogeneous cluster catalytic systems. Clusters so dispersed might bind to the periphery of the support or on the interior surface formed by interstitial spaces of the nano-porous materials such as Zeolite. These nano-porous materials offer a very high surface/volume ratio for high catalytic dispersion and the supported clusters might be bare or ligand coated (for better support and segregation). Improved technologies have facilitated to deposit a monodisperse array of clusters from a cluster or molecular beam on to the surface of a support. Extensive studies to elucidate the electronic states of the supported clusters and the interaction of molecules with them are being carried out using various techniques like spectroscopy, microscopy and diffraction. The support surface in general plays an active role on the reactivity of the supported clusters. The induced changes in the geometric and/or electronic structure of the cluster on interaction with the surface give rise to the support interaction, which might open up new cluster relaxation avenues.

Support induced effects; specifically the defect sites have an important role on the nature and degree of the cluster-support binding and subsequently on the activity of the surface deposited clusters [179-182]. Further the cluster-surface interactions might lead to tunneling of charge either from the surface to the deposited cluster [183] or vice versa[184], which has been well correlated with the change in the electron density in the anti-bonding states. The morphology of the deposited cluster depends on the nature and degree of the support-cluster interaction and the shape and configuration is crucial to determine the adsorption and desorption behavior of the reactants and products which in turn reflect their catalytic property. For instance, a stronger support effect on 2D clusters can be anticipated over 3D clusters [185-187]. One strategy to control and tune the deposited cluster properties is to manipulate the support thickness [188-190]. Further, metal supported thin oxide films have been demonstrated to stabilize 2D structures over 3D structures [191]. Increasing the oxide film thickness lead to similar observations obtained from bulk oxides [184,190,192].

Further, the cluster/support interface gives rise to novel and unique reaction sites, and might lead to different catalytic properties. The chemistry of the support material might control the kinetics of adsorption and diffusion of the adsorbed species, which may also determine the catalytic activity. In this context, the spill-over and reverse spillover effects are of great relevance in the nano-catalysis [193-195]. Considering the presence of impurities in the real time experimental conditions, it becomes essential to gain understanding of the catalytic activity in the presence of co-adsorbents [196,197]. Presence of moisture was observed to enhance the catalytic oxidation of CO over supported gold clusters ($Au/TiO_2, Au/Al_2O_3$ and Au/SiO_2) [198-201]. In summary, studies on reactivity of gas phase and supported cluster model systems provide a molecular level insight into charge transfer and bond activation processes.

1.9 Role of Theoretical and Computational Chemistry

Quoting the words of Marks "*small particle structures cannot be understood purely from experimental data and it is necessary to simultaneously use theoretical or other modeling*" [202]. Experimental efforts in combination with theoretical simulations, have given a detailed insight and revealed more surprises into the strongly size-dependent activation, reactivity and unexpected properties of clusters. Computational and theoretical chemistry underwent a major transformation, over the past two decades, initiated by the availability of inexpensive, supercomputing facilities. Concurrently, significant advances in algorithms and numerical methods have been made by computational chemists to exploit the computational power to simulate molecular behavior and chemical processes.

Theory has played and remains to play a significant lead in the progress of cluster science. A classical example might be the electron microscopy results, where suitable models and hypothesis need to be constructed to test the data with the images produced. In fact, it sometimes becomes tough to even rationalize whether the experimental data acquired is meaningful or not. Experiments conventionally give indirect data on the geometric and electronic properties of clusters. Computational calculations predict these properties rather directly. However, with an increasing size of the system, N the number of possible isomers increases exponentially and the computational effort increases significantly and the task to identify the lowest energy isomer among the several low lying isomer becomes daunting. So computations of high accuracy are limited to small to medium clusters. Tremendous progress in the development of methods for *ab initio* calculations of materials properties and for simulations of processes in materials is achieved in the last two decades. In particular, the cornerstone of this development was laid by density-functional theory (DFT), which gave access to handle many-electron systems quantum mechanically. In this framework, the structural and electronic properties of many electron systems in their ground state can be computed to a reasonable level of accuracy and more importantly much faster in comparison to most quantum chemical wave function based methods. Significant advances are being made to calculate the properties of exited states. Within the scope of this theory, Car-Parrinello method evolved to obtain the total energy and determine the lowest energy structure for a given cluster composition. As realized, many properties of the clusters e.g., binding energy, energy barriers *etc.,* cannot be obtained from experiments directly, theoretical methods and models fused with computational tools have been useful to elucidate the spectroscopic (PeS , UV-Vis spectra) and mass spectroscopic data.

Vice versa, cluster science might present a suitable ground to test range of effectiveness of theoretical models which are derived from the boundaries of atomic, molecular and solid state physics. The present day challenge for theory is to come up with an theory of cluster structure and bonding which might prevail over a wide size range starting from a couple of atoms to thousands of atoms.

1.10 Brief outline of the thesis

The goal of the present thesis is to gain fundamental understanding on isolated and supported metallic clusters and their interactions with gas molecules. These studies have implications towards designing new materials for heterogeneous catalysis. Throughout the work standard codes of density functional theory, within the plane-wave based pseudo-potential framework were used as a tool to illustrate the physico-chemical behavior of all systems in this study. The first part of this thesis involves understanding the quantum size effect on the equilibrium geometries and energetics of small lead clusters in the neutral and charged states. In addition, the effect of an impurity dopant on the geometric and electronic structure of lead clusters was investigated. The second part dealt with the interactions of O_2 with Al doped Au clusters. This work was further extended to study the O_2 interaction with $Al-Au$ nano-composites. The primary objective of these works was to investigate the influence of an electro-positive element like Al on the bonding characteristics of electro-negative Au atoms. The results showed an improved oxidation behavior of Au in presence of Al atoms, be it inside the core for core-shell type structure or at the sub-surface layer for periodic slabs. As a natural continuation of the O_2 adsorption, the CO oxidation mechanism on the $Au-Al$ nano-composites was also investigated. In the third part of the thesis, the role of support on the structure and reactivity of metal clusters was investigated. This was carried out by studying the interaction of Au_n clusters on Al_2O_3 surface and subsequent molecular O_2interactions over them.

2. Methodology

The necessary theory and mathematical foundations of quantum chemistry required for theoretical simulations of electronic structure of atoms, molecules and solids was built as early as 1930s. Computation of microscopic properties from the mathematical laws of physics allows for prediction and explanation of observed phenomena. However, strict use of these laws to explain the main features of complex system results in complex set of equations too complicated to solve. In this context, the objective of development of approximation tools for applying quantum mechanics methods (first principle calculations and *ab initio* modeling) without too much of computation has gained a larger relevance. However, results of simulations of relevant accuracy became possible only for small systems till-today.

This chapter is aimed for a brief review of standard material of such tools employed in the thesis. The purpose is not to present the concrete and rigor mathematical description of different methods rather the emphasis is on the philosophy behind these methods.

2.1 Schrödinger's Equation

In general, predicting the ground-state electronic structure of matter amounts to solving the time-independent Schrödinger equation(SE) [203] (eq. 2.1)

$$E = \langle \psi | \hat{H} | \psi \rangle \qquad \text{eq. 2.1}$$

where E, $\hat{H}$ and ψ represent the total energy, the Hamiltonian operator and wave function respectively, of the N constituent electrons and M atomic nuclei in a given arbitrary system. Solving this equation is a complex mathematical problem and it is indeed a challenge to solve it for the real systems.

In order to compute the properties of a system from first principle methods, we need to describe the Hamiltonian of the system. The Hamiltonian of a system containing of N number of electrons and M nuclei can be written as

$$H = -\hbar^2 \sum_i \frac{\nabla_i^2}{2m} - \hbar^2 \sum_I \frac{\nabla_I^2}{2M_I} + \frac{1}{2} \sum_{i \neq j} \frac{e^2}{|r_i - r_j|} - \sum_{i,j} \frac{Z_i e^2}{|r_i - R_I|} + \frac{1}{2} \sum_{I \neq J} \frac{Z_I Z_J e^2}{|R_I - R_J|} \qquad \text{eq. 2.2}$$

where-in r_i denotes the position of the i^{th} electron, R_I is the position of the I^{th} nucleus, Z_I is the atomic number of the nucleus, m is the mass of the i^{th} electron and M_I is the mass of the I^{th} nucleus respectively. This accurate description of the many electron system considering the intricate electron-electron and nucleus-nucleus interaction terms, makes it an impracticable situation to solve the Schrödinger equation for the Hamiltonian described in eq. 2.2 even using the best computational facility.

Acceptable approximations to simplify the Hamiltonian of the Schrödinger equation with ability to give reasonable solutions to predict various properties of matter have been drawn. Three major approximations drawn to this end are the crux to the electronic structure theory. The first simplification involves separating the electrons into: Core electrons and Valence electrons. The core electrons are the filled, inner shells of the atoms localized around the nuclei and play no role in bonding and determining the electronic properties of the solid *e.g.,* for the free Si atom whose electronic configuration is $1s^2 2s^2 2p^6 3s^2 3p^2$, the $1s^2 2s^2 2p^6$ (filled shells) form the core electrons. Such lumping of the core shells together with the nuclei forms an ion core. In eq. 2.2, I and J denote the core ions and i signifies the valence electrons which occur in the incomplete orbital *i.e.,* $3s^2 3p^2$ in the case of Si.

In view of the large rest mass ratio between electrons and nucleus, the nucleus can be considered stationary on the scale of electronic motion, over a large range of momentum ratios. Thus this Born-Oppenheimer (BO) approximation[204] conveniently decouples the nuclear and electronic degrees of freedom. The many body problem got simplified to the dynamics of the electrons with some frozen ion configuration of the nuclei. In this context, the ion-ion interaction term cannot be ignored because the minimum energy of the system (ground state) can be determined by varying the ionic positions. However this classical treatment of nuclei ignores their quantum spins in order to obtain the ground state. Thus one can freeze the nuclear positions at the origin *i.e.,* the nuclear kinetic energy is zero in the electronic Hamiltonian. The Hamiltonian in eq. 2.2 of the system in reduced to

$$H = T_{elect} + V_{ion-elec} + V_{elec-elec} + V_{ion-ion} \qquad \text{eq. 2.3}$$

Appling the Hartree atomic units, $\hbar = m_e = e = 4\pi\epsilon = 1$

The electron kinetic energy term is

$$T_{elec} = -\frac{1}{2}\sum_i \nabla_i^2$$

The electron-ion potential is written as

$$V_{ion-elec} = -\sum_{i,I} \frac{Z_I}{|r_i - R_I|}$$

The potential energy due to electron-electron interaction is

$$V_{elec-elec} = \frac{1}{2}\sum_{i \neq I} \frac{1}{|r_i - r_j|}$$

and the potential energy due to ion-ion interaction is

$$V_{ion-ion} = \frac{1}{2}\sum_{I \neq J} \frac{Z_I Z_J}{|R_I - R_J|}$$

The Hamiltonian can further be modified by employing pseudopotentials that replace the ion-ion interaction potential of the core electrons.

2.2 Independent-electron approximation

The independent electron approximation is one of the approaches that were made to simplify the solution of the Schrödinger equation of a system having more than one electron. It lays on the assumption that the electron-electron contributions can be handled by a proper choice of a periodic potential $V(r)$, in the one electron Schrödinger equation below

$$[T_{elec} + V(r)]\psi_k(r) = \epsilon(k)\psi_k(r) \qquad \text{eq. 2.4}$$

k, is a wave vector and r denotes the position of the electron. The potential $V(r)$ so chosen should describe the interaction of periodic ions and interactions of other electrons properly. This means that to start with a proper $V(r)$, eq. 2.4 has to be solved for all the other electrons first. This leads to a peculiar situation: in order to choose the potential, prior knowledge of the solution is required and to obtain the solution we need to know the potential *a priori*. This requires a serious mathematical effort. Subsequent to the failure of this approach Hartree proposed a central field approximation [205-207] and subsequently modified by Fock [208].

2.3 Hartree and Hartree-Fock (HF) Approximations

Hartree came up with a simpler classical mean field approach satisfying the variational principle. The solution of the Schrödinger equation for a many body system is expressed as a product of one-electron states.

$$\psi(x_1, \ldots\ldots, x_n) = \psi_1(x_1) \ldots\ldots \psi_N(x_N) \qquad \text{eq. 2.5}$$

where the one electron eigen states represented by $\psi_1(x_1), \psi_2(x_2), \ldots\ldots$ are orthogonal, but un-correlated, since each particle is independent of the other. The potential is defined by separating it into an electron potential (V_{elec}) and an ionic potential V_{ion}. The electrons are presumed to interact only *via* an effective single particle potential which corresponds to the mean coulomb field of all other electrons *i.e.,* each electron moves in its own orbital and feels the average field of all other electrons. This leads to the remaining electrons treated as a smooth distribution of negative charge with their charge density defined as follows,

$$\rho_i(r) = -e \sum_i |\psi_i(r)|^2 \qquad \text{eq. 2.6}$$

The electron potential can be defined afresh by including the charge density term as

$$V_{elec} = e^2 \sum_i \int dr' |\psi_i(r^{'})|^2 \frac{1}{|r - r'|} \qquad \text{eq. 2.7}$$

The Hartree equation is built by substituting V_{elec} and the ordinary ion-ion interaction potential V_{ion} in eq. 2.4,

$$\epsilon_i \psi_i(r) = [T_{elect} + V_{ion}(r) + V_{elec}(r)]\psi_i(r) \qquad \text{eq. 2.8}$$

This assumption ignores the Pauli's exclusion principle [209,210], which demands that the many-body wave function be antisymmetric with respect to interchange of any two electron coordinates and the correlation between the movements of electron under consideration with other electrons. Considering a case of single electron, the Hartree term $V_{elec}(r)$ does not vanish *i.e.,* an unphysical self-interaction energy arises because of the many body interaction of the single electron with its own density. Failure of the above wave function to adhere Pauli's principle makes Hartree approximation highly inaccurate. This approach was improved by including another term called the exchange term, which is known as the HF approximation.

A non-classical mean filed approach, expanding the Hartree approximation has been suggested by Fock [208]. Considering the independent electron approximation, the Hamiltonian (H_{app}) for an N-electron system can be written as a sum of single one-electron Hamiltonians as

$$H_{app} = \sum_{i=1}^{N} H_i = \sum_{i=1}^{N} [T_{elec} + V(r_i)] \qquad \text{eq. 2.9}$$

where $V(r_i)$ represents the one electron potential energy in the field of other nuclei and N is the number of electrons. Alternatively, the H_i can be constructed by including the electron-electron repulsion in some average way. In order to do so, a set of spin-orbitals where x_i can be considered as a combination of spin S_i and orbital position r_i, $x_i = (r_i, S_i)$ are chosen. The Hartree product is still an uncorrelated or independent electron wave equation since a state, $\Psi(x_i)$ with the permutation of x_i is also a solution of the Schrödinger equation and the probability density of finding the electrons in the orbital coordinates is given as a product of one electron probabilities.

$$\rho(x_1, x_2 \ldots\ldots, x_N) = |\psi_1(x_1)|^2\, |\psi_2(x_2)|^2 \ldots\ldots |\psi_N(x_N)|^2 \qquad \text{eq. 2.10}$$

However, the Hartree product still doesn't take account of the indistinguishability of electrons *i.e.,* we still require the state $\Psi(r)$ be anti-symmetric with respect to the interchange of the space and spin coordinates of any two electrons in order to satisfy the Pauli's exclusion principle. One such solution of the Schrödinger equation can be determined by replacing the trivial wave function $\Psi(r)$, by a Slater determinant [211] of one-electron wave functions. If one assumes that the molecular spin orbitals are mutually orthonormal, the Slater determinant for a closed shell system is as follows:

$$\psi(x_1, x_2, \ldots, x_N) = \frac{1}{\sqrt{N!}}\, Det[\psi(x_1), \psi(x_2), \ldots\ldots, \psi(x_N)] \qquad \text{eq. 2.11}$$

where $1/\sqrt{N!}$ is the normalization factor. Interchanging the coordinates of two electrons corresponds to interchanging two rows of the determinant, which changes the sign of determinant and two electrons occupying the same spin orbital corresponds to having two columns of the determinant equal, which makes the determinant zero. Thus not more than one electron can occupy the same orbital (Pauli's exclusion principle completely satisfied). Anti-symmetrizing a Hartree product to obtain a Slater determinant introduces exchange effects, so called because they arise from the requirement that $|\Psi(r)|^2$ to be invariant to the exchange of space and spin of two electrons. The exchange term $-\frac{1}{2}\sum_j \int d^3\, r'\psi_j^*(r')\psi_i(r')\frac{1}{|r-r'|}\psi_j(r)$ in principle acts between electrons of the same spin keeping them correlated and electrons of opposite spin are however left uncorrelated.

The simplest anti-symmetric wave function that can used to describe the ground state of N-electron system is a single Slater determinant. However, the variation principle states that the best wave function of this functional form is the one, which gives the lowest possible energy. By minimizing E_0 with respect to the choice of spin orbitals, one can derive an equation called the HF equation, which determines the optimal spin orbitals. The HF equation is an eigen value equation of the form

$$f(i)\psi_i(x_i) = \epsilon_i\psi_i(x_i) \qquad \text{eq. 2.12}$$

where $f(i)$ is a one-electron operator called Fock operator. Applying the exchange term to the Hartree equation eq. 2.8 leads to the HF equation which is written as:

$$[T_{elect} + V_{ion}(r) + V_{elec}(r)]\psi_i(r) - \frac{1}{2}\sum_j \int d^3 r'\psi_j^*(r')\psi_i(r')\frac{1}{|r-r'|}\psi_j(r) = \epsilon_i\psi_i(r) \qquad \text{eq. 2.13}$$

The essence of the HF equation is to replace the complicated many electron problem by a one electron problem where in electron-electron repulsions are treated in an averaged way. The exchange term introduces some complications to the Hartree equation and causes the HF equation to be difficult to solve because of its non-local nature. Thus, the HF equation, which is non-linear, needs to be solved iteratively by a Self Consistent Field (SCF) algorithm.

Though HF method is a good fundamental-level theory that is practically good at computing the structures and vibrational frequencies of stable molecules, it fails to do well in quantitatively predicting important properties which require a fairly accurate total energy. This approximation fails due to the ignored columbic repulsions of the electrons, which in the approximation is referred to as correlation of electrons. Hence, in the present day modeling Post Hartree-Fock techniques are used to add the appropriate correlation energies to the energies obtained from the HF approximation.

2.4 Post Hartree-Fock Methods

Several methods have been developed beyond the Hartree-Fock approximation for producing wave functions by incorporating the electron correlation properly. The main types are Configuration interaction, many body perturbation theories and Coupled Cluster approaches. However, the boundaries are very thin, different approaches may lead to the same equations finally and moreover combinations can be applied [212].

In the configuration Interaction (CI) method, the wave function is constructed as a linear combination of several determinants based on a HF reference function eq. 2.14. Considering two sets of orbitals: Occupied ($\mathcal{O}$) and Unoccupied ($\mathcal{U}$) and $\psi_{ab\ldots}^{rs\ldots}(r)$ are the exited state determinants, where the electrons from $a, b, \ldots$ have been moved to $r, s, \ldots$, the CI wave function is written as:

$$\psi(r)_{CI} = \psi_0(r) + \sum_{a\in\mathcal{O}} \sum_{r\in\mathcal{U}} d_a^r\, \psi_a^r(r) + \sum_{a<b\in\mathcal{O}} \sum_{r<s\in\mathcal{U}} d_{ab}^{rs}\, \psi_{ab}^{rs}(r) + \ldots\ldots \qquad \text{eq. 2.14}$$

The coefficients d_{ab}^{rs} are determined so as to minimize the energy according to the variational principle. In a full CI calculation, the terms of eq. 2.14 are expanded till all the electrons are in virtual orbitals and it is prohibitively expensive since the method scales exponentially. Practically the progression is truncated after a certain number of excitations (most commonly two *i.e.,* the CISD method).

The many-body perturbation introduced by Moller and Plesset [213] adds higher excitations to the Hartree-Fock theory as a non-iterative correction. The 0^{th} order Hamiltonian is the HF Hamiltonian, which is $\hat{H}_0 = \sum_{i=1}^{n} \hat{f}_i$, where $\hat{f}_i$, the Fock operator is acting on electron i. The perturbation is introduced as a difference to the correct Hamiltonian.

$$\hat{H} = \hat{H}_0 + \lambda V \qquad \text{eq. 2.15}$$

where V is a small perturbation applied to $\hat{H}_0$ and λ is a parameter. The 0^{th} MP energy is obtained as a sum of the orbital energies. The correct HF energy is obtained as a first order correction. So, the first correction is in the Second order, popularly known as MP2 method, The perturbation energy $E_0^{(2)}$ is obtained as a quadruple sum over two-electron MO integrals (eq. 2.16) (where ε_i is the energy of orbital i) .

$$E_0^{(2)} = \frac{1}{4} \sum_{\substack{a,b\in\mathcal{O} \\ r,s\in\mathcal{U}}} \frac{\left| \left\langle a(r_1)b(r_2) \right| \frac{1}{r_{12}} \left| r(r_1)s(r_2) - s(r_1)r(r_2) \right\rangle \right|^2}{\varepsilon_a + \varepsilon_b - \varepsilon_r - \varepsilon_s} \qquad \text{eq. 2.16}$$

The message from eq. 2.16 is that correlation is important when the occupied and virtual orbitals are close in energy, the two occupied orbitals a and b have a stronger contribution to the correlation energy if the Coulomb repulsion between them is strong and virtual orbitals r and s are in close proximity.

2.5 Density Functional Theory

The last two decades have witnessed tremendous progress in the development of methods for calculations of materials properties and for simulation of processes in materials. The cornerstone of this development was laid by density-functional theory (DFT), which casts the difficult complexity of the electron–electron interactions in many-electron systems into an effective one-electron potential, which is a functional of the electron density only.

The aim was to search for accurate and transferable approximations for the electronic exchange-correlation (xc) energy ($E_{xc} = E_x + E_c$] and keeping it scalable. Though the post HF methods have succeeded in achieving the accuracy and transferability, the scalability is poor making the methods highly computing intensive and thus limiting the applicability to only small systems.

DFT offers a completely different approach to the calculation of electronic structure. The fundamental idea of DFT is to rewrite the Schrödinger equation with charge density as a basic variable. It has its original foundation from the Thomas-Fermi model [214,215], which started a new way to study electrons by using the approximate electronic density. In their proposed model, the kinetic energy of the system was represented by a functional of electron density and the subsequent terms such as electron-electron and electron-nuclear interactions were expressed classically to calculate the total energy. Addition of an exchange term later by Dirac [216] and a correction by Weizsäcker [217] made a much improved Thomas–Fermi–Dirac–Weizsäcker density functional theory (TFDW-DFT), but still fell short of expectations because of the totally neglected electron correlation. Hohenberg and Kohn provided the basic framework for modern Density Functional methods in 1964 [218]. According to them "*the total energy of an electron gas enclosed in a large box is a unique functional of electron density* $\rho(r)$ *and that the ground state energy expectation value depends uniquely on the ground state density of the electrons*". The clear-cut consequence of the Hohenberg-Kohn theorem is that the ground state energy E is also uniquely determined by the ground state charge density.

$$\begin{aligned} E[\rho(r)] &= \langle\psi(r)|T+U+V|\psi(r)\rangle \\ &= \langle\psi(r)|T+U|\psi(r)\rangle + \langle\psi(r)|V|\psi(r)\rangle \\ &= F[\rho(r)] + \int \rho(r)\,V(r)dr \end{aligned} \qquad \text{eq. 2.17}$$

where $F[\rho(r)]$ is functional dependent on the charge density $\rho(r)$ alone and not on the potential. Applying variational principle, the ground state energy can be minimized by varying the ground state charge density. Electron density $\rho(r)$ is more attractive as it depends on x, y and z only and eventually, DFT exactly reduces the N-body problem to the determination of a 3-dimensional function $\rho(r)$. However the native form of this is of not much use as the functional form of $F[\rho(r)]$ is unknown. It is necessary to use approximations regarding parts of the functional dealing with kinetic, exchange and correlation energies of the system of electrons.

2.5.1 The Kohn-Sham equations

The problem was reformulated by Kohn and Sham (KS), who proposed a method which involves coupling of wave function and density approach [219]. To understand and obtain the kinetic energy of electrons the KS method relies on mapping the system of interacting electrons onto an auxiliary system of non-interacting electrons having the same ground state charge density. This is frequently called a system of non-interacting electrons. For a system of non-interacting electrons the ground-state charge density which is a scalar function can as well be is represented as a sum over one-electron orbitals $\psi_i(r)$.

$$\rho(r) = \sum_i n_i\, |\psi_i(r)|^2 \qquad \text{eq. 2.18}$$

while n_i denotes the occupation number of the eigen state i, r is any point in real space and the KS orbitals are solutions of the Schrödinger equation,

$$\left(-\frac{\hbar^2}{2m}\nabla^2 + V_{KS}(r)\right)\psi_i(r) = \epsilon_i\psi_i(r) \qquad \text{eq. 2.19}$$

$V_{KS}(r)$ for a given $\rho(r)$ and it can be determined by considering the variational property of the energy. The electron density $\rho(r)$ can be varied by changing the wave function $\psi_i(r)$ of the system. For an arbitrary variation of the $\psi_i(r)$, the variation of E must vanish *i.e.,* if the electron density $\rho(r)$ corresponds to the said wave function, then its total energy is the minimized energy and the whole system is in a ground state. It is convenient to write the total energy of the system which depends on the positions of the atoms as,

$$E(\rho) = T_0[\rho(r)] + V_{ext}[\rho(r)] + V_{elec-elec}[\rho(r)] + E_{xc}[\rho(r)] \qquad \text{eq. 2.20}$$

The first term is the kinetic energy of non-interacting electrons and is obtained by the summation of all contributing effective electrons which are described by wave functions in the state i, in the system.

$$T_o[\rho(r)] = \sum_i n_i \int \psi_i^*(r)\left[\frac{-\hbar^2}{2m}\nabla^2\right]\psi_i(r)dr \qquad \text{eq. 2.21}$$

$V_{ext}[\rho(r)]$ represents the electrostatic potential in lieu of the nuclei interactions and is expressed as

$$V_{ext}[\rho(r)] = \int V_{ext}(r)\rho(r)d^3r \qquad \text{eq. 2.22}$$

The third term describes the repulsion between the electrons in the system. The electron-electron interactions potential can be written as

$$V_{elec-elec} = e^2 \iint \frac{\rho(r_1)\rho(r_2)}{|r_1 - r_2|} d^3r_1 d^3r_2 \qquad \text{eq. 2.23}$$

However, considering a non-interacting system, the interacting terms can be ignored and the total energy can be written as a summation of kinetic energy $T_0[\rho(r)]$ and the external potential $V_{ext}\,[\rho(r)]$. Hence, the ground state non-interacting total energy is given by

$$E(\rho) = T_0[\rho(r)] + V_{ext}\,[\rho(r)] \qquad \text{eq. 2.24}$$

$\rho(r)$, the charge density for the occupied sate can be obtained by self consistency method by solving the KS equation. The KS equation in Hartree atomic units, reduces to

$$\left[-\frac{\nabla^2}{2} + V_{ext}\right]\psi_i(r) = \epsilon_i \psi_i(r) \qquad \text{eq. 2.25}$$

It is mandatory to normalize the wave function $\psi_i(r)$, in order to make sure that $\rho(r)$ satisfies the normalization condition for the number of electrons, N

$$\int \psi_i^*\,(r)\psi_j(r)dr = \sigma_{ij}$$

where i and j represent the eigen states of the wave functions. The non-interacting system, with one external potential can be easily solved, to obtain the total energy of the ground state. Extending this information, the interacting system can be written by including all the terms that were ignored. The total energy in an interacting system is given in eq. 2.20 as

$$E(\rho) = T_o[\rho(r)] + V_{ext}\,[\rho(r)] + V_{elec-elec}\,[\rho(r)] + E_{xc}\,[\rho(r)] \qquad \text{eq. 2.20}$$

The kinetic energy term is still the same KE term, $T_o[\rho(r)]$ of the non-interacting system. However, the exernal potential $V_{ext}\,[\rho(r)]$ is perturbed in the interacting system and generalized into an effective potential, $V_{eff}\,[\rho(r)]$

$$V_{eff} = V_{ext} + V_{Hartree} + V_{xc} \qquad \text{eq. 2.26}$$

$V_{Hartree}$, the Hartree potential, contains the electrostatic interactions among clouds of charge.

$$V_{Hartree} = e^2 \int \frac{\rho(r')}{|r - r'|} d^3r'$$

V_{xc}(eq. 2.27), the exchange-correlation potential, is a functional derivative of the exchange-correlation energy; and takes care of all other contributions *i.e.,* electron exchange, electron correlation, a portion of the kinetic energy which is needed to correct the kinetic energy of an all interacting system ($E_{kin}(\rho) - E_{kin}^{ks}(\rho)$) and the correction for self-interaction introduced by the classical coulomb potential which were not accounted for by previous terms, and is independent of the external potential

$$V_{xc} = \frac{\partial E_{xc}[\rho(r)]}{\partial \rho(r)} \qquad \text{eq. 2.27}$$

So, the Schrödinger equation of one-electron is written as

$$\left[-\frac{\nabla^2}{2} + V_{ext} + V_{Hartree} + V_{xc}\right]\psi_i(r) = \epsilon_i \psi_i(r) \qquad \text{eq. 2.28}$$

and this forms a set of KS equations for an interacting system. The above discussion holds for a non-spin polarized case, where in the system in non-magnetic. However for spin polarized systems, the KS equations will now be based on the electron density of both spins,

$$\rho(r) = \rho_{\uparrow}(r) + \rho_{\downarrow}(r) \qquad \text{eq. 2.29}$$

and the spin density σ of the material. Some terms like V_{xc} heavily depend on the spin density. Finally, the spin-polarized Kohn-Sham equation of an interacting system is expressed as

$$\left[-\frac{\nabla^2}{2} + V_{ext} + V_{Hartree} + V_{xc}^{\sigma}\right]\psi_i^{\sigma}(r) = \epsilon_i^{\sigma} \psi_i^{\sigma}(r) \qquad \text{eq. 2.30}$$

The eigen states ψ_i and the eigenvalues ϵ_i also depend on the spin density $\sigma(r)$ of the material. If both spins are equal, the spin density σ vanishes for the whole system[220], which means the spin density relies on the asymmetry of the spin occupancy.

2.5.2 Exchange-correlation potential

As discussed in the previous sections, the last term of the KS equations the exchange correlation, contains all the contributions that are un-accounted for by the previous terms. Electrons, being fermions need to follow the Pauli Exclusion Principle[209,210], which demands that the wave function to be anti-symmetric, under a particle exchange. Moreover, electronic wave-functions are also correlated by the instantaneous Coulomb interaction irrespective of spin. This weaker correlation is neglected by any mean-field approximation. The energy difference is caused by the small decrease in the coulomb energy due to the small separation of the electrons of different spin caused by their charges. In terms of the explanation above, the correlation energy is always less than the exchange energy. The exchange E_{xc}(eq. 2.31) can be written as a summation of the exchange and the correlation energy

$$E_{xc} = E_x + E_c \qquad \text{eq. 2.31}$$

Considering a situation of two electrons satisfying the exchange-correlation principle, E_{xc} can be written as a function of charge density $\rho(r)$ as

$$E_{xc}[\rho(r)] = \frac{1}{2}\iint \rho(r_1)\rho(r_2)\,(V(r_1) - \mathrm{V}(r_2))d^3r_1d^3r_2 \qquad \text{eq. 2.32}$$

Having evaluated the $E_{xc}[\rho(r)]$, to obtain the total energy $E[\rho(r)]$ of the system, the exchange-correlation potential V_{xc} can be fetched by eq. 2.27. This potential V_{xc} is useful in solving the density functional KS equations. However, a reasonable estimate for the exchange-correlation energy $E_{xc}[\rho(r)]$ and V_{xc} is not known. If the exact form of V_{xc} is known, the solution of the Kohn–Sham equation would generate the correct energy of the total ground state. So while the HF model started with the approximation that the total wave function can be described by a single Slater determinant, and therefore cannot result in an exact solution, the DFT approach is in principle exact. Unfortunately the correct form of $E_{xc}[\rho(r)]$ is not known, so the art of DFT calculations is to find good functional form for this energy. In practice, the utility of the theory rests on the approximation used for $E_{xc}[\rho(r)]$.

2.5.3 Approximations to the exchange-correlation potential

The efforts to develop the approximated exchange correlation potentials is similar to the Jacobs ladder, where in each rung of ladder is introduced with a new set of possible corrections to some quantity *e.g.,* the charge density, its gradient, the kinetic energy density, the orbitals, non-local contributions *etc*., to the E_{xc}. A couple of highly popular approximations to the XC are Local Density Approximation (LDA), Generalized Gradient Approximation (GGA), Meta GGA and Hybrid functionals. Nonetheless, in this section we focus only on the details of LDA and GGA which are used in this thesis.

2.5.3.1 Local Density Approximation

The first rung of approximations was introduced as early as 1965, by Kohn and Sham, the Local density approximation (LDA) [219]. This has the spirit of Hartree theory and the Slater's local exchange ($E_{xc} = 0$). In this approximation, the electron density $\rho(r)$, which defines the electron density locally, is considered to vary smoothly. Under the assumption that an electron at a point r, experiences the same effect from the combination of the surrounding electrons as if the density of the surrounding electrons had possessed the same values throughout the entire space, the exchange correlation energy is approximated as a summation (integral) of the electron contribution from a volume which depends on the electron density $\rho(r)$.

$$E_{xc} = \int \rho(r)\epsilon_{xc}\,[\rho(r)]d^3r \qquad \text{eq. 2.33}$$

where ϵ_{xc} is the XC energy per particle of a homogeneous electron gas (HEG). The LDA is strictly local in space, and is exact in the limit of slowly varying densities. Highly accurate simulations by Ceperley and Alder for the energy of the HEG provided accurate values of the correlation energy density [221]. From theoretical point of view ϵ_{xc} is parameterized by various approaches, by using different analytic forms *e.g.,* Hedin and Lundqvis Approximation [222], Vosko-Wilk-Nusair (VWN) approximation [223], Perdew-Zunger (PZ81) approximation [224], Cole-Perdew(CP) approximation [225], Perdew-Wang (PW92) approximation [226]. Several other expressions for ϵ_{xc} can be found in the literature. The simplest approximation of the DFT, LDA yielded good results especially for solids. The structural and vibrational properties are in general well defined; the most stable crystal lattice is properly obtained; the lattice parameters, bulk modulus and phonon frequencies are accurate within a few percent. LDA behaves well as is it grants a good description of the so-called exchange-correlation hole, which is explained as electrons avoiding each other at a point r, thus obeying the Pauli Exclusion Principle. The exchange-correlation energy includes the coulomb interaction of each electron.

$$E_{xc}[\rho(r)] = \frac{1}{2}\iint \rho(r)\rho_{xc}(r,r^{'})v(r-r^{'})d^3rd^3r'$$

where the density $\rho_{xc}(r,r^{'})$ is regarded as the conditional density due to the fact that if the separation between these two particles approaches zero, it disappears and leaves a hole which is called the exchange-correlation hole. The limitations of LDA are avoided by using functionals, which are deeper and more fundamental in nature. Though LDA behaves well in condensed matter systems, it is less accurate in atomic and molecular physics. It over estimates the cohesive energies (~20% or more) and consequently underestimates the bond lengths[219]. The next rung of functionals, gradient-corrected functionals constructed on a generalized gradient approximation (GGA) are the simplest extension of LDA to inhomogeneous systems.

2.5.3.2 Generalized Gradient Approximation

As neither positive charge nor electronic charge are uniformly distributed in actual molecules, to account for the inhomogeneity of the electron density a non local correlation involving the gradient of $\rho(r)$ is added to the exchange energy. So, GGA takes into account the density of the electron and its gradient at each point in the space. The exchange-correlation functional is constructed by starting from the second order density gradient expansion for the exchange correlation hole surrounding the electron in a system by slowly varying the densities [227,228] and is expressed as

$$E_{xc}(\rho(r)) = \int \epsilon_{xc} f[\rho, \nabla\rho]\rho(r)d^3r \qquad \text{eq. 2.34}$$

where $f[\rho, \nabla\rho]$ is a parameterized analytic function, and $\nabla\rho$ is the gradient density of the electrons. The above equation is based only on the systems of non-spin systems. Considering a spin polarized system, eq. 2.34 above will take the form of spin densities as

$$E_{xc}[\rho_\uparrow, \rho_\downarrow] = \int \epsilon_{xc} f[\rho_\uparrow, \rho_\downarrow, \nabla\rho_\uparrow, \nabla\rho_\downarrow]\rho(r)d^3r \qquad \text{eq. 2.35}$$

The GGA functionals yield much better atomic energies and binding energies than LDA [229,230]. It tends to improve the energy band gap between valence and conduction bands in the cases of semiconductor and insulator materials[231]. GGA functionals are efficient in computational cost and are numerically accurate and reliable. GGA tends to satisfy the demands of quantum mechanics and solid state physics. Accordingly a great number of GGA functionals has been devised for different classes of systems, the most commonly used ones being the functionals proposed by Perdew *et al.* (PW91) [232,233], the Perdew-Burke-Ernzerhof (PBE) [234,235] functional and its revised form proposed by Hammer *et al.* (RPBE) [230].

The meta-GGA functionals are a direct extension of the concept of GGA: in addition to the dependence on the local density $\rho(r)$ and its gradient $\nabla\rho(r)$, the meta-GGA functional depends on either the Laplacian of the electron density $\Delta\rho(r)$ or the electron density $\tau(r)$ defined as $\frac{1}{2}\sum_{k=1}^{N}|\nabla\psi_k(r)|^2$ where the summation extends over all occupied KS eigen states. Some popular functionals of this type are: PKZB [236], tHCTH [237],TPSS [238], RTPSS [239], VSXC [240] and M06L [241]. Hybrid functionals are characterized by mixing nonlocal Fock exchange and local or semi-local DFT exchange in a certain proportion. The most popular hybrid is the three-parameter B3LYP functional [242] constructed by mixing 80% of LDA with 20% of HF exchange and mixing 19% of the Vosko-Wilk-Nusair (VWN) functional [223] with 81% of Lee-Yang-Parr [243] correlation in the correlation part.

PBE0[244] and HSE03[245] functionals are a couple of attempts to reduce the empirical parameters. The PBE0 functional mixes $1/4$ of exact (HF) exchange with $3/4$ of PBE exchange, and describes correlation in the GGA (PBE) and in the HSE03 functional, the Coulomb kernel is separated into a short- and long-range part the mixing of HF and DFT exchange is applied only to the short-range interaction. Further range-separated hybrid functionals are defined to correctly describe the long-range behavior of the exchange-correlation potential [246-248].

2.5.4 Solution of the Kohn Sham equation: Self-consistent Field Procedure

The electronic ground state for a fixed atomic position is cane be found by solving the KS equations self consistently, by diagonalizing the Hamiltonian matrix and then iterating on the charge density until self-consistency is achieved. Therefore, in order to construct the KS equations for the system, the wave functions that build the electronic charge $\rho(r)$ must be known and these wave functions are in actual are a solution of the KS equations. It means that an estimated solution of the Kohn Sham problem needs to be known before it can be solved. An iterative procedure becomes handy in this situation. The geometries of the system for density functional calculation are constructed intuitively or from the knowledge of previous experimental or computational results. The trial electronic density is then constructed from the trial wave function. The exchange correlation operator is subsequently constructed by including the explicit form of the exchange correlation potential. Taking a variational basis set $\{\boldsymbol{\phi_j}\}$ into consideration, this, the Hamiltonian $\boldsymbol{H_{ij}}$ and the overlap matrix $\boldsymbol{S_{ij}}$ elements are calculated. The matrix $\boldsymbol{H - \epsilon S}$ is diagonalized which involves unknown coefficients as follows:

$$(H - \epsilon S)c_{ij} = 0 \qquad \text{eq. 2.36}$$

This gives a set of one particle eigen values with their corresponding coefficients c_{ij} of expansion. The related wave function can be constructed as

$$\psi_i(r) = \sum_j c_{ij}\ \phi_i(r) \qquad \text{eq. 2.37}$$

which can further be used to construct the new electron density $\boldsymbol{\rho(r)}$**,** which is now called the output electron density. If the output density is different from the input density, the output density is used as a new input electron density and the procedure is repeated self consistently until the output density is same as the input. This is known as the Self Consistent Field (SCF) cycle. This algorithm works well only if the error on output is smaller than the error on input. A simple algorithm that generally works, although sometimes slowly, is the simple mixing. When a new input charge density is generated by mixing the input and output charges, the degree of mixing must be chosen empirically in order to get fast convergence. The final resultant electron density is used to calculate the total energy $E[\rho(r)]$. The forces $F_r = -{}^{\partial E}/_{\partial r}$ on the atom in the system can be calculated using the output charge density.

2.6 Technical Aspects of Calculations

2.6.1 Basis Sets

Basis set, the mathematical representation of the molecular orbital forms the core of application of the *ab initio* and the DFT methods for any particular problem. A proper choice of optimal basis set is important for accuracy, transferability and scalability as is the choice of ideal total energy method. The molecular orbitals are usually expanded as a Linear Combination of Atomic Orbitals, which are a pre-defined set of one electron functions known as basis functions. The basis functions collectively form the basis set. The basis set need to be chosen in such a way that the resultant molecular orbital wave function Ψ_i should be single valued, finite, continuous, and quadratically integrable.

Two popular approaches: (a) atom centred basis set, where the basis set is constructed as a small group of functions accurately describing typical wave function for a given system, *e.g.,* Slater type orbitals (STO) [249] and Gaussian type orbitals (GTO) [250] and (b) plane wave basis set, where a universally transferable set of functions are chosen.

STO(s) have the following general form:

$$\phi_i(\zeta, n, l, m; r, \theta, \phi) = N r^{n-1} e^{\zeta r} Y_{lm}(\theta, \phi) \qquad \text{eq. 2.38}$$

where ζ is a constant related to the effective charge of the nucleus, n, l, m are the principal, angular momentum and magnetic quantum numbers respectively, r is the radial distance of the electron from the atomic nucleus, θ, ϕ are the spherical coordinates, N is the Normalization constant and the spherical harmonic $Y_{lm}(\theta, \phi)$ is the angular part of the orbital [249]. STO(s) describe the radial electron distribution fairly well, but handling the many-centre two-electron integrals which requires numerical integration techniques is rather difficult and very time consuming. The general form of GTO(s) are expressed as

$$g(\alpha, x, y, z, i, j, k) = N x^i y^j z^k e^{-\alpha r^2} \qquad \text{eq. 2.39}$$

where N is a normalization constant, α is an exponent similar to ζ of STO(s), x, y, and z are cartesian coordinates, i, j, and k are integral exponents of the cartesian coordinates. GTO(s) have sufficient flexibility and are extremely useful in *ab initio* calculations of polyatomic molecules [251-254]. However, GTO describes the radial electron distribution less satisfactorily especially in the region near the nuclei due to the lack of cusp (Figure 2.1).

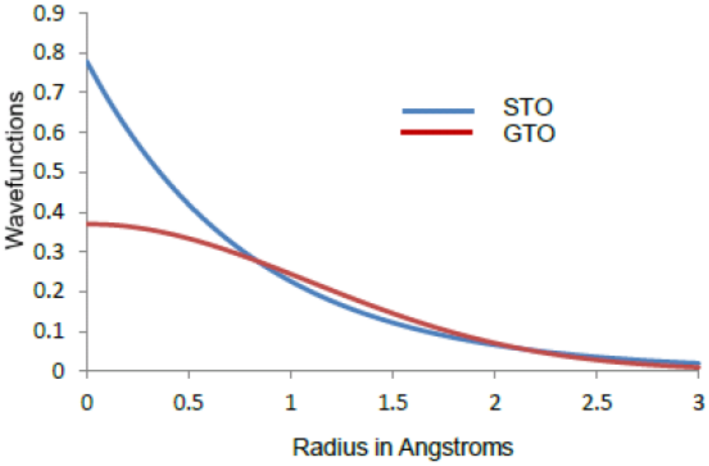

Figure 2.1: Comparison of STO(s) and GTO(s) with increasing radius

This imperfection was reduced by using contracted Gaussian functions where in the STO(s) are approximated by a linear combination of n primitive Gaussian functions or Gaussian type orbitals. This gave rise to the nomenclature of the so-called minimal basis set, such as STO-3G and STO-6G. Moreover, the integrations can be handled analytically, where in many-center two-electron integrals can be reduced to much simpler forms since the product of two GTOs is another GTO.

The minimal basis sets which mimic atomic orbitals might not be satisfactory in describing anisotropic electronic distributions in a molecular environment. The orbitals need to be flexible and perhaps contract/expand to different extent in different situations and especially for the valence electrons. Pople and coworkers [255] have developed a recipe termed as the split valence basis sets such as 3-21G and 6-31G, where the valance orbitals are composed of two or more functions of different sizes or radial distributions. The resultant orbital of intermediate size fits best for the molecular environment. The most important additions to basis sets are polarization functions and diffuse basis functions. Basis set designations such as $n_1 - n_2 n_3 n_4 + +G^{**}$ indicate that the basis set is a split valence basis set (indicated by $-$), to which diffuse functions ($+$) and polarization functions ($*$) have been added [256].

In an infinite periodic system such as crystal, the number of basis sets that are required to describe the wave functions of the infinite number of interacting electrons, will be infinite. As a further technique for practical implementation of DFT, atom-independent Plane Waves (PW) were considered as a perfect basis to describe a free electron wave function. This is an exact eigen function of a homogeneous electron gas and the standard method for periodic boundary condition calculations in crystalline solids. By ignoring the potential caused by the ions, the plane waves become proper solutions of the KS equations. However, in multi-atom systems, the potential is not smooth, and the wave functions in the core states are highly complicated. An extension to the plane wave solution where in the potential is assumed to be symmetric inside the sphere and zero outside is implemented. So, the augmented plane wave is similar to the original plane wave outside the sphere and is continuous at the radius $r = R$ where by

$$\phi(r) = e^{ik.r} \quad \text{eq. 2.40}$$

Since, the continuous behavior of the wave functions at $r = R$ does not adhere to the requirement of the solution for the Schrödinger equation, the wave function is written as an expansion of the plane waves. The wave function of the expanded augmented plane waves can be written in terms of the reciprocal lattice vectors G

$$\psi(r) = \sum_{G} c_G \psi_{k+G(r)} \quad \text{eq. 2.41}$$

Further, the symmetry properties of the crystal can be invoked in-order to reduce the system size to the unit cell of the bulk solid by applying periodic boundary conditions. The translational symmetry is taken into account in the construction of the Hamiltonian and the wave-functions by applying the Bloch's theorem[257]. This leads to the expression of wave functions as the product of two functions, a periodic part and other plane wave function. This is expressed mathematically as:

$$\Psi_{\mathrm{n}\vec{\mathrm{k}}} = \mu_{nk}(r)e^{ik.\vec{r}} \quad \text{eq. 2.42}$$

where n and k represent the band index and the crystal momentum (confined to the first Brillouin zone) of the reciprocal lattice[258], respectively. In eq. 2.42, $\mu_{nk}(\vec{r})$, which is periodic and has the same periodicity as the lattice can be expanded in terms of a discrete plane-wave basis set with wave vectors $\vec{G}$ that are reciprocal lattice vectors. Mathematically, eq. 2.43 represents the definition of this function:

$$\mu_{n\vec{k}}(\vec{r}) = \sum C_{n\vec{k}}^{\vec{G}} e^{i\vec{G}.\vec{r}} \quad \text{eq. 2.43}$$

where $C_{n\vec{k}}^{\vec{G}}$ are the plane wave coefficients and $\vec{G}_i . \vec{a}_j = 2\pi\delta_{ij}$ where $\vec{a}_j$ are the crystal lattice vectors. Thus, substituting eq. 2.43 in eq. 2.42, we obtain the wave functions as the linear combinations of the plane waves as:

$$\Psi_{\mathrm{n}\vec{\mathrm{k}}} = \sum C_{n\vec{k}}^{\vec{G}} e^{i(\vec{G}+\vec{k}).\vec{r}} \quad \text{eq. 2.44}$$

Since the wave functions vary continuously over the Brillouin zone, they do not change much in the neighborhood of a k-point. This makes it feasible to approximate the wave function in the k-space by a wave function at a single k-point. Therefore, the wave functions at a finite set of k-points are chosen and evaluated to sample the entire Brillouin zone. Bloch's theorem reduces the problem of finding an infinite number of wave functions at an infinite number of k-points to finding a finite number of wave functions at only a finite number of k-points sampled on the k-space.

In essence, a finite number of plane waves are required to expand the KS orbitals and the convergence of the kinetic energy cut off E_{cut} can be obtained. The coefficients $C_{n\vec{k}}^{\vec{G}}$ for the plane waves with small reciprocal vectors are typically more important than those with large reciprocal vectors. The plane wave expansion can be truncated to include the plane waves that consist of the kinetic energy less than the energy cut-off as in eq. 2.45

$$\frac{\hbar^2}{2m}|k+q|^2 < E_{cut} \qquad \text{eq. 2.45}$$

The truncation at lower energy cut off will lead to an error when computing the total energy. Including a large number of plane waves up to high frequency (large reciprocal vectors) improves the KS orbital representation. Plane waves by construction are orthonormal and systematically approaching the basis set limit requires no design – simply increasing the E_{cut} and sampling the k-space with a denser grid suffices. Moreover, since they are referenced to the simulation cell rather than the atomic coordinates, the total energy obtained by this basis set is BSSE free and this simplifies the evaluation of the Hellmann-Feynman forces [259].

2.6.2 K-Point Sampling

Bloch’s theorem enabled to consider a finite number of wave functions in the unit cell at a finite number of k-points within the Brillouin zone. The Brillouin zone can be mapped out by a continuous set of k-points (determined by the shape of the Brillouin zone) throughout the region of reciprocal space, which are the loci of the electronic states. Since the electronic wave functions at the k-points that are close together will be identical, the electronic wave functions can be represented over a region of reciprocal space at a single k-point. This allows us to calculate the electronic potential and total energy at a finite number of k-points and choosing a denser grid reduces the error. A metallic system requires a very dense k-point sampling is required to properly define the Fermi surface.

A special k-points method based on an integrated function averaged over the Brillouin zone is used to choose the set of points in the Brillouin zone. This makes the calculation simple and accurate. One can write an integrated function $F(r)$ over the Brillouin zone as

$$F(r) = \frac{\Omega}{(2\pi)^3} \int_{BZ} f(k) d^3k \qquad \text{eq. 2.46}$$

where $f(k)$ is the Fourier transformation of $F(r)$ and represents the complete symmetry of the lattice and Ω is the volume of the unit cell. The Fourier transformation can be written as a summation as

$$f(k) = f_0 + \sum_{m=1} A_m(k) \qquad \text{eq. 2.47}$$

where $A_m(k)$ is the transformation expression defined by

$$A_m(k) = \sum e^{ik.r} \qquad \text{eq. 2.48}$$

where m is any integer and $A_m(k)$ is associated with any shell of the lattice vector and is a real function. This gives an approximate value for the integral in the equation $F(r)$, which can be exact if $A_m(k) = 0$. The set of points so generated are identical with the generated set by Monkhorst and Pack[260] and is unbiased for generating the set of k-points for sampling the Brillouin zone in fractional co-ordinates. These chosen points can satisfy the expression $A_m(k)$ for the infinite set of nearest-neighbor shells represented by the lattice vectors.

2.6.3 Atomic pseudopotentials approximations

2.6.3.1 Overview of the atomic pseudopotentials

It would still be very expensive to do an all electron calculation including both the core and valence electrons, along with the full Columbic potential using a plane wave basis set. The strongly bound core orbitals and the oscillatory behavior of the valence electrons, require a high E_{cut}, which inturn will require a large number of plane waves to accurately describe the electronic wave functions [261]. This difficulty is surmounted by introducing the concept of pseudopotentials [262-264]. In this approach the electrons are partitioned between core and valence states and the strong electron ion potential is replaced by a much weaker and smoother potential, which is called pseudopotential. This approach is justified because the molecular properties usually depend strongly on the characteristics of the valence wave function and the core-states in a molecule or solid usually differ little from those of the corresponding free atom. For heavier atoms, the relativistic effective core potentials (RECP) are constructed by adding the Dirac-Fock calculation result to the potential [265]. Cut-off energies are significantly reduced by the use of pseudopotentials. This reduction is due to the two reasons: (*i*) high-energy core electrons that require a large basis set have been removed and (*ii*) by removing the core electrons, the valence electrons no longer need to be orthogonal to them. The number of nodes is greatly reduced because the valence electron wave functions only need to be orthogonal to each other due to the replacement of the core

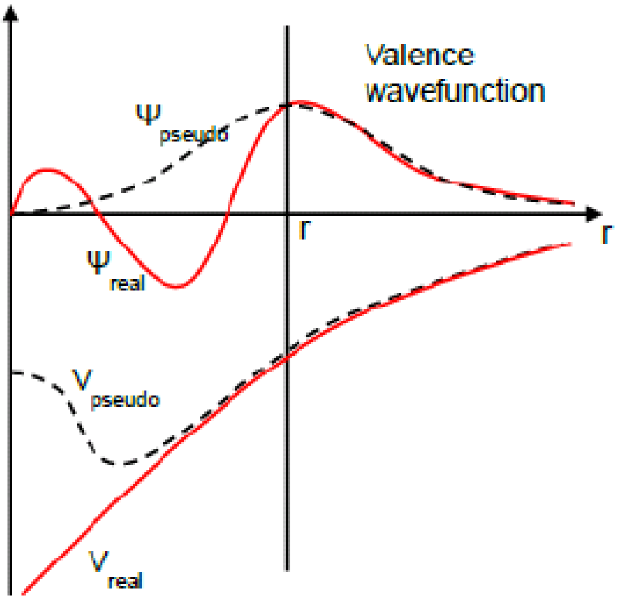

Figure 2.2: Illustrated figure of all electron potential (dashed lines) and pseudo-potential (solid lines) and their corresponding wave function.

electrons by the pseudopotential; this in turn implies a smaller frequency and thus reduced cut-off energy.

A couple of methods for the generation of pseudo potential sets from *ab initio* atomic wave-functions are available. The general objective is to match the all electron wave function and the resulting pseudo wave functions outside a given pseudization radius r_c and preserve the all electron KS eigen values and general properties in the pseudo-wave function. The core radius needs to be chosen carefully, since core electrons might contribute to the bonding of a system. To represent the electron wave functions of the particular shell explicitly, r_c has to be minimum.

A schematic representation of a real potential with pseudopotential is given in Figure 2.2 The pseudo wave function is much smoother than the all electron wave function in the core region since they are node less and do not exhibit fast oscillation arising due to the orthogonality to the core states [266]. However, in the valence electron region, the two potentials match quite well. Hence the pseudo potentials can be effective to compute the properties of the valence electrons of molecules as the core states remain unperturbed. So, the area $r > r_c$ becomes more relevant than $r < r_c$.

Popularly used pseudo-potentials include Norm-conserving pseudo-potentials (NCPP) [265], ultra-soft pseudo-potentials (USPP) [267-269], and projected augmented wave (PAW) method [270,271]. Pseudopotentials are in principle generated by self consistently solving the all electron Schrödinger equation. The resulting valence eigen values are then substituted back into the Schrödinger equation, but with a parameterized pseudo wave function. Inversion of the pseudo wave function then yields the pseudopotential. So the pseudopotentials follow certain criteria *a*) the pseudo wave function must be the same as the all-electron wave function outside a radius r_c *b*) the core charge produced by both sets of wave functions must be the same. This norm conservation requirement can be relaxed though, as discussed earlier *c*) the pseudo wave functions must be continuous at the cut-off radius, as must be the first and second derivatives *d*) the valence all-electron and pseudopotential eigen values must be equal. It should in principle, retain the atomic properties of the element, including the phase shifts on scattering across the core. Since these phase shifts depend on the angular momentum state, the pseudopotential must have projectors for the different angular momentum states *i.e.,* it must be non-local. The most general form can be written as

$$V_{ion} = \sum_{lm} |lm\rangle \, V_l \langle lm| \qquad \text{eq. 2.49}$$

where $|lm\rangle$ are spherical harmonics, and V_l is the pseudopotential for angular momentum l.

2.6.3.2 Norm Conservation and Ultrasoft Potentials

The Kleinman-Bylander (KB) form for the pseudopotential [272] allows V_{ion} to be split into a product of two single sums

$$V_{ion} = V_{loc} + \sum_{lm} \frac{|\psi_{lm}\delta V_l\rangle\langle\delta V_l \psi_{lm}|}{\langle\psi_{lm}|\delta V_l|\psi_{lm}\rangle} \qquad \text{eq. 2.50}$$

where V_{loc} is the local potential and ψ_{lm} are the pseudo wave functions and $\delta V_l = V_{l,nonlocal} - V_{loc}$, where $V_{l,nonlocal}$ is the l angular momentum part of the non-local pseudopotential. This allows the calculation to scale linearly along the size of the basis set. The KB pseudopotentials are norm conserving since the real and the pseudo wave functions generate the same charge density outside the core. This ensures a very simple but relatively hard pseudopotential *i.e.,* the pseudo wave function is no better smoother than the all-electron wave function.

Vanderbilt has proposed an ultrasoft variety of the pseudopotential in which the norm constraint is relaxed and a generalized eigen value formalism is adopted [268]. This led to a substantially softer potential requiring much smaller plane-wave basis set. A non-local overlap operator S is defined as in eq. 2.51

$$S = 1 + \sum_{i,j} Q_{ij}\, |\beta_i\rangle\langle\beta_j| \qquad \text{eq. 2.51}$$

where β_i projectors are functions depending on the ionic positions and Q_{ij} are the matrix elements obtained by $\langle\psi_i|\psi_j\rangle - \langle\phi_i|\phi_j\rangle$. Here ψ and ϕ are the all-electron and pseudo wave functions respectively and $Q_{ij} = 0$ ensures norm conservation. Lifting this condition, gives a non-local operator $V_{non-local}$,

$$V_{non-local} = \sum_{i,j} (B_{ij} + \epsilon_i Q_{ij})|\beta_i\rangle\langle\beta_i| \qquad \text{eq. 2.52}$$

where B is the matrix element, obtained from $B_{ij} = \langle\phi_i|\chi_j\rangle$ and χ is a local wave function obtained from $|\chi_i\rangle = (\epsilon_i - T - V_{loc})|\phi_i\rangle$ where ϕ_i are the solutions of the eigen value problem $(H - \epsilon_i S)|\phi_i\rangle = 0$. This leads to $\langle\phi_i|S|\phi_j\rangle = \langle\psi_i|\psi_j\rangle$, which implies that the amplitudes of the pseudo and all electron wave function are same beyond the cut off radius. Hence relaxing the norm conserving condition helps to construct smoother wave functions with lower cut off energies, which in turn reduces the number of plane wave basis set required.

2.6.3.3 The Projector Augmented Wave (PAW) method

Due to the nonlinearity of the XC functionals in DFT, certain nonlinear core-corrections are required to describe the valence-core interaction in systems where the overlap between core- and valence-electron densities is not negligible. As described in the previous

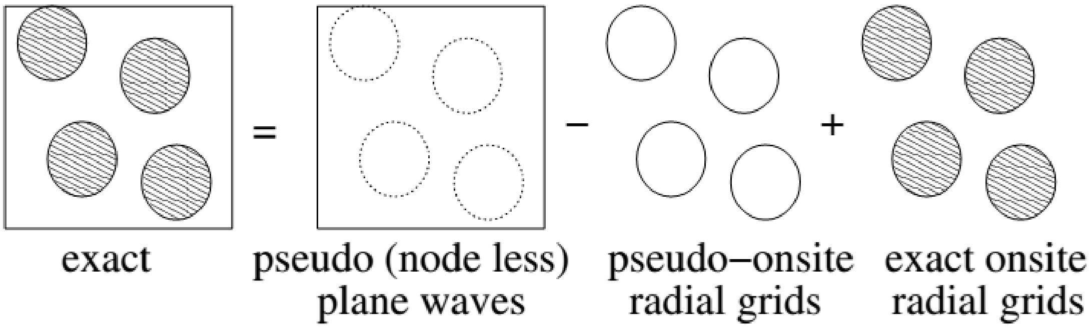

Figure 2.3: Schematic illustration of the Pseudo-potential description under PAW method.

section, ultrasoft pseudopotential methods fail in cases where the core effect is significant. Projector Augmented Wave Method introduced by Blochl [270] is both computationally efficient and accurate than the previous approaches though it is complex to implement. This method unifies all-electron and pseudopotential approaches by physically mapping all the electron valence wave functions (AE) onto non-interacting pseudo wave functions *via* a linear transformation T [273]. The expectation value of any operator $\hat{A}$ can be evaluated accordingly as

$$\langle \hat{A} \rangle = \langle \psi | \hat{A} | \psi \rangle = \langle \tilde{\psi} | \mathrm{T}^{\dagger} \hat{A} \mathrm{T} | \tilde{\psi} \rangle = \left\langle \tilde{\psi} \middle| \hat{\tilde{A}} \middle| \tilde{\psi} \right\rangle$$

with $|\psi\rangle = \mathrm{T}|\tilde{\psi}\rangle$ and $\hat{\tilde{A}} = \mathrm{T}^{\dagger}\hat{A}\mathrm{T}$. The transformation smoothens the all electron wave function in the neighborhood of the nucleus. The linear transformation is constructed as a sum of local atom centred transformations

$$\mathrm{T} = 1 + \sum_{atom} \mathrm{T}_{atom}$$

and each T_{atom} acts with in the augmented region (Ω) defined around each atom. Outside the augmented region, the all electron wave function and the pseudo wave functions are similar having the same scattering properties.

2.7 The Density-Functional Theory Implementation in VASP

With the ever growing importance of DFT methods in many fields, a significant number of implementations of DFT have been developed. Most of the work in this thesis has been carried out by using the plane wave basis set based VASP (*Vienna ab initio Simulation Package*) code [274-278].

The interaction between ions and electrons as carried out in VASP, described by ultrasoft pseudopotentials (USPP) [268,269] or Bloch's projector-augmented wave (PAW) [270,271] method, allow for a considerable reduction of the number of plane-waves per atom and especially for transition metal and first row elements. Generally not more than

100 plane waves per atom are required to describe bulk materials; in most cases, even 50 plane waves per atom will be sufficient for a reliable description. The PAW method implemented in VASP reconstructs the full all-electron density and avoids the necessity of nonlinear core-corrections [271]. A thoroughly tested set of USPP(s) and PAW data sets for all elements of the periodic table, from H to Pu, with a choice between soft and hard potential (for certain elements) are available. A fully relativistic calculation for the core-electrons and scalar relativistic approximation for valence electrons is implemented. Second-variation method [279] is implemented to include the Spin-Orbit coupling by using the scalar-relativistic eigen functions of the valence states.

Several approaches for the iterative calculation of the lowest Kohn-Sham eigen states which include the blocked Davidson scheme [280], the sequential conjugate-gradient (CG) algorithm [281,282] and a variant with direct inversion in the iterative subspace (RMM-DIIS) [283,284] are implemented in VASP [276,277]. For the mixing of the charge density an efficient Broyden/Pulay mixing scheme [283,285] is used. All the four Jacobian rungs of the exchange correlation ladder are accessible from VASP. At the local density approximation level, the parameterization of Perdew and Zunger [224] based on Caperley and Alder [221] results, is implemented and is further extended for spin-polarized cases by the spin-interpolation proposed by Barth and Hedin [286] and Vosko, Wills, and Nusair [223]. Several GGA functionals proposed by Perdew *et al.* in 1991 (PW91) [226,232], the Perdew-Burke-Ernzerhof (PBE) [234] functional, its revised form by Hammer (RPBE) [230], and Armiento and Mattson (AM05) [287] functional are included. In the meta-GGA front TPSS and RTPSS (revised-TPSS) [288], M06-L functional [241], modified Becke-Johnson exchange potential [289,290] have been included. The B3LYP [242,291], PBE0 [234], HSE03 [292] hybrid functionals have been put into effect in VASP [293-295]. All levels are available in a spin-polarized version also. Further, a fully unconstrained noncollinear magnetism [296] calculations within the PAW approach can be done in VASP [297]. The on-site Coulomb corrections, DFT+U based approach based on the work of Duradev and Liechtenstein [298,299] is implemented in VASP. Further to describe correctly the van der Waals interactions, the DFT-D2 method of Grimme [300] is implemented.

VASP provides a wide variety of routines for calculating energies, forces and a wide range of materials properties. Atomic, electronic and magnetic structures, spectra (electronic, optical, vibrational), mechanical properties (elastic moduli, theoretical strength, *etc*), thermodynamic properties (heats of formation, activation energies for phase transformations and chemical reactions, *etc.,*), magnetic properties (moments, susceptibilities, anisotropy energies, *etc*.) can be calculated from the knowledge of eigen states. Symmetry package returning the Bravais lattice and point group symmetry corresponding to the input coordinates is available in VASP. Optimization of structural parameters of the periodic systems at a fixed pressure can be performed in VASP using quasi-Newton, Conjugate-Gradient schemes and damped second order equation of motion for the ions, using the analytically calculated Hellmann-Feynman forces acting on the atoms and the stresses on the unit cell. Static optimizations for clusters, isolated and complex molecules and micro porous solids can be handled by placing them in into large computational cells, large enough to eliminate any interaction with the periodically repeated images. Structural energy differences help to determine the energetically most favorable structure among possible candidates and to investigate the pressure-induced phase-transitions among these structures. Molecular Dynamics simulations in a micro canonical or canonical ensemble using a Nose thermostat [301,302] can be performed. Transition-states on potential-energy surfaces (for the diffusion of atoms, phase-transitions, chemical reactions *etc*.) may be determined using the nudged elastic band (NEB) method [303,304]. Density of states of the material can be determined in VASP by using different smearing functions based on Fermi-Dirac function [305], Gaussian function [306], Methfessel-Paxton [307] function, tetrahedron or tetrahedron with Blochl [308] correction schemes.

2.8 VASP at BARC

All the calculations were done at the supercomputing facility of Computer Division, Bhabha Atomic Research Centre (BARC), Mumbai. BARC has many different deployments of the ANUPUM series of parallel supercomputers using a variety of processors. The work in the present thesis was carried out mainly on two supercomputers namely Ameya and Adhya. The 512-processors ANUPAM-Ameya supercomputer is built using 256 dual Xeon servers as a compute node. Each server has two Xeon, 3.6 GHz processors and 4 GB memory. The inter-communication network is Gigabit Ethernet with a node-to-node communication speed of 1Gbps. Sustained HPL performance of ANUPAM-Ameya is 1.73 TeraFLOPs. Adhya is 4608 core ANUPUM supercomputer built on 576 dual Quad core Xeon servers (3.0GHz and 32 GB memory) as compute node, interconnected by a high-speed DDR Infiniband (20Gbps) communication network. Benchmark performance rating of ANUPAM Adhya supercomputer is 47 TeraFLOPs. The open source Linux operating system is used on each parallel processing node in these two supercomputers. For all the investigations presented in this thesis, intensive benchmark calculations were performed to ensure accuracy and applicability of the employed method. This strengthens our confidence for a particular method for the calculation of the electronic and geometrical structure of investigated cluster. Complete description of different methods used and details of their authentication have been presented as a separate section in each chapter.

3. Structure and Stability of Neutral and Charged Lead Clusters

3.1 Introduction

The structural and physicochemical properties of the Group IV elemental clusters have been subjects of intense research because of the fundamental interest to understand their bonding and growth patterns and the possibility of applications in nanotechnology. Their growth behavior and the nature of bonding differ considerably as one goes down from C to Pb. During the past two decades, a large number of experimental and theoretical studies were carried out in this direction. Much attention has been focusing on understanding the structural similarities and differences among Si, Ge, Sn and Pb clusters. The atomic structures of the Group IV elemental clusters adopt geometries ranging from chain, fullerene cages and nanotubes for carbon [309] and non-compact prolate structures for Si, Ge and Sn [310-338], to compact structures for Pb. Structures of Si and Ge clusters progressively undergo rearrangements with an increase in size and transform into a $3D$ growth. Noda and coworkers [329,339] have reported mass spectrum of tin clusters that resembles those of Si_n and Ge_n clusters but different from that of Pb_n. Shvatrsburg *et al.* [340] have characterized the structures of Si_n, Ge_n, Sn_n and Pb_n clusters using ion mobility measurements. It was observed that the growth patterns of Si, Ge and Sn clusters adopt prolate structures in the small cluster region. However, for lead clusters, near-spherical structures were predicted for all cluster sizes. So, the transition to 'normal' metal cluster growth in Group IV elements occurs near tin and lead. Theoretical studies were carried out for small tin clusters in order to understand the structure and bonding in these systems [141,338]. The results suggest that the strong covalent bond exists between Sn atoms in small clusters. In comparison to the other Group IV elements, studies on the Pb clusters are few. Mühlbach *et al.* [341] from their time of flight mass spectrometric measurements on Pb_n clusters have indicated that clusters with

$n = 7, 10, 13, 17$ and 19 are more stable. Comparison of mass abundance pattern of all Group IV elemental clusters revealed that Pb clusters behave differently from all others. In particular, the mass spectrum of Pb clusters rather resembles with that of inert gas atom van der Waals clusters [83,341], characteristic for close packed geometrical structures. Saito *et al.* [342] and LaiHing *et al.* [343] subsequently carried out photo ionization mass spectroscopy on Pb_n clusters. The ionization potentials measured of lead clusters suggested that for ionization energy of 6.4 eV all lead clusters could be ionized except the atom (IP of Pb atom is 7.2 eV). Gantefor *et al.* [344], Luder *et al.* [345] and Negishi *et al.* [346] have recorded the photoelectron spectra of Sn_n and Pb_n anion clusters. The detachment energies of the ground state cluster anions as well as the vertical detachment energies of the neutral clusters were reported. The results from the photoelectron spectroscopy reveal that electronic structures of Sn_n and Pb_n clusters are different due to the directional and non-directional nature of bonding, respectively. Experimental studies carried out for the fragmentation behavior of neutral and charged clusters of lead [347,348] demonstrated the importance of electronic shell effects on the stability of neutral and charged clusters.

Although few experimental results were reported for Pb_n clusters, theoretical studies are scarce. Balasubramanian *et al.* [349-357] have carried out a series of calculations on Pb clusters with particular emphasis on their spectroscopic properties. These computations were carried out using accurate techniques that included electron correlation effects and spin-orbit coupling simultaneously using a multi-reference relativistic configuration interaction method. Due to the requirement of extensive computation power, these studies were limited to very small clusters *i.e.,* up to $n = 6$. The central feature of these studies showed that spin orbit coupling effect is quite important to describe the energetics of these clusters. The spin-orbit coupling can lower the atomization energies substantially; for example, the dissociation energy of Pb_2 is reduced by a factor of two. This is a consequence of the fact that spin-orbit coupling lowers the energy of the atom substantially more than the cluster. In another theoretical study Molina *et al.* [358-360] have performed the total energy calculations of Pb_n clusters up to $n = 14$ using the plane wave based pseudopotential method (PW-PSP) under the local spin density approximation scheme. They have obtained the atomization energies in very good agreement with that of experimental values. Very recently, Lai *et al.* [361] have calculated Pb_n clusters in the range of $3 < n < 56$ using the n-body Gupta potential [362] to account for the interactions between atoms in the cluster. This chapter presents the *ab initio* molecular dynamics simulations performed using the density functional theory under the framework of generalized gradient approximation to search for the low-lying isomeric structures and energetics of small size Pb_n ($n = 2 - 15$) clusters. The analysis of the relative stabilities of these clusters was carried out based on the total energies calculated that included the spin orbit coupling term. The binding energies, second order energy differences, and the fragmentation behavior of these clusters were analyzed. The results suggest that $n = 4, 7, 10$ and 13 are more stable in this series, which is in agreement with the mass abundance pattern obtained from the photo-ionization experiments [341-343]. Further, in contrast to other Group IV elemental clusters, which adopt less compact prolate shape in the small size range, the ground state geometries of Pb_n ($n = 2 - 15$) clusters favor compact and spherical structural growth pattern.

3.2 Computational Details

The geometry optimization of small Pb clusters was performed using the *ab initio* molecular dynamics simulation with projector augmented wave pseudopotential and plane wave basis set as implemented in VASP code [274-278]. The PAW pseudo-potentials were generated considering scalar relativistic corrections [270,271]. The spin polarized generalized gradient approximation (GGA-PW91) [232,233] was used to calculate the exchange-correlation energy. Thus, all relativistic effects except spin-orbit are included in the total energy calculation for different isomers of Pb_n clusters.

The cut-off energy of the plane waves was taken to be 300.0 eV. A simple cubic super-cell of side 20 Å was used and the Brillouin zone integrations were carried out using only the Γ point. In order to obtain few low lying isomers of Pb_n clusters, large number of initial geometries based on tetragonal, pentagonal or hexagonal growth and those reported for Si, Ge and Sn clusters, were considered. The geometry optimization of each isomer was carried out until the forces on each atom became less than 0.005 eV/Å and the energy converged to an accuracy of 0.001 eV. In most cases, the lowest energy isomer of each cluster was reconfirmed by comparing the energies of the isomers formed by adding or subtracting one atom with the corresponding nearest neighbor structures.

Test calculations were done for dimer and bulk. Results obtained using different exchange-correlation schemes were summarized in Table 3.1. In general, it is found that the interatomic separations between Pb atoms agree with that of experimental values [257,363], however the binding energies were significantly overestimated. Further, Balasubramanian and coworkers carried out several calculations to obtain the ground state geometries and spectroscopic properties of small lead clusters where in it was shown that these clusters have significant spin-orbit effect [349-357]. Motivated by these results, test calculations were carried out for the dimer and bulk cohesive energy of Pb after incorporating the spin-orbit coupling effect. Significant improvement on the binding energies is obtained as can be seen from the values listed in Table 3.1. The bulk cohesive energy using GGA scheme for exchange correlation is found to reduce from 3.0 eV/atom to 2.07 eV/atom, which is in excellent agreement with the experimental values [257]. Since it was observed that spin-orbit effect in Pb clusters is non-negligible, the total energy calculations of the lowest energy isomers of Pb_n clusters were carried out including the spin-orbit coupling [279] effect as employed in VASP software.

LDA[a]	**GGA(PW91)**	**PBE**[b]	**GGA(PW91)/SO**	**Exp.**	**System**
1.45	1.22	1.19	0.67	0.42[c]	Pb_2
3.79	3.00	2.94	2.07	2.03[d]	Bulk

Table 3.1:Comparison of experimental and calculated average binding energy (eV/atom) for dimer and bulk. [a] [221], [b] Perdew-Burke-Ernzerhof [234,235], [c]ref. [363], [d]ref. [257]

In order to verify the quality of the plane wave based DFT results further calculations were performed using the localized Gaussian basis set as employed in Gaussian-98 [250]. The total energies of few low-lying isomers obtained using gradient corrected Becke exchange and Perdew Wang exchange correlation (B3PW91) [226,228,242] method as well as MP2 [213] (Moller Plesset correlation energy correction truncated to second order) method were compared. Los Alamos relativistic effective core potentials with a double zeta valence (LanL2DZ) [364-366] were used as basis to take into account the scalar relativistic effects, including mass velocity and Darwin corrections for the heavy lead atom.

3.3 Results and Discussion

3.3.1 Neutral Pb_n Clusters

3.3.1.1 Geometric Structure

Figure 3.1-Figure 3.7 represent the low-lying isomers of Pb_n clusters. Although a large number of isomers have been considered for each cluster, but for the sake of simplicity, only those isomers that were within 1 eV energy from the lowest energy isomer are shown.

The Pb_2 dimer favors triplet spin configuration with a bond length of 2.9 Å and binding energy of 0.67 eV/atom. For Pb_3 cluster, equilateral triangle (Figure 3.1) with triplet spin configuration showed the lowest energy with $Pb - Pb$ bond lengths of 3.01 Å and an average binding energy of 1.08 eV/atom. These results are in good agreement with those obtained by Balasubramanian and coworkers [352-357] using very accurate methods of CASSCF and MRSDCI, which showed 3.0 Å and 3.07 Å for the interatomic distances between Pb atoms in dimer and trimer, respectively. It needs to be mentioned that unlike other trimers of Group IV elements (Si, Ge and Sn), which form isosceles (C_{2v}) triangle and favored singlet as the lowest energy configuration [313,332-334,338], Pb_3 favors equilateral triangle (D_{3h}) with triplet spin configuration, in consistent with the results obtained from

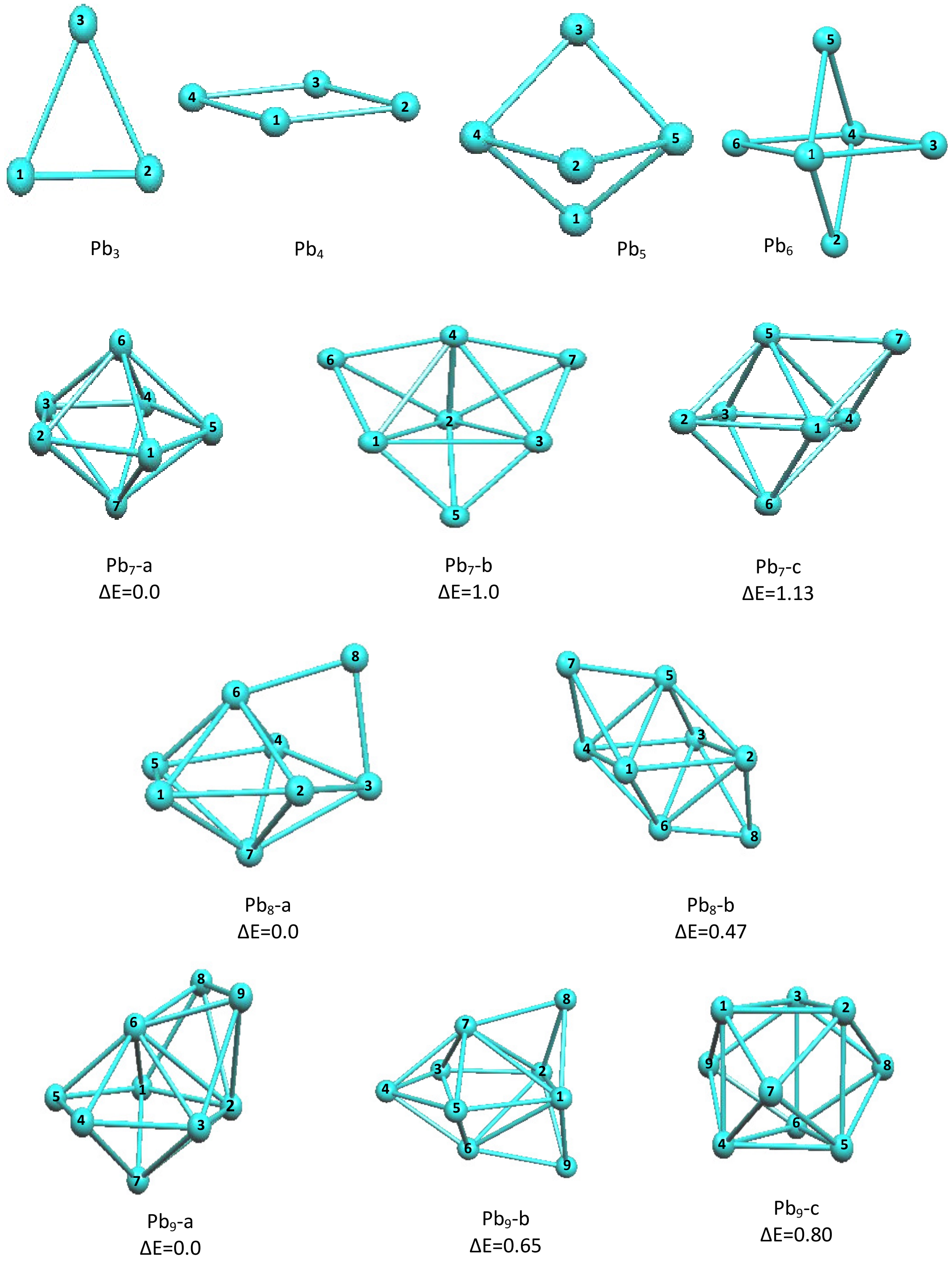
Pb_3

Pb_4

Pb_5

Pb_6

Pb_7-a
ΔE=0.0

Pb_7-b
ΔE=1.0

Pb_7-c
ΔE=1.13

Pb_8-a
ΔE=0.0

Pb_8-b
ΔE=0.47

Pb_9-a
ΔE=0.0

Pb_9-b
ΔE=0.65

Pb_9-c
ΔE=0.80

Figure 3.1: Low-lying isomers within 1.0 eV energy difference of $Pb_n (n = 3 - 9)$ clusters

infrared experiments [363]. The clusters with $n = 4$ to $n = 7$ have similar geometrical configurations as observed for other Group IV elements. The lowest energy isomer of Pb_4 adopts rhombus geometry (D_{2h}) with $Pb - Pb$ distance of 2.98 Å and an internal angle of 63.7º. The Pb_5 cluster shows capped bent rhombus as the ground state geometry, which can otherwise be viewed as an elongated trigonal bipyramid (D_{3h}). The shortest bond length between Pb atoms is found to be 2.97 Å.

For Pb_6, several initial configurations *viz.,* octahedron, trigonal prism and trigonal bipyramid (TBP) with one additional atom capping one of the edges or the triangular faces were optimized. Both face and edge capped TBP relaxed to crossed rhombus (D_{4h}) (Figure 3.1), which is the lowest energy configuration with $Pb - Pb$ distances of 3.06 Å . Among different isomers of Pb_7 tried, the pentagonal bipyramidal (PBP) structure with D_{5h} symmetry is found to be the lowest energy isomer. The $Pb - Pb$ bond distance is estimated to be 3.19 Å. Other isomers, like bicapped-TBP or capped octahedron, which showed significantly higher in energy as compared to the PBP structure, are shown in Figure 3.1. For Pb_8 cluster, the lowest energy isomer is found to favor an edge capped PBP structure. This is similar to the lowest energy isomer of Sn_8 [338] but different from that of Si_8 and Ge_8 which favor bicapped octahedron [312,317-319,332-334] as the lowest energy structure. The bicapped octahedron isomer ($Pb_8 - b$) of Pb_8 lies about 0.47 eV higher in energy.

For Pb_9 cluster, several initial configurations were considered by capping the PBP, prism and octahedron geometries. The lowest energy isomer of the Pb_9 cluster is found to favor bicapped PBP structure with two capping atoms placed on the adjacent triangular faces on the same side of the pentagon (Figure 3.1). Another isomer having tricapped prism ($Pb_9 - c$) configuration shows 0.80 eV higher energy than the lowest energy isomer. For Pb_{10}, initial geometries based on capping different faces of octahedron, PBP and prism/antiprism structures were considered. The lowest energy structure is found to favor capped trigonal-prism as shown in Figure 3.2. Two other isomers based on tricapped PBP $(Pb_{10} - b)$ and pentagonal antiprism (optimized into two fused octahedrons, $(Pb_{10} - c)$

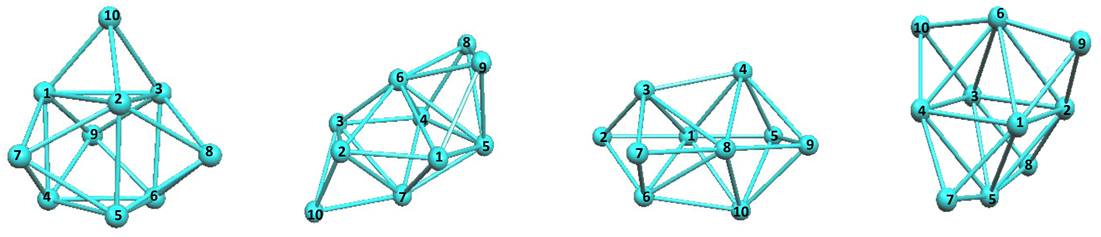

Pb₁₀-a ΔE = 0.0
Pb₁₀-b ΔE = 0.62
Pb₁₀-c ΔE = 1.05
Pb₁₀-d ΔE = 1.08

Figure 3.2: Low-lying isomers within 1.0 eV energy difference of Pb_{10} cluster

show 0.62 eV and 1.05 eV higher energy respectively, with respect to the lowest energy structure. The tetracapped octahedron $(T_d, Pb_{10} - d)$ structure is found to be 1.08 eV higher in energy.

For Pb_{11} cluster, several initial configurations were generated. These were based on capping different faces of PBP structures and those previously reported for other Group IV clusters and by removing one or two atoms from Pb_{12} or Pb_{13} icosahedron structures. Two isomeric structures, one based on pentagonal base and the other based on tetragonal base are found to lie within 0.1 eV energy difference. The lowest energy structure $Pb_{11} - a$ is obtained starting from tetracapped PBP where all four capping atoms were placed on the same side of the base pentagon, which after relaxation adopts icosahedron motif as shown in Figure 3.3. The next higher energy isomer $(Pb_{11} - b)$, which lies very close in energy to

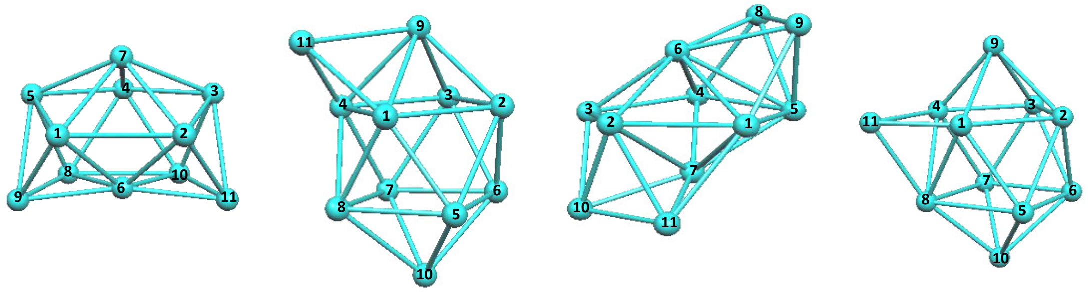

Pb₁₁-a ΔE = 0.0
Pb₁₁-b ΔE = 0.05
Pb₁₁-c ΔE = 0.22
Pb₁₁-d ΔE = 0.37

Figure 3.3 Low-lying isomers within 1.0 eV energy difference of Pb_{11} cluster that of the lowest energy isomer, shows tri-capped tetragonal antiprism with additional Pb atom capping one of the triangular faces. One other isomer of tetracapped PBP ($Pb_{11} - c$), where each two Pb atoms are capping from opposite side of the PBP is 0.22 eV higher in energy. In general, comparison of total energies between the low lying isomers of Pb_{11} cluster suggests that the potential energy surface is rather flat and structural transition might occur at higher temperatures or even by using different approximation in the exchange correlation energy functional. In fact under MP2, the lowest energy isomer of Pb_{11} cluster favors tricapped tetragonal antiprism motif ($Pb_{11} - b$), which by plane wave based pseudopotential method, is ~0.05 eV higher in energy than the lowest energy isomer with pentagonal symmetry. In this context it is worth mentioning that for Si_{11} cluster, multiple nearly degenerate low-energy isomers were found, which have shown structural transition of the lowest energy isomer depending upon the exchange-correlation functional [312].

For Pb_{12} cluster, several isomers based on tetragonal, pentagonal and hexagonal structural motifs were taken into consideration to search for the low-lying isomers. The lowest energy structure shows empty cage distorted icosahedron. The next low-lying isomer is a tetracapped tetragonal antiprism, which is 0.52 eV higher in energy. Both these structures can be viewed as a sequential addition of one more Pb atom to $Pb_{11} - a$ and $Pb_{11} - b$

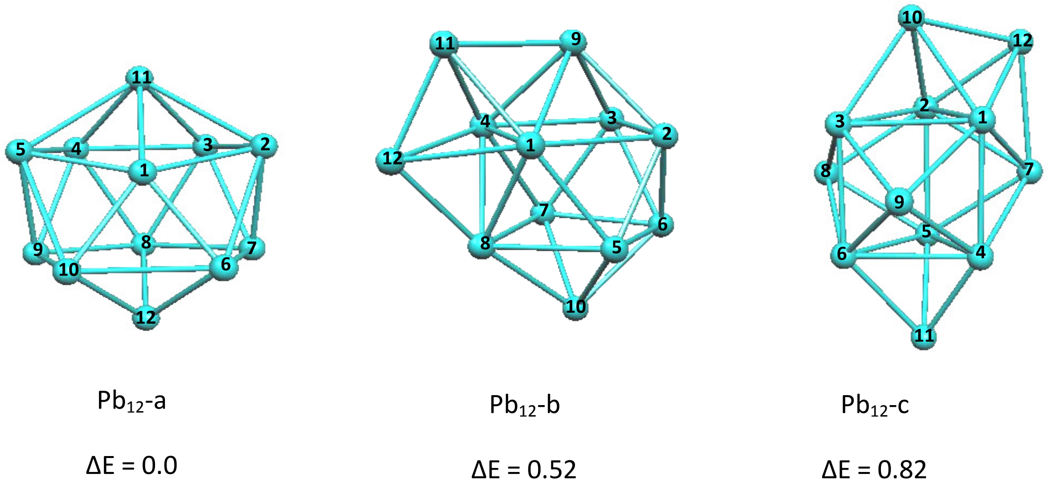

Figure 3.4: Low-lying isomers within 1.0 eV energy difference of Pb_{12} cluster

isomers of Pb_{11}. In this context it is worth mentioning that, while in the case of Pb_{11} cluster the lowest energy isomer which forms a pentagonal base is ~0.05 eV lower than the next lower isomer of tricapped tetragonal antiprism, for Pb_{12} the difference between the pentagonal and tetragonal structure increases significantly (~0.52 eV), implying a trend for an icosahedral growth for larger size clusters. For Pb_{13}, isomers like capped icosahedron, Pb encapsulated icosahedron and a few low lying isomers of other Group IV elemental clusters having less compact prolate shape geometries were considered as initial geometries. Slightly distorted Pb atom encapsulated icosahedron is found to be the most stable isomer while the low lying isomers of the other Group IV elements are found to be at least 0.33 eV higher in energy. This is significantly different from what is commonly observed for other Group IV clusters. The difference in the structural motifs can be related to their bulk structures, which for Pb is a compact *fcc* and for others it is less compact tetragonal [257]. Other isomers, like cuboctahedron or decahedron show significantly higher energy (~1.6-1.7 eV). Previous studies have shown that elements with large compressibility are more likely to exhibit spherical growth of their clusters [89]. The higher compressibility of Pb as compared to those for Si, Ge and Sn further establishes its compact icosahedral growth pattern.

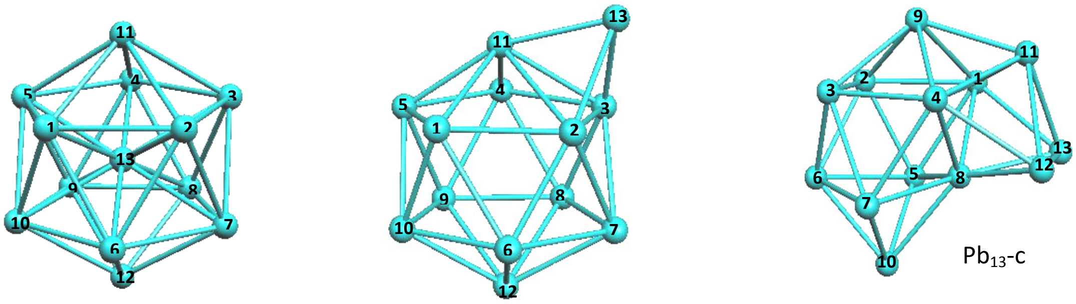

Pb_{13}-a

ΔE = 0.0

Pb_{13}-b

ΔE = 0.33

Pb_{13}-c

ΔE = 0.76

Figure 3.5 Low-lying isomers within 1.0 eV energy difference of Pb_{13} cluster

For Pb_{14}, several isomers *viz.* capped icosahedron, hexagonal layered and *fcc* structures (bulk cut) were optimized. An icosahedron with the additional atom capping one of the triangular faces of the Pb_{13} cluster from outside is found to show the lowest energy

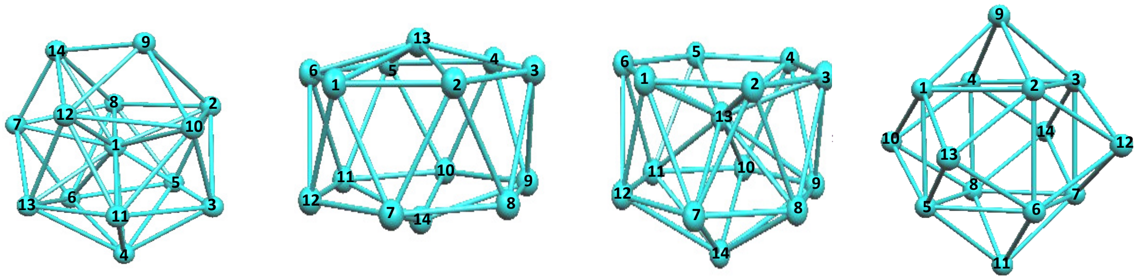

Pb_{14}-a Pb_{14}-b Pb_{14}-c Pb_{14}-d

ΔE = 0.0 ΔE = 0.15 ΔE = 0.46 ΔE = 1.18

Figure 3.6: Low-lying isomers within 1.0 eV energy difference of Pb_{14} cluster

structure. The next low lying isomer of Pb_{14} ($Pb_{14}-b$) shows a similar trend of the close packing by adding one Pb atom on each of the hexagonal plane resulting in a bicapped hexagonal antiprism structure, which is actually found to be a seeding point for larger lead clusters. The energy difference of the capped hexagonal antiprism isomer with respect to the lowest energy isomer is 0.15 eV.

For Pb_{15} cluster, initial configurations were generated based on the pentagonal and hexagonal structural motifs. Some of these consist of capping icosahedrons or hexagonal

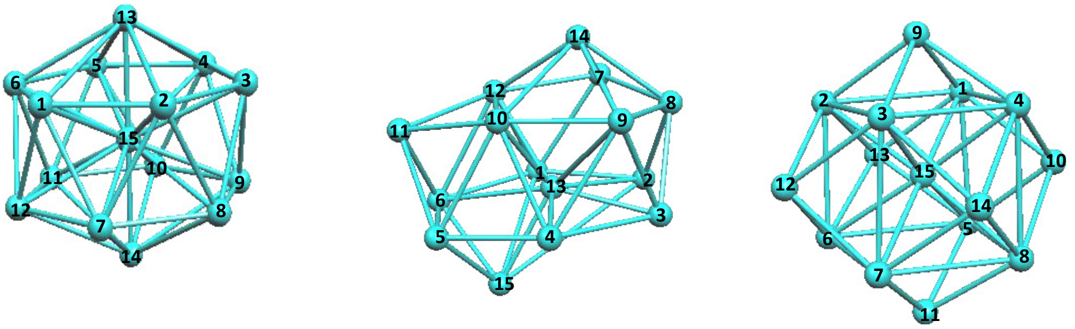

Pb_{15}-a Pb_{15}-b Pb_{15}-c

ΔE = 0.0 ΔE = 0.57 ΔE = 1.52

Figure 3.7 Low-lying isomers within 1.0 eV energy difference of Pb_{15} cluster

antiprism structures as well as encapsulated hexagonal prisms *etc*. Comparison of the total energies among all these isomers after geometry relaxation suggests that the ground state geometry of the Pb_{15} cluster favors encapsulated hexagonal antiprism structure. This further corroborates the compact structural motif of the Pb clusters, which bears a signature of metallic behavior, and significantly different from the other Group IV elemental clusters.

3.3.1.2 Energetics

In order to understand the relative stability of these clusters the average binding energies, second order difference in energy and the fragmentation behavior were estimated based on the total energies obtained for the lowest energy isomers. The average binding energies as a function of cluster size obtained at different levels of theoretical models are represented in Figure 3.8. The average binding energy of these clusters is calculated as

$$BE(Pb_n) = -\frac{[E(Pb_n) - n \times E(Pb)]}{n} \qquad \text{eq. 3.1}$$

It is clear from Figure 3.8 that both PAW/GGA (without spin-orbit correction) and B3PW91 show significantly higher binding energies as compared to the results obtained by incorporating the spin-orbit correction in PAW/PW91 method. Therefore, total energy calculations including the spin-orbit effects are extremely important for these clusters. For

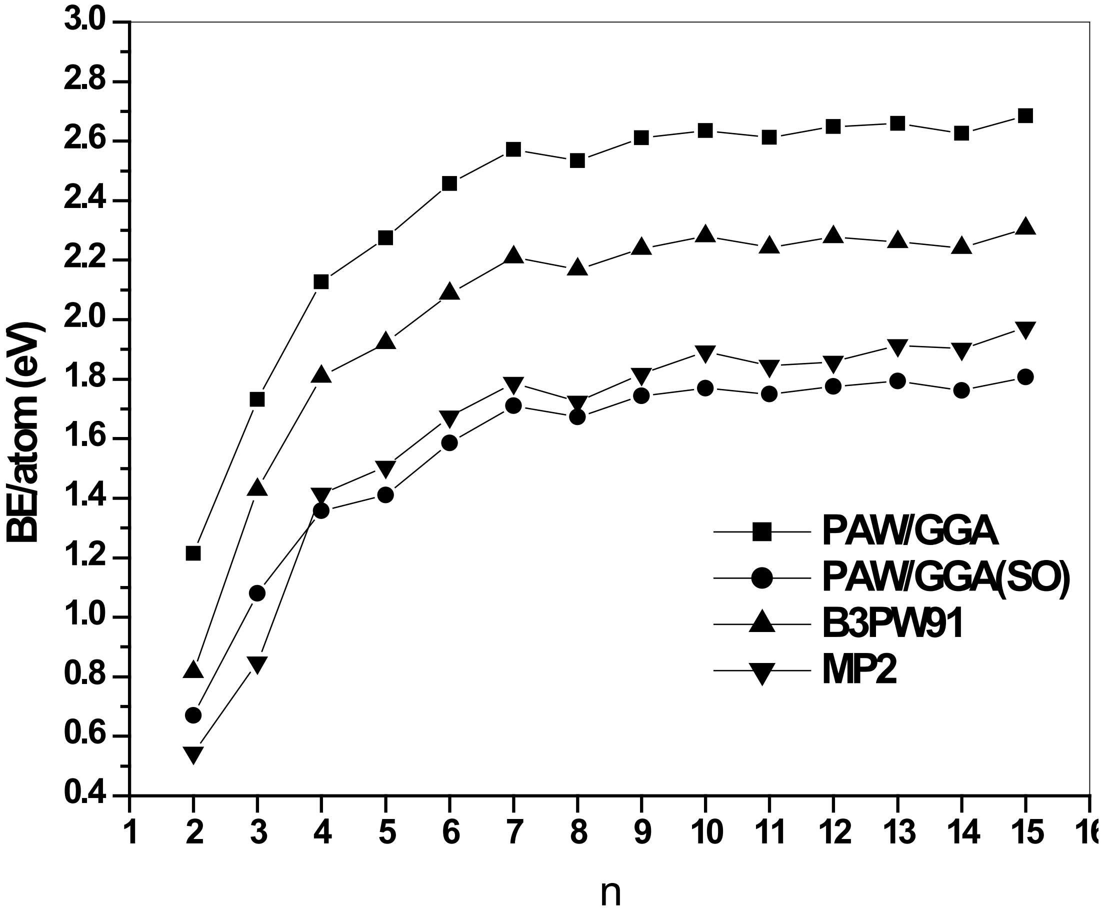

Figure 3.8 Binding energy per atom of Pb_n clusters as a function of cluster size (n)

smaller size clusters (Pb_2 and Pb_3) although the binding energies obtained from MP2 method are closer to the experimental values [347,363] (0.42 eV/atom and 0.77 eV/atom for Pb_2 and Pb_3 respectively) however, it overestimates as the size increases. This is evident from the fact that for $n = 15$ the binding energy obtained from MP2 is already within ~97% of the bulk. On the other hand, though for smaller clusters the binding energies obtained from the PAW/GGA-PW91 (SO) calculations are higher as compared to the experimental values, the cohesive energy of the Pb bulk calculated under PAW/GGA-PW91 (SO) method shows 2.07 eV/atom, in good agreement with experimental observation [257]. Therefore, it is expected that under PAW/GGA (SO) method the binding energy values will converge with experiment as the size of the cluster grows. For small clusters in the range up to $n = 15$, the trend in the binding energy curve shows that in general the BE increases as the cluster size grows with small humps or dips for specific size of clusters indicating their relative stabilities. Accordingly, small humps at $n = 7, 10$ and 13 as observed in Figure 3.8, reflect their higher stabilities over other clusters. These results are in excellent agreement with the experimentally observed mass abundance pattern of Pb_n clusters [341-343].

As discussed previously, magic clusters are those, which show higher stability as compared to its nearest neighbors. Based on the calculated total energies of different clusters one can search for stable clusters by calculating the second energy difference in energy, which has been calculated as

$$\Delta^2 E = 2 \times E(Pb_n) - E(Pb_{n+1}) - E(Pb_{n-1}) \qquad \text{eq. 3.2}$$

From the above expression it is clear that the clusters, which have negative values of $\Delta^2 E$ are more stable than their nearest neighbors. The $\Delta^2 E$ for Pb_n clusters as a function of cluster size as shown in Figure 3.9. Expectedly, it is found that clusters with $n = 4, 7, 10$ and 13 atoms are relatively more stable than their nearest neighbors. This is in agreement with previous experimental observations [341-343].

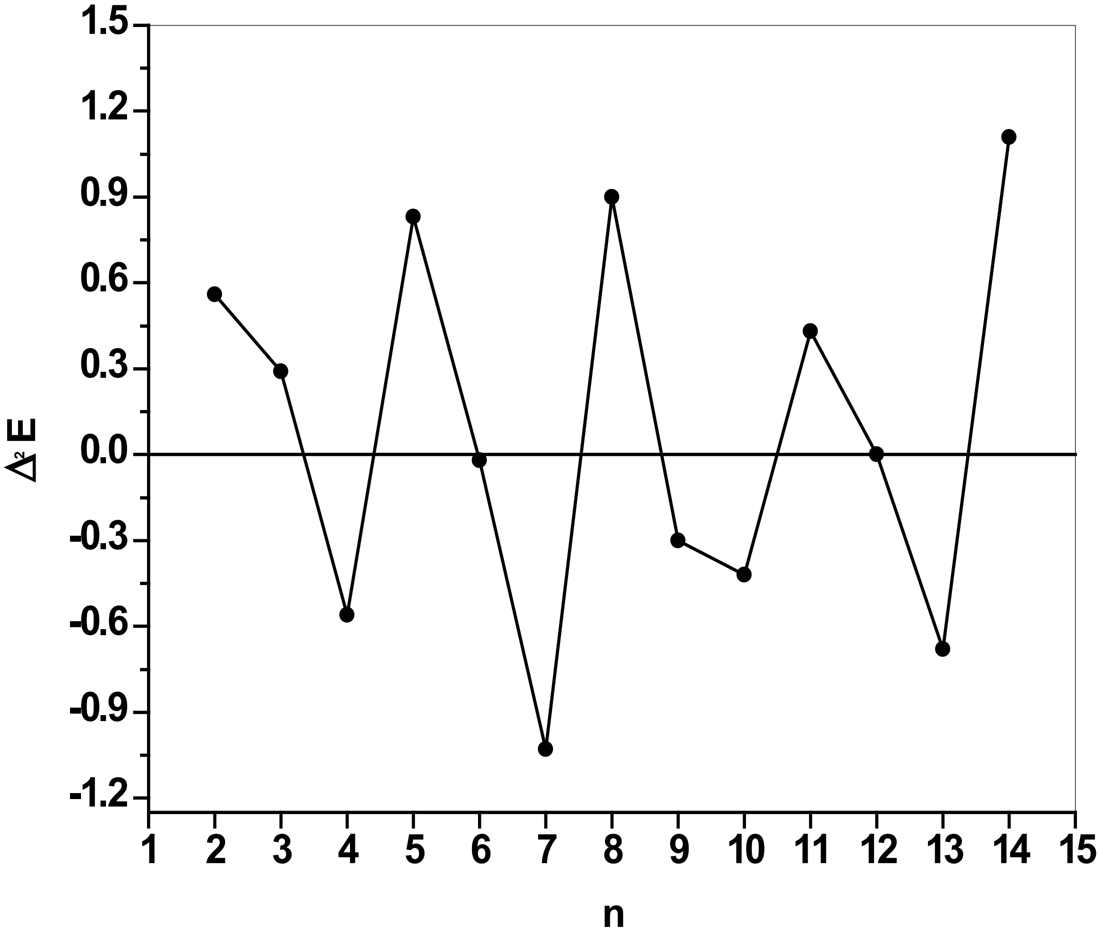

Figure 3.9: Second order difference in total energy of Pb_n clusters as a function of cluster size (n)

It is known that in general the stability of the atomic clusters is governed either by electronic shell model (commonly observed for alkali metal clusters) or by geometrical close packing model (commonly observed for inert gas clusters) [67,68]. According to the electronic shell model, clusters with $2, 8, 18, 20, 34, 40$ .... *etc.,* numbers of electrons are more stable. However, the stability order under the geometrical close packed structures favors clusters with $7, 13, 19, 23$ ... *etc* number of atoms. For covalent clusters, due to the directional bonding, neither of these two models is obeyed [367]. Interestingly, the stability pattern of Pb_n clusters show that $n = 4, 7, 10$ and 13 are magic. Although the higher stabilities of $n = 7$ and 13 of Pb clusters can be explained by geometrical close packing the higher stability of $n = 10$ could be a resultant of both electronic shell filling (40 valence electrons) as well as compact trigonal prism geometries.

3.3.1.3 Fragmentation Behavior

Although it is known that the fragmentation process involves a dissociation barrier and entropy or free energy changes, in the present work it is have assumed the Pb_n clusters undergo spontaneous fragmentation, by only looking at the total energy of the parent and daughters thereby leading to infer about the relative stability of these clusters in the ground state. For this purpose the fragmentation energies were calculated for all possible channels, which can be expressed as

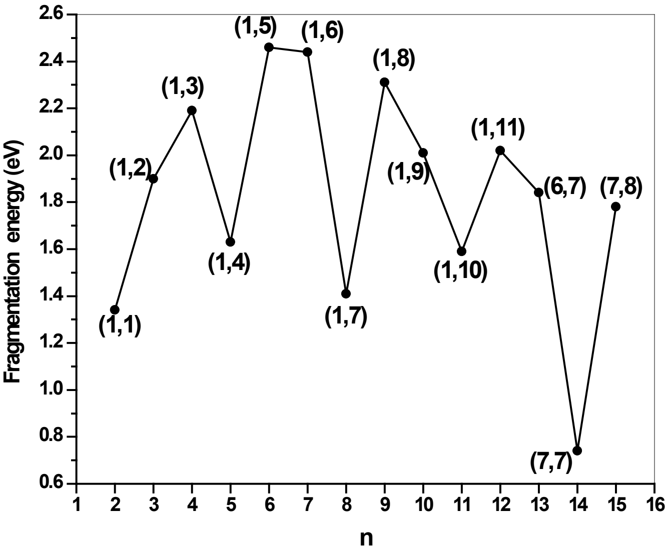

Figure 3.10: The lowest energy fragmentation channels of Pb_n clusters. Product fragments are shown in braces.

$$E_f(Pb_n) = E(Pb_n) - E(Pb_p) - E(Pb_{n-p}) \qquad \text{eq. 3.1}$$

For the sake of simplicity the fragmentation energies of the lowest energy channels as a function of the cluster size as shown in Figure 3.10. The complete list of the fragmentation energies for all possible channels is provided in Table 3.2. From Figure 3.10, it is clear that while smaller size clusters up to $n = 12$, favor monomer evaporation as the lowest energy fragmentation channel, larger clusters ($n > 12$) favor to dissociate into two stable daughter cluster. For $n = 13, 14$ and 15 the lowest energy fragmentation channels were found to be $(6, 7), (7, 7)$ and $(7, 8)$ respectively. The results were subsequently tested and verified by Waldschmidt *et al.*[368], in their work on surface-induced dissociation studies on the energetics and structure of lead clusters The higher abundance of Pb_7 in mass spectrometry experiment [341-343] can therefore be a consequence of the favored fragmentation channel of larger clusters into $n = 7$ as one of the fragmented species. Duncan *et al.* [342] in their photo ionization experiment have noticed that $n = 14$ is missing in the mass spectrum. This

n	p	$n-p$	E_f	n	p	$n-p$	E_f
2	**1**	**1**	**1.34**	11	4	7	1.89
3	**1**	**2**	**1.90**	11	5	6	2.70
4	**1**	**3**	**2.19**	12	**1**	**11**	**2.02**
4	2	2	2.75	12	2	10	2.27
5	**1**	**4**	**1.63**	12	3	9	2.38
5	2	3	2.48	12	4	8	2.50
6	**1**	**5**	**2.46**	12	5	7	2.28
6	2	4	2.75	12	6	6	2.26
6	3	3	3.04	13	1	12	2.02
7	**1**	**6**	**2.44**	13	2	11	2.70
7	2	5	3.56	13	3	10	2.39
7	3	4	3.29	13	4	9	2.21
8	**1**	**7**	**1.41**	13	5	8	2.89
8	2	6	2.51	13	**6**	**7**	**1.84**
8	3	5	3.07	14	1	13	1.34
8	4	4	2.51	14	2	12	2.02
9	**1**	**8**	**2.31**	14	3	11	2.14
9	2	7	2.38	14	4	10	1.54
9	3	6	2.92	14	5	9	1.92
9	4	5	3.19	14	6	8	1.77
10	**1**	**9**	**2.01**	14	**7**	**7**	**0.74**
10	2	8	2.98	15	1	14	2.45
10	3	7	2.49	15	2	13	2.45
10	4	6	2.74	15	3	12	2.57
10	5	5	3.57	15	4	11	2.40
11	**1**	**10**	**1.59**	15	5	10	2.36
11	2	9	2.26	15	6	9	1.91
11	3	8	2.67	15	**7**	**8**	**1.78**

Table 3.2: Fragmentation channels of Pb_n clusters. The bold numbers for the fragmentation energy represent the lowest fragmentation channel

observation can lead to two inferences. The first reason could be due to the very high stability of Pb_{14} cluster for which the ionization potential is higher than the ionizing energy of the photon or due to very low fragmentation energy, which leads to the fragmentation of the Pb_{14}

clusters as soon as they are formed. From this study on the binding energy and fragmentation behavior of Pb_n clusters it can be ascertained that the later reason is correct. The fragmentation energy of Pb_{14} cluster into two Pb_7 daughter clusters is estimated as 0.74 eV (Table 3.2). The low fragmentation energy of Pb_{14} cluster is attributed to the production of two magic clusters of Pb_7 and this further explains its unavailability in the photo ionization experiment.

3.3.2 Charged Pb_n clusters

Although most of the experimental results are derived for the charged clusters, theoretical studies on lead clusters have mainly focused on the neutral clusters. Therefore, to verify the experimental results in proper perspective it is required to understand the influence of removal of an electron on the geometry and energetics of neutral clusters. To accomplish this aspect a systematic study of the structure and energetics of the Pb_n^+ clusters was carried out and compared with the previously obtained results on neutral clusters. The relative stabilities of these clusters was evaluated based on the binding energies, second order energy difference in energy, and their fragmentation behavior derived from the total energies calculated after including the spin orbit coupling term. The chemical stability, which primarily depends on the ordering of the energy levels, was analyzed by evaluating their energy gap between the highest occupied and lowest unoccupied molecular orbital and adiabatic ionization potentials.

3.3.2.1 Geometric Structure

Figure 3.11 represents the lowest energy isomers of neutral and positively charged Pb_n clusters. In order to understand the geometrical changes occurred due to the removal of an electron from the Pb_n clusters and represent the geometries of Pb_n^+ in proper perspective, the geometries of both neutral and cations are discussed in this section. For Pb_2^+, the inter-atomic separation between Pb atoms increases from 2.91 Å to 2.96 Å after the removal of an electron from Pb_2. Moreover, for the dimer cation, the spin configuration of the lowest energy isomer changes from triplet to doublet. The adiabatic ionization potential, estimated by the difference of energy between Pb_2 and Pb_2^+ shows 5.96 eV for the removal of the electron. This is in good agreement with the experimental value of 6.2 eV as reported by Saito *et al.* [342]. For the cation, the ground state geometry of Pb_3^+ retains the triangular

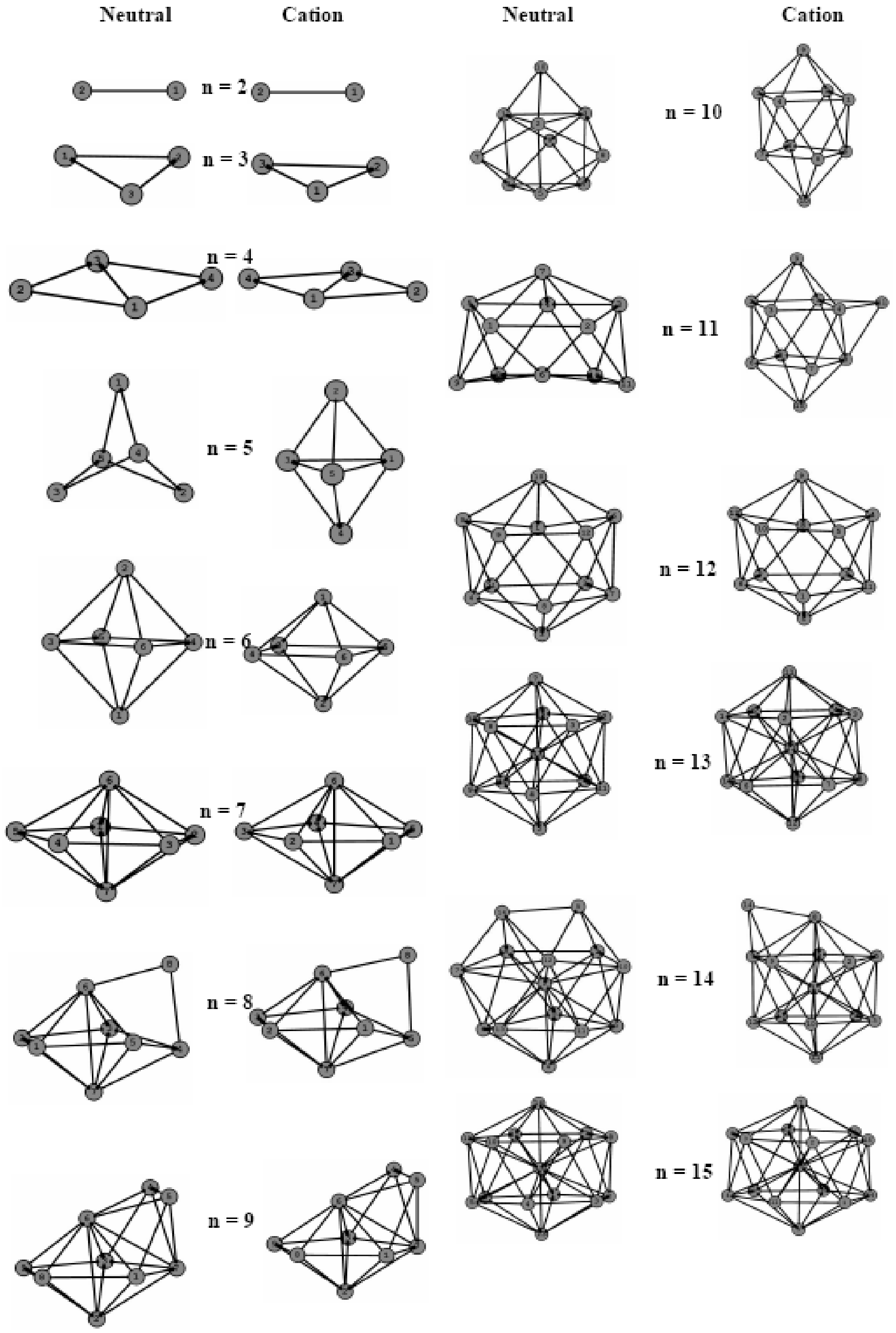

Figure 3.11: The lowest energy isomers of Pb_n and Pb_n^+ clusters calculated using density functional theory and GGA/PW91 approximation including the spin-orbit coupling effects.

geometry of neutral Pb_3 with small elongation of the bond length up to 3.17 Å. The spin configuration of the lowest energy isomer is found to be quartet. These results are found to be in consistent with the results of Balasubramanian *et al.*, carried on small lead clusters at CAS-MCSCF and MRDCI level where the $Pb - Pb$ distances are reported to be 3.16 Å with quartet spin configuration [352]. The ionization potential of Pb_3 cluster calculated at MRSDCI(Q), MP2 and DFT levels show 6.36 eV, 6.42 eV and 6.59 eV, respectively. After inclusion of the spin orbit coupling correction to the MRSDCI, the IP value of Pb_3 cluster is estimated to be 6.12 eV [352]. The present calculation, using the pseudopotential based GGA/PW91-SO method, which is computationally inexpensive in comparison to the MP2 or MRSDCI methods, estimated the IP of Pb_3 cluster as 5.70 eV, which is in good agreement to the experimental value 5.80 eV [342].

The lowest energy isomer of Pb_4 adopts a rhombus geometry (D_{2h}), with a $Pb - Pb$ distance of 2.98 Å and an internal angle of 63.7º. The lowest energy isomer of Pb_4^+ also favors a rhombus structure with a small increase in the internal angle (71.5º). The ionization potential of Pb_4 cluster is calculated to be 5.72 eV, which is in excellent agreement with 5.70 eV, as measured through experiment [342]. Other theoretical reports based on CASSCF, MRDCI predicted 6.23 eV and 6.39 eV, respectively [353,354], which are significantly higher in comparison to the experimental value. Unlike the neutral Pb_5 cluster, which adopts capped bent rhombus (can be viewed as an elongated trigonal bipyramid) (D_{3h}) geometry, upon removal of an electron from Pb_5, the $Pb - Pb$ distances become shorter resulting in more compact TBP configuration with more coordination. For example, the $Pb - Pb$ distances of 3.95 Å in the elongated trigonal base rearranges into an isosceles triangle with 3.17 Å and 3.5 Å for shorter and longer bond lengths, respectively.

For Pb_6^+ cation, the lowest energy isomer shows similar structural pattern to that of the neutral with small increase in the $Pb - Pb$ distances in the basal plane and decrease in the vertical axis thereby resulting in a more spherical motif as can be seen from Figure 3.11. Moreover, it is noted that unlike neutral, where the lowest energy isomer has large difference with next isomer, for Pb_6^+, the edge capped TBP is energetically degenerate with crossed rhombus. For $n = 7, 8$ and 9 the ground state geometries of the Pb_n clusters do not change significantly by the removal of an electron. A pentagonal bipyramid (PBP), an edge capped PBP and bicapped PBP structures are found to be the lowest energy isomers of Pb_7^+, Pb_8^+ and Pb_9^+ clusters, respectively. However, significant structural changes are observed for Pb_{10}^+ and Pb_{11}^+ from the neutral clusters. While Pb_{10} favors tetra capped trigonal prism (TTP) as the lowest energy isomer, Pb_{10}^+ adopts a bicapped tetragonal antiprism geometry. It may be pointed out that for neutral Pb_{10} the bicapped tetragonal antiprism is 1.2 eV higher in energy than the TTP structure. In case of Pb_{10}^+ cation, the difference between these two isomeric structures is found to be only 0.07 eV. For Pb_{11} neutral cluster, a large number of isomers are found to be close in energy. The lowest energy isomer is a pentagonal antiprism based motif. The next higher energy isomer which follows a tetragonal motif is found to be 0.05eV higher in energy. Based on the close lying isomers of Pb_{11} neutrals it may be inferred that its potential energy surface might be shallow and therefore a switch over of the relative stability is possible for these isomers. Unlike this the lowest energy isomer of the Pb_{11}^+ cluster shows deep minima, which adopts a tricapped tetragonal prism structure following the tetragonal motif of Pb_{10} cluster.

The ground state geometries of the neutral and cationic clusters of Pb_{12} and Pb_{13} show similar structural features, except that of small local distortions which are due to the positive charge on the cationic species. The overall growth motif of Pb_{12} and Pb_{13} clusters shows spherical icosahedron structures as the lowest energy isomers. For Pb_{12} an empty cage distorted icosahedron was found to be the lowest energy isomer. The Pb_{12}^+ cluster also adopts similar geometry with an increase of the cage size (the distance between opposite vertex atoms is 4.99 Å). Pb_{13} cluster is found to form regular icosahedron with I_h symmetry. Upon removal of an electron the Pb_{13}^{+} cluster shows small distortions. In contrast to this trend, a significant change in the lowest energy structure is observed between the neutral and cationic species of Pb_{14}. While the initial configuration of a face capped icosahedron undergoes large rearrangements, in case of neutral cluster, the Pb_{14}^{+} shows only a small relaxation from the initial face caped icosahedral structure and retains the geometry as the lowest energy isomer. For Pb_{15}^{+}, initial configurations were generated based on the pentagonal and hexagonal structural motifs. Some of these consist of capping icosahedrons or hexagonal antiprism structures as well as encapsulated hexagonal prisms *etc*. Comparison of the total energies among all these isomers after geometry relaxation suggests that the ground state geometry of the Pb_{15}^{+} cluster favors encapsulated hexagonal antiprism structure which is similar to that observed for neutral Pb_{15} cluster.

3.3.2.2 Energetics

In order to understand the relative stability of these clusters, the average binding energies, second order difference in energy and the fragmentation behavior are estimated based on the total energies obtained for the lowest energy isomers. Figure 3.12 represents the average binding energies as a function of cluster size for the neutral and charged Pb_n clusters. The average binding energy of neutral is calculated as in eq. 3.1 and cationic clusters is calculated as in eq. 3.3

$$BE(Pb_n^{+}) = \frac{-[E(Pb_n^{+}) - (n-1) \times E(Pb) - E(Pb^{+})]}{n} \qquad \text{eq. 3.3}$$

It is seen that the average binding energy of the cations is higher than the corresponding neutrals. This may be explained due to the higher effective nuclear charge for the positively charged cation than for the neutrals. The humps and dips in the BE curve reflect their relative stability order. In general, it is found that the BE curve of the cation is smoother than neutrals except for $n = 8$ and 13. While at Pb_8^{+}, the BE curve shows a dip,

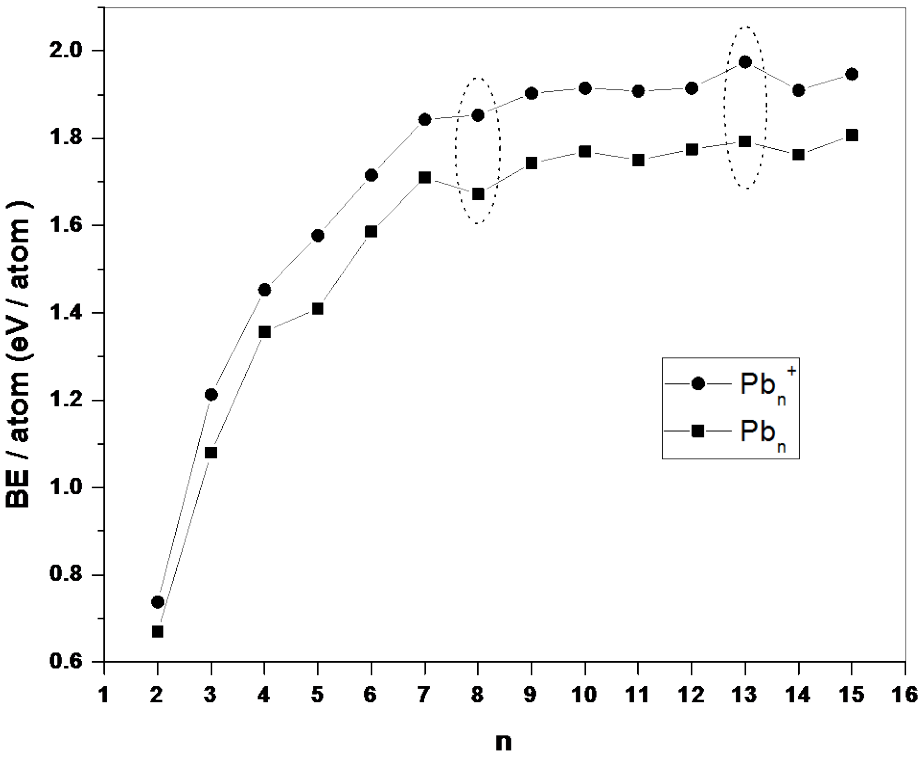

Figure 3.12 The average binding energy of Pb_n and Pb_n^+ clusters as a function of cluster size (n).

significant jump is observed for Pb_{13}^+. The relative stability for a series of clusters can be obtained through the second order difference in energy ($\Delta^2 E$) plot as shown in Figure 3.13.

The $\Delta^2 E$ is calculated as

$$\Delta^2 E = 2 \times E(\,Pb_n^+) - E(\,Pb_{n+1}^+) - E(\,Pb_{n-1}^+) \qquad \text{eq. 3.4}$$

According to these equations, the negative values indicate more stability than neighbors. Overall, it is found that neutral clusters with $n = 4, 7, 10$ and 13 atoms are more stable than their neighbors. This is in agreement with the mass abundance spectrum of the Pb clusters [341-343]. Although it is found that both neutral and cation

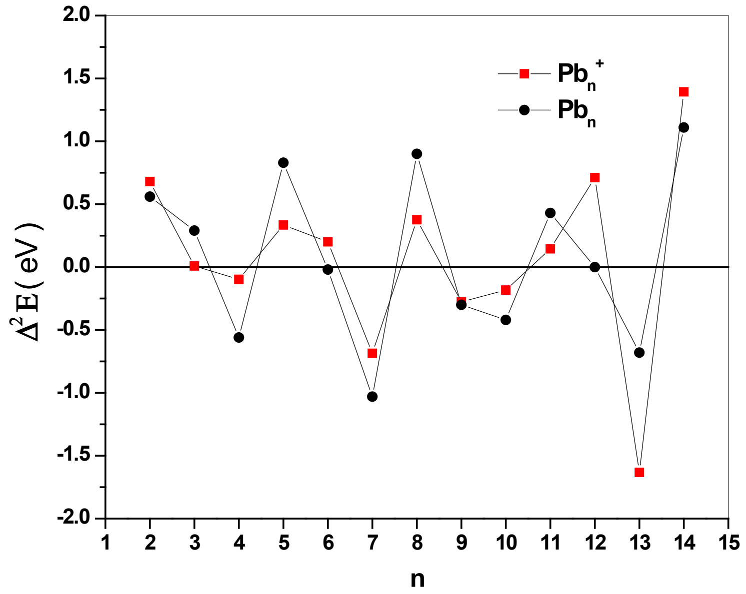

Figure 3.13 Plot of second order difference in total energy of Pb_n and Pb_n^+ clusters as a function of cluster size.

clusters follow similar pattern in the relative stability order, there are differences in the details of their absolute values. In general, the peaks are sharper for neutral clusters, than cations. The exception to this occurs for $n = 13$, where the absolute value of $\Delta^2 E$ is more for Pb_{13}^+ than Pb_{13}. This is due to the higher formation energy of the cation (as reflected in the BE curve) or in other words it indicates that the removal of an electron from Pb_{13} neutral is easier even though it has reasonably higher thermodynamic stability. To illustrate this contradictory effect in the stability of Pb_{13}, detailed analysis of the electronic structure was performed by evaluating the electronic eigen-value spectrum and ionization potential.

3.3.2.3 Fragmentation Behavior

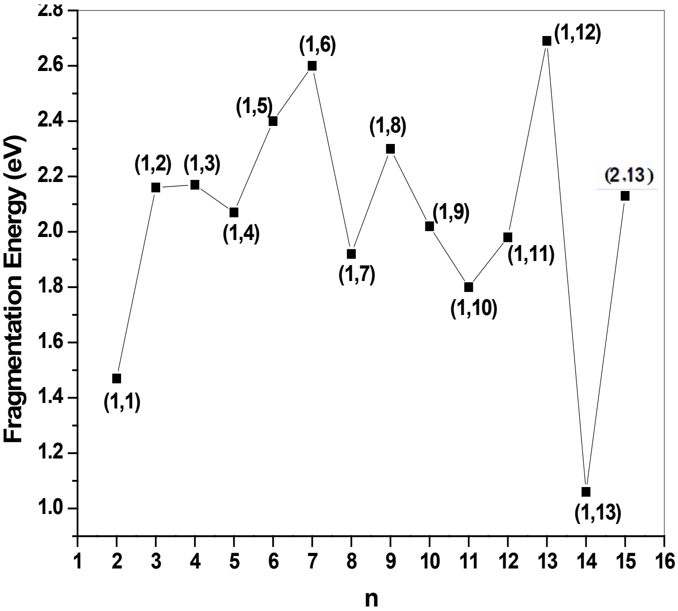

Figure 3.14: The lowest energy fragmentation channels of Pb_n^+ clusters. The neutral and charged fragments are in the brackets.

Apart from binding energy and second order difference in energy, the fragmentation behavior of the Pb_n^+ clusters was analyzed. Although it is known that the fragmentation process involves a dissociation barrier and entropy or free energy changes, in the present work, spontaneous fragmentation of the parent cation into a neutral and charged daughter products is assumed as in eq. 3.5

$$Pb_n^+ \quad \rightarrow \quad Pb_p + Pb_{n-p}^+ \qquad \text{eq. 3.5}$$

For this purpose the fragmentation energies were calculated for all the possible channels, which can be expressed as

$$E_f(Pb_n^+) = E(Pb_n^+) - E(Pb_p) - E(Pb_{n-p}^+) \qquad \text{eq. 3.6}$$

For the sake of simplicity the fragmentation energies of the lowest energy channels as a function of the cluster size are plotted in Figure 3.14. It is found that up to $n = 14$, the Pb_n^+ clusters favor monomer evaporation as the lowest energy fragmentation channel. The higher abundance of Pb_7 and Pb_{13} clusters in mass spectrometry experiment [341-344] can be attributed to the larger fragmentation energy of these clusters as can be seen from Figure 3.14. Moreover, the absence of the Pb_{14}^+ mass peak as reported in the photo ionization experiment [343] is clearly a consequence of the lowest fragmentation energy of the Pb_{14}^+ cluster as compared to the others in the series. Pb_{15}^+ dissociates into Pb_{13}^+ and Pb_2. This reconfirms the higher stability of Pb_{13}^+ cluster in this series.

3.3.2.4 Electronic Structure

The energy difference between the highest occupied and lowest unoccupied molecular orbital (HOMO-LUMO) energy levels is considered to be an important parameter in terms of the chemical stability of small clusters. The larger the energy gap (E_g), the higher is the chemical stability. The energy gap of Pb_n clusters is shown in Figure 3.15. Large energy gaps are found for $n = 5, 6, 10, 12$ and 15. It should be noted that this is in difference to the stability pattern that is obtained from the second order difference in energy, where $n = 4, 7, 10$ and 13 shows higher stability in comparison to their neighbors. In this context it may be mentioned that the energy gap of a cluster precisely depends on the eigen values of the HOMO and LUMO energy levels. For example, although Pb_5 shows less stability in the average binding energy in comparison to its neighboring clusters, its large energy gap is a manifestation of its twenty valence electrons,

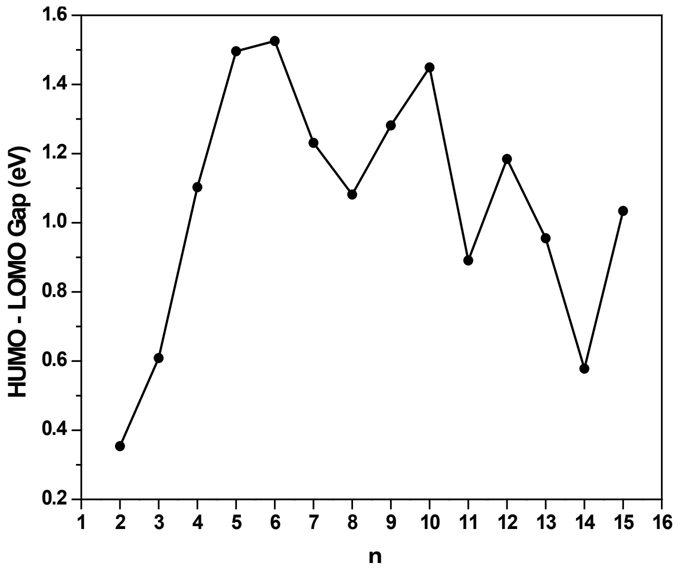

Figure 3.15: Plot of HOMO-LUMO gaps as a function of size (n) of Pb_n clusters.

which is responsible for the electronic shell closing effect. The most important deviation in the stability derived from the total energy and HOMO-LUMO energy gap pattern occurs for Pb_{13} cluster. The compact atomic structure of the Pb_{13} cluster is corroborated by its higher binding energy in comparison to that of Pb_{12} and Pb_{14} clusters. However, the energy gap spectrum does not follow this pattern, which rather shows a monotonic decrease from Pb_{12} to Pb_{14} clusters. This indicates that although Pb_{13} is thermodynamically more stable but it is more reactive than Pb_{12} due to the lowering of the energy gap.

In order to verify this fact the eigen-value spectrum of Pb_{12} and Pb_{13} is plotted in Figure 3.16 after broadening (Gaussian) by 0.1 eV. Each peak in this spectrum has been marked by occupation number which is obtained based on spherical shell filling model [369], which states that for spherically compact (I_h symmetric) clusters, $2(n+1)^2$ electrons will be chemically more stable. For Pb_{13}, the splitting of the $1g$ level results in two important changes in the energy level spectrum: the first one is to create a large gap between the HOMO and HOMO-1 energy levels and secondly, reduce the gap between HOMO and

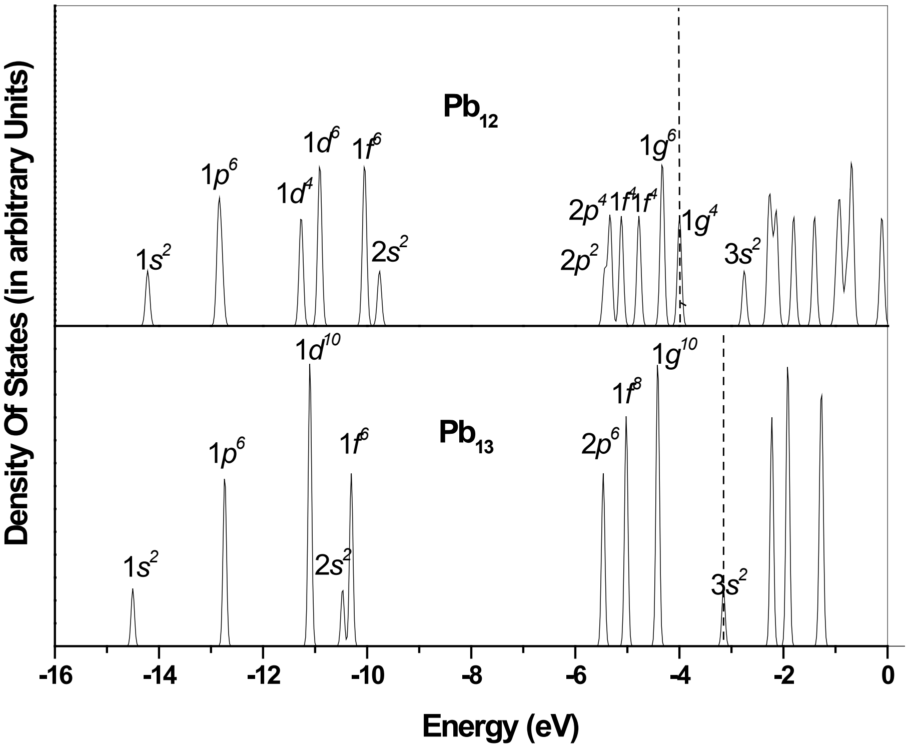

Figure 3.16: Energy eigenvalue spectrum for Pb_{12} and Pb_{13} clusters as obtained from the Kohn-Sham energy states after Gaussian broadening. The dashed line represents the Fermi energy level.

LUMO energy level.

The ionization potential is another important parameter in understanding the trend in their electronic stability. More precisely, the ionization potential reflects the stability of the HOMO energy level over the stability in terms of the total energy. The adiabatic ionization potentials of Pb_n clusters were calculated from the difference in total energy between the neutral and cation clusters. To verify the reliability of the calculated IP values were compared with the available experimental results [342] as well as with previously published results based on more accurate theoretical models [349-357]. A summary of the results are listed in Table 3.3. Interestingly the results on the IP's of Pb_n clusters are in excellent agreement with the experimental values. In fact a comparison between the ionization potentials obtained from the PAW/GGA-PW91 (SO) method and the experimental values clearly suggest that, for Pb clusters, the less expensive PAW/GGA-PW91 (SO) method is able to provide a better estimate in comparison to the results obtained using sophisticated *ab initio* methods such as CASSCF, MRDCI(Q) and MRDCI(Q) including the spin orbit coupling. Following the usual

n	**GGA/SO**	**Exp**[a]	**Theory**[b]
2	5.96	6.2	
3	5.70	5.8	6.59[c], 6.42[d], 6.15[e], 6.36[f], 6.12[g]
4	5.71	5.7	6.39[f], 6.48[g], 6.23[h]
5	5.27	5.7	
6	5.33	5.48	6.6[c], 6.9[d], 6.3[e], 5.3[f], 6.6[i]
7	5.15	5.3	
8	4.64		
9	4.65		
10	4.63		
11	4.38		
12	4.42		
13	3.74		
14	4.01		
15	4.01		

Table 3.3: Ionization potentials of Pb_n clusters in comparison with the experimentally and computationally available results.

[a] ref [342]
[b] ref [350,351]
[c] DFT (B3LYP)
[d] MP2
[e] MRD-CI
[f] MRDCI (Q)
[g] MRDCI (Q)+ SO
[h] CASSCF
[i] CCSD(T)

trend, a decreasing trend in the IP of Pb_n clusters is found as a function of size. However, a close look at the IP curve, as shown in Figure 3.17, indicates the signature of shell filling phenomenon. It is found that a sharp dip occurs after each close shell cluster followed by a plateau of close lying IPs, which may belong to the same shell. According to this the inflection points are obtained at $n = 4, 7, 10$ and 12. It may be noticed that, except Pb_{12}, all represent stable clusters through the second order difference in energy.

The most interesting feature in the IP curve is the finding of the sharp dip at Pb_{13} cluster, albeit of having higher binding energy as shown in Figure 3.17. The difference in the

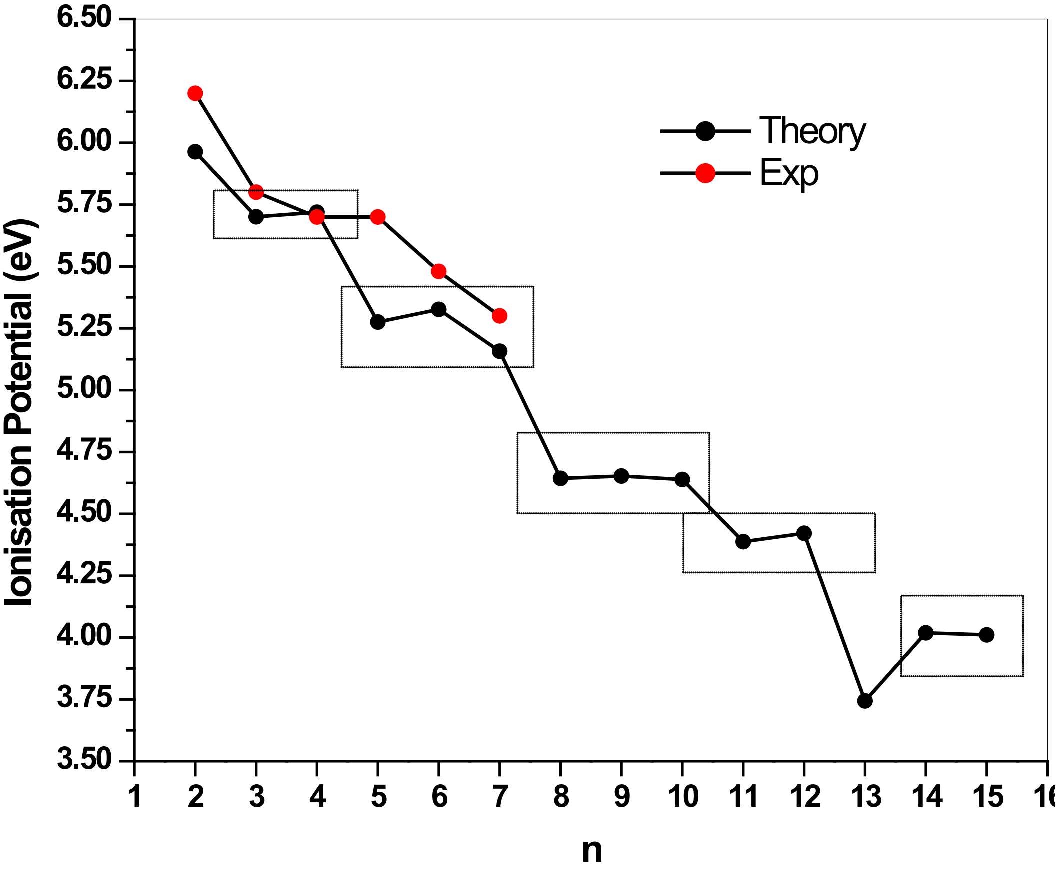

Figure 3.17: Plot of ionization potentials of Pb_n clusters as a function of the size.

stability of Pb_{13} can be explained from the ordering of the energy states, based on the spherical shell model [369] as shown in Figure 3.16. Although Pb_{13} cluster satisfies the spherical geometrical shape through icosahedron arrangements of atoms, it possesses two additional electrons over the shell closing number of 50. Consequently, the HOMO energy level is shifted upwards which actually causes the lowering of ionization potential in spite of its higher stability based on the total energy consideration. In fact the substitution of a Pb atom in Pb_{13} by a divalent Mg atom results in the significant enhancement of the energy gap (2.3 eV) [370]. These results further confirms that while the overall stability of a cluster can be guided by its binding energy its chemical stability could be lower depending on the reordering of the electronic energy levels. Therefore, a clear understanding of both atomic and electronic structures is important in illustrating thermodynamic and chemical stability of a specific cluster.

3.4 Conclusions

In the first section of this chapter the geometric and electronic structures of Pb_n clusters investigated using the *ab initio* molecular dynamics simulation are discussed. Plane wave based pseudo-potential method under the GGA-PW91 (SO) scheme was used to optimize the geometry of several isomers. Further, spin-orbit coupling effect was included to calculate the total energy of the lowest energy isomers. The relative stability of few low-lying isomers was verified by more accurate quantum chemical methods based on hybrid energy functional as well as at the MP2 level theory under the LCAO-MO methods. It is found that the binding energies are significantly improved after the inclusion of spin-orbit effect term. In fact for small clusters like Pb_2, the binding energy, reduced to half. Several low-lying isomers were identified based on tetragonal, pentagonal and hexagonal configurations. A similarity in the ground state geometries of Pb_n clusters up to $n = 7$ with other Group IV clusters was observed. For $n = 8 - 10$, slow transition towards close packed geometries was observed. From $n = 11$ onwards, the lowest energy structures evolved with close packed structures having five or six fold symmetry. Encapsulation of atoms into spherical cages of icosahedron initiates as early as $n = 13$ for Pb_n clusters, unlike other Group IV clusters which start at much larger sizes. Based on these results it was inferred that unlike other Group IV clusters the compact spherical structures are formed for Pb clusters even at smaller size range. This trend is in agreement with their bulk structures, which is diamond like for Si, Ge and Sn elements and fcc for Pb. This nature can further be attributed to the higher compressibility of lead over other elements in Group IV. The relative stability of these clusters was analyzed based on their average binding energy, second order difference in energy, and fragmentation pattern. The results reveal that $n = 4, 7, 10$ and 13 atom clusters have higher stability than the other clusters in this series. This was in excellent agreement with the experimentally observed mass abundance pattern reflecting the confidence in the predicted ground state geometries of these clusters presented in this work. The fragmentation behavior suggested that while small clusters favor monomer evaporation as the lowest fragmentation energy channel, larger clusters $(n > 12)$ favor to dissociate into two stable daughter clusters. The large abundance of $n = 7$ and absence of $n = 14$ clusters in the photo ionization experiment has been clearly demonstrated from the fragmentation analysis of the Pb_{14} cluster. Based on the stability analysis of Pb_n clusters and the available experimental results, which suggests that for $n = 4, 7, 10, 13$ are magic; it can be inferred that both electronic structure and geometric packing are responsible for their stability order of these clusters. The results were subsequently tested and verified by Waldschmidt *et al.* [368], in their work on surface-induced dissociation studies on the energetics and structure of lead clusters.

In the second section, the geometric and electronic structure of the Pb_n^+ clusters were investigated and compared with neutral clusters. The ground state geometries of the singly positively charged Pb_n^+ clusters show compact growth pattern as that observed for neutrals with small local distortions. The chemical stability of these clusters was analyzed by evaluating their energy gap between the highest occupied and lowest unoccupied molecular orbital and adiabatic ionization potentials. The results revealed that although Pb_{13} showed higher stability from the total energy analysis, but its energy gap and ionization potential do not follow the trend. Albeit of higher stability in terms of binding energy, the lower ionization potential of Pb_{13} is interesting and was explained based on its electronic structure through the density of states and electron shell filling model of spherical clusters.

4. Effect of Dopants on the Structure and Electronic Properties of Group IV Clusters: A Case Study with Sn and Pb Clusters

4.1 Introduction

Although an impurity atom can play very important role in the modification of electronic and geometrical properties of homoatomic clusters [370-388], these studies are relatively less due to difficulties in the experimental arrangements and more number of isomeric structures that needs to be evaluated from the theoretical side. Most of the previous works on doped lead clusters [384-388] were carried out mainly using transition metal atoms as dopant. Recently, Neukermans *et al.* have measured the mass abundance pattern of Al doped Pb clusters [386]. While large abundance of Pb_{13} cluster was found in agreement with the results of LaiHing *et al.* [343], a sharp peak was observed for $AlPb_{12}^{+}$ cluster. The enhanced stability of $AlPb_{12}^{+}$ was explained based on 50 electron rule with highly symmetric icosahedral structure [370,386]. Followed by this, Chen *et al.* have calculated the electronic structures and stabilities of cationic $Pb_{12}M^{+}$ clusters, where M represents Group III elements using DFT [387]. Motivated by these works, which showed significant effect of the impurity elements on the stability of lead clusters, a systematic theoretical study on Pb_nM ($M = C, Al, In, Mg, Sr, Ba$ and Pb; $n = 8, 10, 12$ and 14) clusters is carried out. The criteria of choosing different doping elements is based upon their mass, size and number of valence electrons, which in fact governs the nature of interaction. The objective of this study is to understand the inter atomic interactions of different elements with Pb and the influence of the atomic size and valence electrons of the dopant on the geometry, electronic structure and stability of a binary cluster.

4.2 Computational Details

The interaction of an impurity atom with a homoatomic cluster can lead to three different possibilities: the impurity atom can (*a*) occupy the center of the cage formed by the host cluster (*endohedral*), (*b*) adsorb on the surface of the host cluster (*exohedral*) and (*c*) replace one atom from the framework of the host cluster (*substitutional*). Based on this approach, a large number of initial structures for each Pb_nM cluster were generated to explore the lowest energy structures. The geometry optimizations were performed using the plane wave based density functional theory formalism with pseudopotentials generated using PAW method to describe the electron-ion interaction [270,271]. The PAW pseudo-potential was generated considering scalar relativistic corrections. The spin polarized GGA-PW91 was used to calculate the exchange-correlation energy [232,233]. In the previous chapter it was shown that Pb clusters have significant spin-orbit effect. Therefore, all calculations in this work were carried out including the spin-orbit coupling effect in the total energy calculation. A simple cubic super-cell of side 20 Å was used and the Brillouin zone integrations are carried out using only the Γ point. The geometry optimization of each isomer was carried out till the forces on each atom was less than 0.005 eV/Å.

4.3 Results and Discussion

A. Pb_nM ($M = C, Al, In, Mg, Sr, Ba$ and Pb; $n = 8, 10, 12$ and 14) Clusters

4.3.1 Geometric Structure

4.3.1.1 $M - Pb$ Dimers

In order to understand the M atom interaction with Pb, the inter-atomic separations of all $Pb - M$ dimers were optimized. The bond lengths and energetics are summarized in Table 4.1. In general, it is seen that the spin configurations with higher multiplicities are favored for these dimers. The interaction energy of the carbon with lead is found to be the highest and the interaction energy varies in the order of $Pb - C > Pb - Al > Pb - Pb > Pb - In > Pb - Ba > Pb - Sr > Pb - Mg$. Based on these results two things can be inferred: (*i*) $p - p$ interaction is stronger than $s - p$ interaction and (*ii*) The interaction energy of lighter elements are stronger than heavier ones.

$$BE/atom\ (Pb_nM) = -\left[E\ (Pb_nM) - E(M) - n \times E(Pb)\right]/(n+1) \qquad \text{eq. 4.1}$$

$$Interaction\ Energy = E(Pb_nM) - E(M) - E(Pb_n) \qquad \text{eq. 4.2}$$

n		C	Pb	Al	In	Mg	Sr	Ba
1	BE/Atom (eV/atom)	1.36	0.67	0.79	0.61	0.24	0.37	0.51
	$M-Pb$	2.13	3.0	2.75	2.93	2.81	3.19	3.41
	Multiplicity	3	3	4	4	3	3	3
8	BE/atom (eV/atom)	2.0	1.74	1.86	1.79	1.61	1.69	1.76
	$M-Pb$ (Å)	2.50	3.11	2.8	3.0	3.0	3.2	3.4
	Interaction Energy (eV)	4.59	2.31	3.36	2.74	1.13	1.84	2.49
	HLG (eV)	0.74	0.95	0.24	0.22	1.1	0.85	0.91
10	BE/Atom (eV/atom)	2.04	1.79	1.9	1.86	1.77	1.77	1.83
	$M-Pb$ (Å)	2.75	3.1	2.97	3.13	2.9	3.25	3.34
	Interaction Energy (eV)	4.83	1.59	3.22	2.77	1.84	1.9	2.54
	HLG (eV)	0.88	0.89	0.18	0.6	1.79	0.98	1.15
12	BE/Atom (eV/atom)	2.04	1.93	1.93	1.89	1.89	1.82	1.87
	$M-Pb$ (Å)	3.07	3.4	3.0	3.2	3.16	3.2	3.35
	Interaction Energy (eV)	5.29	2.0	3.77	3.27	3.33	2.39	3.06
	HLG (eV)	2	1.13	0.05	0.4	2.3	1.0	1.2
14	BE/Atom (eV/atom)	1.9	1.83	1.88	1.82	1.81	1.81	1.79
	$M-Pb$ (Å)	2.45	3.02	2.84	2.94	2.96	3.21	3.37
	Interaction Energy (eV)	4.0	2.45	3.64	2.45	2.5	2.5	3.02
	HLG (eV)	1.04	1.04	0.12	0.09	1.04	1.01	1.1

Table 4.1: Summary of the average binding energy (E_b), interaction energy (E_I), energy gap between the HOMO and LUMO energy levels (HLG), and the shortest $M-Pb$ bond distances of Pb_nM ($M = C, Al, In, Mg, Sr, Ba$ and Pb; $n = 8, 10, 12$ and 14) clusters.

4.3.1.2 Geometries of Pb_nX ($X = C$ and Pb; $n = 8, 10, 12$ and 14) Clusters

For C and Pb, which have similar valence electronic configuration (s^2p^2), the interactions are governed through $p-p$ interactions. The optimized structures of Pb_nX clusters that are close in energy from the lowest energy isomer are shown in Figure 4.1-Figure 4.7. Carbon, which is the smallest among the Group IV elements (C/Pb~0.52), prefers to be encapsulated starting from Pb_8 onwards (Figure 4.1). It is found that for smaller size clusters, addition of C atom significantly changes the structure of Pb_nC clusters. The lowest energy isomer of the Pb_8C cluster forms distorted square antiprism configuration with impurity C occupying the endohedral position as shown in (Figure 4.1, Pb_8C-a). The stability of this geometry is reconfirmed when few isomers with different initial configurations relaxed to this same geometry. The $Pb_{10}C$ cluster shows preference towards an encapsulated square antiprism geometry (Figure 4.1, $Pb_{10}C-a$). In this context it may be mentioned that unlike this, for $Si_{10}C$, the impurity C atom remains with lower coordination number. This was attributed to the strong covalent

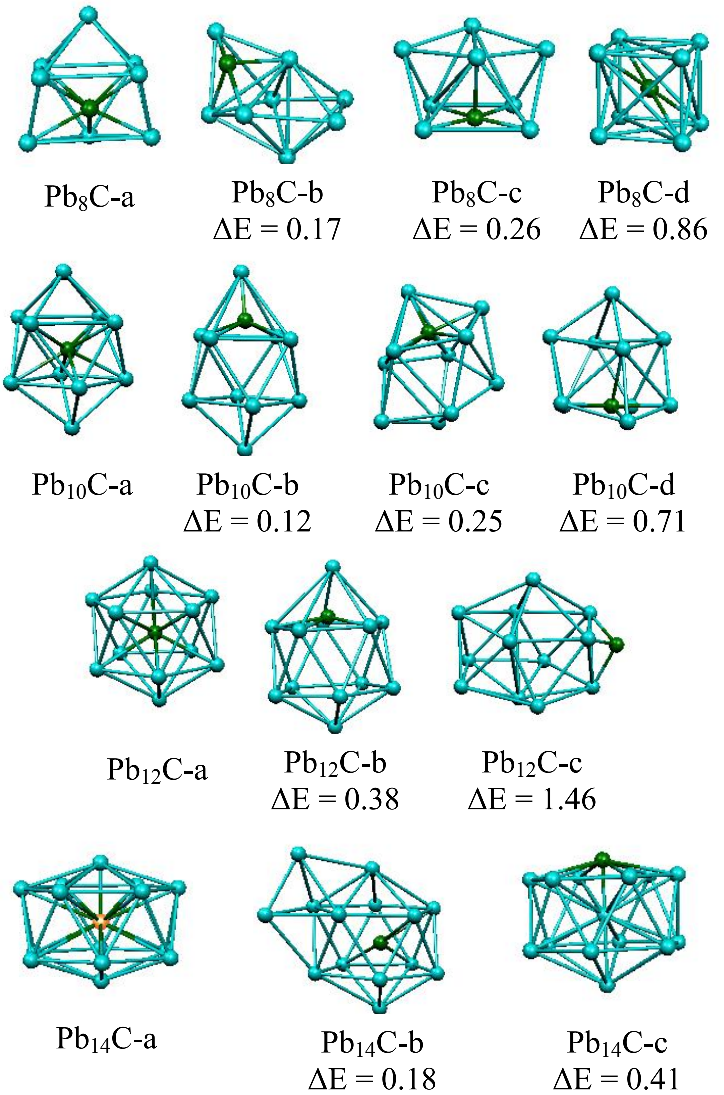
Pb_8C-a
Pb_8C-b $\Delta E = 0.17$
Pb_8C-c $\Delta E = 0.26$
Pb_8C-d $\Delta E = 0.86$
$Pb_{10}C$-a
$Pb_{10}C$-b $\Delta E = 0.12$
$Pb_{10}C$-c $\Delta E = 0.25$
$Pb_{10}C$-d $\Delta E = 0.71$
$Pb_{12}C$-a
$Pb_{12}C$-b $\Delta E = 0.38$
$Pb_{12}C$-c $\Delta E = 1.46$
$Pb_{14}C$-a
$Pb_{14}C$-b $\Delta E = 0.18$
$Pb_{14}C$-c $\Delta E = 0.41$

Figure 4.1: Few of the low-lying isomers of Pb_nC ($n = 8, 10, 12$ and 14) clusters ($\Delta E\ in\ eV$).

character of the $Si-C$ bond in comparison to the $Pb-C$ bond [372]. The binding energy of Pb_8C and $Pb_{10}C$ clusters has been estimated to be 2.0 eV/atom and 2.04 eV/atom, respectively, which are significantly higher than the corresponding Pb_9 (1.74 eV/atom) and Pb_{11} (1.79 eV/atom) clusters. The enhanced stability of Pb_nC clusters in comparison to Pb_{n+1} is due to higher interaction energy of $Pb-C$ than $Pb-Pb$. The interaction of C with Pb_{12} cluster results in an encapsulated icosahedron where C atom occupies the central position. The distance between C and Pb atom is estimated to be 3.07 Å, significantly large as compared to its dimer distance of 2.13 Å. Although in the ground state both $Pb_{12}C$ and Pb_{13} form icosahedron with one atom at the center, the stability order differs for higher energy isomers. The higher energy isomer of $Pb_{12}C$, where the impurity C atom resides outside the cage, is 1.46 eV higher in energy. The binding energy of $Pb_{12}C$ is estimated to be 2.04 eV/atom. It is noted that the $Pb-C$ bond length in $Pb_{12}C$ (3.07 Å) is significantly more that in $Pb_{10}C$ (2.75 Å) cluster. For $Pb_{14}C$, the impurity C prefers to be encapsulated inside the hexagonal cage structure of Pb_{14} cluster as shown in Figure 4.1. Moreover, it is observed that this structure is significantly compressed in comparison to that of $Pb_{12}C$ icosahedron as the $C-Pb$ (center-apex) distance is reduced to 2.45 Å.

4.3.1.3 Geometries of $Pb_nY(Y = Al$ and In; $n = 8, 10, 12$ and $14)$ Clusters

The interaction of Group III elements with Pb_n clusters is different from Group IV in a way that they posses one less electron in the outermost p orbital. To understand the effect of these elements on the structural and electronic properties of Pb_n clusters as a function of size, two different elements *viz.* Al and In were used. Although both these elements have similar valence electronic configuration, they are different in their sizes as well as masses.

The interaction of Al or In atoms with Pb_8 favors a bicapped pentagonal bipyramidal isomer where one vertex Pb is replaced by the Y atom. It may be noted that unlike Pb_8C cluster, where C goes inside the cage, the impurity atom is placed at the peripheral location.

From the atomic arrangement of these structures (Figure 4.2) it is clear that the growth motif is icosahedron, which is further evident from the trend shown by larger clusters. The binding energy of Pb_8Al and Pb_8In clusters are estimated to be 1.86 eV/atom and 1.79 eV/atom, respectively. For $Pb_{10}Al$ cluster, encapsulated tetragonal anti-prism and pentagon-based structures are nearly degenerate (Figure 4.2, $Pb_{10}Al-a$ and $Pb_{10}Al-b$) with an energy difference of 0.06 eV. It has a binding energy of 1.90 eV/atom and encapsulation energy of 3.22 eV. It may be noted that even higher energy isomers of $Pb_{10}Al$ cluster shows encapsulated Al atom at the center. For $Pb_{10}In$, although the lowest energy isomer favors In atom to be encapsulated, higher energy isomers prefer In atom capping from outside. In contrast to the behavior of $Pb_{10}Al$ clusters, which show several lowlying isomers, $Pb_{10}In$ cluster shows a deep minima with pentagon based structural motif as shown in Figure 4.2. The binding energy of $Pb_{10}In$ is calculated to be 1.86 eV/atom. The second higher energy isomer where the In atom caps the square antiprism formed by Pb_{10} cluster is found to be 0.21 eV higher in energy.

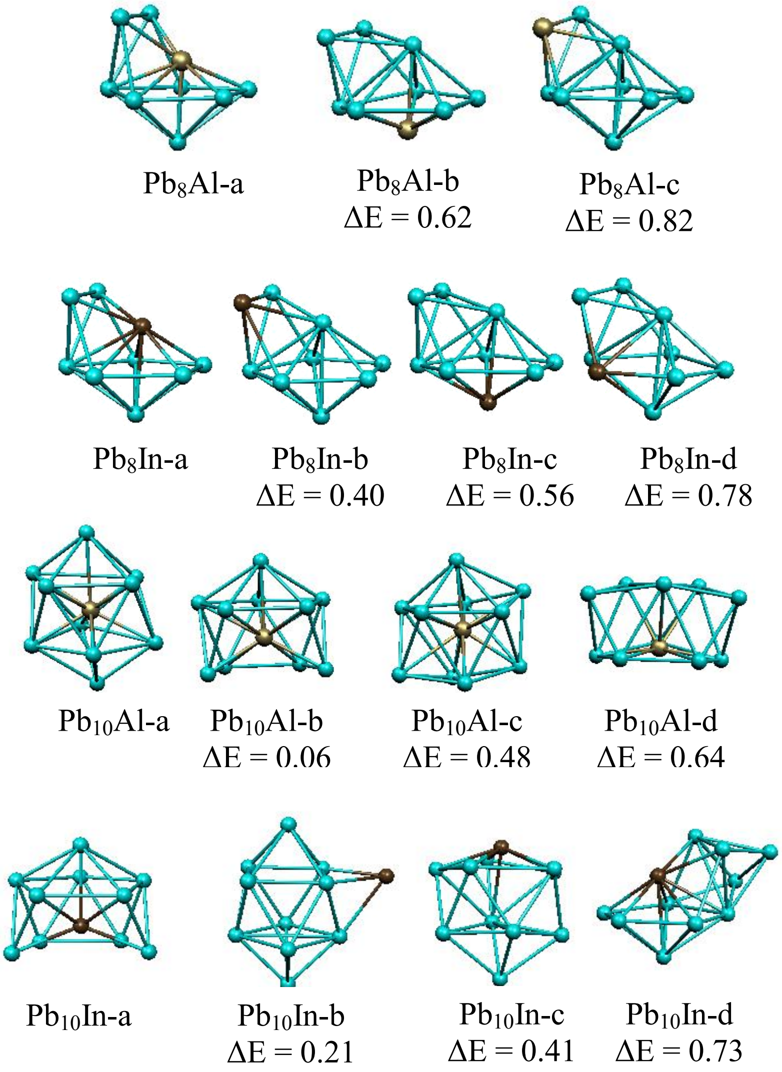
Pb$_8$Al-a
Pb$_8$Al-b ΔE = 0.62
Pb$_8$Al-c ΔE = 0.82
Pb$_8$In-a
Pb$_8$In-b ΔE = 0.40
Pb$_8$In-c ΔE = 0.56
Pb$_8$In-d ΔE = 0.78
Pb$_{10}$Al-a
Pb$_{10}$Al-b ΔE = 0.06
Pb$_{10}$Al-c ΔE = 0.48
Pb$_{10}$Al-d ΔE = 0.64
Pb$_{10}$In-a
Pb$_{10}$In-b ΔE = 0.21
Pb$_{10}$In-c ΔE = 0.41
Pb$_{10}$In-d ΔE = 0.73

Figure 4.2: Few of the low-lying isomers of $Pb_nY(Y = Al$ and In; $n = 8$ and 10) Clusters (ΔE in eV).

The interaction of Al and In atoms with Pb_{12} cluster results in similar ground state geometries *i.e.,* both impurity atoms prefer to occupy the central position of the Pb_{12} icosahedron. However, there are major differences in the higher energy isomers that are obtained for Al and In as shown in Figure 4.3. While for $Pb_{12}Al$, higher energy isomers are formed with Al inside the cage, In diffuses outside the cage replacing one Pb from the peripheral boundary. This feature indicates that for small change in energy or in other words at higher temperature, while In would prefer to replace one of the apex atoms and show exohedral capping as the most favorable structure, Al will remain inside unless the clusters are heated to a very high temperature. The binding energy of $Pb_{12}Al$ and $Pb_{12}In$ clusters are estimated to be 1.93 eV/atom and 1.89 eV/atom respectively. Similar to $Pb_{14}Y$ clusters, both Al and In prefer to substitute the central position of the Pb_{15}, as the lowest energy isomer. Unlike $Pb_{12}In$, for $Pb_{14}In$ cluster, In is stable at the central position, which is evident from the decreased difference in energy between the low-lying isomers. The binding energy

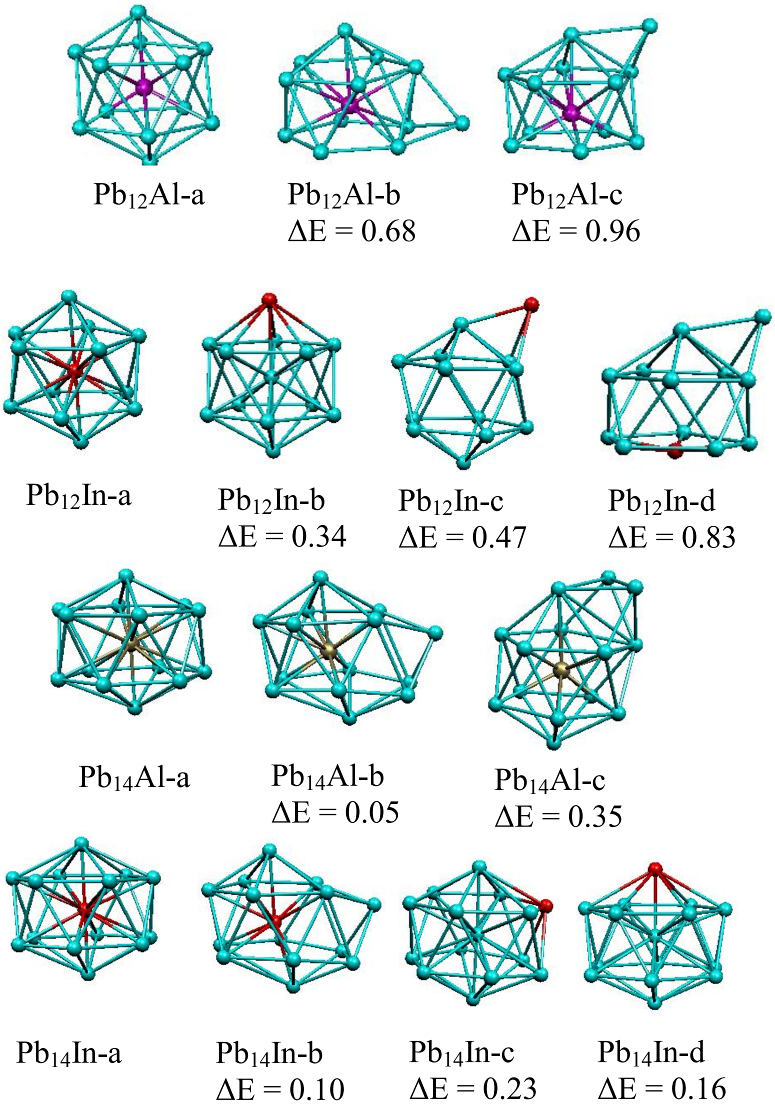

$Pb_{12}Al$-a

$Pb_{12}Al$-b $\Delta E = 0.68$

$Pb_{12}Al$-c $\Delta E = 0.96$

$Pb_{12}In$-a

$Pb_{12}In$-b $\Delta E = 0.34$

$Pb_{12}In$-c $\Delta E = 0.47$

$Pb_{12}In$-d $\Delta E = 0.83$

$Pb_{14}Al$-a

$Pb_{14}Al$-b $\Delta E = 0.05$

$Pb_{14}Al$-c $\Delta E = 0.35$

$Pb_{14}In$-a

$Pb_{14}In$-b $\Delta E = 0.10$

$Pb_{14}In$-c $\Delta E = 0.23$

$Pb_{14}In$-d $\Delta E = 0.16$

Figure 4.3: Few of the low-lying isomers of Pb_nY ($Y = Al, In$; $n = 12$ and 14) clusters (ΔE in eV).

of $Pb_{14}Al$ and $Pb_{14}In$ clusters is estimated to be 1.88 eV/atom and 1.82 eV/atom respectively.

4.3.1.4 Geometries of Pb_nZ ($Z = Mg, Sr$ and Ba; $n = 8, 10, 12$ and 14) Clusters

The alkaline earth metals of Group II have two valence electrons in the outermost s orbital. Due to the filled valence orbital, these elements are relatively inert and interact rather weakly in comparison to the Group III or Group IV elements. The results obtained for the low-lying isomers of Pb_nZ clusters are shown in Figure 4.4. Significant differences are observed in the low-lying isomers of Pb_nZ clusters as a function of the size of host Pb_n clusters. It is clear from Figure 4.4 that for Pb_8Z, all the Z atoms prefers to cap from outside. The larger atoms like Sr and Ba prefer to substitute the Pb atom capping the triangular faces of the bicapped PBP of Pb_9 cluster; Pb_8Mg forms capped distorted square antiprism structure. This indicates a possible threshold volume of the cage that is required to accommodate an impurity atom inside the core. For $Pb_{10}Z$ clusters, the isomers derived from the square antiprism motif, are found to be the most favored structures with the lowest energy (Figure 4.5). It may be noted that while Mg can be encapsulated inside the cage of the Pb_{10} cluster, Ba and Sr atoms cap Pb_{10} from outside. The isomers that were considered by substituting one Pb of the tetracapped PBP isomer of Pb_{11} cluster show substantially higher energy of 0.40 eV and 0.51 eV for Sr and Ba substitution respectively.

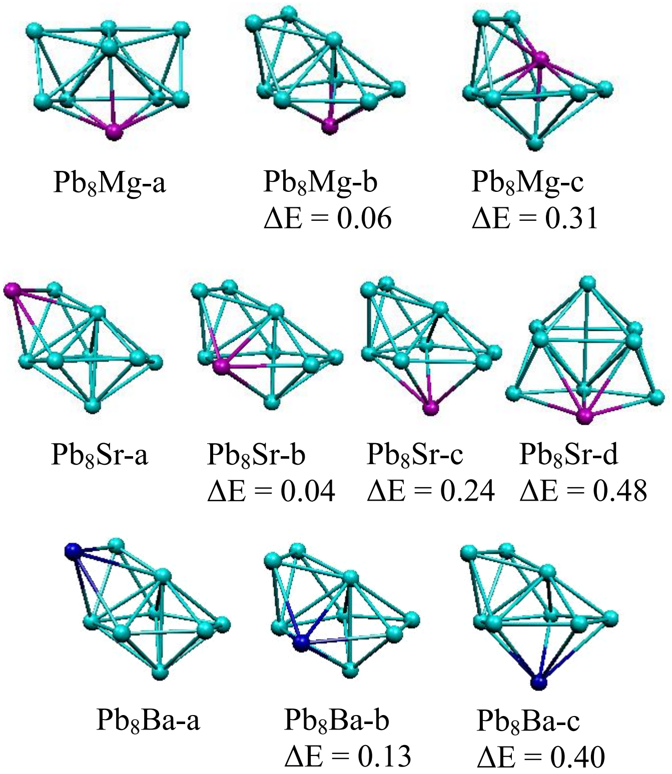

Pb_8Mg-a
Pb_8Mg-b $\Delta E = 0.06$
Pb_8Mg-c $\Delta E = 0.31$
Pb_8Sr-a
Pb_8Sr-b $\Delta E = 0.04$
Pb_8Sr-c $\Delta E = 0.24$
Pb_8Sr-d $\Delta E = 0.48$
Pb_8Ba-a
Pb_8Ba-b $\Delta E = 0.13$
Pb_8Ba-c $\Delta E = 0.40$

Figure 4.4: Few of the low-lying isomers of Pb_8Z ($Z = Mg, Sr$and Ba) Clusters(ΔE in eV).

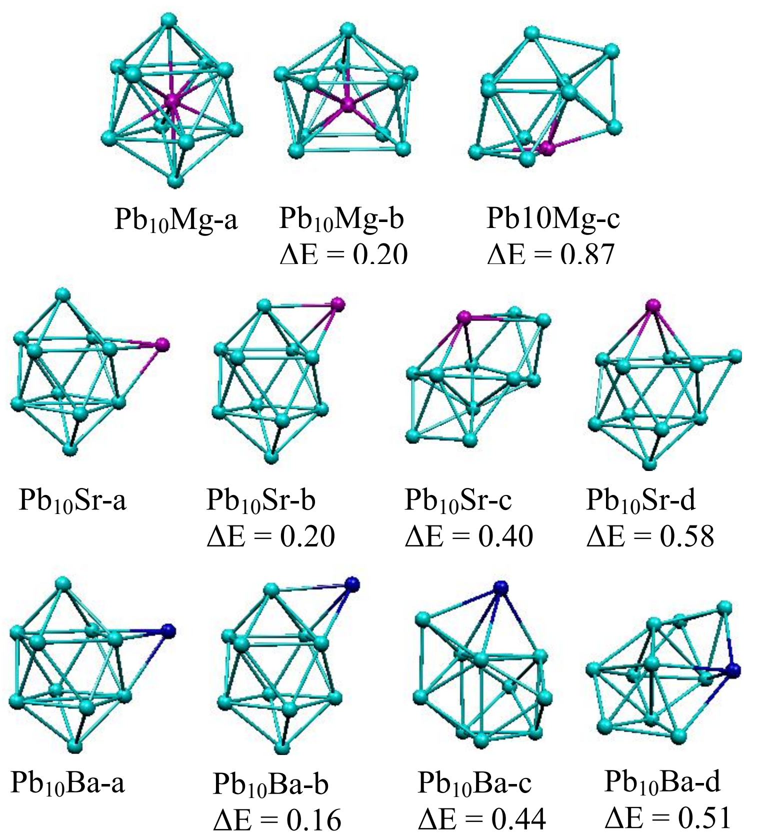
Pb$_{10}$Mg-a
Pb$_{10}$Mg-b ΔE = 0.20
Pb10Mg-c ΔE = 0.87
Pb$_{10}$Sr-a
Pb$_{10}$Sr-b ΔE = 0.20
Pb$_{10}$Sr-c ΔE = 0.40
Pb$_{10}$Sr-d ΔE = 0.58
Pb$_{10}$Ba-a
Pb$_{10}$Ba-b ΔE = 0.16
Pb$_{10}$Ba-c ΔE = 0.44
Pb$_{10}$Ba-d ΔE = 0.51

Figure 4.5: Few of the low-lying isomers of $Pb_{10}Z$ ($Z = Mg, Sr$ and Ba Clusters (ΔE in eV).

The low-lying isomers of $Pb_{12}Z$ ($Z = Mg, Sr$ and Ba) clusters are shown in Figure 4.6. It is seen that while Mg atom gets encapsulated inside the Pb_{12} cage, Sr and Ba atoms still favor to cap the triangular face from outside. The reason for such different behavior among the same group elements is attributed to the atomic size effect. The radius ratio of Mg, Sr and Ba atoms with respect to Pb is calculated to be 0.91, 1.22 and 1.26, respectively. The binding

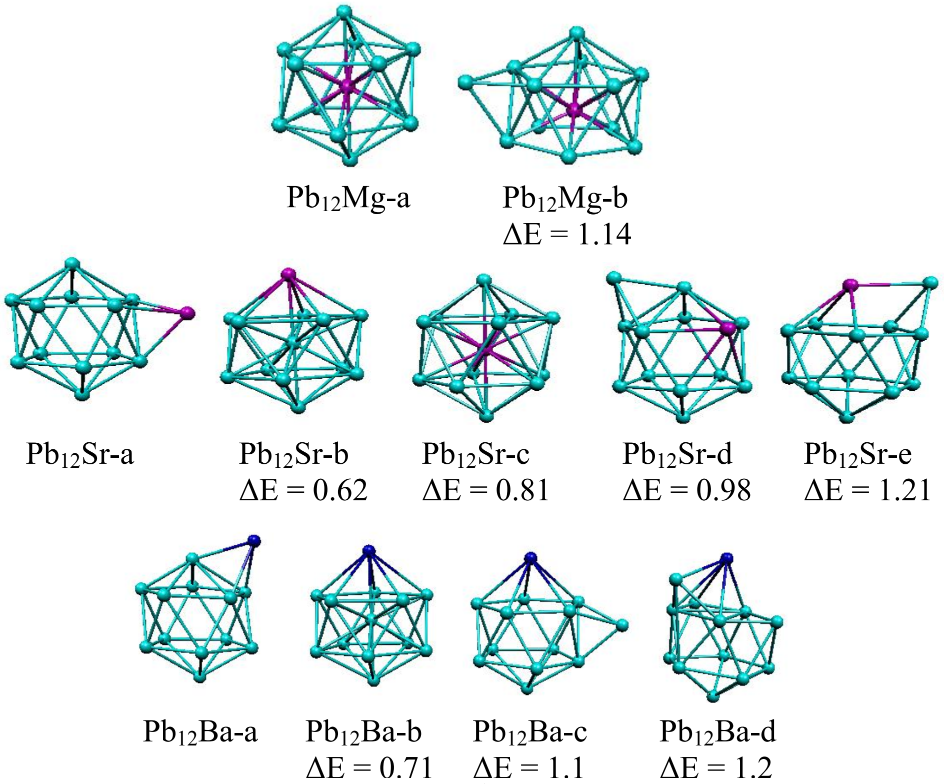
Pb$_{12}$Mg-a
Pb$_{12}$Mg-b ΔE = 1.14
Pb$_{12}$Sr-a
Pb$_{12}$Sr-b ΔE = 0.62
Pb$_{12}$Sr-c ΔE = 0.81
Pb$_{12}$Sr-d ΔE = 0.98
Pb$_{12}$Sr-e ΔE = 1.21
Pb$_{12}$Ba-a
Pb$_{12}$Ba-b ΔE = 0.71
Pb$_{12}$Ba-c ΔE = 1.1
Pb$_{12}$Ba-d ΔE = 1.2

Figure 4.6: Few of the low-lying isomers of $Pb_{12}Z$ ($Z = Mg, Sr$ and Ba) Clusters (ΔE in eV).

energy of $Pb_{12}Mg$, $Pb_{12}Sr$ and $Pb_{12}Ba$ clusters is estimated to be 1.89 eV/atom, 1.87 eV/atom and 1.82 eV/atom, respectively. For $Pb_{14}Z$ clusters, although Mg and Sr occupy the central position of the Pb_{15} cluster, Ba prefers to substitute the Pb atom from outside (Figure 4.7). Two isomers of $Pb_{14}Ba$, with slightly different exohedral substitution site preference are found to be close in energy.

Therefore, a critical cage volume is required to accommodate the impurity atom. As the size of the host cluster grows, it will be able to accommodate larger size impurity atom. This feature is further evident from $Pb_{15}Z$ clusters, where it is found that Mg and Sr can be accommodated inside the cage but Ba atom prefers to remain outside by replacing one of the Pb atoms from the periphery. In this context it should be mentioned that encapsulation of impurity atoms improves the stability of the doped clusters significantly. This feature is manifested from the comparison of Sr interaction energy with Pb_n clusters as a function of size. Until $n = 12$, Sr atom favors to cap the host Pb_n clusters from outside. The Pb_{14} cluster is the smallest size when the cage is sufficient to accommodate Sr atom inside and thereby improves the encapsulation energy (~2.5 eV) of Sr significantly in comparison to the smaller size clusters.

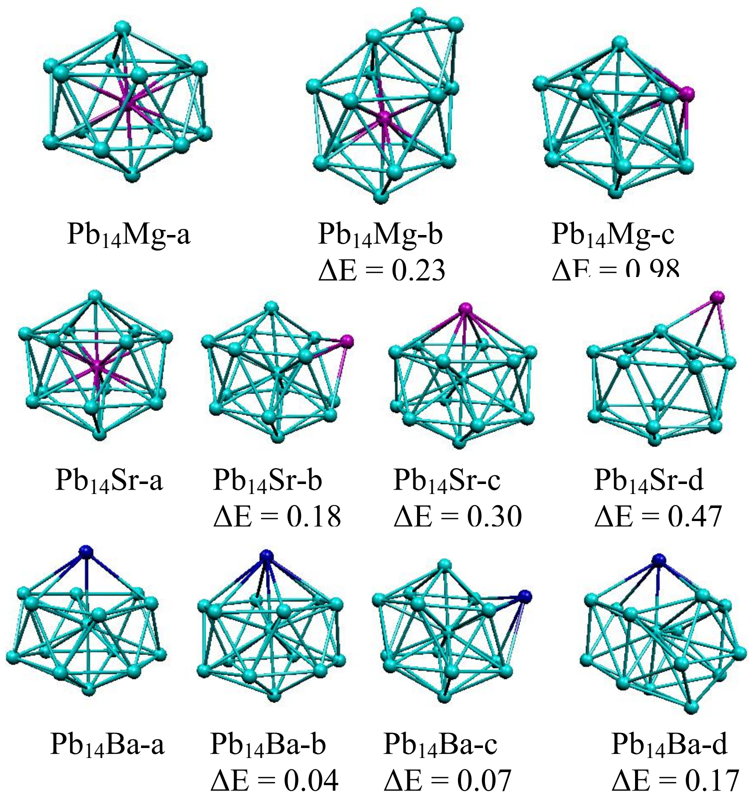

$Pb_{14}Mg$-a
$Pb_{14}Mg$-b ΔE = 0.23
$Pb_{14}Mg$-c ΔE = 0.98

$Pb_{14}Sr$-a
$Pb_{14}Sr$-b ΔE = 0.18
$Pb_{14}Sr$-c ΔE = 0.30
$Pb_{14}Sr$-d ΔE = 0.47

$Pb_{14}Ba$-a
$Pb_{14}Ba$-b ΔE = 0.04
$Pb_{14}Ba$-c ΔE = 0.07
$Pb_{14}Ba$-d ΔE = 0.17

Figure 4.7: Few of the low-lying isomers of $Pb_{14}Z$ ($Z = Mg, Sr$ and Ba) Clusters (ΔE in eV).

4.3.2 Trends in the Stability of Pb_nM Clusters

The stability of a cluster can be described from two aspects *viz.* (*i*) thermodynamic stability, which depends on the total energy of all atoms involved and (*ii*) chemical stability, which depends on the electronic energy level structure. In the following sections, these two issues are discussed separately to understand the stability of different clusters studied in this work with proper perspective.

4.3.2.1 Energetics

A comprehensive summary of the energetics and $M - Pb$ bond distances for all the clusters Pb_nM ($M = C, Al, In, Mg, Sr, Ba$ and Pb; $n = 8, 10, 12$ and 14) is listed in Table 4.1. Further, a comparative trend in the stability order of these clusters is shown below

For PbM: $PbC > PbAl > PbPb > PbIn > PbBa > PbSr > PbMg$
For Pb_8M: $Pb_8C > Pb_8Al > Pb_8In > Pb_8Ba > Pb_8Pb > Pb_8Sr > Pb_8Mg$
For $Pb_{10}M$: $Pb_{10}C > Pb_{10}Al > Pb_{10}In > Pb_{10}Ba > Pb_{10}Pb > Pb_{10}Mg \sim Pb_{10}Sr$
For $Pb_{12}M$: $Pb_{12}C > Pb_{12}Al \sim Pb_{12}Pb > Pb_{12}In \sim Pb_{12}Mg > Pb_{12}Ba > Pb_{12}Sr$
For $Pb_{14}M$: $Pb_{14}C > Pb_{14}Al > Pb_{14}Pb > Pb_{14}In > Pb_{14}Mg > Pb_{14}Sr > Pb_{14}Ba$

The thermodynamic stability of these clusters is analyzed based on the average binding energy and interaction energy of the impurity atoms. Based on the interaction energy of the M atoms with Pb_n clusters, it is found that $p - p$ interaction dominates over the $s - p$ interaction and lighter elements interact stronger than heavier ones. Based on the binding energy it is found that while the substitution of C and Al enhances the stability of the Pb_nM clusters, Mg destabilizes them. It may be noted that although the binding energy of Pb_nC ($n = 8, 10$ and 12) remains flat (~2.04 eV/atom), the interaction energy of C atom increases with the size of the cluster and estimated to be 4.59 eV, 4.83 eV, and 5.29 eV for Pb_8C, $Pb_{10}C$ and $Pb_{12}C$, respectively. The higher interaction energy with increasing cluster size is attributed to the higher coordination number of C atom. Like Group IV, the interaction of Group III elements with Pb host cluster is governed through $p-p$ interactions. In this context it should be noted that the interaction energy depends on both number of electrons as well as the atomic size. While Al atom has less number of valence electrons than Pb but it is smaller than Pb. The results show that doping of Al atoms enhances the stability of Pb_nAl cluster over Pb_{n+1} cluster. However, for Pb_nIn, where the dopant In is larger than Al, the stability depends on the specific size of the host cluster. For example, while Pb_8In and $Pb_{10}In$ shows higher stability than Pb_9 and Pb_{11}, $Pb_{12}In$ and $Pb_{14}In$ are less stable than Pb_{13} and Pb_{15} clusters. Unlike Group III and Group IV, Group II elements interact weakly due to the filled outermost valence orbital. Therefore, replacing one Pb by Group II elements in general reduces the stability. For dimer, it is noted that $Pb-Mg$ interaction is weaker than $Pb-Ba$ and $Pb-Sr$. The larger binding energy of Ba and Sr in comparison to the Mg is due to the involvement of inner d-electrons in the bonding, which is in line with the work of Kumar *et al.* [389]. For Pb_8Z ($Z = Mg, Sr$ and Ba) the binding energy of Pb_8Mg (1.61 eV/atom) is found to be lower than that of Pb_8Ba (1.76 eV/atom) and Pb_8Sr (1.69 eV/atom) clusters, where Z atoms cap the Pb_8 cluster from outside. But the trend is reversed once the impurity atom goes inside the host cage. The improved binding energy of $Pb_{12}Mg$ (1.89 eV/atom) cluster inspite of low $Pb-Mg$ bond strength, illustrates the many body effect or in other words the large coordination that is achieved by the encapsulation of Mg atom inside the Pb_{12} cage. Similar effect was seen for $Pb_{14}Sr$ (1.81 eV/atom), which shows higher binding energy than $Pb_{14}Ba$ (1.79 eV/atom) due to the encapsulation effect. The trend in stability of the clusters in terms of binding energy manifests the importance of both electronic and geometric structures. In general, smaller atomic size, lighter atomic mass and most importantly larger number of valence electrons give strong interaction.

4.3.2.2 Electronic Structure

Apart from the total energy consideration for stability, electronic structure is important to understand the chemical stability of any species. To understand this, the eigen value spectrum of the Pb_nM clusters is obtained from the Kohn-Sham energy states after broadening the electronic energy levels (Figure 4.9-Figure 4.12). The Jellium model, predicts higher stability for clusters corresponding to $8, 20, 34, 40, 58, 68$ ... electrons as the electronic shell closure [68]. For example, the large energy gap of Pb_8Mg despite a low binding energy (1.6 eV/atom) can be explained based on the electronic shell closure with 34 valence electrons. However, symmetry specific deviations could be observed depending on the geometrical features of the cluster structure. This is evident from the smaller energy gap observed for Pb_8C and Pb_9 clusters, where the additional two electrons occupy the anti-bonding HOMO energy level. For $Pb_{10}Mg$, and $Pb_{10}C$ the HLG is estimated to be 1.79 eV and 0.88 eV, respectively. The energy level spectrum (Figure 4.10) shows that the energy levels are ordered according to the D_{4d} splitting, which results in shell closure at $n = 42$ electrons (34 from first shell and 8 from the second shell). Therefore, the higher and lower energy gaps for $Pb_{10}Mg$ (42 electrons) and $Pb_{10}C$ (44 electrons) clusters respectively, can be explained based on the energy level splitting order.

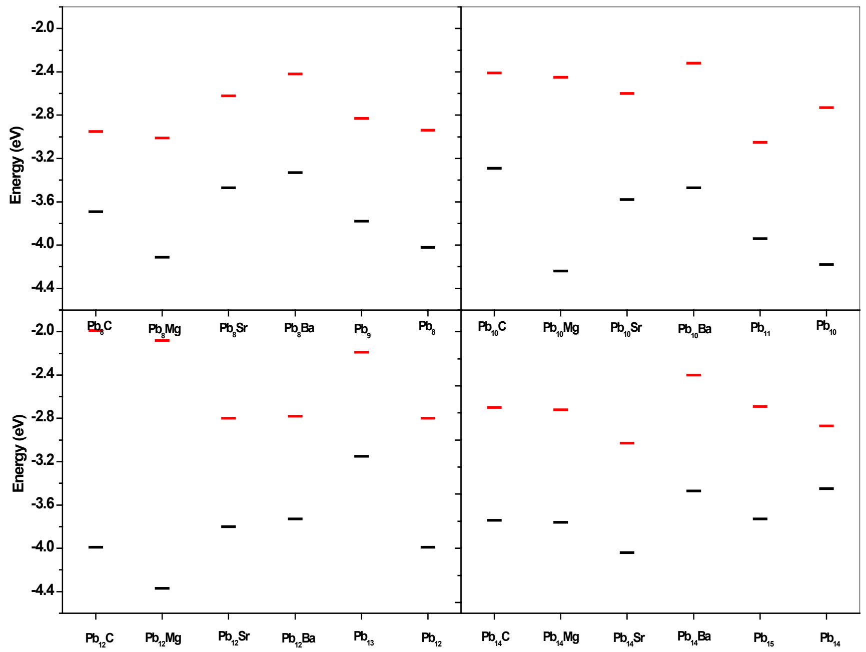

Figure 4.8: HOMO-LUMO energy levels of $Pb_nM(M = C, Al, In, Mg, Sr, Ba$ and Pb; $n = 8, 10, 12$ and $14)$ clusters.

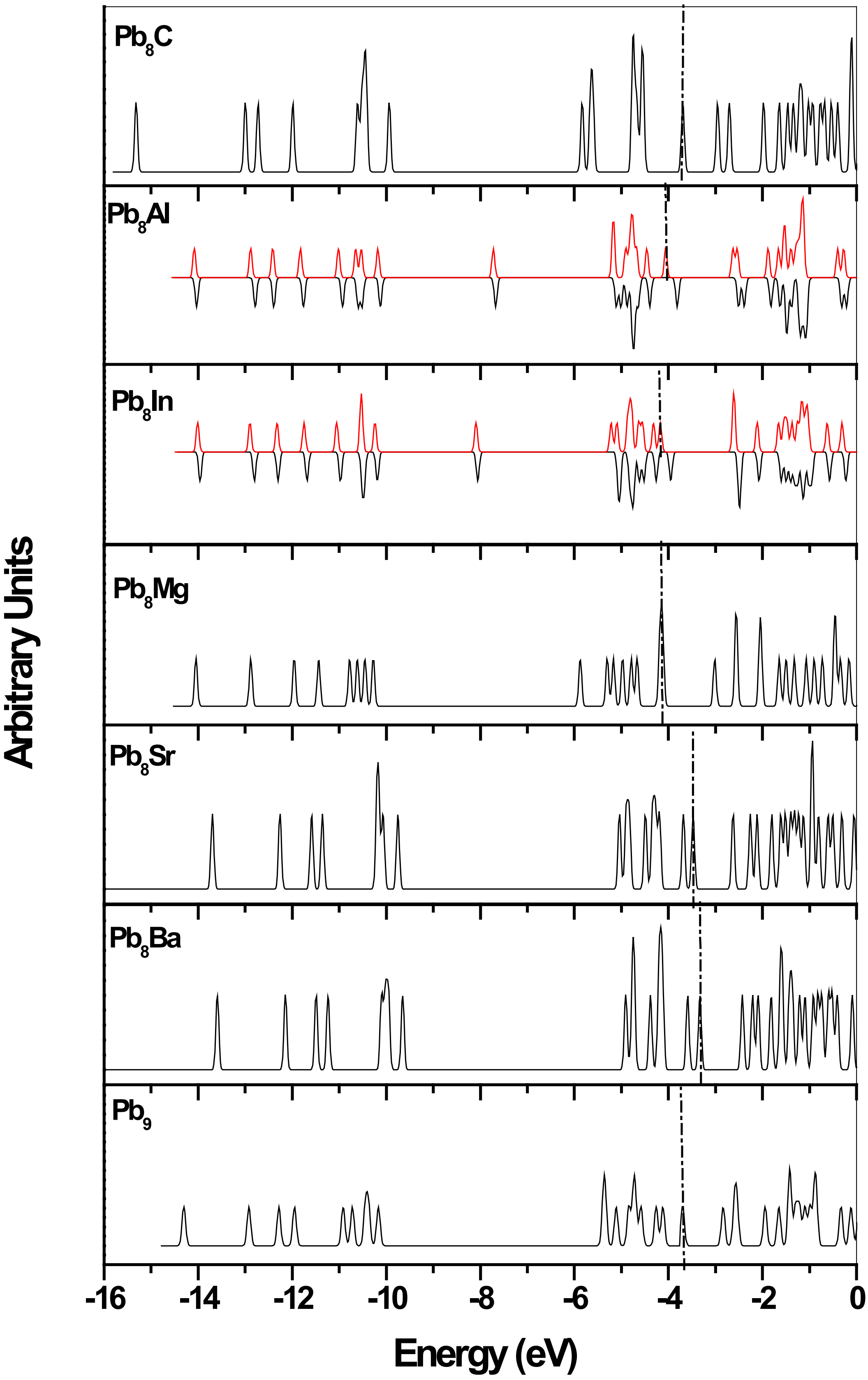

Figure 4.9 EDOS for the lowest energy isomer of Pb_8M ($M = C, Al, In, Mg, Sr, Ba$ and Pb) clusters. Dotted lines indicate the HOMO levels.

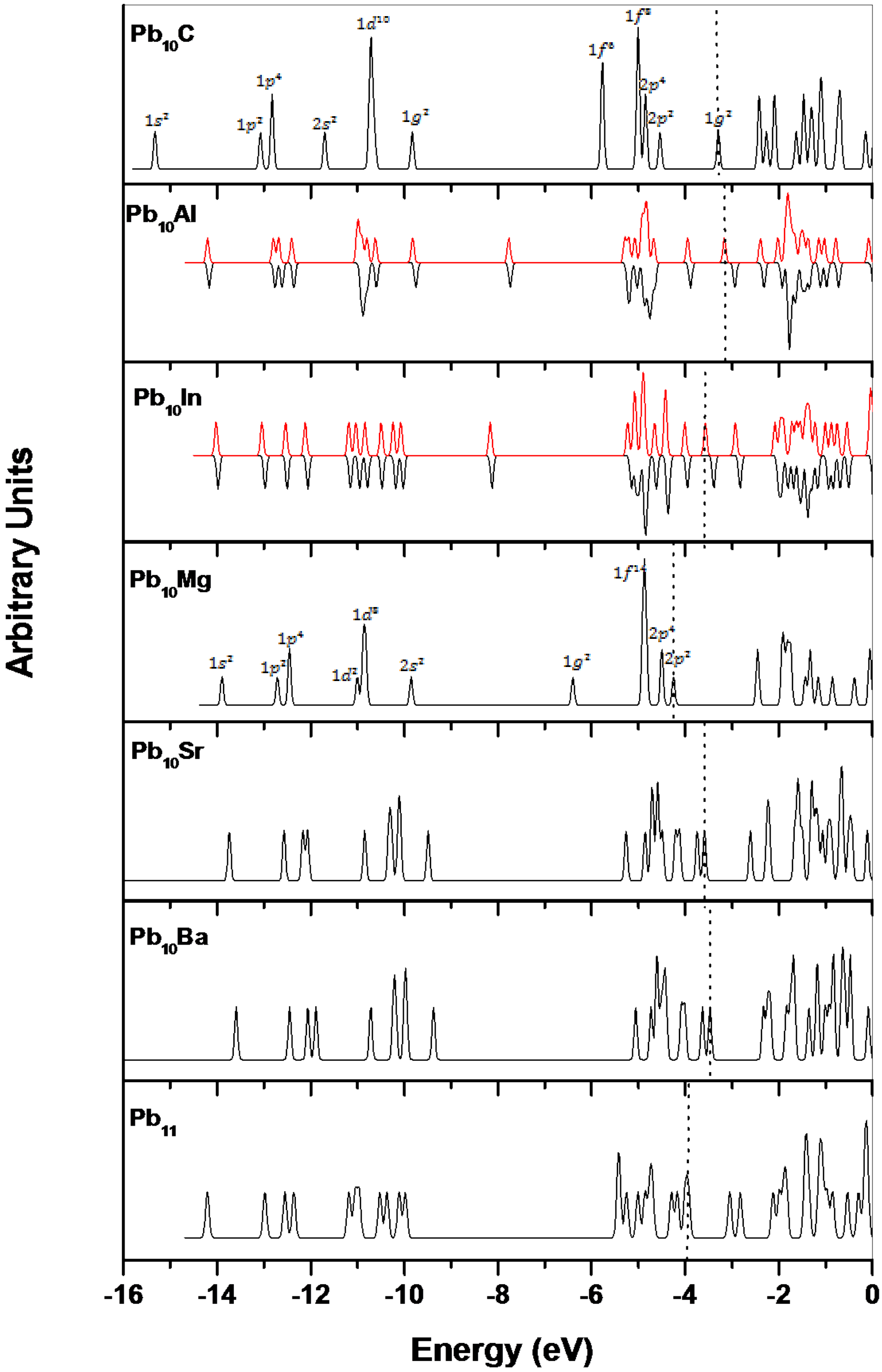

Figure 4.10: EDOS for the lowest energy isomer of $Pb_{10}M$ ($M = C, Al, In, Mg, Sr, Ba$ and Pb) clusters. Dotted lines indicate the HOMO levels.

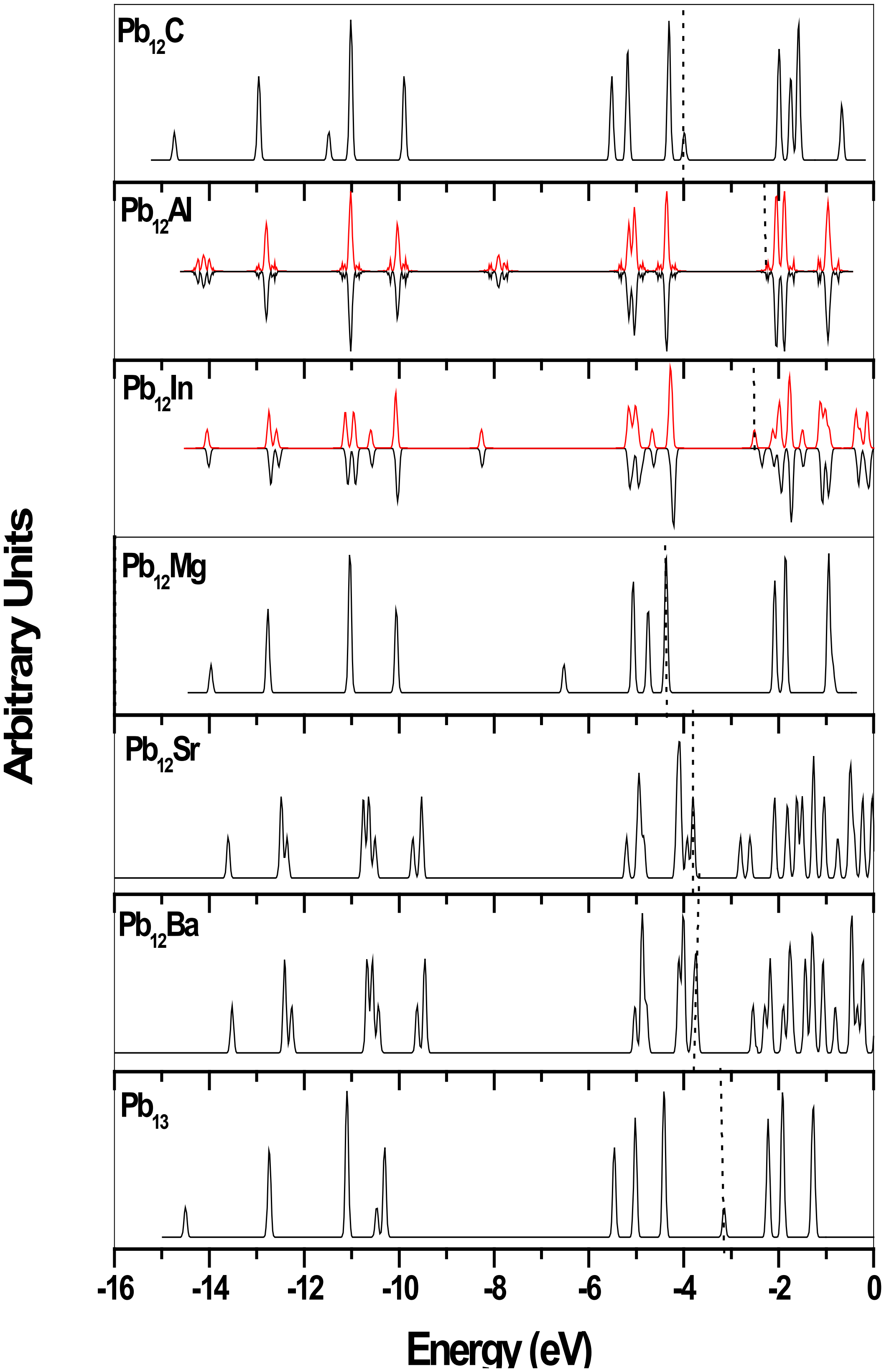

Figure 4.11: EDOS for the lowest energy isomer of $Pb_{12}M(M = C, Al, In, Mg, Sr, Ba$ and Pb clusters. Dotted lines indicate the HOMO levels.

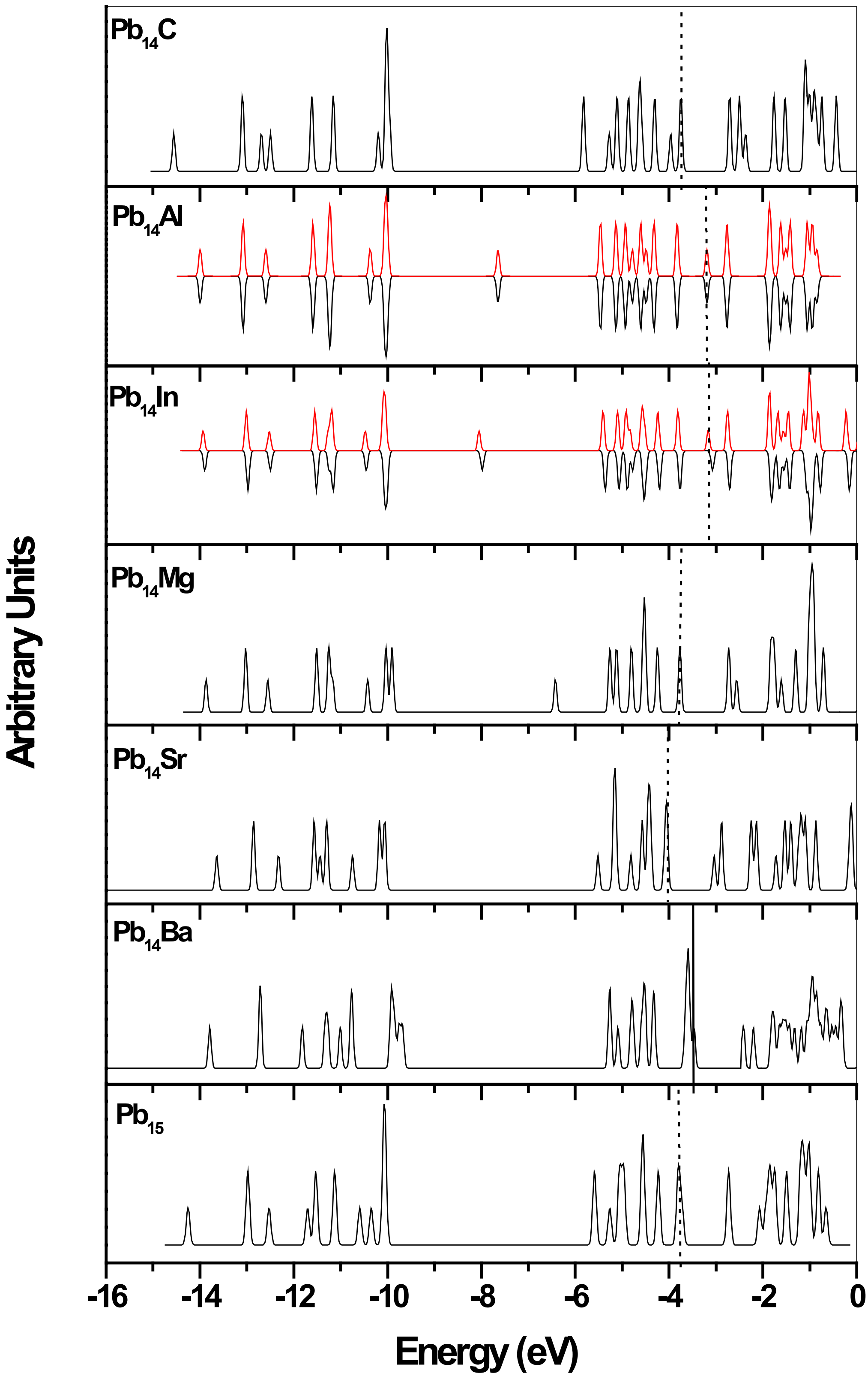

Figure 4.12 EDOS for the lowest energy isomer of $Pb_{14}M(M = C, Al, In, Mg, Sr, Ba$ and $Pb)$ clusters. Dotted lines indicate the HOMO levels.

In terms of geometrical considerations, for clusters with spherical atomic distribution like in icosahedral symmetry, it is found that the magicity follows $2(N+1)^2$ rule, which is a spherical analog to the $4N+2$ rule for cyclic annulenes [67,117]. Consequently $2, 8, 18, 32, 50, 72 \ldots$ number of delocalized electrons would represent higher stability over others. The widening of the energy gap of $Pb_{12}Mg$ cluster results due to the splitting of nine-fold $1g$ orbital into $1g^{10}$ and $1g^{8}$ in the icosahedral field splitting. The HOMO of Pb_{13} is the anti-bonding orbital formed during the splitting of energy levels under the influence of the icosahedral field. When C replaces the central Pb atom of Pb_{13}, the ordering of the energy levels remained similar with a shift in the Kohn-Sham energy states towards higher binding energy (more negative, Figure 4.13). This leads to the larger energy gap of 2.0 eV for $Pb_{12}C$. Unlike the clusters doped with smaller elements, which adopt icosahedral symmetry, for $Pb_{12}Ba$ and $Pb_{12}Sr$ clusters, where impurity atoms are placed outside the cage, the energy level splitting is not governed by the spherical field splitting. This results in lowering of the HLG of these clusters due to the upward shift of the HOMO energy levels.

B. Energy level reordering and stability of $Pb_{12}M$ clusters

In this section the influence of an impurity atom in tuning the stability of small clusters is understood by under scoring the interplay between the atomic and electronic structure to understand the stability of small size clusters by looking at $Pb_{12}X$ clusters more closely. The Pb_{13} cluster, which has higher binding energy but low IP and energy gap, has been used as a model system for this purpose. As discussed in Chapter 3, Pb_{13} prefers a compact Pb atom encapsulated icosahedron as the lowest energy structure. Attention is focused on the $Pb_{12}Mg$ cluster, which is iso-electronic with $Pb_{12}Al^{+}$. While Al atom can show the effect of an additional p electron, the C atom, being lighter in mass, can give useful hints about the interplay between thermodynamic stability and electronic stability. Here by electronic stability it is meant the larger energy gap, which in turn is related to the chemical stability.

Apart from the different geometrical motif, the energetics of Pb_{13} cluster is interesting. Pb_{13} is assigned as magic, which is also reflected by the high abundance of Pb_{13} in the mass spectrum [341-343,386]. In contrast to this, the IP and the HLG of Pb_{13} is found to show a sharp dip as compared to that of Pb_{12} [Figure 3.15]. Therefore, from the total energy point of view, Pb_{13} cluster may be more stable, but its low IP and HLG make the cluster electronically unstable or more reactive. This contradictory feature in stability is interesting and motivates us to understand the bonding and electronic structure of Pb_{13} in detail so that new clusters can be designed with enhanced thermodynamic and electronic stability. To understand the bonding in more detail, the one particle Kohn-Sham energy level structure and charge density surfaces of Pb_{13} cluster are investigated. In Figure 4.13, the energy level spectrum of Pb_{13} obtained from the Kohn-Sham energy states after Gaussian

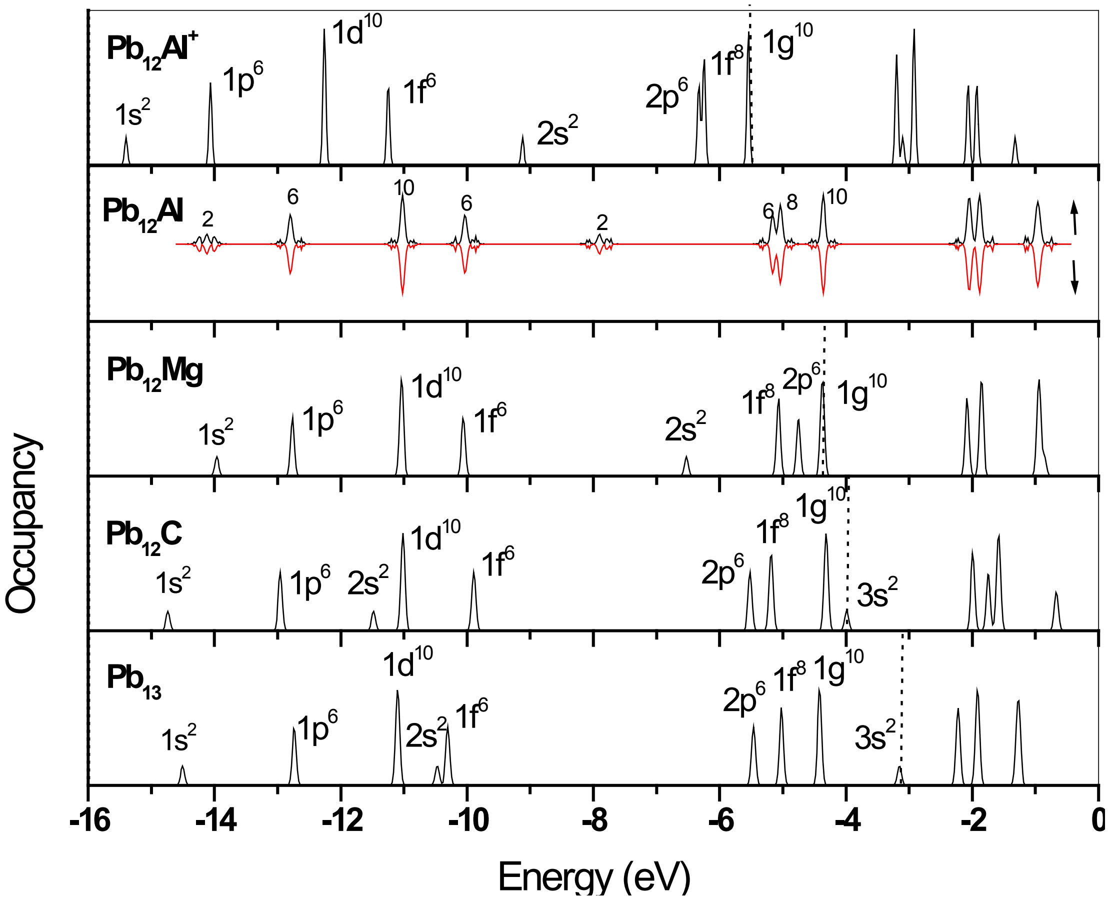

Figure 4.13: Energy eigen value spectrum for $Pb_{12}M(M = C, Mg, Al$ and $Pb)$ clusters as obtained from the Kohn–Sham energy states after Gaussian broadening. The numbers on top of each peak represents the number of electrons occupied in the specified sub-shell.

broadening is shown. Considering the spherical symmetry of Pb_{13} icosahedron, the orbitals are arranged in spherical harmonics. It may be pointed out that the ordering of the energy levels would depend on the electronic field exerted by the icosahedral symmetry and in particular to the splitting of higher order harmonics (high angular momentum) [369,390]. This reordering of energy levels results in the mixing of orbitals from first, second and third spherical progressions. For Pb_{13}, having 52 valence electrons, the HOMO energy level is found to occupy the $3s$ orbital, leaving a large gap between HOMO and HOMO-1, which constitutes of pentuply degenerate $1g$ orbital. The occupancy of each sub-shell is shown at the top of each peak (Figure 4.13). Therefore, it is clear that the occupied $3s$ orbital is primarily responsible for the low IP as well as small energy gap of Pb_{13} cluster. From the electronic structure, the large gap between HOMO and HOMO-1 indicates that the removal of two electrons from the $3s$ orbital of Pb_{13} would result is a closed shell structure with extra stability and large gap. Hence, substitution of one Pb atom with an appropriate divalent impurity could be a good choice to result in large gap material.

Neukermans *et al.* in their studies on Al doped Pb clusters [386] have observed a sharp peak for $Pb_{12}Al^+$, and no peak for $Pb_{12}Al$ was found when neutral species were ionized by a second laser. The enhanced stability of $Pb_{12}Al^+$ was explained based on 50 electron rule with highly symmetric icosahedral structure. To verify this fact, the electronic structure of $Pb_{12}M$ ($M = C, Pb, Al$ and Mg) clusters is investigated and the results are discussed below.

For $Pb_{12}Al$ cluster, the lowest energy structure shows that Al atom prefers to substitute the central Pb atom of the Pb_{13} icosahedron. A small distortion in the bond lengths is observed due to the spin polarized system. The difference in the mass abundance spectrum for $Pb_{12}Al$ and $Pb_{12}Al^+$ observed is related to their thermodynamic and chemical stability. The ionization potential of $Pb_{12}Al$ (IP=2.74 eV) is found to be significantly lower than

6.4 eV, which was used as ionization energy [386]. Thus, the absence of neutral $Pb_{12}Al$ mass peak could be due to ionization and followed by fragmentation by the excess energy. On the other hand, the higher abundance of $Pb_{12}Al^+$ can be explained by the large formation energy in comparison to that of neutral and $Pb_{12}Al$ and is estimated from the following relations

$$Al + Pb_{12} \rightarrow Pb_{12}Al \qquad \Delta H = -3.87 eV$$

$$Al^+ + Pb_{12} \rightarrow Pb_{12}Al^+ \qquad \Delta H = -5.92 eV$$

$$Al + Pb_{12}^+ \rightarrow Pb_{12}Al^+ \qquad \Delta H = -5.38 eV$$

Although the formation energy of $Pb_{12}Al^+$ is very high, it may be unstable in an electrical or magnetic field due to its charge. The divalent Mg atom, with two valence electrons in the outermost $3s$ orbital, is isoelectronic with Al^+. Therefore, it is important to understand the atomic and electronic structure of $Pb_{12}Mg$ cluster. The ground state geometry of $Pb_{12}Mg$ cluster has a similar icosahedron structure of Pb_{13}, where Mg atom replaces the center Pb atom. Most remarkably a large energy gap of 2.30 eV is found between the HOMO and LUMO energy levels of $Pb_{12}Mg$ cluster. It is also noted that other than improving the energy gap from 1.13 eV to 2.30 eV, the incorporation of Mg atom enhances the stability of to 1.89 eV/atom. In general, such a large energy gap is indeed rare among metal clusters. Li *et al.* [391] have reported 2.0 eV energy gap of Au_{20} cluster which forms tetrahedral geometry. Kumar *et al.* have reported the energy gap of $Ge_{12}Mg$ and $Sn_{12}Mg$ as 2.30 eV and 2.0 eV, respectively [378]. Although the energy gap of $Ge_{12}Mg$ is comparable with $Pb_{12}Mg$, but it may be noted that Ge is a semiconductor in bulk and favors covalent bonding. In contrast to this $Pb_{12}Mg$ cluster shows close packed geometry, and bears the signature of metallic bonding.

In order to examine the higher stability of $Pb_{12}Mg$ cluster, the geometry and electronic structure of $Pb_{12}C$ cluster is looked at more closely. The lowest energy structure of $Pb_{12}C$ shows similar structure to that of $Pb_{12}Mg$ and $Pb_{12}Al$ *i.e.,* C atom prefers to replace the central Pb atom from the icosahedron. The inter-atomic distances of $Pb-Pb$ and $C-Pb$ are found to be 3.32 Å and 3.07 Å, respectively. It is observed that while $Pb-Pb$ separation in $Pb_{12}C$ has increased upto 10%, $C-Pb$ distances have increased by 50% in comparison to their respective dimers. The average binding and interaction energy of $Pb_{12}C$ cluster are estimated to be 2.04 eV/atom and 5.29 eV respectively. The energy gap of $Pb_{12}C$ is found to be 2.0 eV, which is higher than Pb_{13} cluster. However, it should be emphasized that even though C is much smaller than Mg, the energy gap of $Pb_{12}Mg$ (2.30 eV) is much larger than $Pb_{12}C$ cluster (2.0 eV). The unusual stability of $Pb_{12}Mg$ is further illustrated from the relative interaction energy of different elements as a function of the size of Pb clusters as shown in Figure 4.14. It is seen that while C, Pb and Al follows a linear trend; Mg atom shows a sharp peak at $n=13$. This is the reason to call $Pb_{12}Mg$ to have unusual stability in these series of clusters and therefore can be used as super atom.

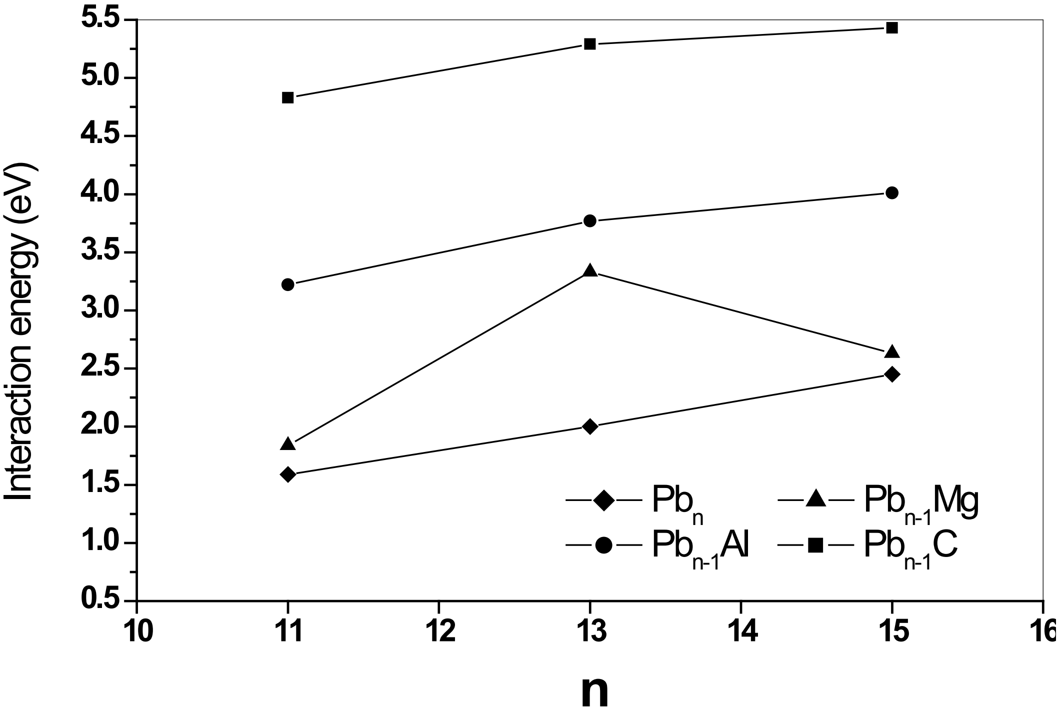

Figure 4.14: The variation in the interaction energy of M atoms as a function of size of $Pb_{n-1}M$ clusters.

The electronic energy level spectrum provides a convenient overall view of the cluster electronic structure and bonding. Figure 4.13 shows a comparison of energy spectrum for

$Pb_{12}M$ clusters as obtained from the Kohn-Sham energy states after broadening with a Gaussian function. It is seen that when the central Pb atom is replaced by C, the ordering of the energy levels remained similar with a shift in the Kohn-Sham energy states towards higher binding energy (more negative). This leads to the larger energy gap of 2.0 eV for $Pb_{12}C$. The stabilization of the energy levels by replacing Pb with C could be due to a small charge transfer from the peripheral atoms to the central atom as shown in Figure 4.15. In this context, it is important to notice that inspite of an increase in the $C-Pb$ distance from 2.13 Å to 3.07 Å for $Pb-C$ dimer to $Pb_{12}C$ cluster, the interaction energy rises from 1.36 eV to 5.29 eV, which can be attributed to the larger coordination of C.

In order to understand the nature of bonding in $Pb_{12}C$ cluster the (*i*) isoelectronic density surface plot (Figure 4.15), (*ii*) the charge distribution analysis and (*iii*) the electron energy level diagram (Figure 4.16) are analysed. It is found that C atom being the lightest in the series and Pb atom being the heaviest in the series, the difference in electronegativity plays very important role for the electron charge transfer. The charge distribution analysis shows that each Pb atom on the periphery of the icosahedron transfers 0.06 esu electronic charge to the central C, thus total negative charge on the central C atom becomes -0.73 esu.

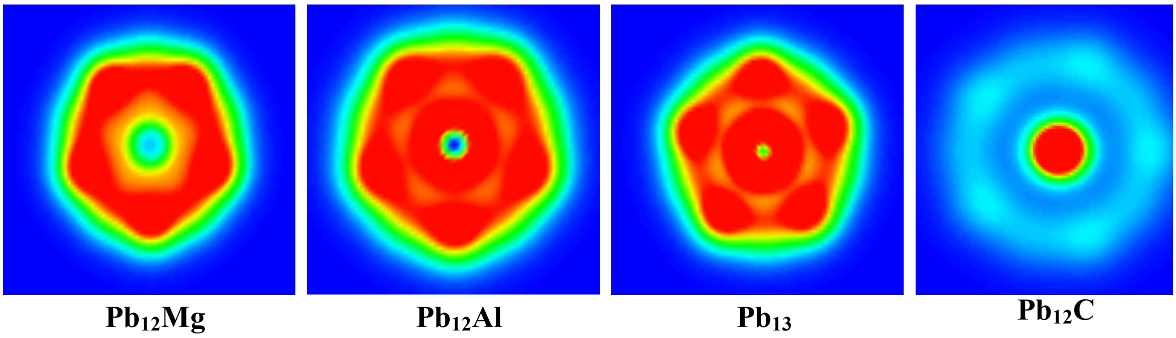

Figure 4.15: Electron density profile of $MPb_{12}(M = C, Mg, Al$ and $Pb)$ clusters projected on the central plane of the icosahedrons. Blue, green and red colors, respectively represent the density values in the increasing order.

The isodensity contour plot also shows the similar feature. From the energy level diagram it is observed that the HOMO energy level of the C atom is much deeper as compared to that of the Pb_{12} cluster and therefore the interaction between them would result in a transfer of charge from Pb_{12} cluster surface to the central C atom. Based on the energy level ordering of Pb_{13} and $Pb_{12}C$ clusters (Figure 4.16), it can be imagined that a substitution on central Pb atom by divalent impurity with lesser electronegativity (will transfer electron charge from centre to peripheral) as compared to Pb should result in a larger energy gap than $Pb_{12}C$. Indeed, a very large energy gap is found when the central atom of Pb_{13} is replaced by Mg. The widening of the energy gap of $Pb_{12}Mg$ cluster is a result of the splitting of nine-fold $1g$ orbital into $1g^{10}$ and $1g^{8}$ as can be seen in Figure 4.13. In fact the energy level ordering of the $Pb_{12}Mg$ cluster is in agreement with $Pb_{12}Al^{+}$ except a small difference that the occupied states of $Pb_{12}Al^{+}$ are shifted to higher binding energy (more negative) which is due to the more attractive force of nucleus on the valence electron for charged species. As it is known that GGA usually underestimates the energy gap, the true gap is expected to be ~30% higher. The charge transfer in these systems is plotted as a two

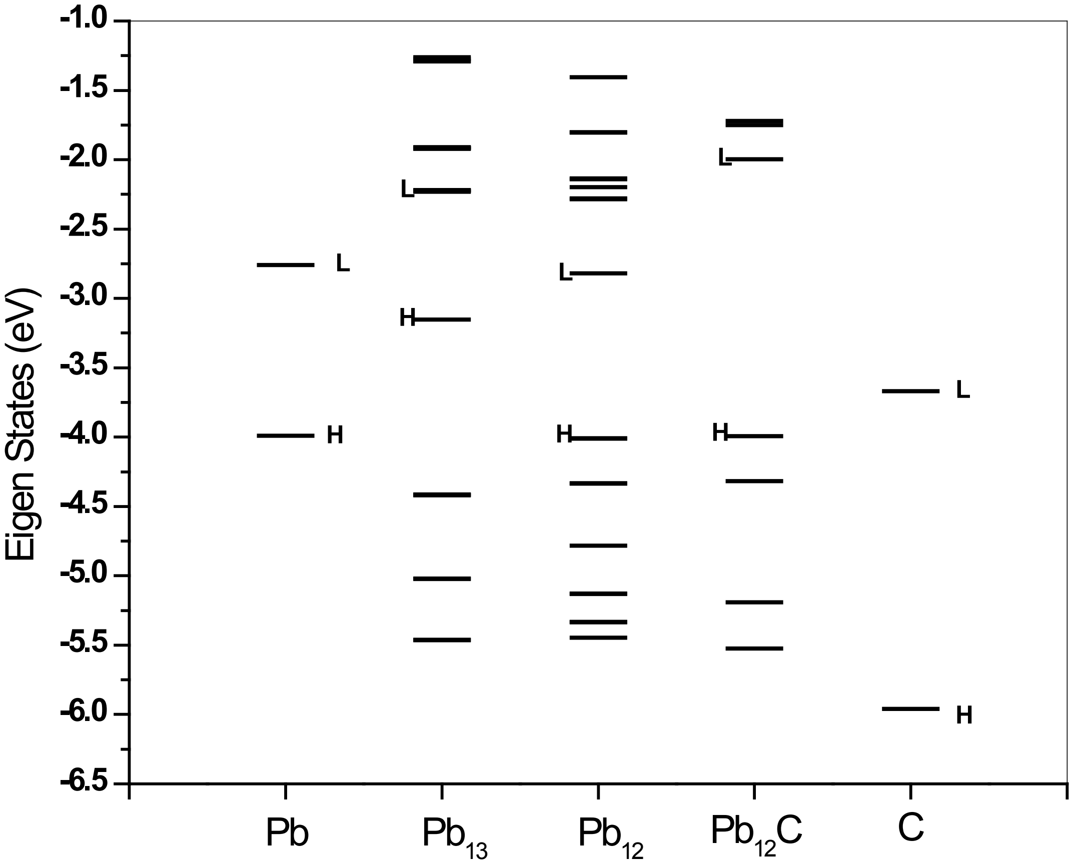

Figure 4.16: Energy level diagram for C,Pb, Pb_{12} and $Pb_{12}C$ clusters. For the sake of simplicity, few relevant occupied and unoccupied energy levels are only shown. 'H" –HOMO and 'L' –LUMO

dimensional map of the electron density of $Pb_{12}Al$ and $Pb_{12}Mg$ clusters (Figure 4.15). It is found that for both cases there is a small charge transfer from the central atom to the Pb surface atoms. This is opposite to the trend observed for $Pb_{12}C$ where a small charge transfer takes place from the surface to the centre. The direction of charge transfer is in line with their electronegativity values, which follow the trend of $C > Pb > Al > Mg$.

C. Structural and electronic properties of $Sn_{n-1}Pb$ and $Pb_{n-1}Sn$ clusters

As understood from the previous sections, the structural transition (non compact to compact) occurs between Sn and Pb clusters among Group IV elemental clusters and significant structural changes are induced by incorporating an impurity element and the extent of change depends on the relative atomic radius and the nature of bonding between the host and impurity elements. While strong covalent bond exists between Sn atoms in small clusters, Pb clusters behave more metallic. Motivated by these observations extensive study on the geometrical isomers of $Sn_{n-1}Pb$ and $Pb_{n-1}Sn$ ($n \leq 13$) clusters were carried out with an objective to understand effect on the growth pattern and stability of Sn_n and Pb_n clusters on doping with Pb and Sn, respectively.

4.3.3 Geometric Structure

Figure 4.17a and Figure 4.17b show the low-lying isomers ($\Delta E < 1.0\ eV$) of Pb_n, Sn_n, $Pb_{n-1}Sn$, and $Sn_{n-1}Pb$ clusters. The binding energy of the homo- and heteroatomic dimers with triplet spin configuration follows the trend: Pb_2 (0.67 eV/atom)$<$ $SnPb$ (0.89 eV/atom) $<$ Sn_2 (1.18 eV/atom), and the bond lengths are 2.91 Å, 2.88 Å and 2.80 Å for Pb_2, $SnPb$ and Sn_2 respectively. The lowest energy configurations of Sn_3 and Pb_3 clusters favor isosceles and equilateral triangles, respectively, with triplet spin multiplicity. For Pb_2Sn, a nonmagnetic open triangle with $\angle PbSnPb$ of 81.4° and the $SnPb$ bond length of 2.77 Å forms the lowest energy isomer. The linear chain configuration of Pb_2Sn is 0.37 eV higher in energy. For Sn_2Pb cluster, isosceles triangle with triplet spin multiplicity

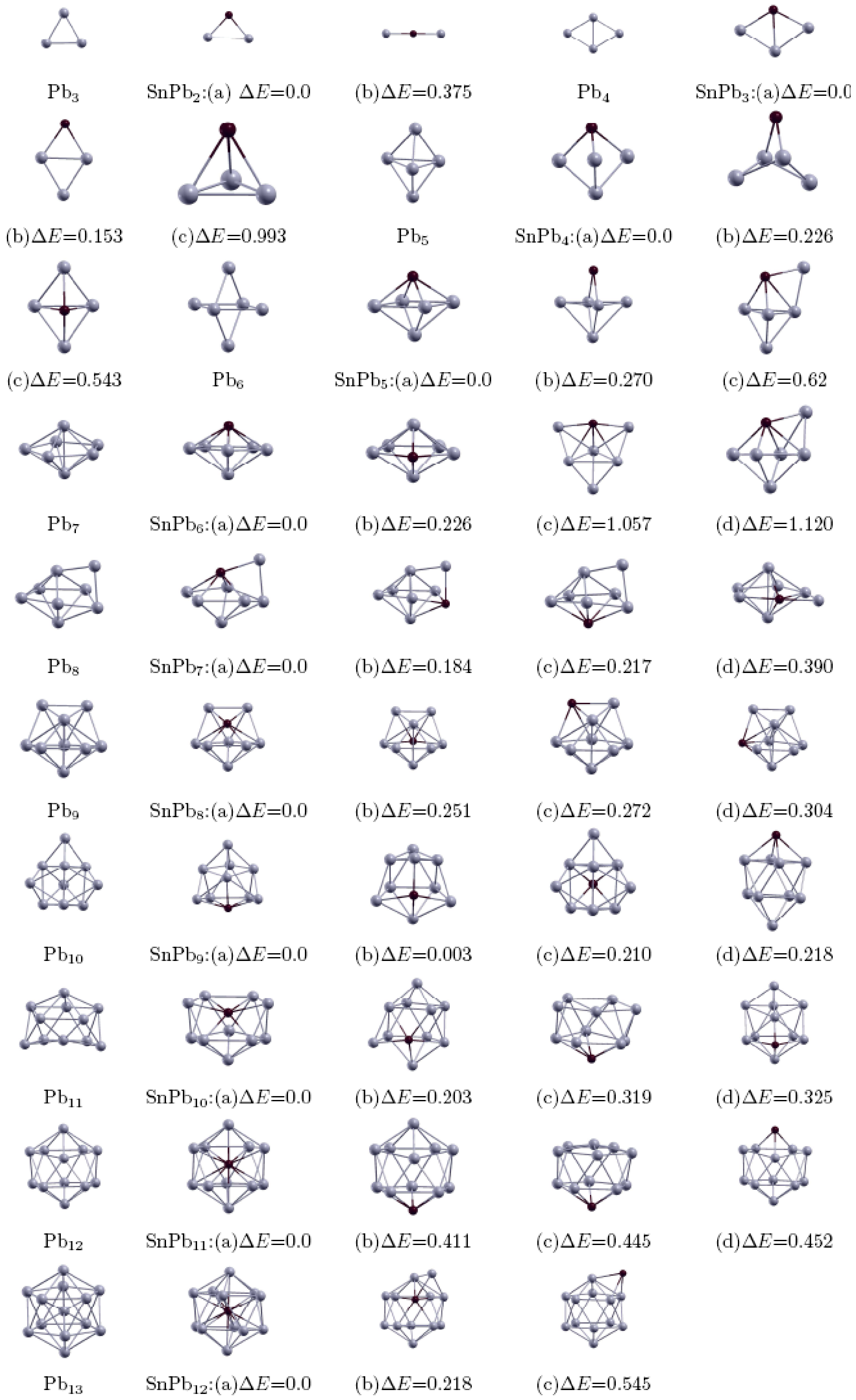

Figure 4.17a: Low-lying structures of $Pb_{n-1}Sn(n = 3 - 13)$ clusters and ground-state structures of pure $Pb_n(n = 3 - 13)$ clusters. Dark ball : Sn atoms; light ball: Pb atoms

shows the lowest energy structure. $Sn - Pb$ and $Sn - Sn$ bond lengths are estimated to be 2.95 Å and 2.85 Å, respectively. We note that the $Sn - Pb$ bond length in Sn_2Pb is larger than that in Pb_2Sn.

The larger size ($n \geq 4$) heteroatomic clusters show non-magnetic ground state similar

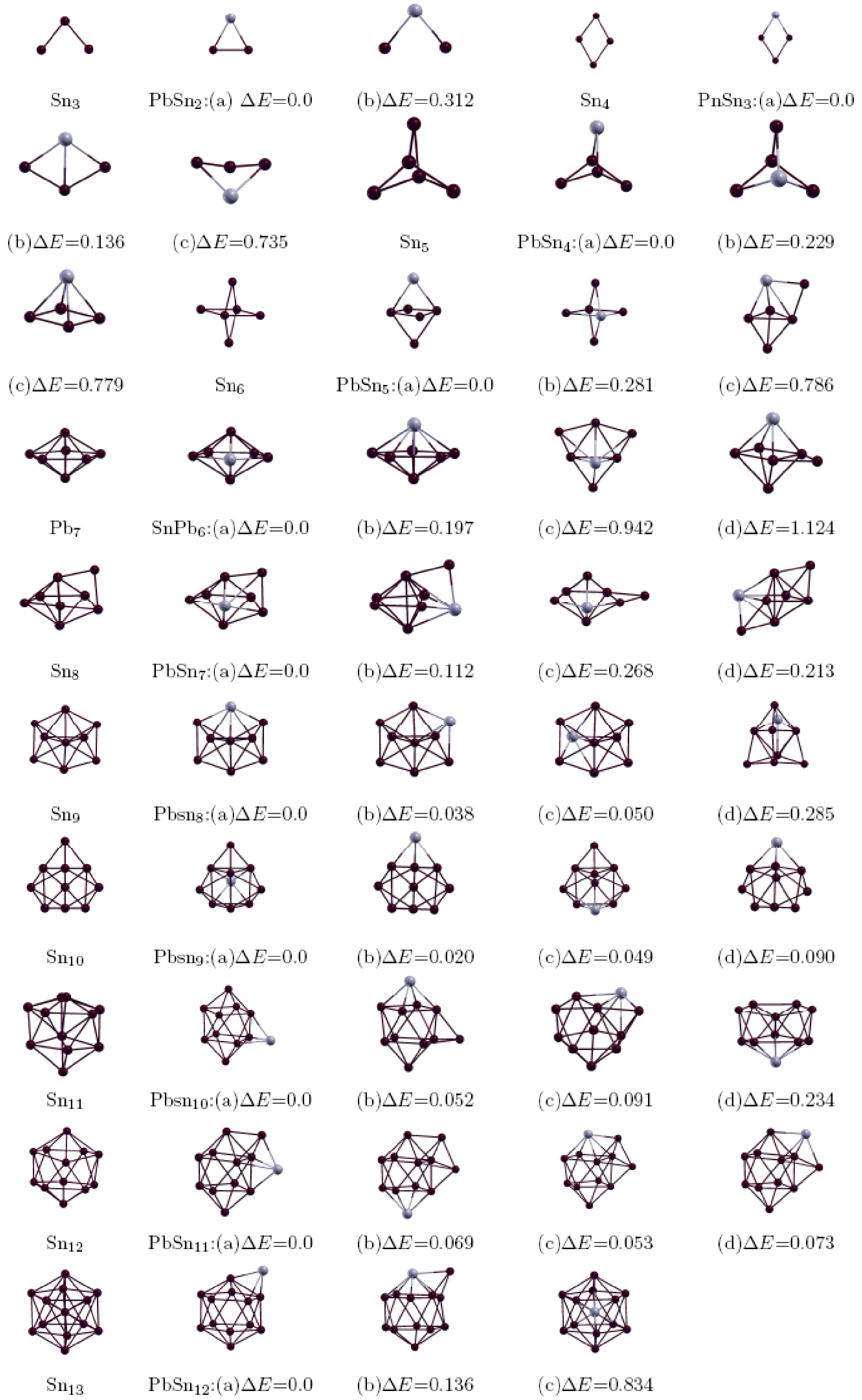

Sn_3 PbSn$_2$:(a) ΔE=0.0 (b)ΔE=0.312 Sn_4 PnSn$_3$:(a)ΔE=0.0

(b)ΔE=0.136 (c)ΔE=0.735 Sn_5 PbSn$_4$:(a)ΔE=0.0 (b)ΔE=0.229

(c)ΔE=0.779 Sn_6 PbSn$_5$:(a)ΔE=0.0 (b)ΔE=0.281 (c)ΔE=0.786

Pb_7 SnPb$_6$:(a)ΔE=0.0 (b)ΔE=0.197 (c)ΔE=0.942 (d)ΔE=1.124

Sn_8 PbSn$_7$:(a)ΔE=0.0 (b)ΔE=0.112 (c)ΔE=0.268 (d)ΔE=0.213

Sn_9 Pbsn$_8$:(a)ΔE=0.0 (b)ΔE=0.038 (c)ΔE=0.050 (d)ΔE=0.285

Sn_{10} Pbsn$_9$:(a)ΔE=0.0 (b)ΔE=0.020 (c)ΔE=0.049 (d)ΔE=0.090

Sn_{11} Pbsn$_{10}$:(a)ΔE=0.0 (b)ΔE=0.052 (c)ΔE=0.091 (d)ΔE=0.234

Sn_{12} PbSn$_{11}$:(a)ΔE=0.0 (b)ΔE=0.069 (c)ΔE=0.053 (d)ΔE=0.073

Sn_{13} PbSn$_{12}$:(a)ΔE=0.0 (b)ΔE=0.136 (c)ΔE=0.834

Figure 4.17b: Low-lying structures of $Sn_{n-1}Pb(n = 3 - 13)$ clusters and ground-state structures of pure $Sn_n(n = 3 - 13)$ clusters. Dark ball: Sn atoms; light ball: Pb atoms.

to pure Pb_n and Sn_n clusters. For $n = 4 - 7$, the lowest energy isomers of these clusters adopt rhombus (D_{2h}), trigonal bi-pyramid (D_{3h}), two intersecting rhombi (D_{4h}) and pentagonal bi-pyramid (PBP, D_{5h}), configurations respectively. It is seen that both Sn_4 and Pb_4 adopt rhombus geometry (D_{2h}) as the lowest energy isomer. After substitution of impurity atoms in the tetramers, Pb_3Sn and Sn_3Pb clusters favor a trapezoidal structure. While for Pb_3Sn, the Sn prefers to substitute the Pb from the obtuse angle vertex; Pb atom substitutes the Sn from the acute angle vertex of Sn_3Pb. For Pb_3Sn A tetrahedron with three-dimensional configurations is found to be 0.99 eV higher in energy compared to the planar isomer. The transition from planar to three-dimensional motif occurs from $n = 5$ onwards, where Pb_5 and Sn_5 favor capped bent rhombus structures. For Pb_4Sn, an elongated trigonal bi-pyramidal structure is found to be the lowest energy configuration, where Sn occupies the vertex. The $Sn - Pb$ and $Pb - Pb$ bond lengths are found to be 2.90 Å and 2.99 Å, respectively. In line with Sn_5, the lowest energy structure of the Sn_4Pb cluster adopts a bent rhombus structure capped by the Pb atom. The $Sn - Pb$ and $Pb - Pb$ bond lengths are found to be 2.91 Å and 2.84 Å, respectively. For $n = 6$, several initial configurations *viz.* crossed rhombus, octahedron, capped trigonal bi-pyramid were considered. For the homoatomic Pb_6 and Sn_6 clusters, the crossed rhombus geometry was found to be the lowest energy isomer. For the hetero-atomic Pb_5Sn, an octahedron isomer with Sn atom substituting the Pb atom at the vertex is found to be the lowest energy isomer. The average distance between Sn and Pb atoms is estimated to be 2.98 Å. Other low-lying isomers *viz.* crossed rhombus, capped trigonal bi-pyramid which show higher energy are presented in Figure 4.17a. Contrary to this, the Sn_5Pb cluster (Figure 4.17b) forms a crossed rhombus structure with Pb atom replacing the Sn atom at the vertex. The $Sn - Pb$ bond length is found to be 2.98 Å and the distance between the Sn atoms is ~2.93 Å.

For $n = 7$ both Pb_7 and Sn_7 prefer PBP structure as the lowest energy isomer and are found in abundance in their respective cluster mass spectra. Substitution of Sn or Pb in these clusters lead to different geometrical isomers Among different isomers of Pb_6Sn, the pentagonal bi-pyramid with Sn atom replacing the vertex Pb was found to be the lowest energy isomer. The $Sn-Pb$ bond length is estimated to be 3.09 Å and the average $Pb-Pb$ distance from the apex to the pentagonal base of the PBP and that among the pentagonal ring are 3.24 Å and 3.18 Å respectively. On the other hand, when Pb replaces Sn from Sn_7, the lowest energy isomer is formed by replacing one of the Sn atoms from the pentagonal base of the PBP. The $Pb-Sn$ bond length in the pentagonal base is 3.13 Å and that from the apex to the base atom is 3.12 Å. The lowest energy isomers of Pb_8 and Sn_8 clusters are found to be an edge capped PBP. The lowest energy isomers of Pb_7Sn and Sn_7Pb were obtained by edge capping of Pb_6Sn and face capping of Sn_6Pb clusters respectively. In the ground state geometry of Pb_7Sn, the $Pb-Sn$ bond lengths vary from 2.89 Å to 3.13 Å and the distance between the Pb atoms varies from 3.15 Å to 3.32 Å. In Sn_7Pb configuration, the distance between the Pb atom and the capped Sn atom is 3.75 Å and other $Pb-Sn$ bond lengths varies from 3.15 Å to 3.24 Å. A few higher energy isomers are shown in Figure 4.17a. For $n = 9$, while Sn_9 favors a tetra-capped TBP isomer, Pb_9 is found to prefer a bi-capped PBP as the lowest energy conformer. To obtain the ground state configuration of Pb_8Sn and Sn_8Pb clusters, several substituted low-lying isomers of Pb_9 and Sn_9 clusters were optimized with the dopant atom replacing one host atom at different sites. The lowest energy isomer of the Pb_8Sn turns out to be a bi-capped PBP structure with a Sn atom at the vertex and with two capping atoms placed at the adjacent triangular faces on the same side of the pentagon (Figure 4.17a). In this structure the shortest $Sn-Pb$ bond length is 3.04 Å. The lowest energy structure of Sn_8Pb was obtained by replacing Sn atom with Pb atom at the vertex of the lowest energy isomer of Sn_9 cluster (tetra capped TBP) as shown Figure 4.17b. The average distance between Pb and Sn atoms is ~3.21 Å and between Sn atoms ~2.97 Å. A capped trigonal prism structure is found to be the lowest energy configuration for Pb_{10} and Sn_{10} clusters. Several initial configurations by capping different faces of octahedral, PBP and prism or antiprism structures were optimized exhaustively to find the minima for Pb_9Sn and Sn_9Pb clusters. For Pb_9Sn, two low-lying isomers along with the lowest energy configuration (Figure 4.17a) were obtained by changing the substitution sites of the Sn atom on the ground state geometry of Pb_{10} cluster with the shortest $Sn - Pb$ bond length of 2.9 Å. A bi-capped tetragonal antiprism structure (Figure 4.17a and Figure 4.17b) is found to be 0.21 eV higher in energy compared to the ground state configuration. A tetra-capped trigonal prism (TTP) motif with the Pb atom capping one of the rectangular planes is preferred by Sn_9Pb. The isomer where Pb atom caps the triangular face of TTP is found to be nearly degenerate being only 0.02 eV higher in energy compared to the ground state configuration. The $Pb - Sn$ bond lengths are found to vary from 3.09 Å to 3.15 Å while the $Sn - Sn$ bond lengths vary from 2.91 Å to 3.36 Å.

In this context, it is worth mentioning that for Group IV clusters, the existence of multiple nearly degenerate low energy isomers was observed, which have shown structural transition of the lowest energy isomer depending upon the exchange-correlation functionals for $n = 11$. So for $Pb_{10}Sn$ cluster, several initial geometries were constructed from the low-lying isomers of Pb_{11} cluster as well as from the capped Pb_9Sn clusters. A truncated icosahedral structure, where Sn atom is centrally located was found to be the lowest energy (shown in Figure 4.17a) isomer. In this configuration, the $Sn - Pb$ bond lengths vary from 3.07 Å to 3.15 Å and that between Pb atoms vary from 3.16 Å to 3.5 Å. The lowest energy isomer of the $Sn_{10}Pb$ cluster was obtained by capping an Pb atom on the tetragonal antiprism structure of Sn_{10} cluster. The bond lengths between Sn and Pb atoms vary from 2.99 Å to 3.66 Å and that between the Sn atoms vary from 2.96 Å to 3.10 Å. The low-lying isomers of $Pb_{11}Sn$ and $Sn_{11}Pb$ clusters are shown in Figure 4.17a and Figure 4.17b. The interaction of the Sn atom with Pb_{11} cluster is carried out by capping the different faces of the low-lying isomers of Pb_{11} cluster and by replacing one atom from Pb_{12} cluster at different substitutional sites. The lowest energy configuration is obtained by replacing a Pb atom with a Sn atom in the pentagonal ring. The relaxed geometry as shown in Figure 4.17a reveals the fact that Sn atom tries to move inwards to the center such that the co-ordination of Sn atom is at a maximum. The $Sn-Pb$ bond lengths varied from 3.06 Å to 3.40 Å. The ground state isomer of $Sn_{11}Pb$ is obtained by capping an Sn atom on the ground state structure of $Sn_{10}Pb$ cluster. For $n = 13$, the lowest energy isomer of $Pb_{12}Sn$ cluster is formed by encapsulating the Sn atom inside the icosahedral cage of Pb_{12} cluster. In contrast, for $Sn_{12}Pb$, the additional Pb interacts with Sn_{12} exohedrally, *i.e.,* by capping one of its triangular faces from outside.

Based on the above discussion it is inferred that while for $Pb_{n-1}Sn$ $(n = 10-13)$ clusters, the low-lying isomers prefer a peripheral substitution or endohedral encapsulation of the impurity Sn atom, for $Sn_{n-1}Pb$ $(n = 10-13)$, Pb always remains at the peripheral location. The reason for such difference is attributed to the radius ratio of $Sn\colon Pb$, which plays a very significant role for the structural evolution of these clusters.

4.3.4 Energetics

In order to understand the relative stability of $Pb_{n-1}Sn$ and $Sn_{n-1}Pb$ clusters in comparison to the host Pb_n and Sn_n clusters, the trend in average binding energies, second order difference in energy and the fragmentation behavior are analyzed based on the energetics of the lowest energy isomers. The average BE, defined as the energy gained in assembling the cluster from its isolated constituent atoms is expressed as

$$BE(Pb_n) = -[E(Pb_n) - n \times E(Pb)]/n \qquad \text{eq. 4.3}$$

$$BE(Sn_n) = -[E(Sn_n) - n \times E(Sn)]/n \qquad \text{eq. 4.4}$$

$$BE(Pb_{n-1}Sn) = -[E(Pb_{n-1}Sn) - (n-1) \times E(Pb) - E(Sn)]/n \qquad \text{eq. 4.5}$$

$$BE(Sn_{n-1}Pb) = -[E(Sn_{n-1}Pb) - (n-1) \times E(Sn) - E(Pb)]/n \qquad \text{eq. 4.6}$$

Figure 4.18 represents the average BE of $Pb_{n-1}Sn$ and $Sn_{n-1}Pb$ clusters respectively as a function of cluster size (n) in comparison with their native clusters. As it was understood from the previous sections that the spin-orbit effect is quite significant on Pb clusters, the binding energies of $Pb_{n-1}Sn$ as well as Pb_n clusters are calculated using PAW pseudo potential method without and with incorporation of spin-orbit correction. It is realized that the SO correction in total energy significantly lowered the average BE of these clusters but the trend remained unaltered with or without the SO effect (Figure 4.18). For small clusters in the range up to $n = 13$, the trend in the binding energy curve shows that in general it increases as the cluster size grows with small humps or dips for specific size of clusters indicating their relative stabilities. Accordingly, small humps at $n = 4, 7$ *and* 10 for Pb_n clusters (Figure 4.18a) and Sn_n clusters (Figure 4.18b) reflect their higher stabilities over neighboring clusters. The average BE curve of $Pb_{n-1}Sn$ which is plotted along with the Pb_n clusters suggest that the Sn doped Pb_n clusters have higher binding energy compared to the

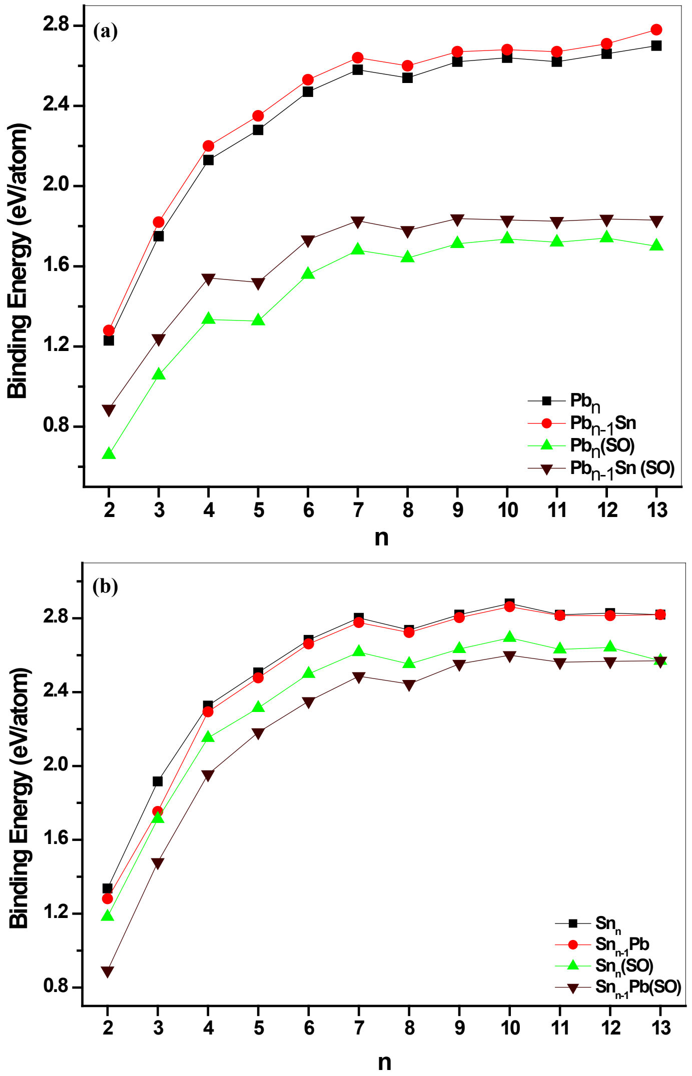

Figure 4.18 : Comparison of binding energies of (a) Pb_n and $Pb_{n-1}Sn$ clusters (b) binding energies of Sn_n and $Sn_{n-1}Pb$ clusters including the spin-orbit coupling factor

host clusters, thus imparting extra stability to the doped clusters. Similar humps are observed at $n = 6, 7$ and 9 in the binding energy plot of $Pb_{n-1}Sn$ clusters (Figure 4.18a), reflecting the extra stability of these clusters over their neighbors. From Figure 4.18b, it is observed that the average BE of $Sn_{n-1}Pb$ clusters is less than the native Sn_n clusters. The clusters with $n = 7, 10$ are extra stable compared to their nearest clusters. The presence of shallow minima corresponds to less stable clusters, *e.g.,* in the present case Sn_8 and Sn_7Pb are less stable clusters compared to their nearest neighbor in their respective series.

In addition to the binding energy pattern, the second order difference in energy (Δ^2E) which also reflects the stability of these clusters is calculated. This is defined as:

$$\Delta^2E(M_n) = 2 \times E(M_n) - E(M_{n+1}) - E(M_{n-1})\ M = Pb\ or\ Sn \qquad \text{eq. 4.7}$$

$$\Delta^2E(Pb_{n-1}Sn) = 2 \times E(Pb_{n-1}Sn) - E(Pb_nSn) - E(Pb_{n-2}Sn) \qquad \text{eq. 4.8}$$

$$\Delta^2E(Sn_{n-1}Pb) = 2 \times E(Sn_{n-1}Pb) - E(Sn_nPb) - E(Sn_{n-2}Pb) \qquad \text{eq. 4.9}$$

From this definition it is clear that the clusters which have negative values of Δ^2E are more stable than their nearest neighbors and correspond to magic clusters. The plot of Δ^2E *vs* cluster size for both Pb_n and $Pb_{n-1}Sn$ as obtained from eq. 4.7 and eq. 4.8 are shown in Figure 4.19a indicate that the clusters with $n = 4, 7, 9$ and 12 are relatively more stable than their nearest neighbors. The second order energy differences in total energy of Sn_n and

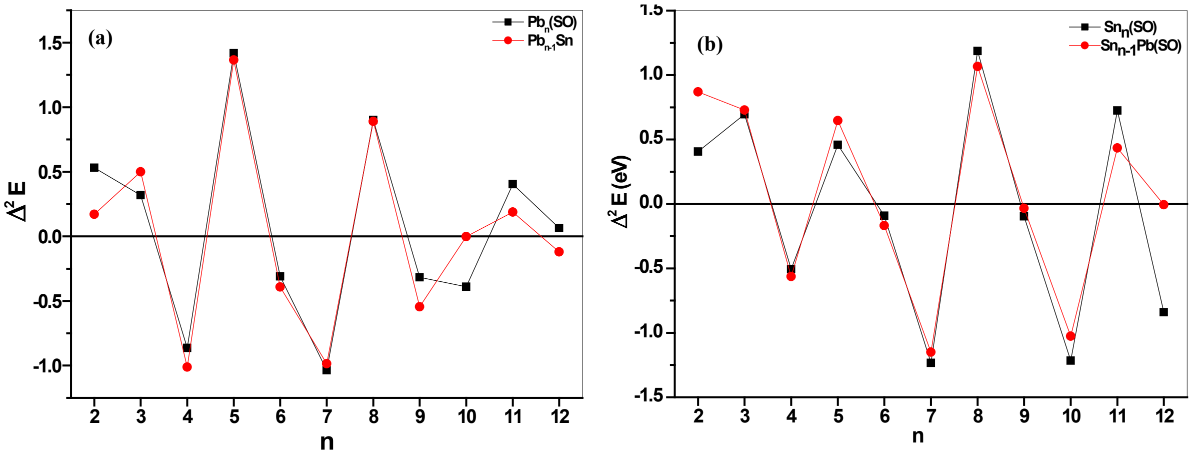

Figure 4.19: (a) Plot of second order energy difference in total energy as a function of cluster size of Pb_n and $Pb_{n-1}Sn$ clusters. (b) Plot of second order energy difference in total energy as a function of cluster size of Sn_n and $Sn_{n-1}Pb$ clusters.

$Sn_{n-1}Pb$ clusters is calculated using eq. 4.7 and eq. 4.9 and the plot is shown in Figure 4.19b. It is observed that for both Sn_n and $Sn_{n-1}Pb$ clusters with $n = 4, 7, 10$ have negative values of $\Delta^2 E$, thus are relatively more stable compared to their adjacent clusters.

4.3.5 Fragmentation behavior

The fragmentation behavior of these clusters, which is important in terms of stability of the clusters, is also studied. Although in practice, fragmentation process involves a dissociation barrier and entropy for free energy change, for simplicity the fragmentation process is considered to occur along the lowest energy pathways with no activation barrier.

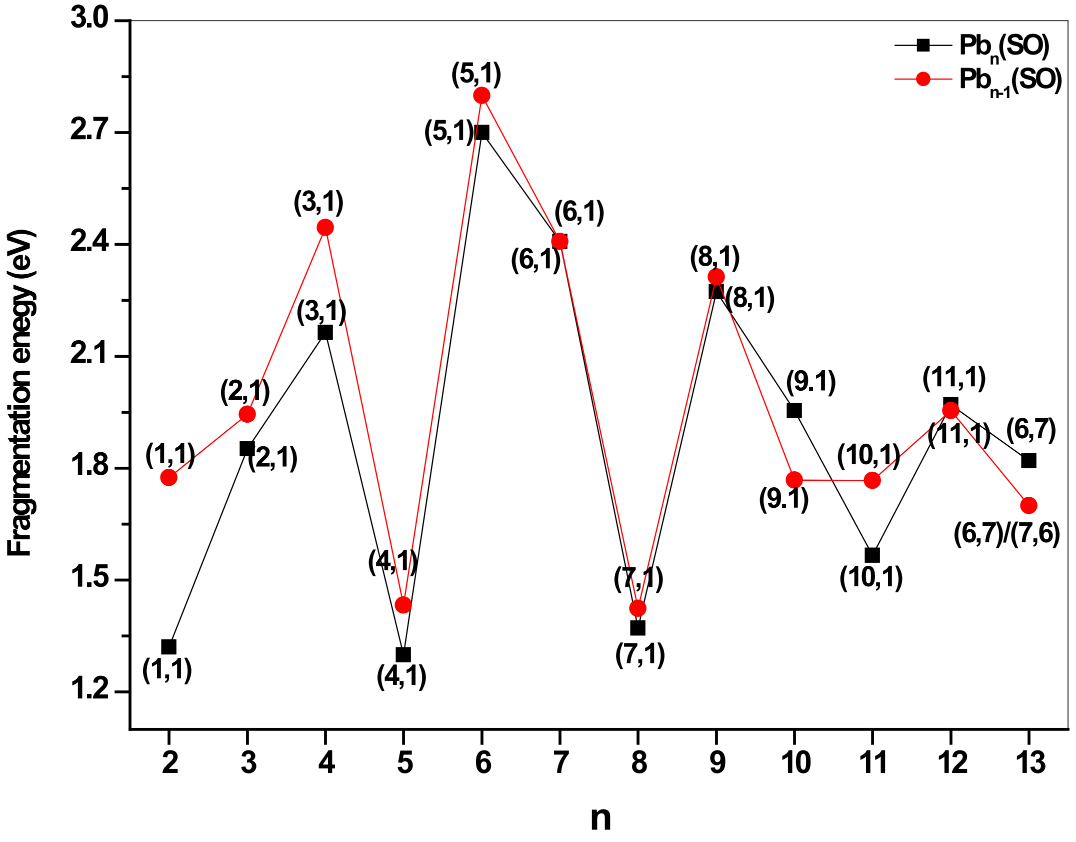

Figure 4.20: The lowest energy fragmentation channels for Pb_n and $Pb_{n-1}Sn$ clusters. For Pb_n clusters the numbers in the bracket represent the two product Pb clusters formed after fragmentation while for $Pb_{n-1}Sn$ series, the first term indicates $Pb_{q-1}Sn$ cluster fragment and the second number represents Pb_p product, where $n = p + q$.

Fundamentally, the fragmentation energy is estimated by looking at the total energy of the parents and daughters only. The complete list of the fragmentation energies for all possible channels of $Pb_{n-1}Sn$ clusters is given in Table 4.2. The theoretical results are found to be in agreement with the experimental fragmentation pattern of Sn_nPb^+ and Pb_nSn^+ clusters

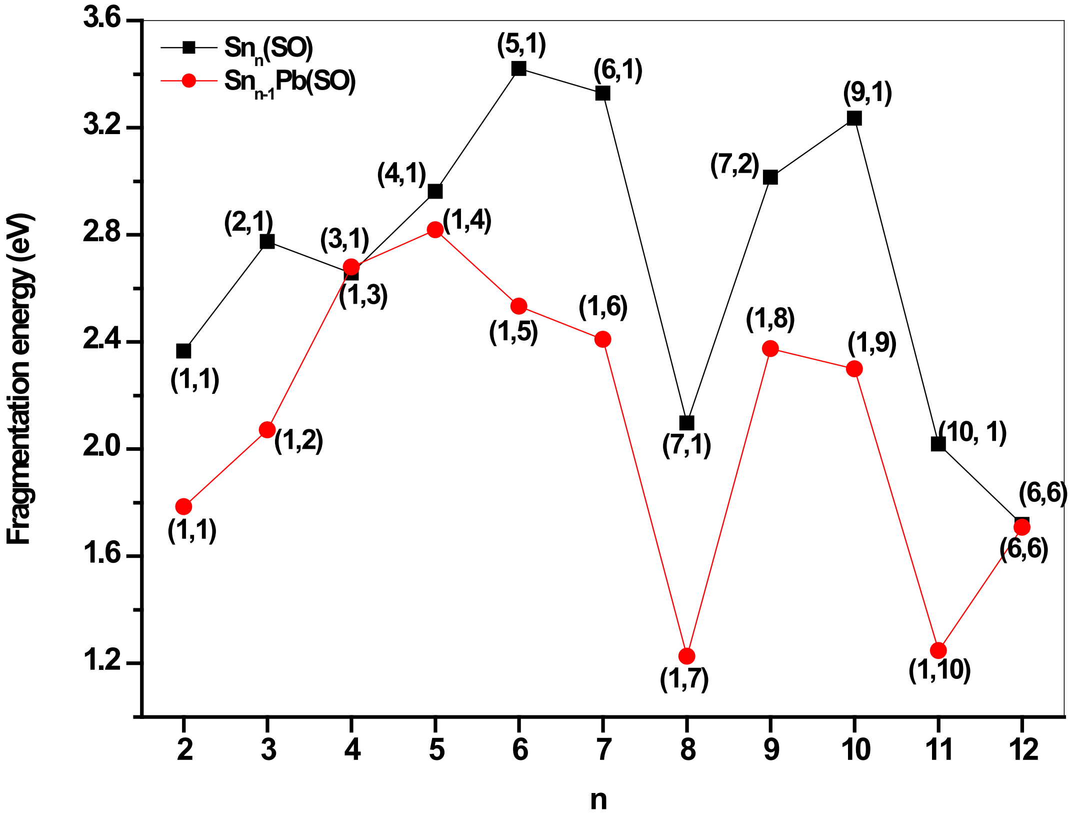

Figure 4.21: Thelowest energy fragmentation channels for Sn_n and $Sn_{n-1}Pb$ clusters. For Sn_n clusters the numbers in the bracket represent the two product Sn clusters formed after fragmentation while for $Sn_{n-1}Pb$ series, the first term indicates $Sn_{q-1}Pb$ cluster fragment and the second number represents Sn_p product, where $n = p + q$.

investigated by tandem time-of flight mass spectrometry [392]. From Figure 4.20 it is clear that Pb_n clusters up to $n = 12$, favor monomer evaporation as the lowest energy fragmentation channel. In line with this trend, the $Pb_{n-1}Sn$ clusters also prefer a monomer evaporation of the Pb atom from the doped cluster. This is consistent with the stronger $Sn - Pb$ bond compared to the $Pb - Pb$ bond, which suggests that it would be easier to knock out an Pb atom from the cluster rather than Sn atom. For Sn_n clusters, which show more covalent nature in their bonding, it is found that small clusters with $n < 11$ favor atom evaporation, while for larger clusters, a fission type fragmentation is more favorable. An exception to this was found for $n = 9$, where it fragments to $(7, 2)$, which has been attributed to the extra-ordinary stability of Sn_7 cluster. From the fragmentation analysis of $Sn_{n-1}Pb$ clusters (Table 4.2 and Figure 4.21), it was observed that removal of Pb atom from $Sn_{n-1}Pb$ clusters tends to be most favorable path of fragmentation for $n \leq 11$ and for $n > 11$,

$Sn_{n-1}Pb$ prefers a fission into two large daughter products. The results are is in full accordance with the low-energy surface-induced dissociation patterns of Sn_nPb^+ and Pb_nSn^+ clusters which were carried out by Waldschmidth *et al.* [392].

Table 4.2: Fragmentation channels of the, $Pb_{n-1}Sn$ and $Sn_{n-1}Pb$ clusters.

	$\boldsymbol{Pb_{n-p}Sn}$	$\boldsymbol{Pb_p}$	E_f (eV)		$\boldsymbol{Sn_{n-p}Pb}$	$\boldsymbol{Sn_p}$	E_f (eV)
$\boldsymbol{PbSn}$	$\boldsymbol{Sn}$	$\boldsymbol{Pb}$	1.77	$\boldsymbol{PbSn}$	$\boldsymbol{Pb}$	$\boldsymbol{Sn}$	1.77
$\boldsymbol{Pb_2Sn}$	$\boldsymbol{PbSn}$	$\boldsymbol{Pb}$	1.94	Sn_2Pb	$PbSn$	Sn	2.65
	Sn	Pb_2	2.40		$\boldsymbol{Pb}$	$\boldsymbol{Sn_2}$	2.07
$\boldsymbol{Pb_3Sn}$	$\boldsymbol{Pb_2Sn}$	$\boldsymbol{Pb}$	2.44	$\boldsymbol{Sn_3Pb}$	Sn_2Pb	Sn	3.38
	$PbSn$	Pb_2	3.07		$PbSn$	Sn_2	3.66
	Sn	Pb_3	2.99		$\boldsymbol{Pb}$	$\boldsymbol{Sn_3}$	2.67
$\boldsymbol{Pb_4Sn}$	$\boldsymbol{Pb_3Sn}$	$\boldsymbol{Pb}$	1.43	$\boldsymbol{Sn_4Pb}$	Sn_3Pb	Sn	2.81
	Pb_2Sn	Pb_2	2.55		Sn_2Pb	Sn_2	3.83
	$PbSn$	Pb_3	2.65		$PbSn$	Sn_3	3.71
	Sn	Pb_4	2.26		$\boldsymbol{Pb}$	$\boldsymbol{Sn_4}$	2.03
$\boldsymbol{Pb_5Sn}$	$\boldsymbol{Pb_4Sn}$	$\boldsymbol{Pb}$	2.79	$\boldsymbol{Sn_5Pb}$	Sn_4Pb	Sn	3.46
	Pb_3Sn	Pb_2	2.91		Sn_3Pb	Sn_2	3.91
	Pb_2Sn	Pb_3	3.50		Sn_2Pb	Sn_3	4.52
	$PbSn$	Pb_4	3.28		$PbSn$	Sn_4	3.71
	Sn	Pb_5	3.76		$\boldsymbol{Pb}$	$\boldsymbol{Sn_5}$	2.53
$\boldsymbol{Pb_6Sn}$	$\boldsymbol{Pb_5Sn}$	$\boldsymbol{Pb}$	2.40	$\boldsymbol{Sn_6Pb}$	Sn_5Pb	Sn	3.29
	Pb_4Sn	Pb_2	3.88		Sn_4Pb	Sn_2	4.39
	Pb_3Sn	Pb_3	3.46		Sn_3Pb	Sn_3	4.44
	Pb_2Sn	Pb_4	3.75		Sn_2Pb	Sn_4	4.35
	$PbSn$	Pb_5	4.39		$PbSn$	Sn_5	4.04
	Sn	Pb_6	3.45		$\boldsymbol{Pb}$	$\boldsymbol{Sn_6}$	2.40
$\boldsymbol{Pb_7Sn}$	$\boldsymbol{Pb_6Sn}$	$\boldsymbol{Pb}$	1.42	$\boldsymbol{Sn_7Pb}$	Sn_6Pb	Sn	2.14
	Pb_5Sn	Pb_2	2.51		Sn_5Pb	Sn_2	3.07
	Pb_4Sn	Pb_3	3.45		Sn_4Pb	Sn_3	3.76
	Pb_3Sn	Pb_4	2.72		Sn_3Pb	Sn_4	3.12

	$\boldsymbol{Pb_{n-p}Sn}$	$\boldsymbol{Pb_p}$	E_f (eV)		$\boldsymbol{Sn_{n-p}Pb}$	$\boldsymbol{Sn_p}$	E_f (eV)
	Pb_2Sn	Pb_5	3.87		Sn_2Pb	Sn_5	3.54
	$PbSn$	Pb_6	3.10		$PbSn$	Sn_6	3.77
	Sn	Pb_7	2.46		$\boldsymbol{Pb}$	$\boldsymbol{Sn_7}$	1.22
$\boldsymbol{Pb_8Sn}$	$\boldsymbol{Pb_7Sn}$	$\boldsymbol{Pb}$	2.31	$\boldsymbol{Sn_8Pb}$	Sn_7Pb	Sn	3.24
	Pb_6Sn	Pb_2	2.41		Sn_6Pb	Sn_2	3.02
	Pb_5Sn	Pb_3	2.97		Sn_5Pb	Sn_3	3.54
	Pb_4Sn	Pb_4	3.60		Sn_4Pb	Sn_4	3.54
	Pb_3Sn	Pb_5	3.74		Sn_3Pb	Sn_5	3.40
	Pb_2Sn	Pb_6	3.46		Sn_2Pb	Sn_6	3.36
	$PbSn$	Pb_7	3.00		$PbSn$	Sn_7	2.68
	Sn	Pb_8	3.40		$\boldsymbol{Pb}$	$\boldsymbol{Sn_8}$	2.37
$\boldsymbol{Pb_9Sn}$	$\boldsymbol{Pb_8Sn}$	$\boldsymbol{Pb}$	1.76	$\boldsymbol{Sn_9Pb}$	Sn_8Pb	Sn	3.21
	Pb_7Sn	Pb_2	2.76		Sn_7Pb	Sn_2	4.08
	Pb_6Sn	Pb_3	2.33		Sn_6Pb	Sn_3	3.46
	Pb_5Sn	Pb_4	2.57		Sn_5Pb	Sn_4	3.28
	Pb_4Sn	Pb_5	4.07		Sn_4Pb	Sn_5	3.79
	Pb_3Sn	Pb_6	2.79		Sn_3Pb	Sn_6	3.19
	Pb_2Sn	Pb_7	2.82		Sn_2Pb	Sn_7	3.24
	$PbSn$	Pb_8	3.40		$PbSn$	Sn_8	3.80
	Sn	Pb_9	2.90		$\boldsymbol{Pb}$	$\boldsymbol{Sn_9}$	2.30
$\boldsymbol{Pb_{10}Sn}$	$\boldsymbol{Pb_9Sn}$	$\boldsymbol{Pb}$	1.76	$\boldsymbol{Sn_{10}Pb}$	Sn_9Pb	Sn	2.18
	Pb_8Sn	Pb_2	2.21		Sn_8Pb	Sn_2	3.02
	Pb_7Sn	Pb_3	2.67		Sn_7Pb	Sn_3	3.39
	Pb_6Sn	Pb_4	1.93		Sn_6Pb	Sn_4	2.17
	Pb_5Sn	Pb_5	3.04		Sn_5Pb	Sn_5	2.51
	Pb_4Sn	Pb_6	3.12		Sn_4Pb	Sn_6	2.55
	Pb_3Sn	Pb_7	2.15		$\boldsymbol{Sn_3Pb}$	$\boldsymbol{Sn_7}$	2.04
	Pb_2Sn	Pb_8	3.22		Sn_2Pb	Sn_8	3.32
	$PbSn$	Pb_9	2.89		$PbSn$	Sn_9	2.69

	$\boldsymbol{Pb_{n-p}Sn}$	$\boldsymbol{Pb_p}$	E_f (eV)		$\boldsymbol{Sn_{n-p}Pb}$	$\boldsymbol{Sn_p}$	E_f (eV)
	Sn	Pb_{10}	2.71		$\boldsymbol{Pb}$	$\boldsymbol{Sn_{10}}$	1.24
$\boldsymbol{Pb_{11}Sn}$	$\boldsymbol{Pb_{10}Sn}$	$\boldsymbol{Pb}$	1.95	$\boldsymbol{Sn_{11}Pb}$	$Sn_{10}Pb$	Sn	2.61
	Pb_9Sn	Pb_2	2.40		Sn_9Pb	Sn_2	2.43
	Pb_8Sn	Pb_3	2.31		Sn_8Pb	Sn_3	2.87
	Pb_7Sn	Pb_4	3.46		Sn_7Pb	Sn_4	2.64
	Pb_6Sn	Pb_5	2.59		Sn_6Pb	Sn_5	1.83
	Pb_5Sn	Pb_6	2.26		$\boldsymbol{Sn_5Pb}$	$\boldsymbol{Sn_6}$	1.70
	Pb_4Sn	Pb_7	2.67		Sn_4Pb	Sn_7	1.84
	Pb_3Sn	Pb_8	2.73		Sn_3Pb	Sn_8	2.65
	Pb_2Sn	Pb_9	2.90		Sn_2Pb	Sn_9	2.66
	$PbSn$	Pb_{10}	2.89		$PbSn$	Sn_{10}	2.08
	Sn	Pb_{11}	3.10		Pb	Sn_{11}	1.84
$Pb_{12}Sn$	$Pb_{11}Sn$	Pb	1.83	$Sn_{12}Pb$	$Sn_{11}Pb$	Sn	2.59
	$Pb_{10}10Sn$	Pb_2	2.47		$Sn_{10}Pb$	Sn_2	2.84
	Pb_9Sn	Pb_3	2.38		Sn_9Pb	Sn_3	2.25
	Pb_8Sn	Pb_4	1.99		Sn_8Pb	Sn_4	1.99
	Pb_7Sn	Pb_5	3.00		Sn_7Pb	Sn_5	2.27
	$\boldsymbol{Pb_6Sn}$	$\boldsymbol{Pb_6}$	**1.71**		Sn_6Pb	Sn_6	1.00
	$\boldsymbol{Pb_5Sn}$	$\boldsymbol{Pb_7}$	**1.71**		$\boldsymbol{Sn_5Pb}$	$\boldsymbol{Sn_7}$	**0.96**
	Pb_4Sn	Pb_8	3.13		Sn_4Pb	Sn_8	2.33
	Pb_3Sn	Pb_9	2.29		Sn_3Pb	Sn_9	1.87
	Pb_2Sn	Pb_{10}	2.78		Sn_2Pb	Sn_{10}	2.01
	$PbSn$	Pb_{11}	3.16		$SnPb$	Sn_{11}	2.65

4.4 Conclusion

In summary, the ground state geometries and energetics of Pb_nM ($M = C, Al, In, Mg, Sr, Ba$ and Pb; $n = 8, 10, 12$ and 14) clusters using the density functional theory and generalized gradient approximation scheme are discussed in this section. In general, it is found that the atomic size of the impurity atom and its interaction energy with host cluster plays the crucial role to determine the structure and stability of the system. If the atomic radius of the impurity atom is small, it prefers to be encapsulated, which in turn improves the binding energy or stability of the cluster. In case the size of the impurity atom is bigger, it is difficult to be accommodated inside the cage formed by the host cluster. Therefore, an optimum cage diameter of the host cluster is required to encapsulate the impurity atom of a specific size. The trend in stability of these impurity-doped clusters is analyzed based on the binding energy, interaction energy and the energy gap between the HOMO and LUMO energy levels. Apart from geometrical effects, it is found that stability of these clusters can be tuned by the ordering of their energy levels. It is found that although the binding energy of Pb_{13} is more than Pb_{12} and Pb_{11}, the ionization potential and HOMO-LUMO energy gap is very small. However, it is possible to tailor the electronic properties by suitably choosing M atoms. While $Pb_{12}C$ shows the highest stability in terms of binding energy, incorporation of Mg atom enhances the energy gap even more than C doping. In fact, the energy gap of $Pb_{12}Mg$ (2.30eV) calculated in this work presents the largest gap reported so far for any clusters constituting of *all metal atoms*. Moreover, while the interaction energy of C, Pb and Al atoms with Pb_n ($n = 10, 12$ and 14) clusters show a linear increase as a function of cluster size, Mg atom shows sharp rise in the interaction energy at $n = 12$. This unusual increase in the interaction energy of Mg with Pb_{12} and the largest HLG of $Pb_{12}Mg$ cluster has been explained based on the 50 electrons rule for icosahedral structures. The energy gap, which is inversely related to the reactivity, should be utilized to use $Pb_{12}Mg$ as a super atom to build cluster assembled materials. Further, considering the structural transition (non compact to compact) that occurs between Sn and Pb clusters among Group IV elemental clusters, extensive study on the geometrical isomers of $Sn_{n-1}Pb$ and $Pb_{n-1}Sn$ clusters is carried out with an objective to understand effect on the growth pattern and stability of Sn_n and Pb_n clusters on doping with Pb and Sn, respectively. The results reveal that the influence of the impurity atoms is negligible in these clusters except small changes localized around the impurity atoms. The trend in the interaction energy between these two elements is: $Sn - Sn > Sn - Pb > Pb - Pb$. In line with this trend, it is found that while incorporation of Sn as impurity enhances the stability of Pb_n clusters, Pb atom as impurity in Sn_n clusters reduces their binding energy. The second order difference in energy showed that for $Sn_{n-1}Pb$, $n = 4, 7$ and 10 clusters and for $Pb_{n-1}Sn$ clusters, $n = 6, 7$ and 9 clusters are more stable than their neighbors. Based on the fragmentation pattern it is seen that for $Sn_{n-1}Pb$ and $Pb_{n-1}Sn$ clusters favor monomer evaporation of the Pb atom up to $n = 11$ and $n = 12$, respectively. Unlike this trend, larger cluster like $Sn_{11}Pb$ prefers to undergo fission type fragmentation into Sn_5Pb and Sn_6 clusters. The results compared well with experimental fragmentation behavior carried out using surface induced dissociation process. A good agreement between these two results further gives confidence on the ground state geometries that are obtained in this study. Therefore, the thermodynamic and chemical stability can be tuned properly to design novel materials with desired physico-chemical properties.

5. Reactivity of Gold Nano-alloy Clusters

5.1 Introduction

Gold clusters have been receiving considerable attention since some time because of their exceptional physical and chemical properties. Gold, which is inert in the bulk, is highly reactive in its nano form. Application of nanoscale gold particles towards biology, nanotechnology and especially catalysis is on a surge [174,180,188,393-408]. In particular, the high catalytic activity of gold nanoparticles supported on metal-oxide surfaces towards low temperature CO oxidation [395-399] has emerged as one of the key research areas for understanding the fundamental process of CO oxidation.

Extensive experimental and theoretical studies were out to elucidate the geometric and electronic structure of gold clusters [115,409-427]. Studies have shown that the ground state structures of small gold clusters are planar up to $n = 11$ [428]. Further studies have shown that the ground state structures of small gold clusters differ from other coinage metal clusters [410,413,426-430]. For example, using experimental and theoretical techniques Weis and co-workers [426] have shown that Ag_n^+ clusters adopt three dimensional structures from pentamer onwards. The reason for the preference of planar structures by gold clusters up to large cluster sizes is attributed to the relativistic effects that cause a shrinking of the size of the s orbitals and thus enhance the $s-d$ hybridization. While Gottfried *et al.* have shown that bulk gold surfaces are inert towards O_2 [431], studies have consistently revealed that neutral Au_n clusters interact with O_2 rather weakly, insufficient to activate molecular oxygen [432,433]. Several studies were carried out to understand the interaction of Au_n^- clusters towards O_2 [434-437]. It was observed that while the molecular addition of O_2 is observed for even atom clusters, the odd atom clusters are inert. It is worthwhile to mention that a similar, even-odd alternation trend is also observed for the electron affinities of Au_n clusters [115], suggesting a probable electron transfer from Au_n^- to O_2 [435]. Subsequent PeS studies have revealed that even-numbered $Au_nO_2^-$ are indeed molecularly chemisorbed complexes [436,437]. Interestingly, Stolcic and co-workers have shown that charge transfer takes place from O_2 to Au_2 and Au_4 in neutral Au_2O_2 and Au_4O_2 clusters owing to the high electronegativity of Au [436]. A systematic PeS study of the $Au_nO_2^-$ ($n = 1-7$) cluster complexes by Wei *et al.* confirmed the molecular chemisorption nature of O_2 on even Au_n systems and physisorbed $Au_n^- - O_2$ complexes are observed for the odd-sized $Au_nO_2^-$ ($n = 1, 3, 5$ and 7) clusters [438].

Considering the sensitivity of the stability and reactivity of nanoparticles on the size and shape, it has become important to study the effect of doping which will modify the electronic and geometric structure of these clusters [181,439-446]. A thoughtful selection of the impurity atoms for tuning their chemical reactivity might lead to enhanced performance of these clusters. Photo-fragmentation experiments by Neukermans *et al.* on Au_nM^+, clusters with M varying from Sc to Ni have shown higher intensity for specific sizes of the clusters, which correspond to the highly stable Au_nM^+ clusters [441]. In this series, $Au_5X^+(X = V, Cr, Mn, Fe, Co, Zn)$ clusters showed extra stability, which was explained based on the structural planarity and the delocalized electrons [443,444]. The enhanced stability of Au_5Zn^+ cluster was explained based on the stabilization induced via σ-aromaticity with six delocalized s electrons [447]. The effect of transition metal atom (Mo, W and Zr) doping in Au_{12} and Au_{14} clusters was found to increase the energy gap between HOMO and LUMO energy levels. The enhanced stability of the metal-doped Au_{12} cluster was attributed to the aurophilic attractions, relativistic effects, and closed-shell electron configuration. In another work the existence of tetrahedral MAu_4 ($M = Ti, Zr, Hf$ and Th) was predicted [448]. The charge distribution analysis of these clusters showed that the gold carries a formal negative charge and acts as a halogen. On the other hand using the photoelectron spectroscopy, Kiran *et al.* [449] have reported the hydrogen like behavior of Au in $SiAu_4$ with an analogy of SiH_4. In a recent study on electronic structure and magnetic properties of transition-metal-doped Au clusters, MAu_6 ($M = Ti, V$ and Cr), it is found that all the MAu_6^- and MAu_6 clusters not only form planar structures, but also the M atoms possess atom-like moments [450]. For Ti doped Au_n clusters, it is found that up to $n = 7$, the equilibrium geometry prefers planar configuration and for $n = 12 - 16$, Ti gets encapsulated inside a spherical cage formed by Au atoms [451]. Pyykko and Reneberg theoretically predicted the possibility of highly stable $M@Au_{12}$ ($M = W, Ta^-$ and Re^+) endohedral gold-cage clusters [452-454], which was subsequently detected by Wang and co workers [455] using photo-electron spectroscopy. In fact a series of $M@Au_n$ ($n = 9 - 17$; $M = TM, Na - K$) clusters with 18 valence electrons were studied by several groups, and some of these clusters were predicted to show high catalytic activities [456-458]. Molina *et al.* based on DFT calculations have reported that Na-doped Au_{20} clusters are more reactive than the bare pyramidal Au_{20} clusters [459]. More recently, it was shown that in case of small Au doped clusters the electrostatic effects play as an alternative to charge transfer in promoting the catalytic activity of Au clusters and also alloying can improve the catalyst stability [460]. Motivated by these results, in the first section of this chapter studies on Al doped Au clusters ($Au_{n-1}Al$ clusters, $n = 2 - 7$ and 21) and the oxidation reaction of a few stable clusters are reported.

Further, the high catalytic activity of metal oxide supported gold nano particles towards low temperature CO oxidation as observed by Haruta *et al.* [395-399], has surged the efforts towards understanding CO oxidation over Au clusters. In order to understand the reactivity of gold clusters with O_2 and decipher the catalytic effects observed for gold nanoparticles several experimental and theoretical studies were carried out for free gas-phase clusters and supported clusters in well defined ultra-high vacuum model systems and industry-like catalytic conditions [188,401,403-406]. Several computational studies were carried out to investigate the CO oxidation on supported and unsupported gold clusters [459-472]. Density functional theory based calculations within the local-spin-density approximation carried out to study the CO oxidation on MgO-supported Au_8 clusters suggested low reaction barrier (< 0.2 eV) for this reaction [472]. Detailed mechanism of the CO oxidation on planar gold surfaces was carried out by Lieu *et al.* [466]. CO oxidation studies on isolated small gold clusters revealed that oxidation is particularly easy on the Au_{10} cluster with a relatively low reaction barrier < 0.4 eV [461]. Besides pure gold clusters, gold alloy clusters have also attracted attention owing to their tunable properties [469,470]. Based on above results it was found that negatively charged Au clusters with even number of Au atoms are particularly more sensitive for CO oxidation reaction. This is because these Au clusters can easily donate an electron to the anti-bonding molecular orbital of the O_2 there by weakening the $O - O$ bond. Therefore, one of the most important criteria of Au clusters to be more reactive is to have additional electronic charge to donate. To create a similar situation in a neutral cluster would be to form a bimetallic cluster of gold where the other element is electro-positive. Based on this idea attempt has been made to make $AlAu$ bimetallic clusters as model systems to study the CO oxidation behavior.

A. Oxidation of Al doped Au_n clusters

Although most of the studies have focused on the interaction of Au clusters with transition metal atoms, few are available to show the interactions of s and p block elements with Au clusters [473-476]. A study on the atomic and electronic structure of Au_5M clusters where M atom represents the second period elements revealed that with the exception of S, impurities with p electrons (Al, Si, P) adopt non-planar geometries while those with s electrons (Na, Mg) prefer planar geometries [475,476]. In this section, the atomic and electronic structure of $Au_{n-1}Al$ clusters $(n = 2 - 7, 21)$ are presented and the results are elucidated with a view to understand how chemical bonding influences the stability and structure of small size atomic clusters. It should be mentioned here that although $Al\,(3s^2, 3p^1)$ and $Au\,(5d^{10}, 6s^1)$ are metals in their bulk and have similar crystal packing arrangements (fcc), the atomic states have large difference in their electronegativity values. According to the Pauling's scale, the electronegativity of Au and Al are 2.54 and 1.61, respectively [477]. Therefore, it is expected that the interaction between Al and Au would involve significant charge transfer or in other words the chemical bonding will have more ionic than covalent character. Based on these motivations, in this work the equilibrium structures of small $Au_{n-1}Al\,(n = 2 - 7, 21)$ clusters are investigated followed by their oxidation reactions. The objective of this study can be divided into two parts: (i) to investigate the effect of electropositive Al atom in disturbing the stable planar conformations of small Au clusters, and (ii) the oxidation mechanism of the Al doped Au clusters.

5.2 Computational Details

All the calculations were performed using the density functional theory with projector augmented wave pseudopotentials and plane wave basis set as implemented in the VASP code[274-278]. The spin polarized Perdew–Wang generalized gradient approximation has been used to calculate the exchange correlation energy [232,233]. A simple cubic super cell of side 20 Å was used and the Brillouin zone integrations were carried out using only the gamma point. The cutoff energy for all calculations was 500 eV, which ensured a good convergence of the energy. The self-consistent equations were solved with an iterative matrix diagonalization scheme and the geometries were considered to be converged when the forces on each atom became 0.01 eV/Å or less. The total-energy convergence was tested with respect to the plane-wave basis set size and simulation cell size and the total energy was found to be accurate to within 1 meV.

Test calculations were done for Au bulk and the dimers of Au and Al in order to verify the accuracy of our computational methodology. The computed results obtained along with the experimental values are summarized in Table 5.1. From our calculations the lattice parameters of the Au bulk is found to be 4.13 Å, which is quite close (~1% error) to the experimental value of 4.09 Å. The bulk cohesive energy is estimated to be 3.61 eV/atom, which is close with the experiment (3.81 eV/atom) [257]. Further, for Au_2 dimer, the corresponding values of bond length and binding energy are estimated to be 2.53 Å and 1.17 eV/atom, which are in good agreement with experimental values of 2.47 Å and 1.16 eV/atom, respectively [477]. Similar good agreement is obtained for the Al_2 dimer. The bond length and binding energies are estimated to be 2.51 Å and 0.70 eV/atom, which agree quite well with the experimental values of 2.46 Å and 0.69 eV/atom [477].

System	**Bond length (Å)**		**BE/atom (eV/atom)**	
	Comp.	**Exp.**	**Comp.**	**Exp.**
Au_2	2.53	2.47[b]	1.17	1.16 (±0.005)[b]
$Au-Al$	2.32	--	1.83	1.68 (±0.06)[b]
Al_2	2.51	2.46[b]	0.70	0.69 (±0.06)[b]
Au-bulk	4.13	4.09[a]	3.6	3.8[a]

Table 5.1: Computed and experimental binding energies and bond lengths of the dimers and bulk.

a) Ref [257] b) Ref. [477]

Initial calculations were carried out to obtain the ground state geometries of $Au_n (n = 2-7, 20)$ clusters. The lowest energy geometries of $Au_n (n = 2-7)$ clusters form planar W structures and Au_{20} a T_d structure, respectively. These results are found to be consistent with previously reported results using different techniques [115,409-427]. To obtain the equilibrium geometries of $Au_{n-1}M$ clusters, the initial geometries were prepared by adding the M atom on each possible site of a few low-lying 2D and 3D isomers of Au_{n-1} host cluster as well as by substituting one Au by M atom from the Au_n cluster.

5.3 Results and Discussion

5.3.1 $Au_{n-1}Al$ Clusters

5.3.1.1 Geometric Structures

The optimized bond lengths of Au_2, $Au-Al$ and Al_2 are 2.53 Å, 2.32 Å, and 2.51 Å respectively, and the bond strength follows the trend as $Al-Al < Au-Au < Au-Al$ (Table 5.1). This has further been corroborated by the higher binding energy and shorter bond length of $Au-Al$ dimer, which are 1.83 eV/atom and 2.32 Å respectively. The interaction of Al with Au_2 dimer forms a bent shape structure with $\angle AuAlAu$ of 132° and the $Al-Au$ distance of 2.34 Å. This is similar to that of Au_3 cluster, which also forms an open triangle with $\angle AuAuAu$ angle of 137°. The average binding energy of the Au_2Al cluster is calculated to be 1.96 eV/atom. The geometry of the tetramer cluster is important, as it is the smallest size for the onset of three-dimensional configurations. Previous studies on pure and transition metal impurity doped gold clusters suggested that, at least up to hexamer, they favor planar configurations. For Au_3Al, a planar D_{3h} symmetric structure (Figure 5.1) is found to be the most stable isomer, which is quite similar to that of $AlCl_3$. The $Au-Al$ bond length and $\angle AuAlAu$ are found to be 2.36 Å and 120°, respectively. Another isomer of the Au_3Al cluster, which forms a three-dimensional capped triangle, is 0.5 eV higher in energy. The average binding energy of Au_3Al is estimated to be 2.25 eV/atom.

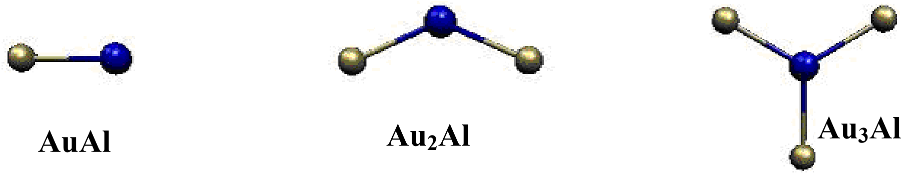

AuAl **Au_2Al** **Au_3Al**

Figure 5.1: Lowest energy isomers of $Au_{n-1}Al$ ($n = 2-4$) clusters.

For Au_5, the ground state geometry forms a W shaped planar structure. When Al replaces one Au atom, the most stable isomer of the Au_4Al cluster adopts three-dimensional tetrahedral shapes as shown in Figure 5.2. A close look at this structure reveals that this structure consists of two parts: Au_2Al and Au_2 joined. The interaction energy between Au_2

and Au_2Al is estimated to be 2.49 eV. The shortest $Au - Au$ and $Au - Al$ bond lengths are found to be 2.68 Å and 2.45 Å, respectively. The binding energy is estimated to be 2.13 eV/atom. The planar isomers of Au_4Al formed by capping the Au_3Al cluster in plane were found to be at least 0.15 eV higher in energy. The hexamer of Au prefers to form a planar triangle structure as the lowest energy isomer. When Al replaces one Au, the most stable geometry of the Au_5Al cluster forms a capped rhombus where Al atom is capping the rhombus formed by Au atoms and the additional Au atom connects at the top site of the Al atom. Other isomers with tetrahedron and octahedron motifs were found to be 0.36 eV and 0.66 eV higher in energy respectively. The differences in the total energy for other low-lying isomers are indicated in the Figure 5.2. The binding energy and the shortest $Au - Al$ bond length are found to be 2.25 eV/atom and 2.38 Å respectively.

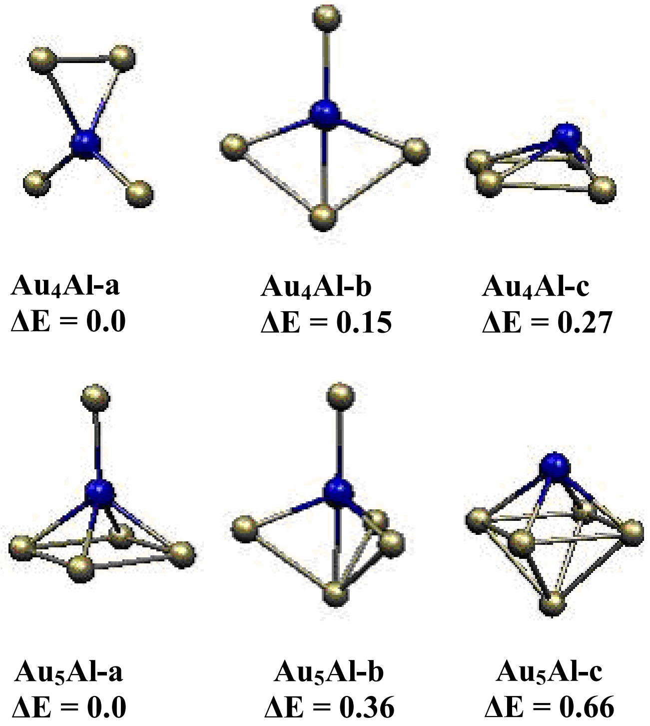

Au$_4$Al-a **ΔE = 0.0**

Au$_4$Al-b **ΔE = 0.15**

Au$_4$Al-c **ΔE = 0.27**

Au$_5$Al-a **ΔE = 0.0**

Au$_5$Al-b **ΔE = 0.36**

Au$_5$Al-c **ΔE = 0.66**

Figure 5.2: Lowest energy isomers of Au_4Al and Au_5Al clusters (ΔE in eV).

For heptamer, the Au cluster continues to favor planar configuration over three

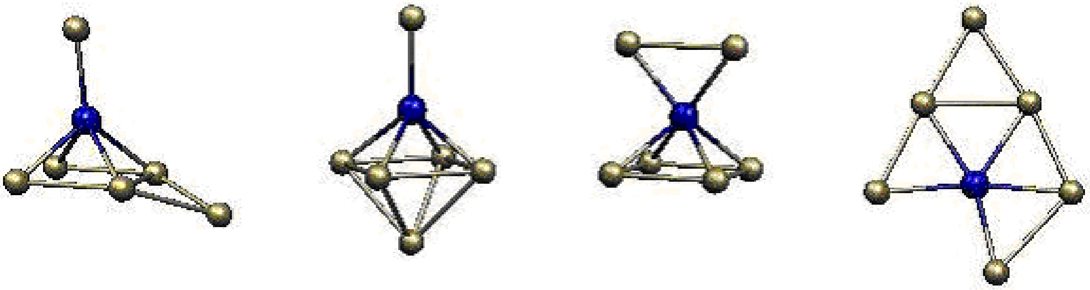

Au$_6$Al-a **ΔE = 0.0**

Au$_6$Al-b **ΔE = 0.23**

Au$_6$Al-c **ΔE = 0.27**

Au$_6$Al-d **ΔE = 0.43**

Figure 5.3:Lowest energy isomers of Au_6Al clusters (ΔE in eV).

dimensional geometry and forms an edge capped triangle structure. For Au_6Al cluster, three-dimensional structural motifs continue to grow. The formation of the Au_6Al can be viewed from three different perspectives: the Al atom can interact with Au_6, the Al atom can substitute one Au atom from Au_7 cluster and one Au atom is added with Au_5Al cluster. The results show that the most stable geometry of the Au_6Al cluster follows the trend of Au_5Al cluster, where the additional Au atom is connected at the edge site of the rhombus formed by four Au atoms. The average binding energy is estimated to be 2.18 eV/atom and the smallest $Au-Al$ bond length is found to be 2.32 Å. Interestingly, we note that the planar isomer of Au_6Al cluster, similar to Au_7 was found to form one of the low-lying isomers with an excess energy of 0.43 eV.

Li *et al.* have shown that Au_{20} cluster prefers T_d geometry as the lowest energy isomer with nine atoms of Au on each face of the tetrahedron [391]. The Au atoms on the tetrahedral face have similar atomic arrangement to that of $Au(111)$ surface with reduced coordination. Several possible sites including the top, bridge, edge capping, triangular capping, substitutional and interstitial positions were considered for the generation of the initial isomers for $Au_{20}Al$ cluster. A comparison of total energy among all these isomers suggest that Al atom prefers to cap the three-fold hollow site of the Au_{20} cluster from outside as shown in Figure 5.4. Another isomer with Al occupying the interstial space of Au_{20} was also found to be stable on the PES but 0.80 eV higher in energy compared to the lowest

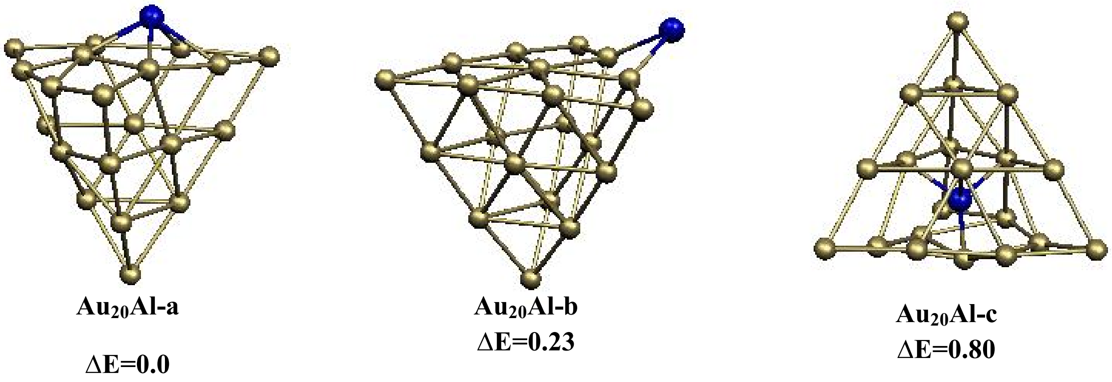

Figure 5.4: Lowest energy isomers of $Au_{20}A$l clusters (ΔE in eV).

energy isomer. The shortest $Au-Al$ distance is found to be 2.68 Å, which is longer compared to the $Au-Al$ distances in the smaller clusters, which might be the result of the increased coordination. The binding energy of $Au_{20}Al$ is found to be 2.41 eV/atom.

5.3.1.2 Energetics

The average binding energy (BE) of Au_n and $Au_{n-1}Al$ clusters is calculated as

$$BE(Au_n) = \frac{-[E(Au_n) - n \times E(Au)]}{n} \qquad \text{eq. 5.1}$$

$$BE(Au_{n-1}Al) = \frac{-[E(Au_{n-1}Al) - (n-1) \times E(Au) - E(Al)]}{n} \qquad \text{eq. 5.2}$$

$$IE(Au_{n-1}Al) = E(Au_{n-1}Al) - E(Au_n) - E(Al) \qquad \text{eq. 5.3}$$

System	BE/atom (eV /atom)	Bond length (ºA)	IE (eV)	HOMO-LUMO Gap (eV)	Charge
$AuAl$	1.83	2.32	3.66	2.4	+1.21
Au_2Al	1.96	2.34	3.49	0.75	+2.04
Au_3Al	2.25	2.36	5.36	2.55	+2.86
Au_4Al	2.13	2.38; 2.45	4.41	0.52	+2.92
Au_5Al	2.25	2.38; 2.45	4.99	1.92	+2.98
Au_6Al	2.18	2.40; 2.47	3.68	0.2	+2.98
$Au_{20}Al$	2.41	2.68	3.30	0.28	+2.15

Table 5.2:Summary of the average binding energy (E_b), interaction energy (IE), HLG and the shortest $Au-Al$ bond distances of $Au_{n-1}Al$ ($n = 2-7, 21$) clusters and charge on the Al atom.

Figure 5.5 shows the binding energy of Au_n and $Au_{n-1}Al$ clusters as a function of the total number of atoms. Apart from an odd even alteration in the stability pattern, two important points are noted from this binding energy plot: (*i*) the incorporation of Al atom improves the overall stability of the host Au clusters, and (*ii*) Au_3Al is the most stable cluster in this series. The higher stability of the $Au_{n-1}Al$ clusters is attributed to the higher bond strength of the $Au - Al$ bond than that of $Au - Au$ bond (3.66 eV and 2.34 eV respectively). The trend in the relative stability of $Au_{n-1}Al$ and Au_n clusters as understood by calculating the second order difference in energy is calculated as in eq. 5.4 and eq. 5.5 and shown in Figure 5.6.

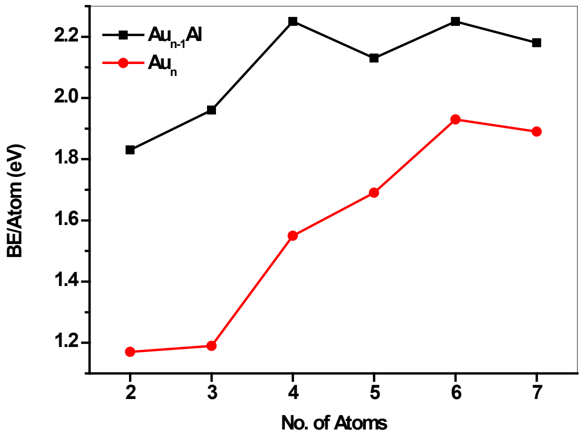

Figure 5.5: The average binding energy of Au_n (circles) and $Au_{n-1}Al$ (squares) clusters ($n = 2 - 7$).

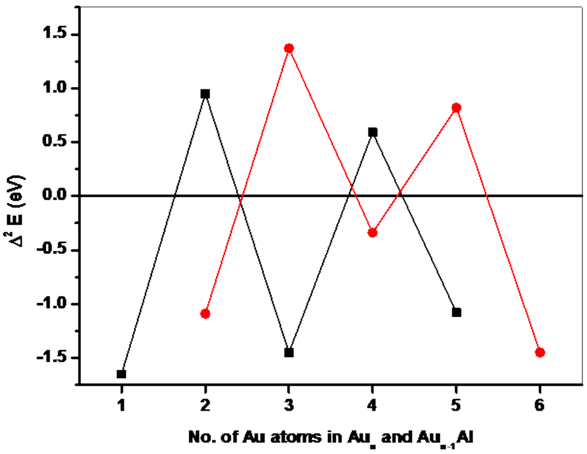

Figure 5.6: Second-order difference in total energy ($\Delta^2 E$) of Au_n (red) and $Au_{n-1}Al$ (black) clusters ($n = 2 - 7$) as a function of n

$$\Delta^2 E(Au_n) = 2 \times E(Au_n) - E(Au_{n-1}) - E(Au_{n+1}) \qquad \text{eq. 5.4}$$

$$\Delta^2 E(Au_{n-1}Al) = 2 \times E(Au_{n-1}Al) - E(Au_nAl) - E(Au_{n-2}Al) \qquad \text{eq. 5.5}$$

The effect of the odd-even alteration in the relative stability order is evident from the oscillatory pattern. For the series of $Au_{n-1}Al$ clusters, the results suggest that Au_3Al and Au_5Al are more stable as compared to their neighbors. The higher stability of these clusters has been corroborated by the large energy gaps between HOMO and LUMO levels which are estimated to be 2.55 eV and 1.92 eV for Au_3Al and Au_5Al respectively (Table 5.2). In order to verify the electronic stability of these clusters, the adiabatic ionization potentials are calculated and estimated to be 6.8 eV and 7.38 eV for Au_5Al and Au_3Al respectively. In addition to the even number of electrons, these two clusters have more reasons to be extra stable. The Au_5Al cluster has 8 valence electrons, which corresponds to the closed configuration of electron shell model. For Au_3Al cluster, it contains six number valence electrons and it is planar geometrically. Both these criteria could be contributing to achieve extra stability of the Au_3Al cluster through resonance (aromatic) stabilization.

5.3.1.3 Electronic Structure

To understand the electronic stability of Au_n clusters in presence of Al atom, the HOMO and LUMO energy levels of Au_n and $Au_{n-1}Al$ clusters are plotted in Figure 5.8 and the energy gap is tabulated in Table 5.2. A large energy gap is observed for $AuAl$, Au_3Al and Au_5Al clusters and estimated to be 2.4 eV, 2.5 eV and 1.92 eV respectively. It is noticed that the energy gap of Au_n ($n = 2$ and 4) has increased by Al substitution. But for Au_6, the Al substitution lead to reduced energy gap. This is attributed to the additional stability of pure Au_6 cluster due to planar aromatic nature of the cluster.

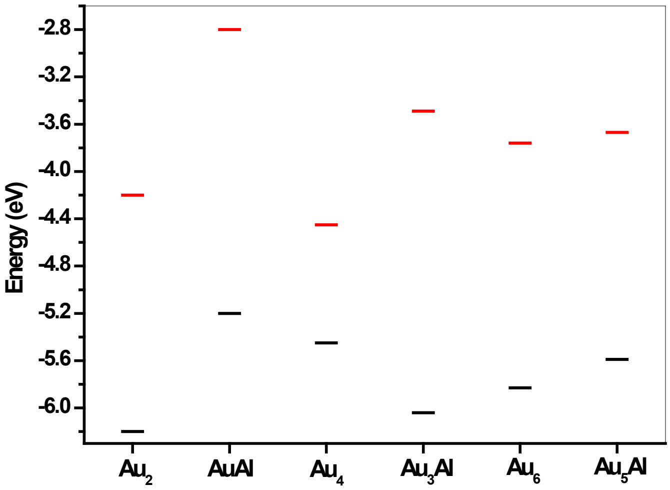

Figure 5.8: The HOMO and LUMO energy levels of Au_n and $Au_{n-1}Al$ clusters.

To further analyze the nature of bonding and the effect of the Al doping on the Au_n clusters, the electronic density of state (EDOS) spectrum is analysed. For the sake of simplicity the EDOS of even atom numbered clusters (Au_2, Au_4 Au_6, $AuAl$, Au_3Al and Au_5Al) only are shown in Figure 5.7. In general, it is seen that the presence of Al in gold clusters results in red shift of the eigen value spectrum. This has been attributed to the electronic charge transfer from Al to the host Au clusters. However, an exception was observed for Au_4

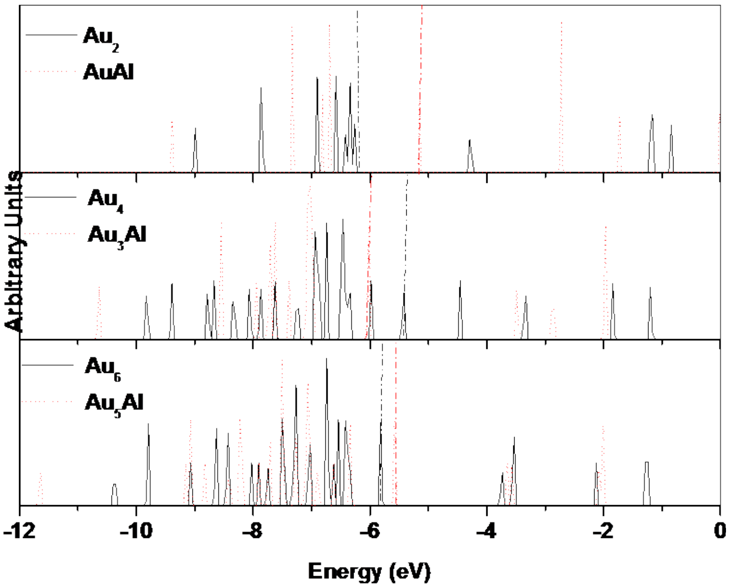

Figure 5.7: The EDOS for $Au_{n-1}Al$ (dotted line) and Au_n clusters (line) for $n = 2, 4,$ and 6 clusters

cluster. The HOMO of the Au_4 cluster is destabilized because of the anti-aromatic nature of 4 electrons. But after the substitution of one of the Au atoms by Al, the HOMO becomes stabilized significantly. To further illustrate the charge transfer of Al to Au host, he charge density difference of the $AuAl$ and Au_3Al clusters is plotted as shown in Figure 5.9 which clearly shows significant charge depletion (blue) from the Al atom and charge accumulation (red) on the Au atoms

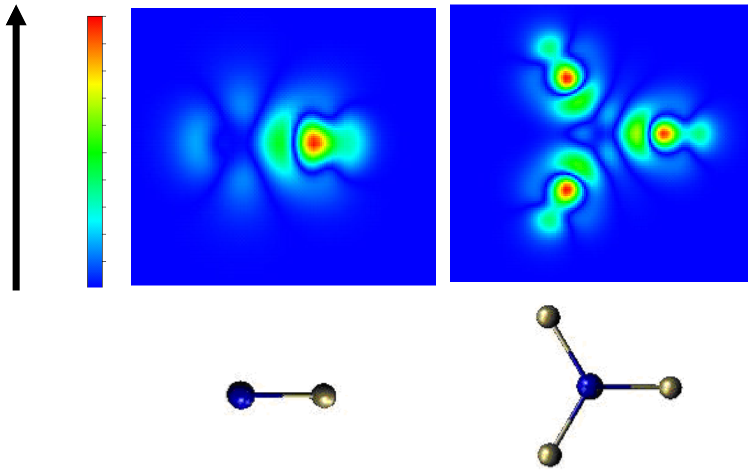

Figure 5.9: Two-dimensional projection of the charge density for $AuAl$ $[\rho(AuAl)-\rho(Au)-\rho(Al)]$ and Au_3Al $[\rho(Au_3Al)-\rho(Au_3)-\rho(Al)]$ as obtained from the difference of the constituent species

5.3.2 Oxidation of $Au_{n-1}Al$ clusters

In order to understand the fundamentally important oxidation of metal nanoparticles studies on the interaction of O_2 molecule with stable Al doped Au clusters are performed. Before attempting to calculate the oxidation reactions, the calculated bond lengths and binding strength of $Al-O$ and $Au-O$ are compared with the experimental data. From the optimized geometry we have estimated the binding energy of $Au-O$ and $Al-O$ as 1.15 eV/atom and 2.53 eV/atom respectively which are in good agreement with the experimental values of 1.15 eV/atom and 2.59 eV/atom [477]. The bond lengths are found to be 2.15 Å and 1.61 Å, which are also consistent with the experimental values of 2.3 Å and 1.61 Å, respectively.

5.3.2.1 Interaction of Au and Al with O_2

In order to understand the interaction of O_2 with atomic Au and Al, the geometry optimization of $Al-O_2$ and $Au-O_2$ complexes is performed by keeping the molecular identity of oxygen as well as its atomic form. The comparison of total energy values suggest that when oxygen is attached with Al in the atomic form ($O-Al-O$), the structure is 1.17 eV lower in energy in comparison to the isomer where oxygen interacts with Al in the molecular way ($Al-O_2$). Unlike Al, the most stable conformation of $Au-O_2$ complex is obtained when O_2 molecule interacts with Au in the molecular form and the ground state configuration form an angled ($Au-O-O$) structure. The initial and final configurations of $Au-O_2$ and $Al-O_2$ are given in Figure 5.10. The interaction energy of $O-Al-O$ and $Au-O-O$ are found to be 4.3 eV and 0.48 eV respectively. The interaction energy of the oxygen molecule with $Au_{n-1}Al$ is calculated by

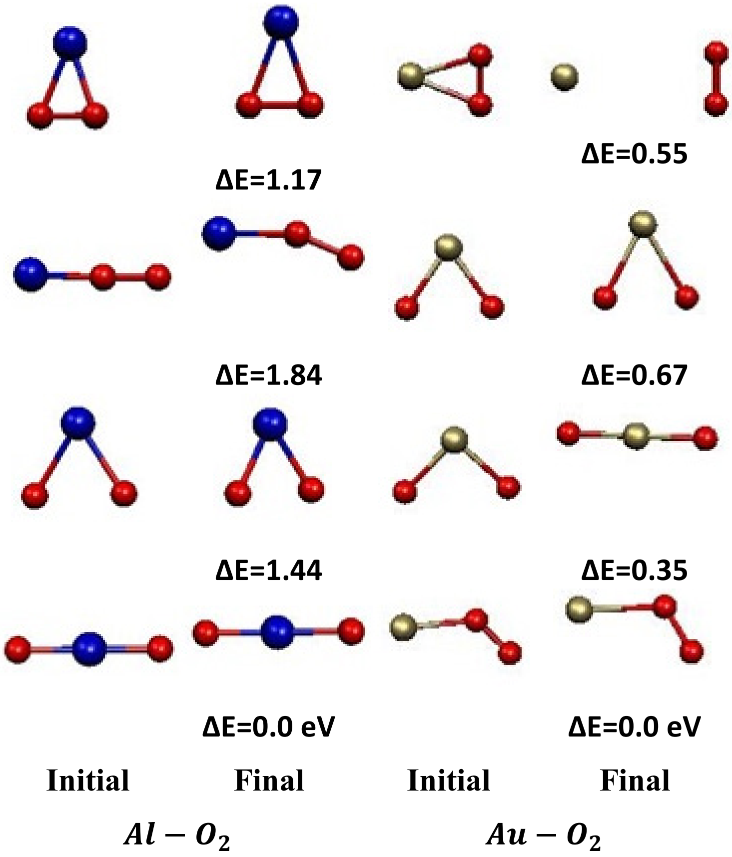

Figure 5.10: Initial and final configurations of the interaction of O_2 with Au and Al atoms (ΔE in eV)

$$Interaction\ Energy(IE) = -[E(Au_{n-1}Al-O_2) - E(Au_{n-1}Al)] - E(O_2)] \qquad \text{eq. 5.6}$$

5.3.2.2 Interaction of $AuAl$ with O_2

From our previous discussion it was concluded that $Al-Au$ forms partial ionic bond where Al transfers electronic charge to Au. Thus it is of interest when O_2 interacts with $Au-Al$ dimer, whether it approaches from Au side or Al side and how the interaction energy differs in comparison to their atomic species (Au or Al). Initial configurations generated keeping O_2 in different orientations with respect to $Al-Au$ were optimized. The result shows that when O_2 approaches towards Au, the interaction energy is very small and it remains in the molecular form (Figure 5.12). However, when O_2 approaches towards Al side, the $O-O$ bond dissociates. In this case, the interaction energy is estimated to be 1.85 eV. Similar atomic configuration was found to be stable when two pre-dissociated O atoms were allowed to react with $AuAl$ cluster. The $Al-O$ bond length is found to 1.73 Å and $\angle OAlO$ is found to be 84.2°. It should be noted that the interaction energy of Al with O_2 in $AuAl$ cluster has reduced in comparison to the interaction of the naked Al atom. This is attributed to the positive charge induced on the Al atom, which results in stabilizing the Al energy levels and reduced overlap (or reactivity) of the frontier orbitals of Al with O_2 molecule. This is further corroborated by the blue shift of the PDOS of Al atom in $AuAl-O_2$ cluster as compared to $AuAl$ dimer (Figure 5.11) indicating an increased positive charge on Al atom or in other words a charge transfer from the Al atom to the oxygen molecule leading to dissociation.

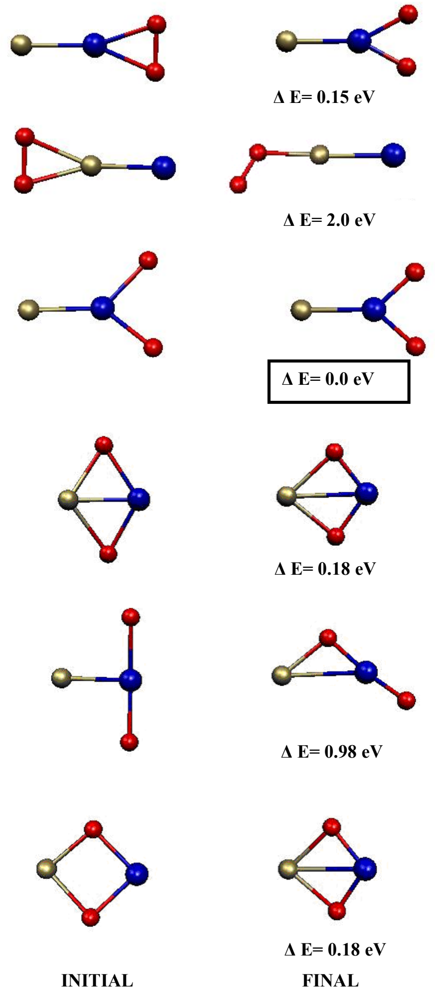

Figure 5.12: Initial and final configurations of the interaction of O_2 with the Au_2Al cluster.

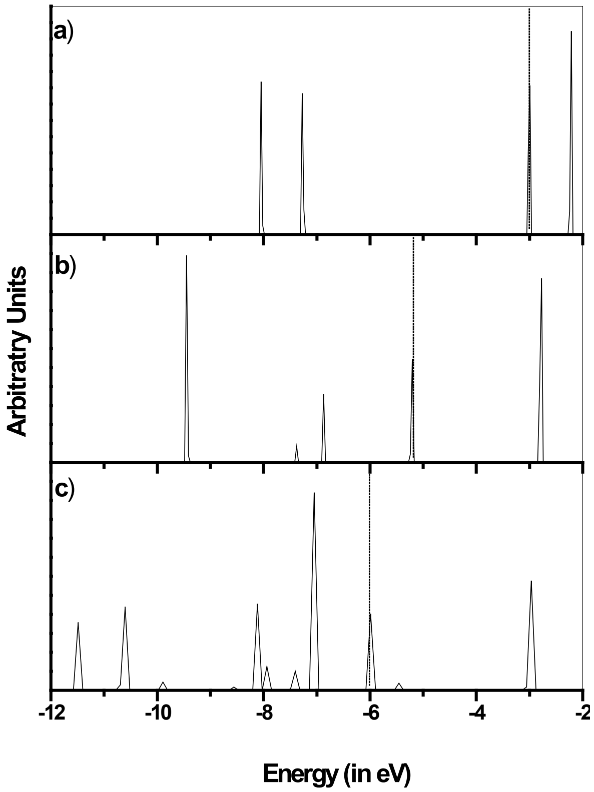

Figure 5.11: Comparison of the PDOS plot for Al atom in the (a) gas phase (b) $AuAl$ dimer, and (c) $AuAl$– O_2 complex.

It is known that spin conservation rule

plays an important role to control the reactions of oxygen in gas phase [478]. Recent works by Burgert *et al.* [479] and Chretien *et al.* [480] demonstrated this fact by studying the reactions of the oxygen molecule with the Al cluster anion and $Au/TiO_2(110)$ surface, respectively. In order to illustrate the importance of spin conservation in studying reactions involving oxygen, $AuAl$ dimer is used as a model cluster. The total energy and geometry optimizations were carried out by modifying the interatomic separation of the $O-O$ bond for their respective spin states as well as by fixing the total spin state of the product as shown below:

$$AuAl + O_2(singlet) \rightarrow AuAl\text{–}O_2(singlet) \qquad \Delta H = -1.73\ eV \qquad \text{eq. 5.7}$$

$$AuAl + O_2(triplet) \rightarrow AuAl\text{–}O_2(triplet) \qquad \Delta H = -1.85\ eV \qquad \text{eq. 5.8}$$

The results reveal that when singlet O_2 interacts with $AuAl$, the reaction does not favor bond dissociation. However, when triplet O_2 interacts with $AuAl$, the reaction undergoes $O-O$ bond dissociation. Moreover, from the total energy consideration, the stability of the triplet product is 0.51 eV more stable than the singlet.

5.3.2.3 Interaction of Au_3Al with O_2

Au_3Al cluster is found to be the most stable cluster with a high binding energy, large HOMO- LUMO gap (2.55 eV) and high interaction energy. From the comparison of EDOS Au_3Al and Au_4 clusters (Figure 5.7) it is observed that the frontier orbitals of Au_3Al are more stabilized compared to Au_4. Therefore, in order to understand the chemical reactivity of Au_3Al with O_2, molecular O_2 is allowed to interact with cluster approaching from different orientations in space and a few low-lying isomers are shown in Figure 5.13. It was observed that when molecular oxygen was allowed to interact with Au_3Al cluster through Au atoms, it does not interact with them. In order to understand the preferential mode of interaction between the molecular and atomic forms of O_2 with the Au atoms of Au_3Al, calculations were carried out with the $O - O$ bond elongated to the dissociation limit and oriented in the same molecular plane of the Au_3Al cluster. It was observed after the geometry optimization that molecular oxygen separates out of the cluster, which clearly reflects a reduced reactivity of the Au atoms. On the other hand when molecular oxygen approaches in a perpendicular direction to the basal plane of Au_3Al, O_2 dissociates and the dissociative adsorption is predicted to induce large relaxations in the gold part of the complex (Figure 5.13). The large structural relaxation involved stabilizes the $Au_3Al - O_2$ complex. The interaction energy is found to be 2.56 eV, which is higher compared to $AuAl$ cluster interaction energy with oxygen molecule.

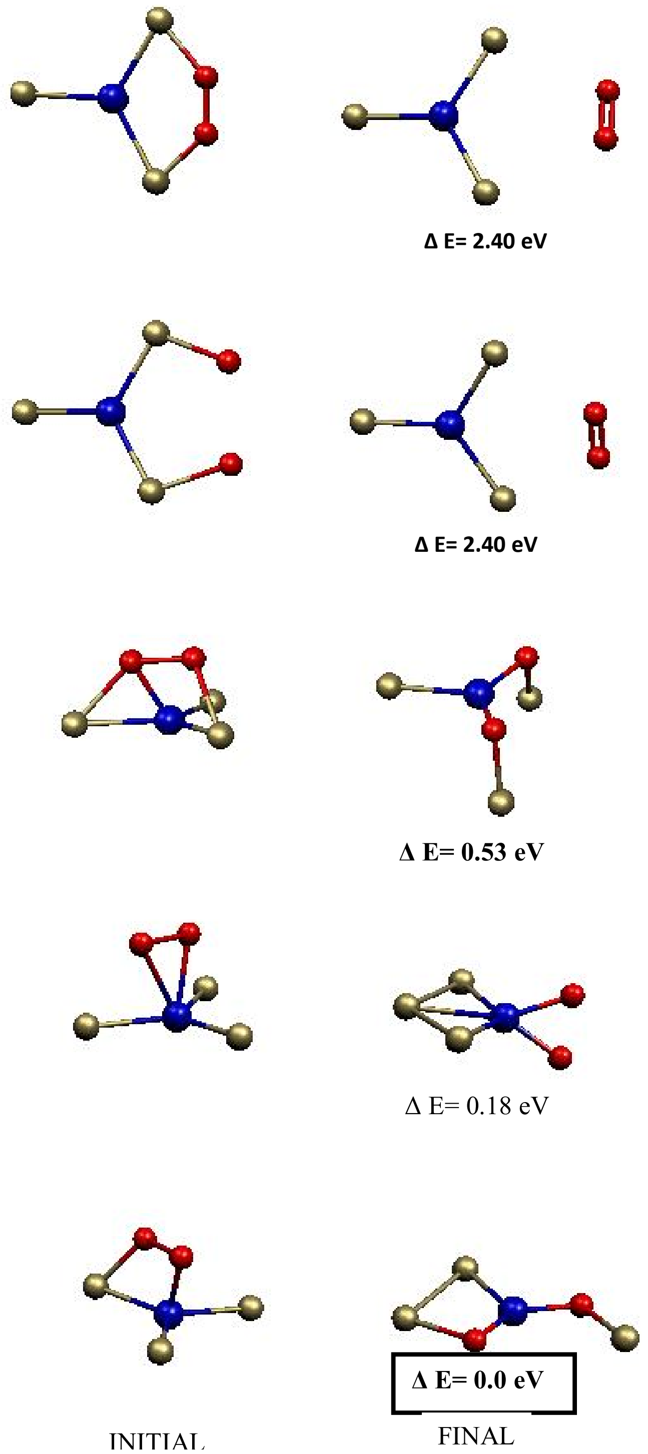

Figure 5.13:The initial and final configurations of the interaction of O_2 with Au_3Al cluster.

5.3.2.4 Interaction of $Au_{20}Al$ with O_2

Several orientations were tried to scan the possible modes of approach of the oxygen molecule to interact with $Au_{20}Al$ cluster. Basically, molecular O_2 and atomic oxygen species were allowed to interact with $Au_{20}Al$ and the final configurations are given in Figure 5.14. It was observed that when oxygen adsorbs on the Al atom as a molecule, it dissociates into its atomic form. The inter oxygen distances was estimated to increase to 1.50 Å. The $\angle OAlO$ angle was found to be 47.5°. Further it was observed that when the O_2 molecule approaches linearly to the Al atom, the $Au_{20}Al-O_2$ also relaxed into the same configuration. It was also found that when pre-dissociated O species were allowed to react with the cluster, with $\angle OAlO < 65^{\circ}$, the cluster relaxed into the same old configuration that was observed in the first two cases. However, for $\angle OAlO > 65^{\circ}$ (configuration 4, of Figure 5.14), the optimized geometry was totally different, where $\angle OAlO$ was estimated to be 143° and O atom is connected to both Al and Au. This configuration was found to be the lowest energy configuration with additional stabilization energy of 0.6 eV.

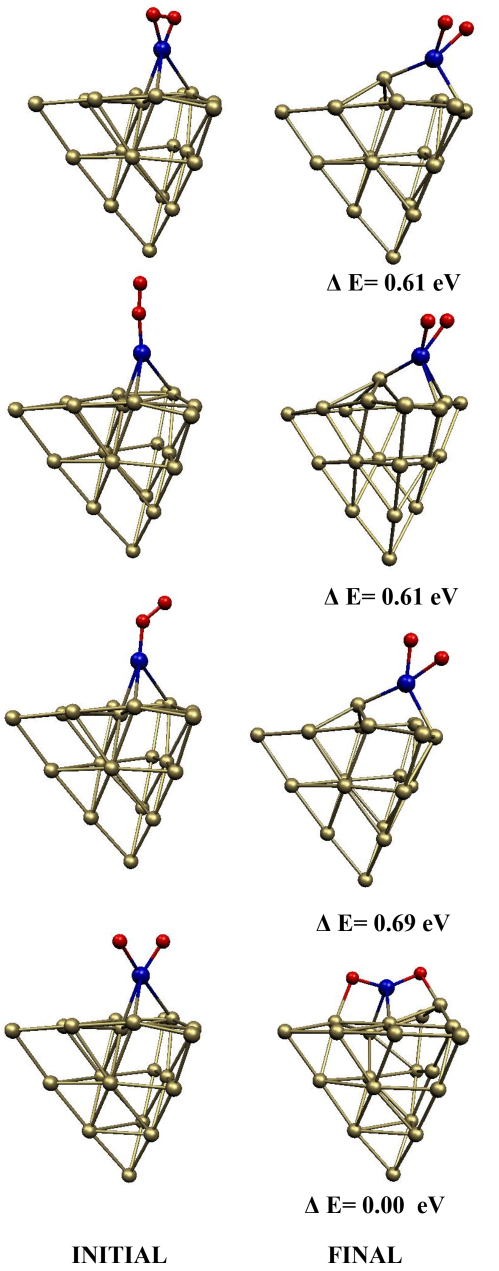

Figure 5.14: The initial and final configurations of the interaction of O_2 with $Au_{20}Al$ cluster.

5.4 Conclusions

In this section several geometrical isomers of Al doped Au clusters ($Au_{n-1}Al$ clusters, $n=2-7$ and 21 are presented and the oxidation reaction of few stable clusters is performed. The stability of these clusters is analyzed based on their binding energy, second order difference in energy, energy gap between the HOMO and LUMO energy levels. For small clusters, it is found that Au_3Al and Au_5Al clusters are more stable than their neighbors.

The reason for such higher stability is attributed to their specific electronic structures related to the planar resonance stabilization and electron shell filling effect for Au_3Al and Au_5Al clusters, respectively. The electron charge density analysis of these clusters suggests that Al atom transfers electronic charges towards Au, resulting in higher electronic charge on the Au atoms. This is corroborated by the shift of energy levels to less negative values or in other words imparts activity in its electronic level diagram. The fundamentally important interaction of oxygen carried out on most stable Al doped Au clusters, suggests that oxygen prefers to bind at the Al site to Au and the adsorption of oxygen favors dissociative chemisorptions mechanism. However, the interaction energy of O_2 with $Au_{n-1}Al$ clusters is smaller in comparison to the interaction of the naked Al atom and is attributed to the reduced positive charge on the Al in $Au_{n-1}Al$ clusters.

B. CO Oxidation on $Au - Al$ nano composites

Besides doping of gold clusters, gold alloy clusters have also attracted attention owing to their tunable properties [469,470]. More recently, it has been shown that in case of small Au doped clusters the electrostatic effects play as an alternative to charge transfer in promoting the catalytic activity of Au clusters and also alloying can improve the catalyst stability [460]. The structural optimization of bimetallic $Pd - Au$ nanoclusters showed that Au atoms prefer to segregate on the surface and thus forms Pd_core Au_shell ordering [481]. Recently, Ramachandran *et al.* [482] reported the structure and properties of mixed carbon-gold clusters. The effect of alloying on the optical properties of $Ag-Au$ nanoclusters was reported by Barcaro and co-workers [483]. Results from a large number of experimental and theoretical studies, both in gas phase and on support have suggested that negatively charged Au atoms are particularly more sensitive for CO oxidation reaction. Therefore, one of the most important criteria of Au clusters to be more reactive is to have additional electronic charge to donate. To create a similar situation in a neutral cluster would be to form a bimetallic cluster of gold where the other element is electro-positive. In our previous section, we have shown that Au binds with Al through ionic bonds, where Al donates electronic charge to Au. Motivated by these studies, $AlAu$ bimetallic clusters (Al_6Au_8, $Al_{13}Au_{42}$) are used as model systems to study the CO oxidation behavior. The studies are further extended for a periodic substrate by replacing the subsurface layer of $Au(111)$ surface by Al atoms.

This section is organized as: (*i*) Computational details and validation of the DFT calculations by comparing the results of bulk Au, clean $Au(111)$ surfaces with experimental and previous studies (*ii*) Results on the geometry and stability of the clusters Al_6Au_8, $Al_{13}Au_{42}$ clusters, and $Au(111)-Al$ surface (*iii*) Interaction of molecular O_2 with these nanocomposites and (iv) CO oxidation studies by E-R and L-H mechanisms.

5.5 Computational Details

The details of the computational set up are as discussed under section 5.2. In order to establish the accuracy of the present method calculations of bulk Au and the clean surface were performed. The calculated lattice constant of bulk gold is 4.17 Å and the corresponding experimental value is 4.08 Å [257]. Thus, the DFT-GGA result slightly overestimates the lattice parameter but agrees well with previous DFT-GGA results, where value of 4.19 Å is reported [484]. The theoretical DFT-GGA cohesive energy of Au is 3.6 eV/atom and the experimental result is 3.81 eV/atom [257].

For the surface calculation, the $Au(111)$ surface was modeled by seven-layer slab and a large vacuum distance of 10 Å separates the slabs. Calculations were done on $Au(111)$ surface using 3×3 surface unit cells (each layer contains 9 Au atoms) and $7 \times 7 \times 1$ k-point mesh. Structural analysis on the interlayer separations revealed that that the top inter-layer distance increased by 1.55%, and the second inter-layer distance decreased by 0.72% which are consistent with previous DFT studies [485]. The surface energy is estimated as 1.21 J/m^2, which is below the experimental value of 1.51 J/m^2 [486,487].

5.6 Results and Discussion

5.6.1 $Al-Au$ nano-composites (Al_6Au_8, $Al_{13}Au_{42}$ and $Au(111)-Al$)

5.6.1.1 Geometries of $Al-Au$ nano-composites

The lowest energy isomer of the Al_6Au_8 cluster forms an empty cage structure by inter-connecting Al and Au atoms as shown in Figure 5.15. Moreover, it is seen that an elongated cage is energetically more favorable by 0.12 eV than spherical cage. The elongated isomer can be viewed as layer structure where Al and Au tetramers are stacked alternately, which can otherwise be described as a double icosahedron. From the ground state geometry of the Al_6Au_8 cluster it is observed that the two axial Al atoms are elongated from the basal plane (Jahn-Teller distortion or elongation forced by Au). The formation energy of Al_6Au_8 is found to be highly exothermic, suggesting high stability of this bimetallic cluster. The average binding energy is found to be 2.73 eV/atom and the high stability of the bimetallic Al_6Au_8 cluster is attributed to the stronger $Au-Al$ bond (1.83 eV/atom) as compared to $Au-Au$ (1.17 eV/atom) and $Al-Al$ (0.70 eV/atom) bond strengths. Based on the spin-polarized calculations, the energy gap between the HOMO and LUMO energy levels of the Al_6Au_8 cluster is estimated to be 1.12 eV.

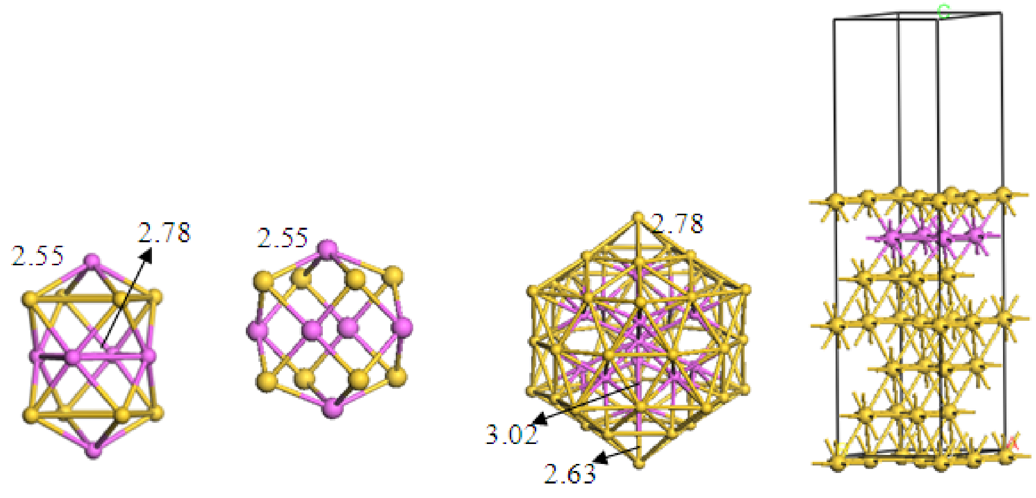

Al_6Au_8-1

Al_6Au_8-2
$\Delta E = 0.12$ eV

$Al_{13}Au_{42}$

Au (111)-Al

Figure 5.15: Ground state geometries of atomic structures of Al_6Au_8, $Al_{13}Au_{42}$ and $Au(111)-Al$ slab. Representative bond lengths (in Å) have been shown in the figure.

Earlier studies have shown that Al_{13} cluster forms an icosahedral structure [488]. Based on the structural motif of the Al_6Au_8 cluster, Al_{13} icosahedron is wrapped by 42 Au atoms to model $Al_{13}Au_{42}$. In this context, it needs to be mentioned that six gold atoms form each triangular face of the fifty five-atom icosahedron, similar structure of the isolated Au_6 cluster. The ionic optimization of the $Al_{13}Au_{42}$ cluster was carried out without any symmetry constraint. The $Au-Au$ bond length on the surface is observed to be 2.90 Å, which is longer than the surface $Au-Au$ bonds of Au_{55} (2.85 Å). The longer $Au-Au$ bond length in presence of Al atoms is due to negatively charged surface atoms. In this context it can be mentioned that for nanoalloy clusters, where the constituents are bound by covalent bonds, the atomic size of the elements plays an important role to decide the intra-layer and inter-layer distances [489]. The average binding energy is calculated to be 2.84 eV/atom which is higher compared to Au_{55} (2.53 eV/atom), Al_{13} (2.33 eV/atom) and Al_{55} (2.66 eV/atom) clusters. Vibrational analysis of lowest energy isomers has established them as stationary points on their respective PES.

As a third model of the $Al-Au$ nanocomposite, a periodic $Au(111)$ slab, where the second layer of Au atoms was replaced by Al atoms as in Figure 5.15 was used. In order to obtain the equilibrium geometry of this slab, ionic relaxation was carried out on all the atoms in the slab. Based on the optimized parameters it is seen that the interlayer separation between the top and second layer (Al layer) is compressed by 7.9% and between second and third layer is compressed by 8.1%. However, the interlayer separation between the third layer and fourth layer is found to relax outwardly by 7%.

5.6.1.2 Electronic Properties of $Au-Al$ nano-composites

To understand the nature of chemical interaction in these systems the EDOS of $Al_6Au_8$and $Al_{13}Au_{42}$ clusters are compared by broadening the electronic energy levels with gaussian function (Figure 5.16). In case of $Al-Au$ dimer, the HOMO level is red shifted

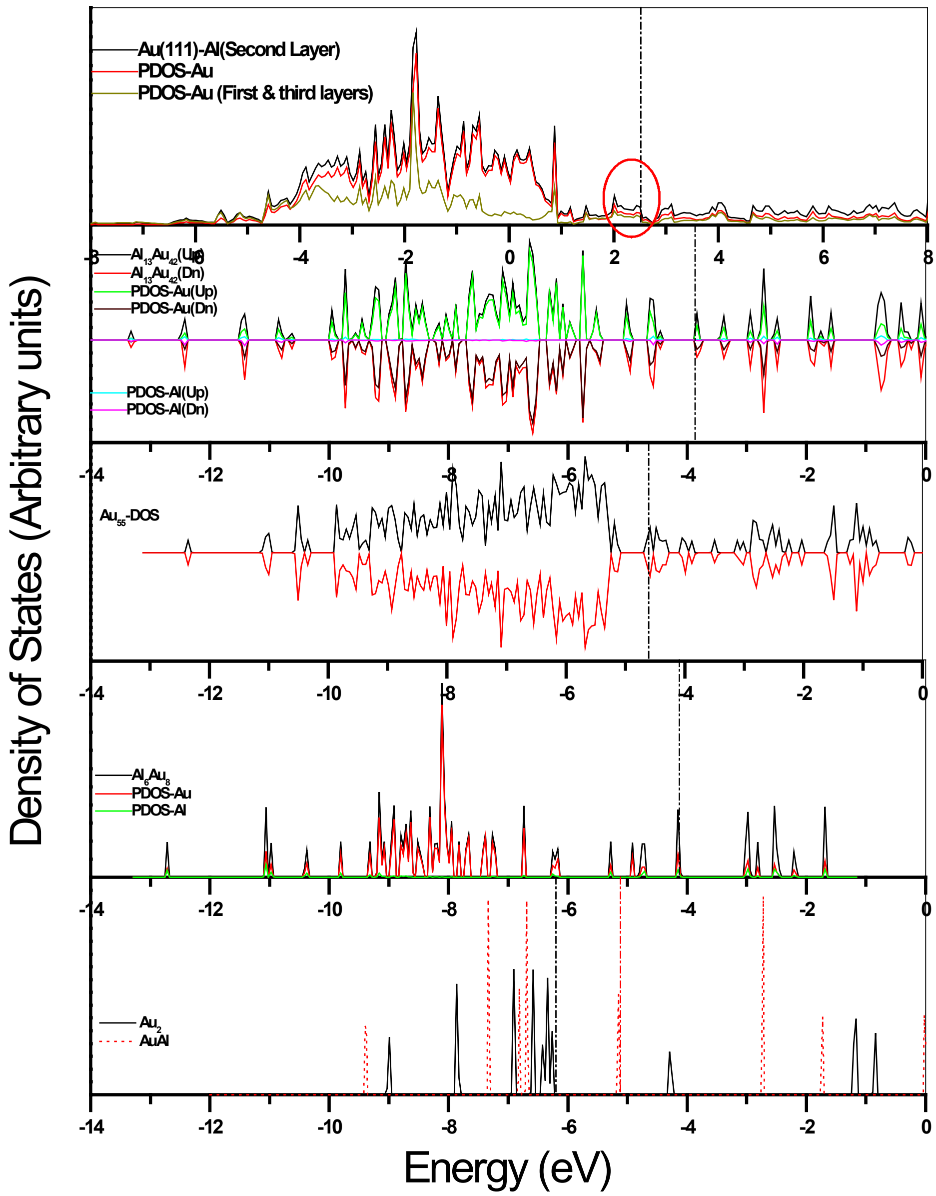

Figure 5.16: The plot of PDOS of Au_2, $AuAl$ and Al_6Au_8 and $Al_{13}Au_{42}$ clusters along with Au_{55} for comparison.

than Au_2 dimer. This is due to the electronic charge transfer from Al to Au, suggesting ionic bond character between Au and Al atoms. The HOMO energy level of $Al_{13}Au_{42}$ clusters is also red shifted compared to HOMO of Au_{55} cluster. From the projected DOS spectrum it is further noticed that the HOMO energy levels are primarily comprised by the atomic orbitals of Au atoms. Thus, the red shift in the HOMO energy levels of $Al - Au$ bimetallic clusters suggest enhanced chemical reactivity of these systems. To further understand the charge transfer in these systems, the charge density difference $(\rho[Al_m@Au_n]- \rho[Au_m]- \rho[Al_n])$ is plotted. Figure 5.17 shows the isosurfaces of the electronic charge density difference of the mixed clusters ((a)Al_6Au_8 and (b) $Al_{13}Au_{42}$) and it is clear that there is significant charge transfer from Al to Au atoms and this leads to charge accumulation on the surface of these clusters. Further, the difference in the electronic charge densities of $Au(111) - Al$ slab and the sum of the charge densities of $Au(111)$ and the Al layer keeping the same positions as in the mixed bulk [$\rho[Au(111) - Al]$- $\rho[Au(111)]$- $\rho[Al]$] is calculated, in order to understand the role of the Al layer. In general, the Au atoms are seen to be enriched with more charge as shown in Figure 5.17c and specifically, the Au atoms in the first and the third layer have gained extra charge. This excess charge distribution on the surface makes the surface more reactive.

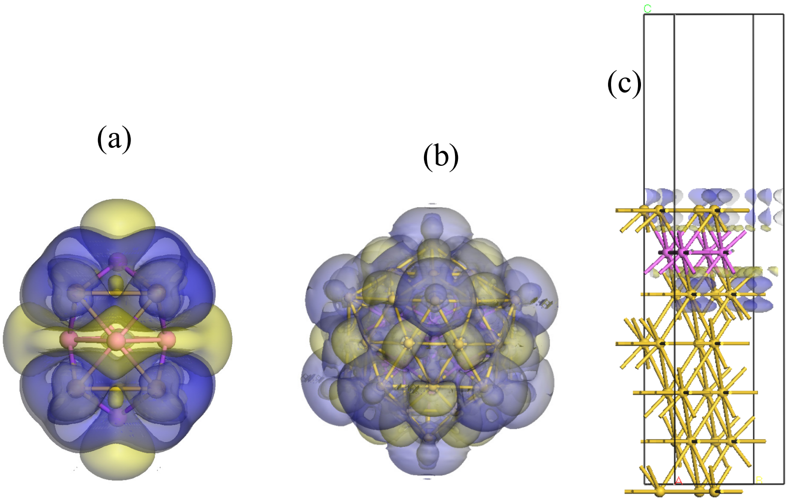

Figure 5.17: Isosurfaces of the charge density difference of the mixed clusters [(a) Al_6Au_8 and (b) $Al_{13}Au_{42}$ and (c)$Au(111) - Al$ slab] Blue and yellow colours represent charge accumulation and depletion respectively.

5.6.2 Interaction of O_2 with $Au - Al$ nano-composites

One of the most important uses of these nano-composite materials is their potential in the field of heterogeneous catalysis. To verify this aspect the CO oxidation study on this $Al - Au$ system is carried out. The objective is to underscore the role of charge transfer (from inner Al to the outer Au atoms) on the efficiency of the oxidation process. For CO oxidation, the activation of the $O - O$ bond is the most important step, which depends on the extent of charge transfer from the clusters to the anti-bonding orbital of O_2 molecule. For this purpose initial investigations were carried out on the interaction of oxygen with these modeled systems. From the test calculations on the simple dimers, the binding energy of $Au - O$ and $Al - O$ is estimated to be 1.15 eV/atom and 2.53 eV/atom respectively which are in good agreement with the experimental values of 1.15 eV/atom and 2.59 eV/atom [477]. The bond lengths are found to be 2.15 Å and 1.61 Å which are also consistent with the experimental values of 2.3 Å and 1.61 Å and, respectively [477]. Similarly for CO, the bond length and the binding energy are estimated to be 1.15 Å and 5.89 eV/atom, whose corresponding experimental values are found to be 1.15 Å and 5.57 eV/atom [477].

Several orientations of O_2 molecule were tried to scan the possible modes of interaction with Al_6Au_8, $Al_{13}Au_{42}$ clusters and on the surface of $Au(111) - Al$. The lowest energy isomers are shown in Figure 5.18. It was observed that O_2 molecule adsorbs in molecular form on one of the triangular faces (formed by $AuAuAl$) of the Al_6Au_8 cluster. The $O - O$ bond distance is elongated to 1.40 Å which is of the tune of $O - O$ bond length in peroxides (*e.g.*, $O - O$ bond length in H_2O_2 is 1.47 Å). The triangular face is a highly active

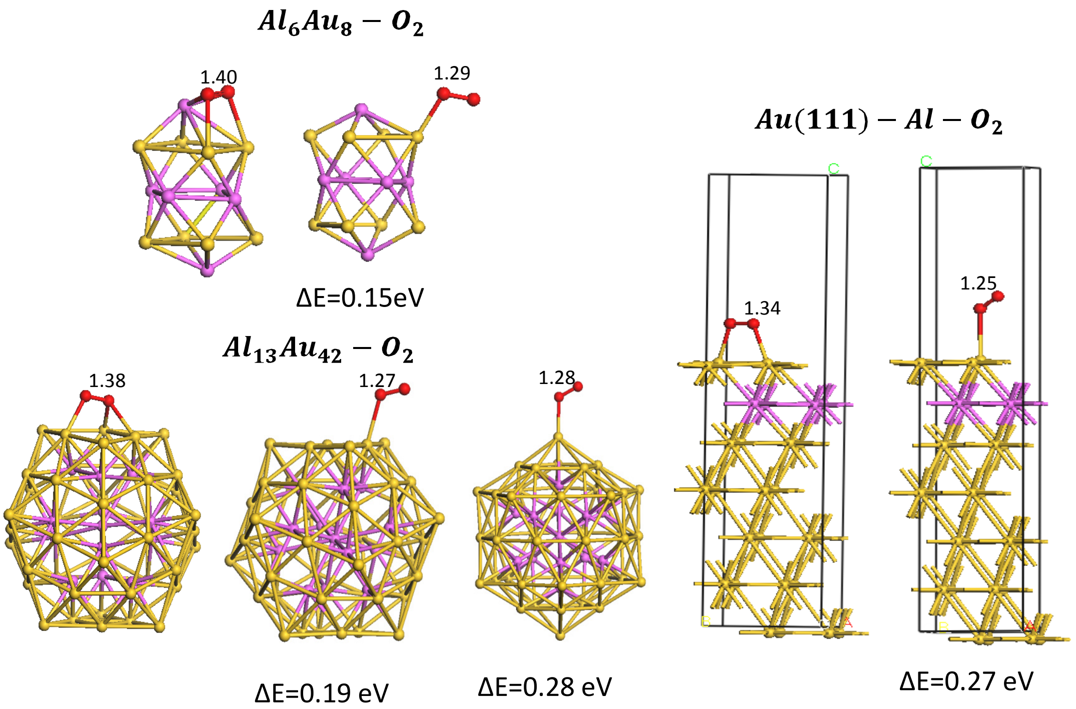

Figure 5.18: Ground state geometries of $Al_6Au_8 - O_2$, $Al_{13}Au_{42} - O_2$ and $[Au(111) - Al] - O_2$.The $O - O$ distances are given in Å.

surface with the Au atoms having a partial negative charge, resulting in a charge transfer from the face to the anti bonding orbital of O_2. This results in the bond elongation or in other words weakening of the $O-O$ bond. Further, it is observed that the interaction of O_2 molecule with a vertex Au atom results in the $O-O$ bond elongation up to 1.29 Å, but this configuration is higher in energy (0.15 eV) than the lowest energy conformer. In case of $Al_{13}Au_{42}$, a few important configurations: O_2 interaction with vertex Au, Au atom on the edge, on top of Au on the face, $Au-Au$ bridge and parallel configurations on the triangular face (similar to Au_6) were tried. In all cases the $O-O$ bond elongation is observed. Moreover, it is observed that O_2 prefers to orient parallel to icosahedron face to form the most stable complex. The $O-O$ bond is elongated up to 1.38 Å, signature of an activated state of O_2 molecule, which can get easily ruptured for oxidation reactions. This is attributed to the charge transfer from the exterior Au atoms, which gain charge from the inner Al atoms, to the anti-bonding orbitals of O_2 molecule.

For oxygen adsorption on the surface, different sites, which included the top, hcp- and fcc- hollow sites, which are threefold-coordinated sites directly above the second- and third-layer atoms, respectively were considered. Molecular O_2 interaction parallel to the $Au(111)$ surface was found to be the energetically most favourable mode of adsorption, with adsorption energy of 0.16 eV. However, previous calculations have shown that the O_2 interacts very weakly with the clean $Au(111)$ surface [485]. This shows that the Al layer makes the Au surface chemically active. The $O-O$ bond elongates to 1.34 Å. Further, on top adsorption of molecular O_2 on Au atom is 0.27 eV higher in energy and results in $O-O$ bond elongation (1.25 Å).

5.6.3 CO-Oxidation over $Au-Al$ nano-composites

After establishing the fact that, $Al-Au$ nano-composites are able to bind the O_2 molecule and weaken the $O-O$ bond, it is envisaged that these systems can be utilized for

CO oxidation. The oxidation of the CO molecule occurs either by (i) Eley-Rideal (ER) or (ii) Langmuir-Hinshelwood (LH) mechanism. To test the ER mechanism, several configurations where the CO molecule was allowed to approach the O_2 bound complexes in different directions were optimized. In all these configurations the CO molecule was placed at least 3.0 Å away from complex so that an unbiased geometry optimization could be performed. On the basis of the results it is found that when CO reacts with $O_2 - Al_6Au_8$ complex, CO_2 molecule forms spontaneously without any reaction barrier. Consequently, a large enthalpy of formation is estimated (eq. 5.9). The other O atom relaxed to bind on the bridge site of $Au - Al$ bond. However, subsequent approach of the second CO molecule

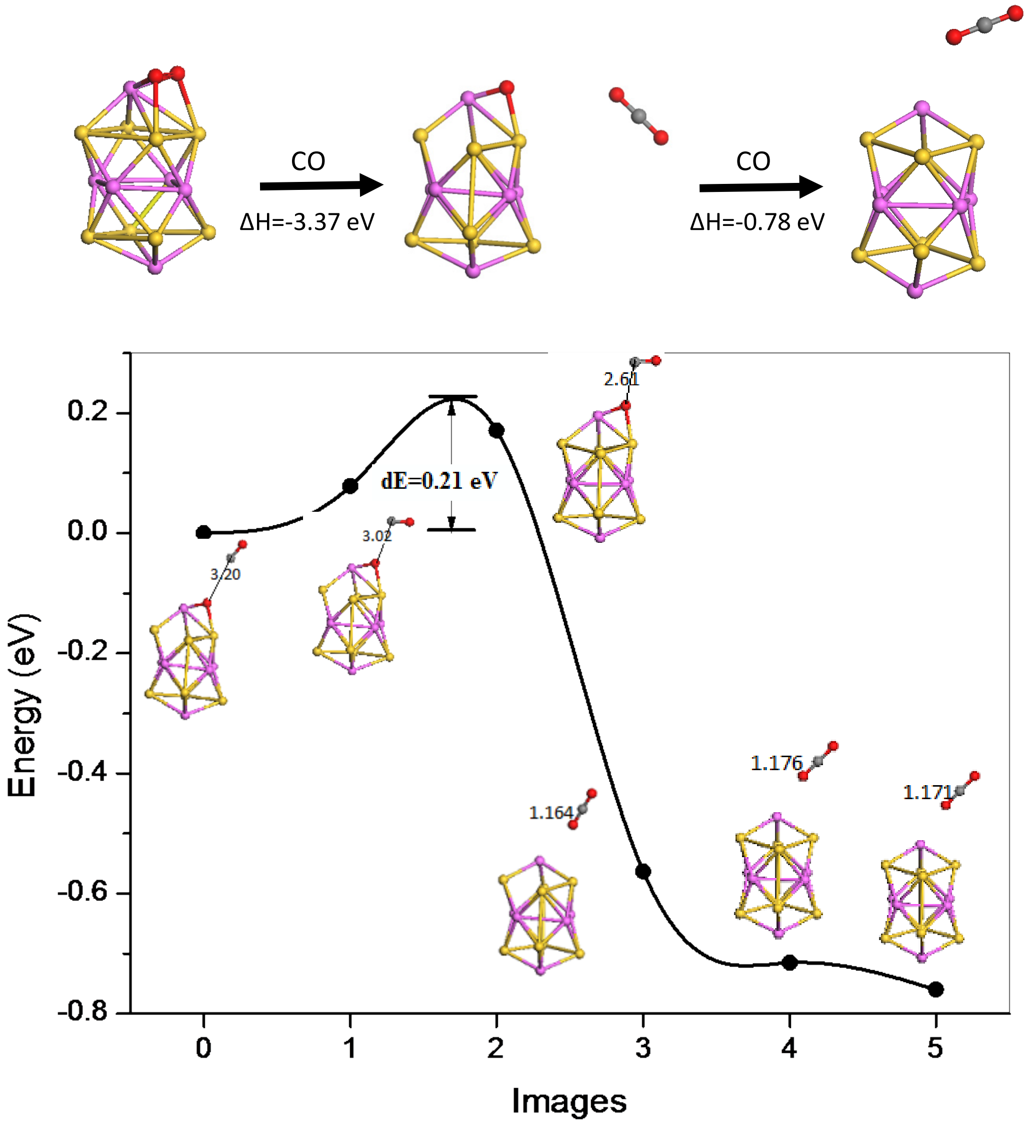

Figure 5.19: (a) CO oxidation reaction on $Al_6Au_8 - O_2$ cluster by E-R mechanism. (b) minimum energy path for the evolution of the second CO_2 molecule from Al_6Au_8O. (Distances in Å)

doesn't lead to spontaneous CO_2 evolution. This is because of the tightly bound oxygen on the Al_6Au_8 cluster surface. Thus it is expected that the second CO_2 formation might take place only by crossing an activation barrier. To verify this, the nudge elastic band (NEB) [303,304] method is employed to calculate the activation energy. Four images between the reactant and product states were generated. The minimum energy path of this process is shown in Figure 5.19. The energy barrier is calculated to be 0.21 eV for the formation of a second CO_2 molecule.

$$Al_6Au_8 - O_2 + CO \rightarrow Al_6Au_8 - O + CO_2 \qquad \Delta H = -3.37 eV \qquad \text{eq. 5.9}$$

$$Al_6Au_8 - O + CO \rightarrow Al_6Au_8 + CO_2 \qquad \Delta H = -0.78 eV \qquad \text{eq. 5.10}$$

In contrast to the case of Al_6Au_8, both the CO oxidation steps occurred spontaneously for $Al_{13}Au_{42} - O_2$ complex. Initially, when CO approached the bound O_2 whose bond is considerably weakened ($O \xrightarrow{1.38Å} O$); a spontaneous rupturing of the $O - O$ bond took place to form CO_2(Figure 5.20). The enthalpy of the reaction is found to be -3.14 eV (eq. 5.11). The remaining oxygen atom relaxed on the bridge site of $Au - Au$ bond with $Au - O$ distance of 2.20 Å. This is slightly elongated as compared to the $Au - O$ dimer. Further interaction of the second CO molecule, brought in the vicinity of the bound O atom, is spontaneous too and exothermic (ΔH = -3.20 eV) (eq. 5.12).

$$Al_{13}Au_{42} - O_2 + CO \rightarrow Al_{13}Au_{42} - O + CO_2 \qquad \Delta H = -3.14 eV \qquad \text{eq. 5.11}$$

$$Al_{13}Au_{42} - O + CO \rightarrow Al_{13}Au_{42} + CO_2 \qquad \Delta H = -3.20 eV \qquad \text{eq. 5.12}$$

The contrasting thermodynamic behavior can be attributed to the stronger $Al - O$ bond formation in $Al_6Au_8 - O$ complex, which does not allow spontaneous second CO oxidation. As discussed earlier, O_2 adsorbs on the $Au(111) - Al$ surface with an elongated $O - O$ bond ($O \xrightarrow{1.34Å} O$). This activation of the $O - O$ bond contributes to overcome the activation barrier to participate in the oxidation of CO spontaneously. The other oxygen atom

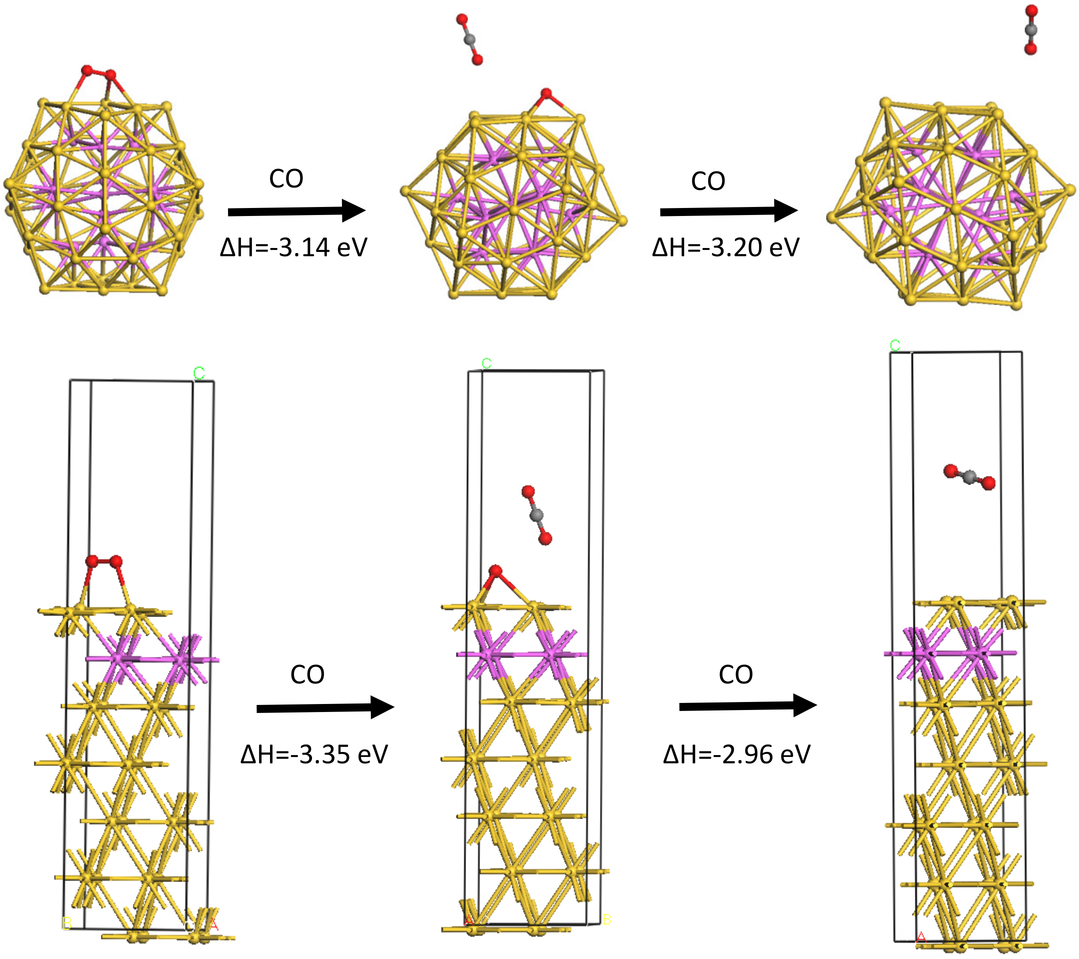

Figure 5.20 Reaction steps of CO oxidation on $Al_{13}Au_{42}-O_2$ and $Au(111)-Al-O_2$ by E-R mechanism.

reorganizes itself to stay on the bridge site of the surface $Au-Au$ bond with $Au-O$ distance of 2.24 Å. Followed by this, the second CO oxidation is also found to be spontaneous with evolution of large heat energy.

$$Au(111)-Al-O_2+CO \rightarrow Au(111)-Al-O+CO_2\ \Delta H=-3.35\,eV \qquad \text{eq. 5.13}$$

$$Au\,(111)-Al-O+CO \rightarrow Au\,(111)-Al+CO_2\quad \Delta H=-2.96eV \qquad \text{eq. 5.14}$$

For LH mechanism, the reacting species are co-adsorbed on the substrate before undergoing the reaction. This involves formation of an intermediate complex and desorption of the CO_2 molecule. In order to obtain the minimum energy path of CO oxidation, a constrained search for intermediate states has been identified by decreasing the distance between C of CO molecule and O of the O_2 molecule until a maximum in the energy is found at a particular $C-O$ inter-atomic distance. In order to investigate the LH mechanism, CO and

O_2 molecules are co-adsorbed on the $Au-Al$ nano-composites. In case of Al_6Au_8 cluster, it is observed that CO adsorbs adjacent to the O_2 binding site on the $Au-Al$ bond as shown in Figure 5.21. While the positive C atom of CO binds to the negative Au atom, the negative O binds to the positive Al atom. The $C-O$ bond length is stretched to 1.21 Å. Few other configurations by placing the CO molecule around the O_2 binding site results in the spontaneous elimination of CO_2. Thus under both ER and LR mechanisms, the CO oxidation on the Al_6Au_8 cluster occurs spontaneously. In this context it is of importance to note that for Al_6Au_8 cluster, all atoms reside on the surface. But the situation is different for $Al_{13}Au_{42}$ cluster, where Al atoms are not exposed to the surface and therefore, have no chance to interact with O_2 or CO molecules directly. For this reason, it is expected that the CO oxidation on the $Al_{13}Au_{42}$ cluster will give stable intermediates under L-H mechanism.

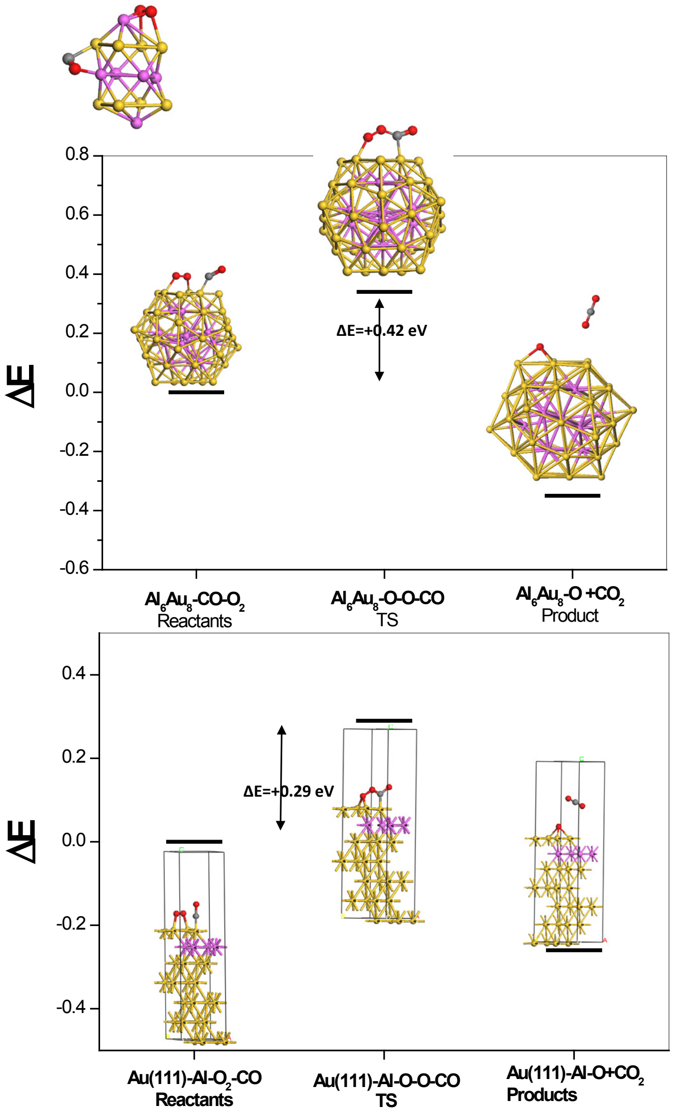

Figure 5.21: Schematic representation of the CO oxidation on $Al-Au$ nanocomposites through L-H mechanism

In order to study the LH mechanism over $Al_{13}Au_{42}$ cluster, preliminary studies were carried out to compare the CO adsorption behavior over Au_{55}, and $Al_{13}Au_{42}$ clusters. The objective is twofold: (*i*) to ascertain the surface charge effect and (*ii*) the influence of O_2 during co-adsorption. In case of Au_{55}, it is found that the CO preferred to adsorb on the low coordinated site with a binding energy of 1.65 eV. The $Au-C$ and $C-O$ bond lengths were found to be 2.12 Å and 1.18 Å, respectively. The most preferred configuration of interaction of CO with $Al_{13}Au_{42}$ and Au_{55} is found to be similar. However, the binding strength is weaker by 0.45 eV. The weaker binding between CO and $Al_{13}Au_{42}$ is attributed to the extra negative charge on the cluster surface, which weakens the $Au-CO$ bond, as opposed to pure Au_{55} cluster. During the co-adsorption of CO and O_2 on $Al_{13}Au_{42}$, CO is found to adsorb on the Au atom adjacent to the binding site of O_2 (Figure 5.21). The results reveal that the presence of O_2 improves the binding strength of CO with $Al_{13}Au_{42}$ cluster by 0.27 eV. The bound O_2 withdraws a partial negative charge from the adjacent Au atom facilitating an improved CO binding. The search for the intermediate state by the constrained path search method, has lead to a carbonate like intermediate, as shown in Figure 5.21 with $C-O$ and $O-O$ bond lengths of 1.31 Å, and 1.38 Å, respectively. From the total energy analysis, it is found that the formation of the carbonate like intermediate species requires an activation barrier ($\Delta H^{\dagger}$) of 0.42 eV.

$$Al_{13}Au_{42}-O_2+CO\xrightarrow{\Delta H^{\dagger}=+0.42eV}Al_{13}Au_{42}-O-O-CO\rightarrow Al_{13}Au_{42}-O\ +CO_2 \qquad \text{eq. 5.15}$$

For CO oxidation on the Al substituted $Au(111)$ surface through LH mechanism, CO and O_2 molecules were co-adsorbed on the surface, and the most preferred configuration is shown in Figure 5.21. Like in case of $Al_{13}Au_{42}$, CO adsorption behavior is investigated on both clean $Au(111)$, and Al substituted $Au(111)$ surfaces. Based on the total energy of the optimized structures, the binding strength of CO on $Au(111)$ and Al substituted $Au(111)$ surfaces is found to 1.31 eV and 0.92 eV, respectively. For the case when both CO and O_2 are co-adsorbed on the Al substituted $Au(111)$ surface, it is seen that the CO prefers to bind with Au, which is adjacent to the O_2 binding site. The improved binding strength of CO on the $Au(111)-Al$ surface (1.19 eV), is due to redistribution of charge on the adjacent Au atoms near O_2 binding site. The CO_2 evolution over the $Au(111)-Al$ surface is found to go through carbonate like intermediate formation as found in the previous case. The $O-O$ bond of the carbonate species is elongated (~1.44 Å) with the C and terminal O atoms bound with two Au atoms on the surface. This intermediate species is 0.29 eV higher in energy than the initial geometry of the co-adsorbed state. This energy barrier for CO oxidation is lower than that has been found over $Al_{13}Au_{42}$ cluster.

$$Au(111)-Al-O_2 \xrightarrow{\Delta H^{\dagger}=+0.29eV} Au\,(111)-Al-O-O-CO \rightarrow Au(111)-Al-O+\ CO_2 \qquad \text{eq. 5.16}$$

Based on the above results it is inferred that in general, the LH mechanism proceeds *via* an intermediate species (CO_3^-) with a high transition barrier. Thus in the present case, where $Al-Au$ nano-composite is a support with surface negative charge, the ER mechanism could be favorable over the LH pathway.

5.7 Conclusions

In this section the DFT based investigation of CO oxidation with $Au-Al$ nano alloys is presented. The results are summarized as follows: When Au atoms are mixed with small Al clusters (Al_6), it forms a hollow cage nano-alloy cluster. When Au atoms are mixed with mid-sized Al clusters like Al_{13}, it forms a core-shell nano-cluster. In both cases, there is a significant charge transfer from the Al atoms to the Au atoms, thereby making Au atoms chemically more reactive. To prove the above conjecture, CO oxidation on these $Al-Au$ nano-composites by following both ER and LH mechanism is carried out. Similar reaction is carried out on a model $Au(111)$ surface, where the second Au layer is replaced by Al atoms. Finally, on the basis of these results it is inferred that a nano-composite material of $Al-Au$ is more effective for oxidative catalysis.

6. Stability and Growth of Supported Au_n clusters on Alumina

6.1 Introduction

Oxide supported precious metal clusters have recently gained considerable attention as low temperature oxidation catalyst, a significant step in chemical industry [490-496]. In this context, a systematic investigation of an interface between atomic clusters and oxide support is important to illustrate a variety of interface phenomena that influence the structure and property of the adsorbed clusters. During past decade a large number of experimental and computational studies have been carried out in this field and the results showed significant change in the electronic and geometric structure of the adsorbed clusters, which are responsible for tuning the charge state and subsequently their chemical activity [180,407,459,472,497-505]. In particular, $\alpha - Al_2O_3(0001)$ surface has received a significant importance with a view that it serves as a prototype oxide surface.

First principles calculations were reported on the adsorption behavior of late transition metal atoms on regular Al-terminated and hydroxylated $\alpha - Al_2O_3(0001)$ surfaces [506-517]. These studies have primarily focused to identify the most favorable adsorption site of the alumina surface and the binding strength. The results suggest that in general metal atoms favor to bind with one of the surface Al atoms. Hernandez and co-workers have observed that Ag and Au atoms bind very weakly on the alumina surface [508]. Molecular dynamics simulations have revealed the preferential 3D structures of deposited Pd_n clusters over the $\alpha - Al_2O_3(0001)$ surface [518]. Gomes *et al.* [519] have carried out theoretical studies on the interaction of small Pd_n clusters with the relaxed Al-terminated $\alpha - Al_2O_3(0001)$ surface. Zhou *et al.* [520] have reported the interaction of small Pt_n clusters with $\alpha - Al_2O_3(0001)$ surface. Recently, Nigam *et al.* have reported the structural and electronic properties of Ag_n and Pd_n clusters on alumina surface [521,522]. It was observed that small Ag_n and Pd_n clusters get adsorbed with a puckered configuration, with alternate Ag/Pd

atoms up and down, and the distortion in the gas phase geometry after deposition was more for palladium clusters.

As discussed in the previous chapter, the high catalytic activity of metal oxide supported gold nanoparticles towards low temperature CO oxidation reported by Haruta *et al.* [395-399] led to a large number of experimental and theoretical studies on isolated gas-phase clusters as well as on supported clusters in ultra-high vacuum and industry-like catalytic conditions [188,401-406]. Theoretical studies reported on the deposited gold clusters are mainly confined to rutile TiO_2 and MgO surfaces [180,181,523,524]. It was noted that Au_n clusters supported on metal supported thin MgO film bear partial negative charge [190,525-527]. DFT studies carried out Frondelius *et al.* [528,529] have revealed that of Au_n clusters deposited on $MgO(0001)$ surface and on an ultrathin $MgO(0001)$ film supported by Mo metal, become singly charged cluster anions. Moreover, it was also reported that while upright adsoption configuration is favored over a clean MgO surface, a flat configuration of Au cluster parallel to the MgO surface became more favorable by creating O vacancy defect or by forming an ultra-thin MgO film over a metal substrate. The objective of the surface modulation is to create electron rich surface, which can easily transfer electronic charge to the adsorbed Au atoms, and thereby change its electronic and geometrical structure and chemical properties.

In contrast to the clean MgO surface, which is a model system for smooth surface, a regular $\alpha - Al_2O_3(0001)$ surface is rough as Al and O atoms are not co-planar. Studies on the structure of small gold clusters deposited over Al_2O_3 surface by Nasluzov *et al.* [530] using a embedded cluster approach have showed that small gold clusters favor planar configurations oriented parallel to the surface. The cluster model approach has its own limitations, due to the absence of periodic boundary conditions. Therefore, it is of interest to investigate the geometries of Au_n clusters on the periodic $Al_2O_3(0001)$ surface. The basic step to understand the catalysis of CO oxidation over the Au_n clusters deposited over alumina surface is to comprehend the interaction of O_2 with these clusters on a support. In the present work, a systematic study on the structural and electronic properties of Au_n $(n = 1 - 7, 10)$ clusters on $\alpha - Al_2O_3(0001)$ surface is presented. The objective of this study is to underscore two important issues; (i) whether the ground state geometries of isolated Au_n clusters retain their identity over alumina support? (ii) What is the mode of oxygen interaction with deposited Au_n cluster, a molecular adsorption or dissociative chemisorption?

6.2 Computational details

All the calculations were performed using plane wave based pseudo-potential approach as implemented in VASP [274-278]. The electron–ion interaction was described by the full-potential all-electron projector augmented wave (PAW) method [270,271]. The PAW pseudo-potential was generated taking scalar relativistic corrections into account. The spin polarized generalized gradient approximation, PBE [234,235] was used to calculate the exchange-correlation energy. The cut off energy for the plane wave basis set was fixed at 400 eV for all calculations performed in this study. The geometry optimizations were performed by ionic relaxation, using a conjugate gradient minimization. The geometries were considered to be converged when the force on each ion becomes 0.01eV/Å or less. The total energy convergence was tested with respect to the plane-wave basis set size and simulation cell size, and the total energy was found to be accurate within 1 meV. The spin polarized calculations of gas-phase clusters were carried out by placing the clusters in a 15×15×15 cubic box to prevent interaction between clusters. The Brillouin zone integrations are carried out at the Γ point only.

In order to obtain accurate description of $Al_2O_3(0001)$ surface, test calculations were carried out for the bulk $Al_2O_3(0001)$. The calculated lattice parameter (using $5 \times 5 \times 5$ K-points, a=b=4.76 Å and c=12.99 Å) are found to be in good agreement with the experimental values [531]. The band gap is found to be 6.2 eV, which is in accordance with the previously reported results [532] but lower than, the experimental band gap of be 8.8 eV [533]. However, DFT is known to underestimate the band gaps. The calculated cohesive energy of 32.8 eV/mole for bulk alumina, compares well with its experimental value of 32 eV [477]. After bulk calculation, the $\alpha - Al_2O_3(0001)$ surface is modeled as a 18 atomic layer slab obtained by truncating the bulk $\alpha - Al_2O_3$ structure with a vacuum thickness of 13 Å between slabs. Because the main objective of the present study is to extract details of cluster/surface interactions, a 2×2 supercell (30 atoms/cell) is considered to ensure a large lateral surface (surface area ≈ 91 Å^2). In this setup, the smallest distance between metal atoms and their periodic image assured to be larger than 5 Å. Overall supercell dimensions were 9.53×9.53 ×25.99 Å^3 containing 120 atoms. To make the reading easy, each adsorption site is labeled with a letter and a number indicating the type of the atom and the atomic layer in the slab, respectively. Figure 6.1 displays the five different atomic layers, represented by, $Al(1)$, $O(2)$, $Al(3)$, $Al(4)$, and $O(5)$. A Monkhorst–Pack set of $5 \times 5 \times 1$ K-points were used for all the slab calculations. Further to care of the image interactions, all the calculations in case of Au_{10} deposition were carried out using a 3×3 supercell having a

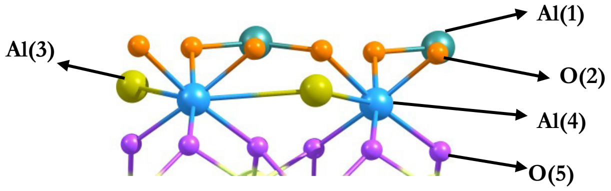

(a) Side View of top five layers of α-$Al_2O_3(0001)$ surface

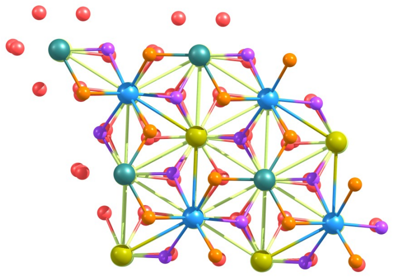

(b) Top View of α-$Al_2O_3(0001)$ surface

Figure 6.1: Side and Top views of $\alpha - Al_2O_3$ surface

dimension of 14.30×14.30×25.99 Å^3 (surface area ≈204.4 Å^2) and contains 270 atoms. For structural relaxation, all 18 atomic layers were allowed to relax and relaxation was performed including the dipole correction to avoid any error due to interaction of the slab images due to dipole moments [534]. The geometry optimization of the modeled 18-atomic layer Al-terminated slab shows large structural relaxation (compression) in which the Al atoms of the first layer move inward by -0.70 Å (83%), ending up almost coplanar with oxygen atoms. The large inward relaxation reduced the charge on the Aluminum atom compared to the bulk, and the calculated $Al-O$ distance, which is 1.86 Å in the bulk, decreases to 1.69 Å at the surface. The relaxation of second, third and fourth layer with respect to un-relaxed geometry is found to be -6%, 46% and 21% respectively. Calculated surface relaxations are consistent with previous reports [518]. The huge relaxation is attributed to the re-hybridization of the surface Al atom to an sp^2 orbital configuration, which favors the planar structure or it might be because of the reduction of the ionicity of the surface relative to the bulk due to the outer Al^{3+} ion becomes strongly coordinated to the first layer O^{2-} ions to counteract the excess of positive charge [535-537]. The surface energy of the relaxed surface is calculated to be 1.41 J/m^2 and agrees well with the previous reports [538,539]. The average adsorption energy of Au_n cluster on $\alpha-Al_2O_3$ surface is calculated as

$$\Delta E = \frac{-[E(Au_n - Al_2O_3) - E(Al_2O_3) - E(Au_n)]}{n} \qquad \text{eq. 6.1}$$

Initial calculations were carried out to obtain the ground state geometries of Au_n ($n = 1\text{–}7,10$) clusters. In line with the previously reported results on gas phase Au_n clusters [410,540-542], the ground state geometry of Au_n ($n = 1\text{–}7,10$) clusters are found to have planar structures. The lowest energy structure of gold cluster are presented in Figure 6.2 along with the bond lengths of the $Au-Au$ bonds The dimer bond length and disassociation energy are found to be 2.52 Å and 1.42 eV which are consistent with the experimental values [477]. For $n = 3$, it favors an open triangle with an angle of 155º. For $n = 4$, a planar rhombus is found to be the most stable. The lowest energy geometries of Au_5 and Au_6 clusters form planar W and stacked triangle structures, respectively. The growth motif of larger clusters $(n = 7{,}10)$ shows capping of the side arms in the same plane by additional Au atoms.

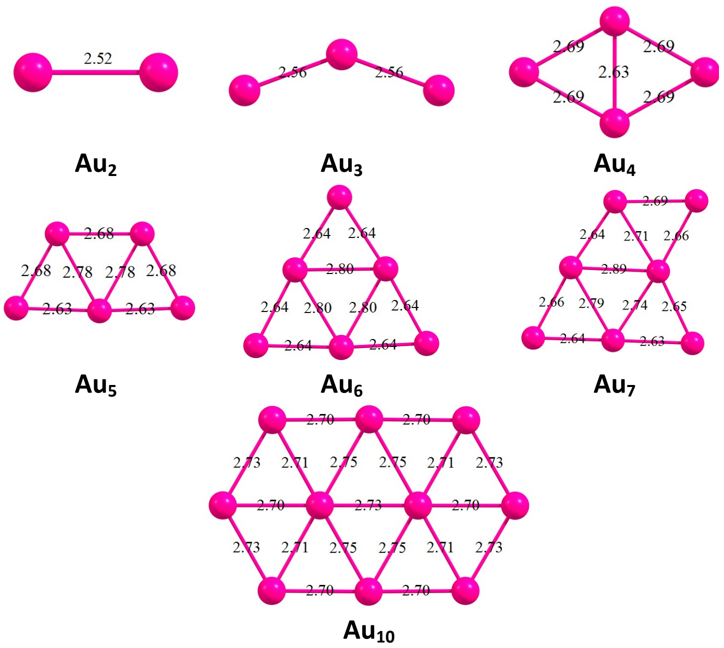

Figure 6.2: Lowest energy configurations of the Au_n clusters.

6.3 Result and Discussion

6.3.1 Au_n clusters ($n = 1$– 7 and 10) on $\alpha - Al_2O_3$ Surface

6.3.1.1 Geometric structures

In order to identify the most preferred adsorption site of the Au atom on the $\alpha - Al_2O_3(0001)$ surface, ionic relaxations of Au atom on the alumina support was carried out by placing Au at different well-defined locations on the surface *viz* (*a*) on Al in the top layer (*b*) on O in the second layer (this can be referred as hollow sites, in which Al binds with three surface oxygen atoms), (*c*) bridge position of the $Al - O$ bond on the Al_2O_3 surface. On the basis of the total energies, it is observed that Au prefers to bind with a surface Al atom at a tilted angle with respect to the surface plane, similar to reported results on the adsorption of single Au atom on Al_2O_3 surface by Fernandez *et al.* [543]. The shortest Au–Al bond distance is ~2.49 Å. During the process of Au adsorption, the surface Al atom moves upward by 0.41 Å, which in other words can be viewed as reverse relaxation of surface Al atoms. The adsorption energy of Au on the Al_2O_3 surface is ~0.79 eV. In this context these results are compared with the results of other noble metal atoms like Ag and Pd [521,522]. Like Au, Ag also binds the Al_2O_3 surface weakly with adsorption energy of 0.46 eV. In contrast, Pd atom binds with Al_2O_3 strongly with a binding energy of 1.49 eV. The difference in the adsorption strength is attributed to the effect of d-electrons, which are primarily responsible for the binding of Pd. In the following sections, the adsorption of larger size Au_n clusters on the alumina surface is discussed. The geometry of the lowest energy isomers of Au_n clusters is presented in Figure 6.3. A couple of low-lying isomers Au_n/Al_2O_3 clusters are shown in Figure 6.4

The adsorption of two Au atoms on the alumina support is fundamentally very important as it gives clues about the growth pattern of larger clusters. For the adsorption of two Au atoms on the Al_2O_3 surface, two approaches are adopted: (i) The Au_2 dimer is placed on the surface in parallel and perpendicular orientations through various angles and (ii) two Au atoms are placed at large distance on the surface. The most stable configuration of Au_2 on the Al_2O_3 surface is shown in Figure 6.3. It is observed that Au_2 dimer binds at an angle (tilted) to the surface, where one Au is bound with one of the top Al (first layer) and the other

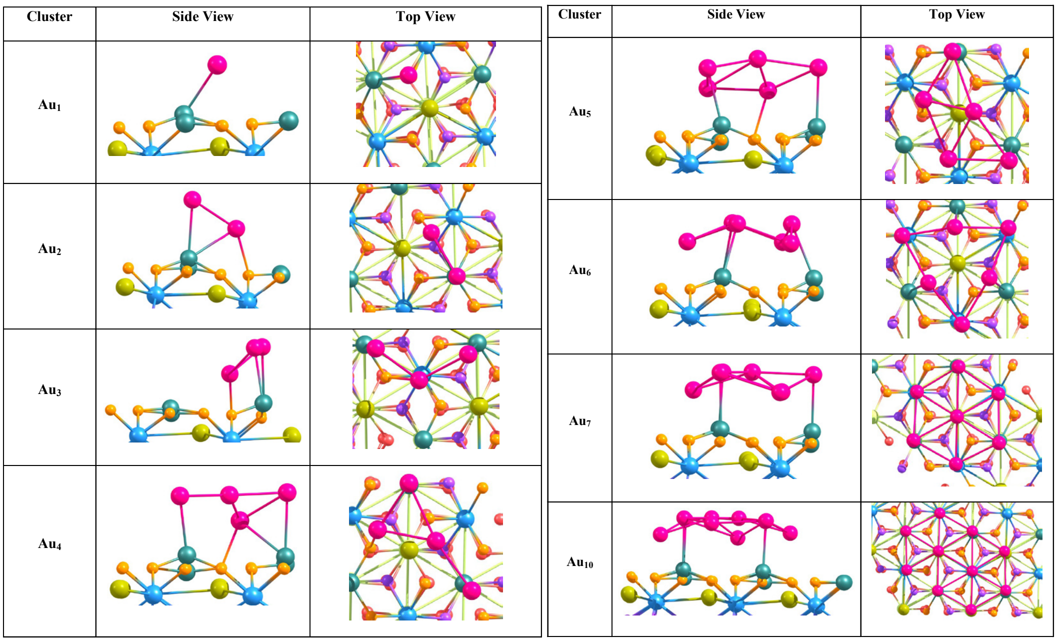

Figure 6.3: Side and top view of lowest energy configurations of the Au_n clusters deposited on $\alpha-Al_2O_3(0001)$ surface

Au atom projects upward sitting on the bridge site of the $Al - O$ bond as shown in Figure 6.3. The $Au - Al$, $Au - Au$ and $Au - O$ bond lengths are found to be 2.61 Å, 2.57 Å, and 2.20 Å respectively. The Au_2 cluster induces structural relaxation in its vicinity where in the Au bound Al is pulled out ~0.4 Å. The adsorption energy of Au_2 is found to be 1.41 eV. For the second case, when two Au atoms are placed far (~4 Å-5 Å) away and allowed to relax, they do not move towards each other to form an Au_2 dimer. However, from the stability point of view this atomic mode of adsorption is 0.85 eV higher in energy than dimer structure. The lower stability of the atomic adsorption mode is attributed to the absence of strong $Au - Au$ bond. Thus, it is inferred that for Au adsorption, clustering of atoms with $Au - Au$ bonds is more favorable in comparison to attachment of isolated Au atoms on the alumina surface albeit a kinetic barrier that exists between these two configurations. This is in line with the results of Anderson and co-workers [544], who have reported agglomeration of gold atoms on alumina surface is more extensive at room-temperature in comparison to the samples prepared by low-temperature deposition followed by annealing at the room temperature.

Figure 6.4: Side views of low lying configurations of the Au_n clusters deposited on $\alpha - Al_2O_3(0001)$ surface

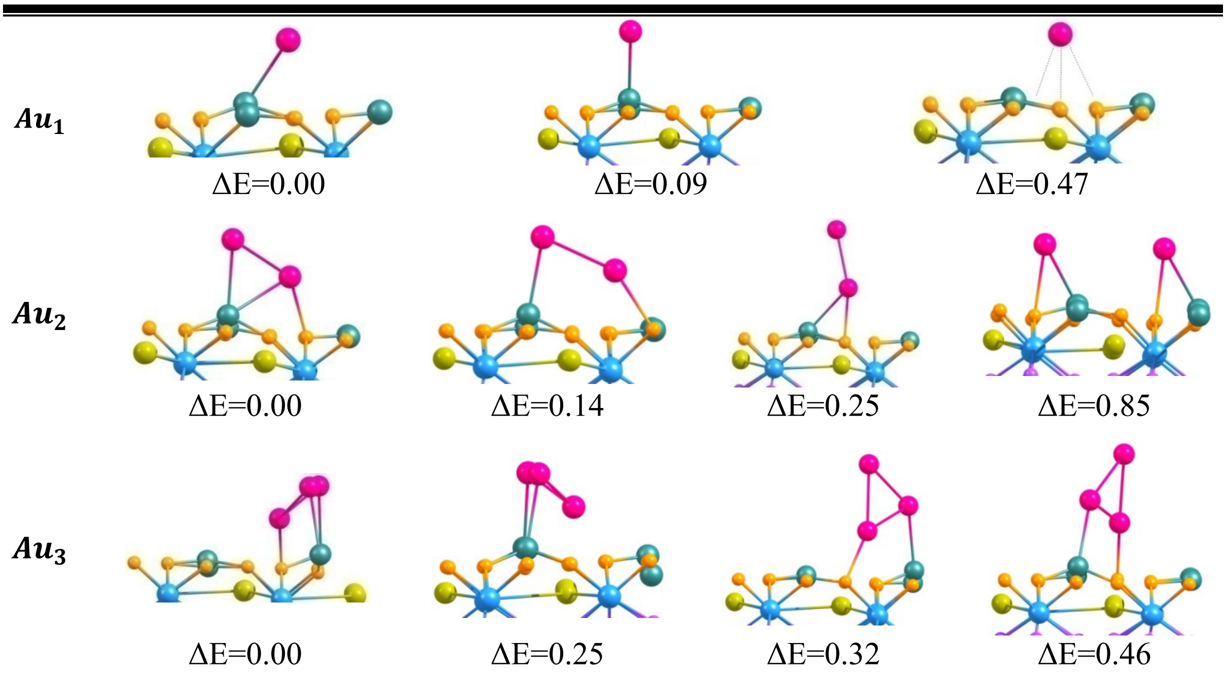

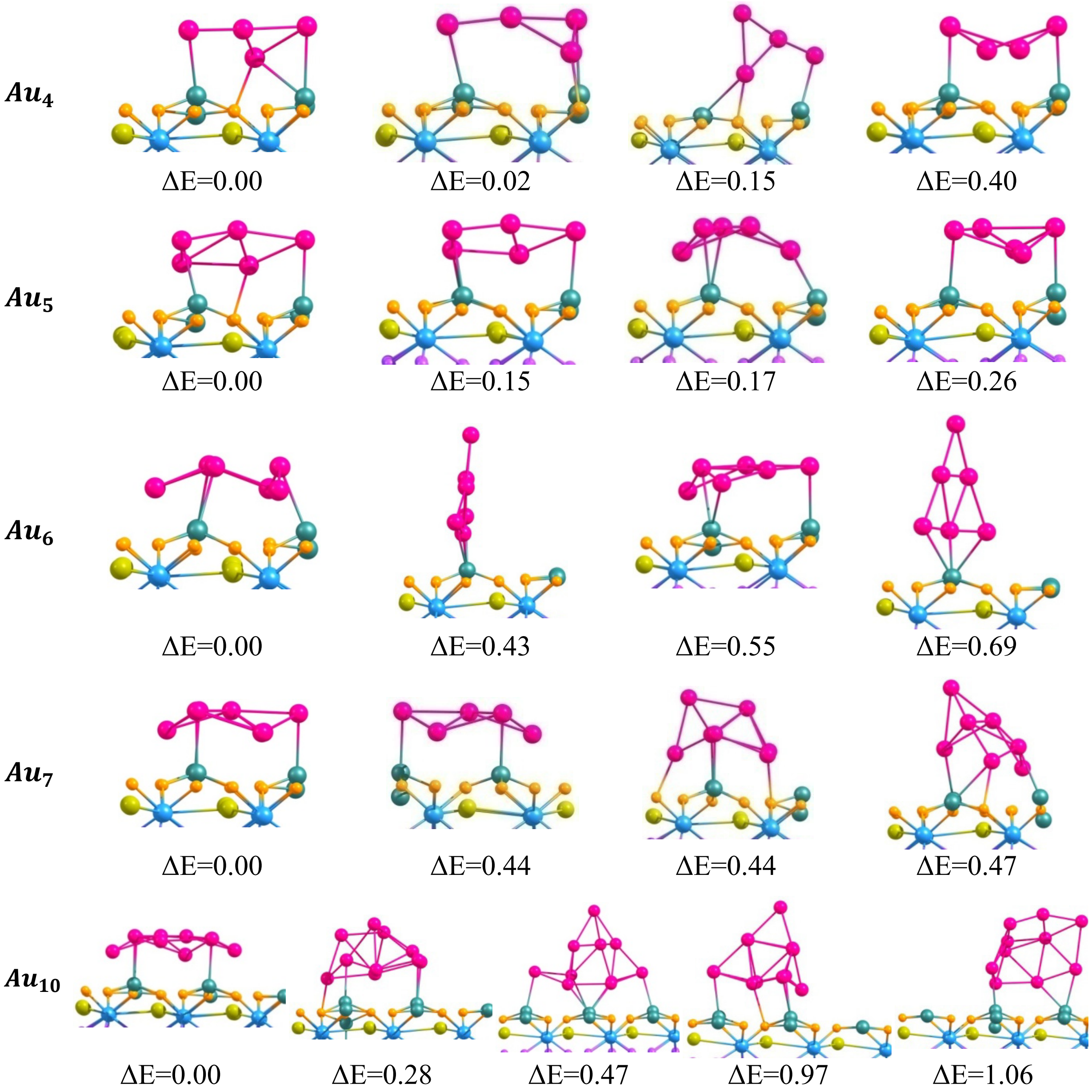

To determine the ground state geometry of the Au_3 cluster on Al_2O_3, several initial structures were optimized with the similar approach that was adopted for the dimer. On the basis of the adsorption pattern of Au and Au_2 dimer on the alumina substrate, where Au preferentially binds with surface Al atoms, it is envisaged that there will be charge transfer from the Al site to Au, leading to negatively charged Au clusters. Hence, we have also optimized few gas phase structures of anionic Au clusters. Based on the results it is found that the Au_3 (trimer) prefers to adopt an open triangle structure on the Al_2O_3 surface, with the central Au atom tilted towards surface O atom, and other two Au atoms are bound with two

Al atoms as shown in Figure 6.3. The $Au-Au$ distance and $\angle AuAuAu$ are found to be 2.62 Å and 96.7°, respectively. As a consequence of $Au-Al$ bond formation, two surface Al atoms shifted upwards (out of plane) by about 0.35 Å. The binding energy of Au_3 on the Al_2O_3 surface is estimated to be 2.07 eV. Apart from other isomeric structures, we have specifically checked the stability of the Au_3 cluster placed vertically on the Al_2O_3 surface and the result shows that this is 0.32 eV higher in energy as compared to the lowest energy isomer.

The tetramer of Au is important as the neutral and anionic Au_4 clusters show different ground state geometries in the gas phase. While neutral Au_4 adopts rhombus structure (D_{2h}), Au_4^- forms Y shaped geometry (C_{2v}). Hence, it is of special interest to investigate the ground state geometry of the deposited Au_4 cluster on the Al_2O_3 surface. In order to find the lowest energy isomer, several starting geometries including both neutral and anionic isomers of Au_4 in the gas phase were deposited and optimized. Based on the total energy of the optimized structures, it is noticed that the deposited Au_4 cluster adopts Y shaped configuration as the most stable geometry on the Al_2O_3 surface. Importantly, this geometry is very close to the geometry of the Au_4 anionic cluster in the gas phase. The $Au-Al$ distances are found to be 2.52 Å and 2.70 Å. The $Au-Au$ distances are found to be 2.58 Å, 2.64 Å, 2.70 Å, and 2.71 Å which are slightly longer than the $Au-Au$ bond lengths in the gas phase structure of Au_4^- (2.63 Å, 2.70 Å). The binding energy of Au_4 cluster on the Al_2O_3 surface is found to be 2.24 eV. Au_5 cluster adopts two dimensional edge capped rhombus structure as the lowest energy isomer in the gas phase. Upon interaction with the Al_2O_3 surface, Au_5 forms capped bent rhombus as the most stable configuration with three Au atoms bonded to three Al atoms on the top layer and other two Au atoms are on top of the $Al-4$ hollow site. The average $Au-Al$ and $Au-Au$ bond lengths are found to be ~2.62 Å, and ~2.8 Å respectively. The binding energy of Au_5 on the Al_2O_3 surface is estimated to be 1.97 eV.

Au_6 is one of the most stable Au_n clusters and adopts a planar triangle in both neutral and anionic state. In order to find out the most favored geometry of Au_6 cluster on the Al_2O_3 surface several initial geometries were generated by placing the triangular moiety of Au_6 cluster at different orientations on the surface. On the basis of the total energy of all optimized structures it is observed Au_6 cluster forms a puckered structure on the Al_2O_3 surface, wherein the alternate Au atoms are bonded to Al atoms with an average $Au-Al$ bond length of 2.63 Å. This reflects that Au_n clusters favor maximal wetting on the Al_2O_3 surface. Other configurations, where the Au_6 cluster is oriented perpendicular to the surface plane, with one atom or three atoms connecting the surface, are found to be higher in energy. The average $Au-Au$ bond length on the periphery is found to be ~2.78 Å and the average inner bond lengths are found to be around ~2.85 Å. The calculated binding strength of Au_6 on Al_2O_3 is 2.12 eV.

In gas phase Au_7 clusters prefer capped planar triangle structure as the lowest energy isomer. Remarkably, this structure rearranges itself on the alumina surface to form zigzag patterned hexagonal structure with three gold atoms binding atop $Al(1)$ site and other three occupying the $Al(4)$ hollow site and the seventh atom (*i.e.,* the central atom) resides over the $Al(3)$ site. The average $Au-Al$ and $Au-Au$ bond lengths are found to be ~2.62 Å, and ~2.78 Å respectively. It is worth mentioning here that Vajda and co-workers [86] in their studies on the propene epoxidation on Au_7 cluster deposited on Al_2O_3 surface found significant reconstruction at the cluster substrate interface. It is known that odd Au_n clusters have unpaired electron and thus show spin moment in the gas phase. Interestingly, the spin moment of Au_7 cluster is fully quenched upon deposition on the alumina substrate. This can be explained by the significant amount of charge transfer from the substrate to the Au_n cluster that occurred as the size of the Au clusters increases and in particular, a charge $0.85e$ is transferred from the surface to Au_7 cluster. The adsorption energy of Au_7 is found to be

2.20 eV. In line with the Au_7 cluster, the Au_{10} cluster also forms zigzag patterned hexagonal structure with four gold atoms binding atop aluminum ($Al(1)$) site and other four atoms reside over the $Al(4)$ hollow site and remaining two atoms (*i.e.,* the central atoms) reside over the $Al(3)$ site. The adsorption energy of Au_{10} on the alumina surface is calculated to be 2.35 eV.

6.3.1.2 Energetics

After establishing the most stable geometrical conformations of Au_n clusters on the Al_2O_3 substrate, the stability and energetics trend are analyzed as a function of cluster size. Figure 6.5 shows the variation in binding energy of isolated clusters along with their adsorption energy as a function of cluster size. The binding energy shows clear odd-even alteration in stability with an increasing trend as the size increases. Interestingly, based on embedded cluster calculation Nasluzov *et al.* [530] have predicted that adsorption energies increase with cluster size, up to $n = 4$, but drop for larger sizes. However, in this study, the average adsorption energy shows a monotonous decreasing trend. It needs to be noted that for gold clusters with even number of atoms ($n = 2, 4$ and 6), have higher binding than the neighboring odd clusters ($n = 1,3$ and 5). In general, higher the stability of the isolated clusters, lower is the energy released

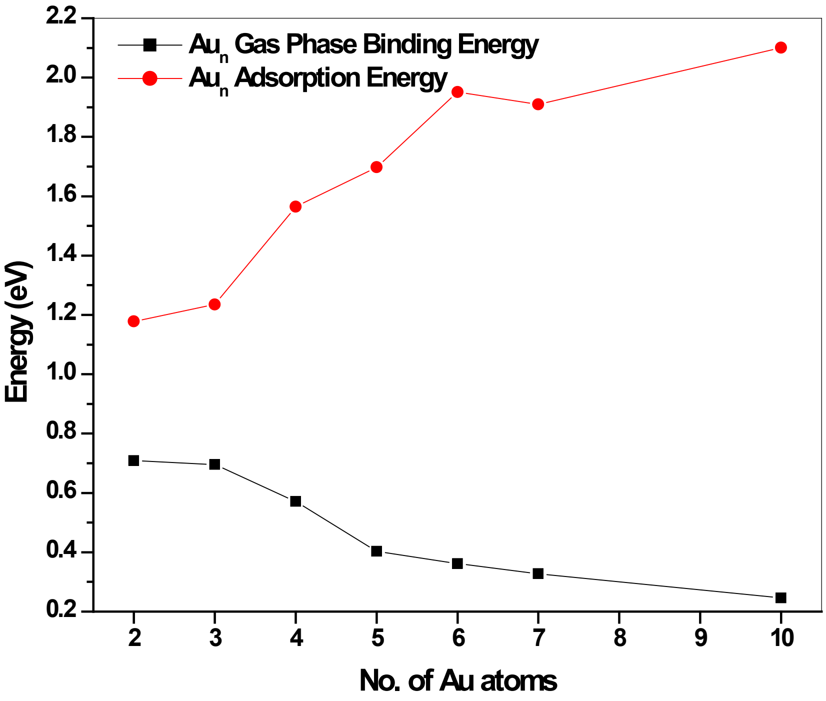

Figure 6.5: Variation in the average adsorption energy (eV/atom) of deposited Au_n clusters on $\alpha - Al_2O_3(0001)$

upon adsorption. However, an opposite trend in the adsorption energy of Au clusters is observed in the present work, which can be explained by considering large charge transfer at the interface between Au clusters and Al_2O_3 surface or in other-words looking from the perspective of gold anions. For anionic gold clusters, odd clusters are more stable than even clusters in the gas phase. Therefore, after deposition, even clusters bind relatively stronger than odd clusters.

6.3.1.3 Charge and Electronic structure analysis

A qualitative interpretation of the nature of bonding can be obtained by understanding the charge difference analysis. The charge density difference at the interface of Au_n cluster and alumina surface is calculated as

$$\Delta\rho = \rho(Au_n - Al_2O_3) - \rho(Al_2O_3)_{fix} - \rho(Au_n) \tag{eq. 6.2}$$

where $\rho(Au_n - Al_2O_3)$ is the charge density of the total system, $\rho(Al_2O_3)_{fix}$ is the charge density of the alumina surface and $\rho(Au_n)$ is the electron density of the isolated cluster. In

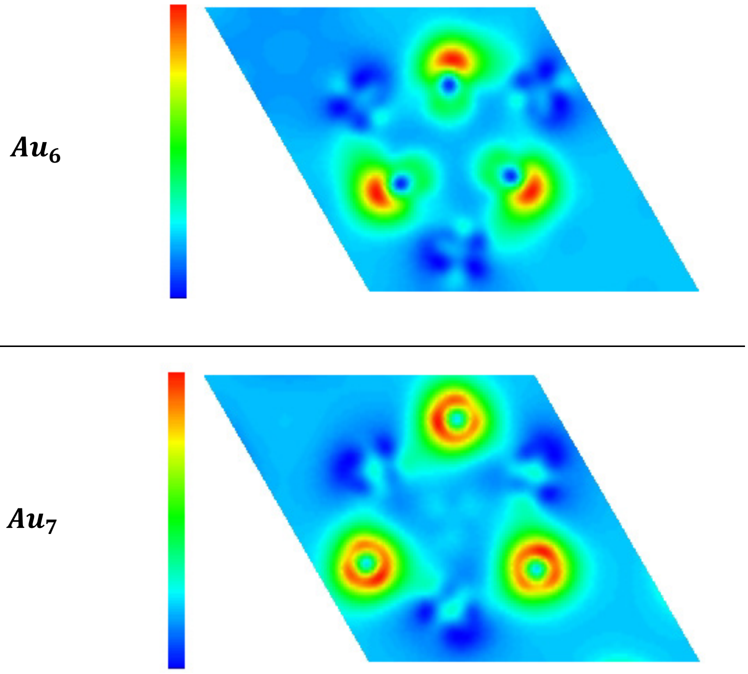

Figure 6.6: Two-dimensional projection of the charge density for $Au_{6/7} - Al_2O_3$ [$\rho(Au_{6/7} - Al_2O_3)$-$\rho(Au_{6/7}) - \rho(Al_2O_3)$] obtained from the difference of the constituent species.

general, it is noticed that an overall charge transfer occurs from the surface to the Au_n cluster. Figure 6.6 depicts two representative charge density difference contours for Au_6 and Au_7 clusters on the Al_2O_3 surface. It is found that when Au atom is deposited on the Al_2O_3 surface, electronic charge is transferred from the surface Al atom to the Au atom. For the deposited Au_6 cluster, accumulation and depletion of charge density at alternate Au atoms is observed. Bader analysis carried out to quantify the atomic charge distribution revealed a substantial charge gain by Au_n clusters from the surface. In case of Au atom deposited on the Al_2O_3 surface, which binds with one of the surface Al atoms, attains a partial negative charge of about 0.3e. In case of Au_2, an overall charge transfer of $0.31e$ to the Au dimer is observed. Bader analysis of Au_3 cluster has revealed that while the terminal Au atoms gain $0.50e$ charge , the central Au atom has a charge depletion of ~$0.45e$ *i.e.,* the Au_3 cluster has an overall benefit of $0.56e$ charge. For the deposited Au_4 cluster, a charge of $0.55e$ and $0.33e$ got accumulated on the two Au atoms bound to the Al atom while the remaining two Au have charge depletion of $0.07e$ and $0.26e$. An overall charge gain of $0.76e$ was observed for the Au_5 cluster. As discussed in the charge density difference analysis, charge accumulation of $0.43e$ and depletion of $0.17e$ is observed on the alternate Au atoms of the Au_6 cluster, with an overall charge gain of $0.78e$. The observation of negative charge on the gold cluster is in line with the STM and conductance spectroscopy results of gold particles adsorbed on alumina/$NiAl(110)$ [545,546].

The chemical reactivity of a material is related to the electronic structure. Thus, it is important to get an insight on the electronic structure of Au_n clusters after adsorption on the Al_2O_3 substrate. For this purpose the local density of states (LDOS) of Au_n clusters before and after deposition on Al_2O_3 we have plotted LDOS projected on the gold atomic orbitals has been shown in Figure 6.7. This was prepared and analyzed by separating out the contributions from the adsorbed Au_n clusters and the Al_2O_3 surface to the total-DOS of the system. The most stable configurations of Au_3 and Au_{10} clusters were considered to represent the variation in the LDOS of Au cluster as shown in Figure 6.7. It is seen that after adsorption of Au on the Al_2O_3 substrate a set of new peaks appeared in the gap, which are

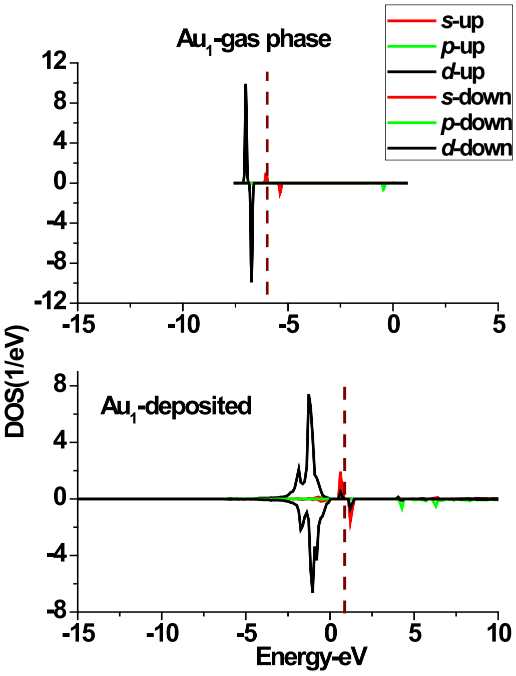

Au

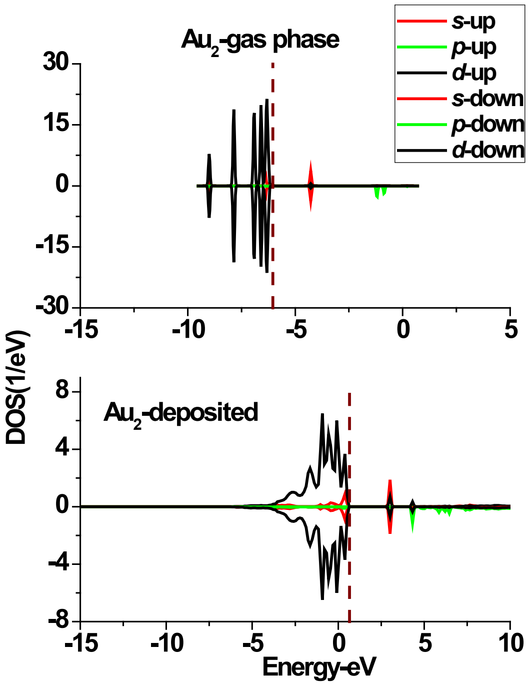

Au_2

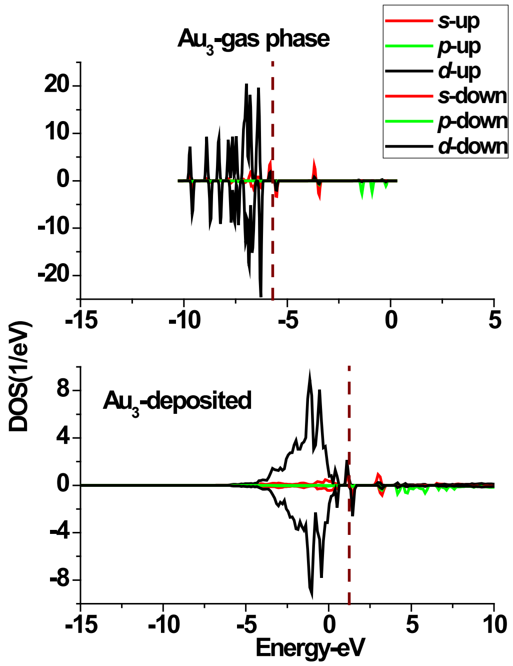

Au_3

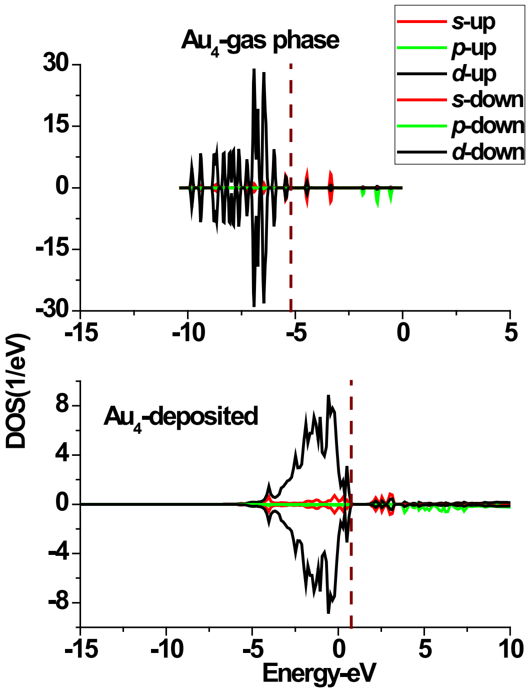

Au_4

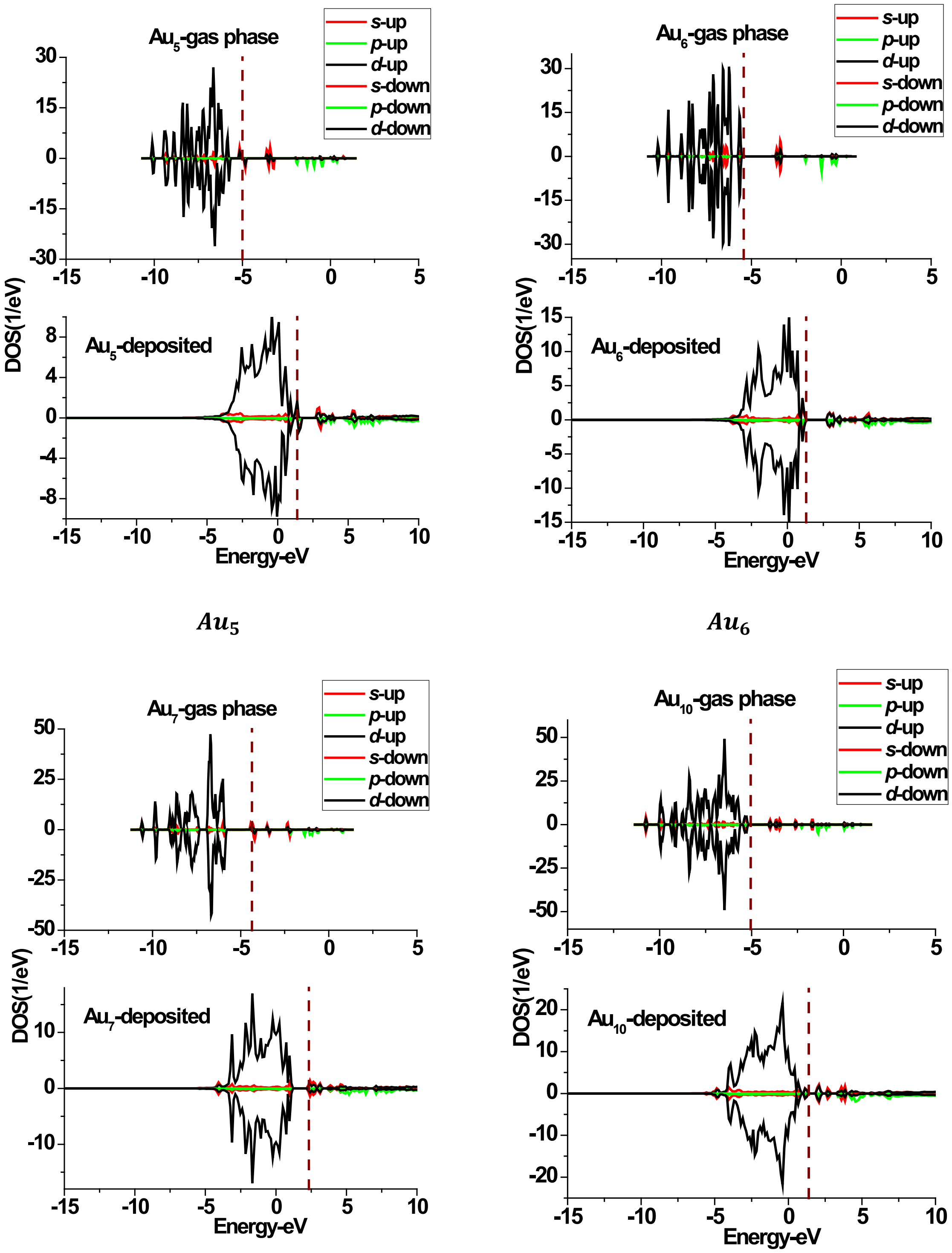

Au_5 Au_6

Au_7 Au_{10}

Figure 6.7: Comparison of the density of the states (LDOS) plot of Au_n clusters before and after deposition on alumina surface. The vertical dashed line indicates the Fermi level.

assigned to $6s$ states appeared in the gap, which are assigned to $6s$ states of Au. A significant red shift in the electronic states of the Au_n clusters was observed upon adsorption of Au_n on Al_2O_3 substrate. This is in accordance with the charge accumulation on the deposited Au

atoms, which destabilizes the energy levels to the higher side (less negative energy). In this context it should be recalled that similar red shift is observed in gold anions (more predominantly in even Au clusters), which is primarily responsible for higher catalytic activity of these clusters. It is also important to note that the Fermi energy level of the $Al_2O_3 - Au_n$ systems is less negative in energy as compared to the clean Al_2O_3 and Au_n components. Furthermore, it is seen that the Fermi energy level is predominantly contributed by the energy states from Au atoms. This corroborates the electronic charge transfer from the surface to the gold clusters.

6.3.2 Oxidation of alumina supported Au_n clusters

Chemical reactivity of small Au clusters toward CO oxidation has been a subject of numerous investigations. For CO oxidation, the activation of the $O - O$ bond is the most important step. So, one of the interesting questions being asked is at what size does the deposited Au_n clusters start-activating O_2 molecule. Theoretically, Hakkinen *et al.* [174] first predicted that gold dimer anion (Au_2^-) is the smallest cluster in gas phase which catalyzes the CO oxidation reaction. Subsequently, Socaciu *et al* [173] demonstrated the oxidation ability of Au_2^- through molecular beam experiment. Although several gas phase studies on O_2 reactions with Au_n clusters are available [173,174,547,548], studies on deposited Au_n clusters are few [549,550]. In particular it is of interest to understand how the interface charge transfer between clusters and metal oxide substrate can influence the oxidation behavior of gold nanoclusters. For this purpose small Au_n clusters, up to $n = 5$, are used as model representatives. The oxidation of these deposited clusters was carried out in two modes; (*i*) placing the oxygen molecule at different location on the cluster (molecular adsorption) and (*ii*) two oxygen atoms are placed separately on the Au_n cluster (dissociative chemisorption). It is worth mentioning that a significant barrier may exist between these configurations (molecular and dissociative adsorption) [551]. However, the focus of this study is only on the energy difference between the two modes, since the aim is to determine the most stable configuration.

For Au/Al_2O_3, the most stable conformation of $Au-O_2$ complex is formed when O_2 interacts in dissociative mode rather than molecular way. Figure 6.8 shows the optimized geometry of the O_2-Au_n/Al_2O_3 complexes with a relative stability of the next best possible mode of interaction. It is obvious from the figure that O_2 prefers to interact with Au_n/Al_2O_3 dissociatively. It is observed that one of the oxygen atoms prefer to form a bridge between the Au_n clusters and surface Al atom. The strong $Au-O$ interaction also elongates the $Au-Au$ bond of the cluster. The molecular adsorption is higher in energy. However, in both molecular and dissociative adsorption, it is observed that oxygen molecule prefers to connect with both surface and cluster simultaneously, leading to infer that the dissociative mechanism is supported by the Al atoms on the surface. These observations are in line with results reported by Fortunelli and co-workers [551] on Ag_3 and Au_3 clusters supported on MgO(0001) surface which favor dissociative adsorption over molecular adsorption.

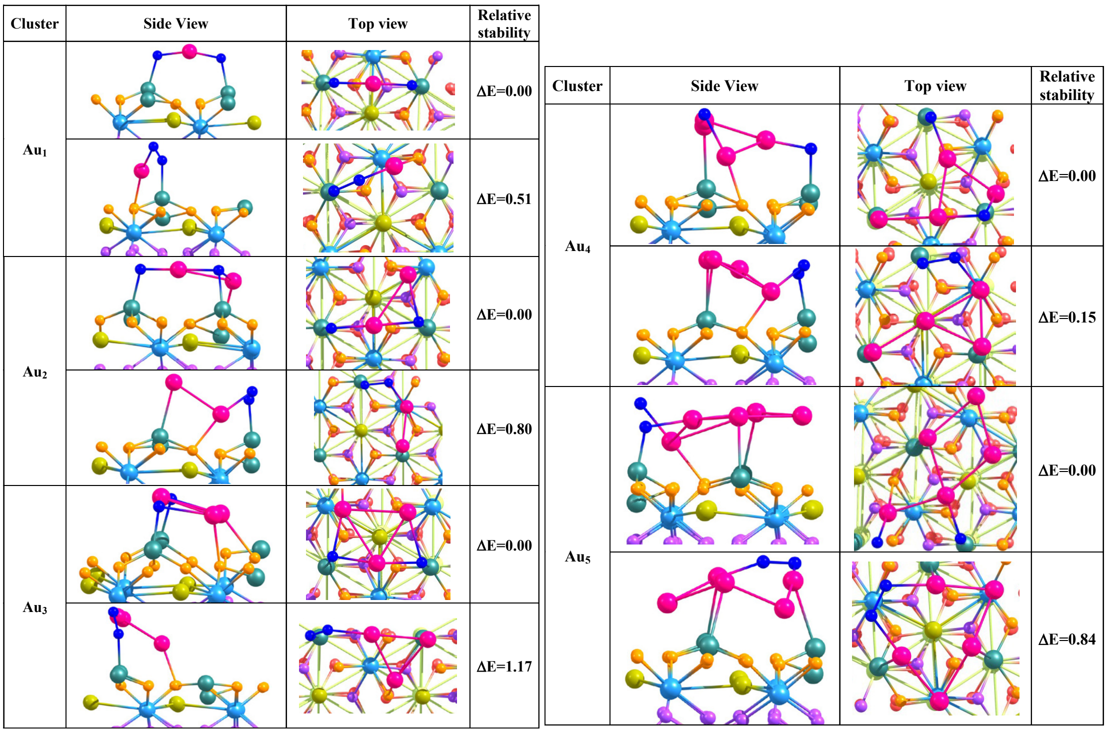

Figure 6.8: Interaction of O_2 with $Au_n(n=1-5)$ clusters deposited on the $Al_2O_3(0001)$ surface.

6.4 Conclusions

In summary, in this chapter, structure and electronic properties of small Au clusters on the alumina support are presented. The results reveal that Au atom binds weakly on the Al_2O_3 surface and it favors to bind with one of the Al atoms on the surface layer. Despite weak interaction, there is diffusion barrier for Au atoms on the support. On the basis of the total energy calculations it is concluded that clustering of Au atoms is more favorable than dispersion on the Al_2O_3 surface by atomic adsorption. In general, Au_n clusters preferentially adsorb with a puckered conformation to the surface. The charge transfer is further reflected by red shift in the energy levels of the density of states spectrum, a signature for higher chemical reactivity. Further reaction of oxygen molecules with these Au_n/Al_2O_3 systems shows dissociative chemisorptions is more favorable than molecular adsorption.

7. Conclusions and Future Perspectives

The goal of the present thesis is to gain fundamental understanding of atomic structure, bonding, electronic and chemical properties of isolated and supported metallic clusters and their interactions with gas molecules. These studies have implications towards elucidating microscopic aspects of several condensed-phase phenomena and designing new materials for heterogeneous catalysis. While bare and doped lead clusters were used as models for elucidating the evolution of geometric and electronic structures and bonding, gold cluster models were used to study and differentiate the electronic and chemical properties of pure, doped and supported clusters. Throughout the work standard codes of density functional theory, within the plane-wave based pseudo-potential framework were used as tools to illustrate the physico-chemical behavior of all the systems considered in this thesis and compared with available experimental data whenever available.

The evolution of geometric and electronic structure of Pb_n and Pb_n^+ clusters ($n = 2-15$) has been elucidated and compared with other Group IV elemental clusters. The results suggest that unlike Si, Ge, and Sn clusters, which favour less compact prolate shape in the small size range, Pb clusters favour compact spherical structures consisting of fivefold or six fold symmetries. The central feature of these studies showed that spin orbit coupling effect is quite important to describe the energetics of these clusters. The relative stability of Pb_n clusters, analyzed based on the calculated binding energies and second difference in energy suggests that $n = 4, 7, 10$ and 13 clusters are more stable than their respective neighbours, which is in good agreement with experimental observations. Charged Pb_n^+ clusters also showed compact growth pattern as those observed for neutrals with small local distortions. Based on the fragmentation pattern it is seen that while smaller clusters favor monomer evaporation, larger ones fragment into two stable daughter products. The experimental observations of large abundance for $n = 7$ cluster and lowest abundance of $n = 14$ cluster have been demonstrated from their fragmentation pattern. The results were subsequently tested and verified by Waldschmidt *et al.* [368], in their work on surface-induced dissociation studies on the energetics and structure of lead clusters. The chemical stability of these clusters was analyzed by evaluating their energy gap between the highest occupied and lowest unoccupied molecular orbitals and adiabatic ionization potentials. Albeit higher binding energy of Pb_{13}, the lower ionization potential was explained based on its electronic structure through the density of states and electron shell filling model of spherical clusters.

Considering the fact that introduction of an impurity atom can play a very important role in the modification of electronic and geometrical properties of homoatomic clusters, the structural and electronic properties of Pb_nM ($M = C, Al, In, Mg, Sr, Ba$ and Pb; $n = 8, 10, 12$ and 14) clusters were studied. The results revealed that the location of the impurity atom depends on the nature of interaction between the impurity atom and the host cluster and the size of the impurity atom. While the impurity atoms smaller than Pb, favor to occupy the endohedral position, the larger atoms form exohedral capping of the host cluster. Based on the interaction energy of the M atoms with Pb_n clusters, it was found that $p-p$ interaction dominates over the $s-p$ interaction and smaller size atoms interact more strongly. The stability analysis of these clusters suggests that while the substitution of Pb by C or Al enhances the stability of the Pb_n clusters, Mg lowers the stability. The energy gap analysis revealed that while the substitution of Mg atom widens the HLG, all other elements reduce the gap of the Pb_nM clusters. The unusual increase in the interaction energy of Mg with Pb_{12} and the largest HOMO–LUMO gap of $MgPb_{12}$ cluster has been explained based on the 50 electrons rule for icosahedral structures. Further investigations of the stability of Pb_nM clusters revealed that the interplay between the atomic and electronic structure is crucial to understand the stability of these clusters. Further fragmentation behavior of the bimetallic cluster ions Sn_nPb^+ and Pb_nSn^+ were investigated which were more amenable for contemporary experiments. A systematic theoretical study of the structure and electronic properties of $Sn_{n-1}Pb$ and $Pb_{n-1}Sn$ ($n = 2 - 13$) clusters was done. Fragmentation studies have revealed that, for Sn_nPb^+ first the single lead atom is split off; in contrast the Pb_nSn^+ clusters dissociate mainly in fragments retaining the single tin atom, which is in full accordance with the low-energy surface-induced dissociation patterns of Sn_nPb^+ and Pb_nSn^+ clusters which were carried out by Waldschmidth *et al.* [392]. For larger collision energies the complete set of smaller tin fragment ions Sn_{n-m}^+ with $m < n$ is found for Sn_nPb^+, whereas the Pb_nSn^+ clusters decay into two series of $Pb_{n-m}Sn^+$ and Pb_{n-m}^+ fragments with $m < n$. Though it might be a computationally expensive exercise, global minimum methods should be used to test all the possible isomers chosen after using Mote Carlo, or after annealing quenching sequences.

Gold, which is inert in the bulk, is found to be highly active in its nano form and the chemical reactivity of the Au clusters can be tuned by the incorporating a dopant in it. The atomic and electronic structure of $Au_{n-1}Al$ ($n = 2 - 7$) clusters are elucidated with a view to understand how chemical bonding influences the stability and structure of small size Au clusters. The optimized geometries of $Au_{n-1}Al$ clusters indicate that the substitution of Au by Al results an early onset of three-dimensional structures from tetramer onwards. Based on the energetics, Au_3Al and Au_5Al clusters are found to be extraordinary stable. The oxidation of $Au_{n-1}Al$ clusters undergoes *via* dissociative mechanism, albeit significant charge transfer from Al to Au. Moreover, the O_2 molecule prefers to attach at the Al site rather than at the Au site.

On the basis of the above results CO oxidation behavior of $Au - Al$ nano-composites in three different size ranges; (*i*) a small cluster Al_6Au_8, (*ii*) a mid-sized cluster $Al_{13}Au_{42}$, and (*iii*) a periodic slab of $Au(111)$ surface, where the Au atoms in the second layer is substituted by Al atoms has been carried out. While the Al_6Au_8 forms a cage like structure with both the Au and Al atoms on the surface of the cage, $Al_{13}Au_{42}$ forms core-shell type symmetric icosahedral structure. For the Al substituted $Au(111)$ surface, the ionic relaxation results in compression between the interlayer separations. The charge distribution analysis suggests that in all cases Al atoms donate electronic charges to the Au atoms. This has been corroborated by the red shift in the density of states spectrum, a signature of more negative charge state whence a higher chemical reactivity. The CO oxidation was investigated through both Eley-Rideal (E-R) and Langmuir-Hinshelwood (L-H) mechanism. The interaction of O_2 molecule with these systems occurs non-dissociative way with elongation of the $O-O$ bond. Further interaction with CO molecule leads to the formation of CO_2 spontaneously. On contrary, the CO_2 evolution by co-adsorption of O_2 and CO molecules undergoes through an intermediate complex of higher energy. On the basis of the results it is inferred that the efficient CO oxidation of the $Al-Au$ nanocomposite is due to negatively charged surface Au atoms. The results showed an improved oxidation behavior of Au in presence of Al atoms, be it inside the core for core-shell type structure or at the sub-surface layer for periodic slabs. As a future perspective the results obtained on the steps of the catalytic oxidation of CO on a metallic surface at fixed chemical potentials of the reactants by DFT calculations, might be fed into kinetic Monte Carlo simulations to obtain detailed information of the reaction under experimental pressure and temperature conditions and at real time scales. Studies on the catalyst stability and coverage effects (multiple CO and O_2 adsorption) will be carried out in future.

Motivated by the pioneering work of Haruta *et al*, which showed low temperature CO oxidation of supported Au clusters these studies, a systematic study on the adsorption of $Au_n (n = 1-6)$ clusters on a regular $\alpha - Al_2O_3(0001)$ surface and the role of support on the structure and reactivity of metal clusters was carried out by studying the interaction of $O_2$with the deposited clusters. The results reveal that Au atom binds weakly on the Al_2O_3

surface and it favors to connect with one of the Al atoms on the surface layer. Despite weak interaction, there is a diffusion barrier for Au atoms on the support. The adsorption studies results revealed clustering of atoms with $Au-Au$ bonds is more favorable in comparison to dispersion on the alumina surface albeit a kinetic barrier that exists between these two configurations. In general, Au_n clusters preferentially adsorb with a puckered conformation on the Al_2O_3 surface. The adsorption energies of Au_n clusters showed strong odd-even variations on Al_2O_3 surface, with local maxima at $n = 2, 4, 6$ which were established to be stable by experiment. The charge transfer is further reflected by red shift in the energy levels of the density of states spectrum, a signature for higher chemical reactivity. Further reaction of oxygen molecules with these Au_n/Al_2O_3 systems shows dissociative chemisorptions is more favorable than molecular adsorption.

With the understanding and knowledge gained on the interactions of O_2 CO on deposited Au_n clusters and experience on handling CO oxidation over different systems, future studies would be carried out on a few similar reactions. A natural continuation of these studies is to determine a better support by trying different support oxide surfaces. One of our immediate interests is to study and gain insights on the enhanced activity of water shift reaction ($CO + H_2O \rightarrow CO_2 + H_2$), on deposited Au_n clusters on various oxide surfaces. Further, the preferential oxidation of CO, which is important in proton exchange membrane fuel cells is being studied on different catalysts like Pt/Al_2O_3 , $Pt/A-zeolite$, Au/Fe_2O_3 *etc*. We would extend these studies on deposited gold clusters as probable catalyst candidates for this reaction using a combination of DFT modeling techniques and explain the performance of Au and Pt catalysts. Another project of near future is to give a mechanistic rationale for the recent experimental results that have shown the potential of gold/carbon as good candidate for the direct epoxidation of propene and larger alkenes. A concluding remark: computational modeling of materials for various applications has emerged from the convergence of many different computational methods and the introduction of high-performance computers and the fundamental insight into various mechanisms of different processes can only be realized by breakthroughs in theoretical insight and computational methods.

References

[1] R. Pool, Science 248 (1990) 1186.

[2] M. Faraday, Phil. Trans. 147 (1857) 145.

[3] P.J. Coulier, J. Pharm. Chim. 22 (1875) 165.

[4] C.G. Knott (Ed.)^(Eds.), Collected scientific papers of John Aitken. LL.D., F.R.S. The University Press, Cambridge, 1923.

[5] J.G. Wilson, The principles of cloud-chamber technique in N. Feather, D. Shoenberg (Eds.), Cambridge monographs on physics. University Press, Cambridge Eng., 1951, p. 113.

[6] C.G. Suits, H.E. Way (Ed.)^(Eds.), The Collected works of Irving Langmuir. Pergamon press, Oxford; London, 1962.

[7] S.A. Ochs, R.E. Cote, P. Kusch, J. Chem. Phys. 21 (1953) 459.

[8] N.F. Ramsey, Phys. Rev. 74 (1948) 286.

[9] A. Kantrowitz, J. Grey, Rev. Sci. Instrum. 22 (1951) 328.

[10] G.B. Kistiakowsky, W.P. Slichter, Rev. Sci. Instrum. 22 (1951) 333.

[11] E.W. Becker, K. Bier, W. Henkes, Z. Physik. 146 (1956) 333.

[12] P.G. Bentley, Nature 190 (1961) 432.

[13] W. Henkes, Z. Naturforsch. Pt. A 16 (1961) 842.

[14] E.W. Becker, P. Lohse, R. Klingelhofer, Z. Naturforsch. Pt. A 17 (1962) 432.

[15] H. Hintenberger, J. Franzen, K.D. Schuy, Z. Naturforsch. Pt. A 18 (1963) 1236.

[16] O.F. Hagena, P.G. Schuller, Z. Angew. Physik. 17 (1964) 542.

[17] R.E. Leckenby, P.A. Trevalion, E.J. Robbins, Proc. R. Soc. Lond. A 280 (1964) 409.

[18] R.E. Leckenby, E.J. Robbins, Proc. R. Soc. Lond. A 291 (1966) 389.

[19] J.B. Anderson, R.P. Andres, J.B. Fenn, Adv. Chem. Phys. 10 (1966) 275.

[20] T.A. Milne, F.T. Greene, J. Chem. Phys. 47 (1967) 4095.

[21] H. Burghoff, J. Gspann, Z. Naturforsch. Pt. A 22 (1967) 684.

[22] G. Hortig, M. Muller, Z. Physik. 221 (1969) 119.

[23] M. Arshadi, R. Yamdagni, P. Kebarle, J. Phys. Chem. 74 (1970) 1475.

[24] D. Golomb, R.E. Good, R.F. Brown, J. Chem. Phys. 52 (1970) 1545.

[25] R.J. Gordon, Y.T. Lee, D.R. Herschba, J. Chem. Phys. 54 (1971) 2393.

[26] A.W. Castleman, Jr., I.N. Tang, Nature-Phys. Sci. 234 (1971) 129.

[27] I.N. Tang, H.R. Munkelwitz, A.W. Castleman, Jr., Nature-Phys. Sci. 230 (1971) 175.

[28] A.W. Castleman, Jr., I.N. Tang, H.R. Munkelwitz, Science 173 (1971) 1025.

[29] I.N. Tang, A.W. Castleman, Jr., J. Chem. Phys. 57 (1972) 3638.

[30] T.R. Dyke, B.J. Howard, Klempere.W, J. Chem. Phys. 56 (1972) 2442.

[31] J. Fricke, W.M. Jackson, W.L. Fite, J. Chem. Phys. 57 (1972) 580.

[32] G.D. Stein, J.A. Armstrong, J. Chem. Phys. 58 (1973) 1999.

[33] B. Raoult, J. Farges, Rev. Sci. Instrum. 44 (1973) 430.

[34] D.M. Mann, J. Appl. Phys. 44 (1973) 4950.

[35] J.M. Calo, Nature 248 (1974) 665.

[36] J.Q. Searcy, J.B. Fenn, J. Chem. Phys. 61 (1974) 5282.

[37] W.D. Knight, K. Clemenger, W.A. Deheer, W.A. Saunders, M.Y. Chou, M.L. Cohen, Phys. Rev. Lett. 52 (1984) 2141.

[38] H.W. Kroto, J.R. Heath, S.C. Obrien, R.F. Curl, R.E. Smalley, Nature 318 (1985) 162.

[39] B. Donn, J. Hecht, R. Khanna, J. Nuth, D. Stranz, A.B. Anderson, Surf. Sci. 106 (1981) 576.

[40] A. Léger, L.d. Hendecourt, N. Boccara, Polycyclic aromatic hydrocarbons and astrophysics, D. Reidel Pub. Co., Dordrecht ; Boston, Norwell, MA, U.S.A., 1987.

[41] D.J. McGinty, J. Chem. Phys. 55 (1971) 580.

[42] J.J. Burton, J. Chem. Soc. Farad. T 2 (1973) 540.

[43] J.K. Lee, J.A. Barker, F.F. Abraham, J. Chem. Phys. 58 (1973) 3166.

[44] L.S. Bartell, J. Phys. Chem. 99 (1995) 1080.

[45] S.H. Tolbert, A.P. Alivisatos, Annu. Rev. Phys. Chem. 46 (1995) 595.

[46] M. Boudart, Nature 372 (1994) 320.

[47] Z. Xu, F.S. Xiao, S.K. Purnell, O. Alexeev, S. Kawi, S.E. Deutsch, B.C. Gates, Nature 372 (1994) 346.

[48] S.N. Khanna, P. Jena, Phys. Rev. Lett. 69 (1992) 1664.

[49] W. Kratschmer, L.D. Lamb, K. Fostiropoulos, D.R. Huffman, Nature 347 (1990) 354.

[50] P. Jena, S.N. Khanna, B.K. Rao, M. Manninen, MRS Online Proceedings Library 206 (1990) null.

[51] O.F. Hagena, W. Obert, J. Chem. Phys. 56 (1972) 1793.

[52] S.B. Ryali, J.B. Fenn, Berich. Bunsen. Gesell 88 (1984) 245.

[53] R. Campargue, Rev. Sci. Instrum. 35 (1964) 111.

[54] D.E. Powers, S.G. Hansen, M.E. Geusic, A.C. Puiu, J.B. Hopkins, T.G. Dietz, M.A. Duncan, P.R.R. Langridgesmith, R.E. Smalley, J. Phys. Chem. 86 (1982) 2556.

[55] A.N. Patil, D.Y. Paithankar, N. Otsuka, R.P. Andres, Z. Phys. D: At., Mol. Clusters

26 (1993) 135.

[56] R.S. Bowles, J.J. Kolstad, J.M. Calo, R.P. Andres, Surf. Sci. 106 (1981) 117.

[57] H.R. Siekmann, C. Lüder, J. Faehrmann, H.O. Lutz, K.H. Meiwes-Broer, Z. Phys. D: At., Mol. Clusters 20 (1991) 417.

[58] W. Begemann, K.H. Meiwesbroer, H.O. Lutz, J. Phys-Paris 50 (1989) 133.

[59] P. Fayet, J. Wolf, L. Wöste, Phys. Rev. B: Condens. Matter 33 (1986) 6792.

[60] A.R. Waugh, J. Phys. D: Appl. Phys. 13 (1980) L203.

[61] P. Sudraud, C. Colliex, J. Vandewalle, J. Phys. Lett-Paris 40 (1979) L207.

[62] W. Wien, Ann. Phys.-Berlin 301 (1898) 440.

[63] G. Scoles, Atomic and molecular beam methods, Oxford University Press, New York, 1988.

[64] W.A. Deheer, P. Milani, Rev. Sci. Instrum. 62 (1991) 670.

[65] A.G. Marshall, C.L. Hendrickson, G.S. Jackson, Mass Spectrom. Rev. 17 (1998) 1.

[66] S. Bjornholm, J. Borggreen, O. Echt, K. Hansen, J. Pedersen, H.D. Rasmussen, Z. Phys. D: At., Mol. Clusters 19 (1991) 47.

[67] M. Brack, Rev. Mod. Phys. 65 (1993) 677.

[68] W.A. Deheer, W.D. Knight, M.Y. Chou, M.L. Cohen, Solid State Phys. 40 (1987) 93.

[69] W. Ekardt, Phys. Rev. Lett. 52 (1984) 1925.

[70] W. Ekardt, Phys. Rev. B: Condens. Matter 29 (1984) 1558.

[71] K. Clemenger, Phys. Rev. B: Condens. Matter 32 (1985) 1359.

[72] C. Brechignac, P. Cahuzac, F. Carlier, M. Defrutos, J. Leygnier, J. Chem. Soc. Faraday. T 86 (1990) 2525.

[73] I. Katakuse, T. Ichihara, Y. Fujita, T. Matsuo, T. Sakurai, H. Matsuda, Int. J. Mass Spectrom. Ion Processes 74 (1986) 33.

[74] G. Gantefor, M. Gausa, K.H. Meiwesbroer, H.O. Lutz, J. Chem. Soc., Faraday Trans. 86 (1990) 2483.

[75] D.G. Leopold, J. Ho, W.C. Lineberger, J. Chem. Phys. 86 (1987) 1715.

[76] C.L. Pettiette, S.H. Yang, M.J. Craycraft, J. Conceicao, R.T. Laaksonen, O. Cheshnovsky, R.E. Smalley, J. Chem. Phys. 88 (1988) 5377.

[77] C.Y. Cha, G. Gantefor, W. Eberhardt, J. Chem. Phys. 99 (1993) 6308.

[78] B.J. Winter, E.K. Parks, S.J. Riley, J. Chem. Phys. 94 (1991) 8618.

[79] S. Bjornholm, J. Borggreen, O. Echt, K. Hansen, J. Pedersen, H.D. Rasmussen, Phys. Rev. Lett. 65 (1990) 1627.

[80] T.P. Martin, T. Bergmann, H. Göhlich, T. Lange, Z. Phys. D: At., Mol. Clusters 19

(1991) 25.

[81] J. Pedersen, S. Bjornholm, J. Borggreen, K. Hansen, T.P. Martin, H.D. Rasmussen, Nature 353 (1991) 733.

[82] T.P. Martin, S. Bjornholm, J. Borggreen, C. Brechignac, P. Cahuzac, K. Hansen, J. Pedersen, Chem. Phys. Lett. 186 (1991) 53.

[83] O. Echt, K. Sattler, E. Recknagel, Phys. Rev. Lett. 47 (1981) 1121.

[84] A.L. Mackay, Acta Crystallographica 15 (1962) 916.

[85] J. Farges, M.F. Deferaudy, B. Raoult, G. Torchet, J. Chem. Phys. 84 (1986) 3491.

[86] L.L. Boyer, J.Q. Broughton, Phys. Rev. B: Condens. Matter 42 (1990) 11461.

[87] J.G. Allpress, J.V. Sanders, Aust. J. Phys. 23 (1970) 23.

[88] C. Rey, L.J. Gallego, M.P. Iniguez, J.A. Alonso, Physica B 179 (1992) 273.

[89] T.P. Martin, Phys. Rep. 273 (1996) 199.

[90] T.P. Martin, T. Bergmann, H. Göhlich, T. Lange, Chem. Phys. Lett. 176 (1991) 343.

[91] T.P. Martin, U. Naher, T. Bergmann, H. Gohlich, T. Lange, Chem. Phys. Lett. 183 (1991) 119.

[92] T.P. Martin, T. Bergmann, J. Chem. Phys. 90 (1989) 6664.

[93] D. Rayane, P. Melinon, B. Cabaud, A. Hoareau, B. Tribollet, M. Broyer, Phys. Rev. A: At. Mol. Opt. Phys. 39 (1989) 6056.

[94] T.P. Martin, U. Näher, H. Schaber, Chem. Phys. Lett. 199 (1992) 470.

[95] M. Sakurai, K. Watanabe, K. Sumiyama, K. Suzuki, J. Chem. Phys. 111 (1999) 235.

[96] M. Pellarin, B. Baguenard, J.L. Vialle, J. Lermé, M. Broyer, J. Miller, A. Perez, Chem. Phys. Lett. 217 (1994) 349.

[97] F.A. Reuse, S.N. Khanna, S. Bernal, Phys. Rev. B: Condens. Matter 52 (1995) R11650.

[98] M.B. Knickelbein, J. Chem. Phys. 115 (2001) 5957.

[99] F. Baletto, R. Ferrando, A. Fortunelli, F. Montalenti, C. Mottet, J. Chem. Phys. 116 (2002) 3856.

[100] F. Baletto, R. Ferrando, Rev. Mod. Phys. 77 (2005) 371.

[101] V. Rosato, M. Guillope, B. Legrand, Philos. Mag. A 59 (1989) 321.

[102] P. Weis, S. Gilb, P. Gerhardt, M.M. Kappes, Int. J. Mass spectrom. 216 (2002) 59.

[103] G. Vonhelden, M.T. Hsu, P.R. Kemper, M.T. Bowers, J. Chem. Phys. 95 (1991) 3835.

[104] P.R. Kemper, M.T. Bowers, J. Phys. Chem. 95 (1991) 5134.

[105] A.A. Shvartsburg, M.F. Jarrold, Chem. Phys. Lett. 261 (1996) 86.

[106] E. Oger, N.R.M. Crawford, R. Kelting, P. Weis, M.M. Kappes, R. Ahlrichs, Angew.

Chem. Int. Ed. 46 (2007) 8503.

[107] J. Farges, B. Raoult, G. Torchet, J. Chem. Phys. 59 (1973) 3454.

[108] B. Raoult, J. Farges, M.F. Deferaudy, G. Torchet, Philos. Mag. B 60 (1989) 881.

[109] D. Reinhard, B.D. Hall, P. Berthoud, S. Valkealahti, R. Monot, Phys. Rev. Lett. 79 (1997) 1459.

[110] D. Reinhard, B.D. Hall, D. Ugarte, R. Monot, Phys. Rev. B: Condens. Matter 55 (1997) 7868.

[111] C.Y. Ng, Adv. Chem. Phys. 52 (1983) 263.

[112] H. Haberland, H. Kornmeier, H. Langosch, M. Oschwald, G. Tanner, J. Chem. Soc., Faraday Trans. 86 (1990) 2473.

[113] K.J. Taylor, C.L. Pettiette, M.J. Craycraft, O. Chesnovsky, R.E. Smalley, Chem. Phys. Lett. 152 (1988) 347.

[114] G. Gantefor, M. Gausa, K.H. Meiwesbroer, H.O. Lutz, Faraday Discuss. 86 (1988) 197.

[115] K.J. Taylor, C.L. Pettiettehall, O. Cheshnovsky, R.E. Smalley, J. Chem. Phys. 96 (1992) 3319.

[116] W.A. Saunders, K. Clemenger, W.A. Deheer, W.D. Knight, Phys. Rev. B: Condens. Matter 32 (1985) 1366.

[117] W. de Heer, Rev. Mod. Phys. 65 (1993) 611.

[118] Z. Penzar, W. Ekardt, Z. Phys. D: At., Mol. Clusters 17 (1990) 69.

[119] M.M. Kappes, M. Schar, U. Rothlisberger, C. Yeretzian, E. Schumacher, Chem. Phys. Lett. 143 (1988) 251.

[120] J. Ho, K.M. Ervin, W.C. Lineberger, J. Chem. Phys. 93 (1990) 6987.

[121] I. Katakuse, T. Ichihara, Y. Fujita, T. Matsuo, T. Sakurai, H. Matsuda, Int. J. Mass Spectrom. Ion Processes 67 (1985) 229.

[122] C. Brechignac, P. Cahuzac, F. Carlier, M. Defrutos, J. Leygnier, J. Chem. Phys. 93 (1990) 7449.

[123] M. Manninen, J. Mansikkaaho, H. Nishioka, Y. Takahashi, Z. Phys. D: At., Mol. Clusters 31 (1994) 259.

[124] S. Kruckeberg, L. Schweikhard, J. Ziegler, G. Dietrich, K. Lutzenkirchen, C. Walther, J. Chem. Phys. 114 (2001) 2955.

[125] J.L. Martins, J. Buttet, R. Car, Phys. Rev. B: Condens. Matter 31 (1985) 1804.

[126] P. Buffat, J.P. Borel, Phys. Rev. A: At. Mol. Opt. Phys. 13 (1976) 2287.

[127] S.L. Lai, J.Y. Guo, V. Petrova, G. Ramanath, L.H. Allen, Phys. Rev. Lett. 77 (1996)

99.

[128] R.M. Lyndenbell, D.J. Wales, J. Chem. Phys. 101 (1994) 1460.

[129] R. Stephen Berry, T.L. Beck, H.L. Davis, J. Jellinek, Adv. Chem. Phys. 70 (1988) 75.

[130] M. Schmidt, R. Kusche, T. Hippler, J. Donges, W. Kronmuller, B. von Issendorff, H. Haberland, Phys. Rev. Lett. 86 (2001) 1191.

[131] D. Frenkel, B. Smit, Understanding molecular simulation : from algorithms to applications, Academic Press, San Diego, 2002.

[132] D.D. Frantz, J. Chem. Phys. 115 (2001) 6136.

[133] T.P. Martin, U. Naher, H. Schaber, U. Zimmermann, J. Chem. Phys. 100 (1994) 2322.

[134] C.E. Bottani, A.L. Bassi, B.K. Tanner, A. Stella, P. Tognini, P. Cheyssac, R. Kofman, Phys. Rev. B: Condens. Matter 59 (1999) 15601.

[135] A.A. Shvartsburg, M.F. Jarrold, Phys. Rev. Lett. 85 (2000) 2530.

[136] M. Schmidt, J. Donges, T. Hippler, H. Haberland, Phys. Rev. Lett. 90 (2003) 103401.

[137] J.L. Wang, G.H. Wang, F. Ding, H. Lee, W.F. Shen, J.J. Zhao, Chem. Phys. Lett. 341 (2001) 529.

[138] C.L. Cleveland, W.D. Luedtke, U. Landman, Phys. Rev. Lett. 81 (1998) 2036.

[139] C.L. Cleveland, W.D. Luedtke, U. Landman, Phys. Rev. B: Condens. Matter 60 (1999) 5065.

[140] Y.J. Lee, R.M. Nieminen, E.K. Lee, S. Kim, Comput. Phys. Commun. 142 (2001) 201.

[141] K. Joshi, D.G. Kanhere, S.A. Blundell, Phys. Rev. B: Condens. Matter 66 (2002) 155329.

[142] G.A. Breaux, R.C. Benirschke, T. Sugai, B.S. Kinnear, M.F. Jarrold, Phys. Rev. Lett. 91 (2003) 215508.

[143] S. Chacko, K. Joshi, D.G. Kanhere, S.A. Blundell, Phys. Rev. Lett. 92 (2004) 135506.

[144] J. Akola, M. Manninen, Phys. Rev. B: Condens. Matter 63 (2001) 193410.

[145] U. Naher, S. Bjornholm, S. Frauendorf, F. Garcias, C. Guet, Phys. Rep. 285 (1997) 245.

[146] W. Begemann, S. Dreihöfer, K.H. Meiwes-Broer, H.O. Lutz, Z. Phys. D: At., Mol. Clusters 3 (1986) 183.

[147] W. Begemann, K.H. Meiwes-Broer, H.O. Lutz, Phys. Rev. Lett. 56 (1986) 2248.

[148] C. Bréchignac, P. Cahuzac, J. Leygnier, R. Pflaum, J.P. Roux, J. Weiner, Z. Phys. D: At., Mol. Clusters 12 (1989) 199.

[149] C. Brechignac, P. Cahuzac, J. Leygnier, J. Weiner, J. Chem. Phys. 90 (1989) 1492.

[150] C. Brechignac, P. Cahuzac, F. Carlier, M. Defrutos, Phys. Rev. B: Condens. Matter 49 (1994) 2825.

[151] C. Brechignac, P. Cahuzac, F. Carlier, J. Leygnier, A. Sarfati, Phys. Rev. B: Condens. Matter 44 (1991) 11386.

[152] C. Yannouleas, U. Landman, C. Brechignac, P. Cahuzac, B. Concina, J. Leygnier, Phys. Rev. Lett. 89 (2002) 173403.

[153] T.P. Martin, U. Naher, H. Gohlich, T. Lange, Chem. Phys. Lett. 196 (1992) 113.

[154] C. Brechignac, P. Cahuzac, F. Carlier, J. Leygnier, Phys. Rev. Lett. 63 (1989) 1368.

[155] C. Brechignac, P. Cahuzac, F. Carlier, M. Defrutos, Phys. Rev. Lett. 64 (1990) 2893.

[156] C. Brechignac, in: E.B. Campbell, M. Larsson (Eds.), The physics and chemistry of clusters : proceedings of Nobel Symposium 117, World Scientific, Singapore ; River Edge, N.J., 2001, p. 278.

[157] T.P. Martin, J. Chem. Phys. 81 (1984) 4426.

[158] W.A. Saunders, Phys. Rev. Lett. 64 (1990) 3046.

[159] W.A. Saunders, N. Dam, Z. Phys. D: At., Mol. Clusters 20 (1991) 111.

[160] H. Koizumi, S. Sugano, Y. Ishii, Z. Phys. D: At., Mol. Clusters 26 (1993) 264.

[161] H. Koizumi, S. Sugano, Y. Ishii, Z. Phys. D: At., Mol. Clusters 28 (1993) 223.

[162] M. Nakamura, Y. Ishii, A. Tamura, S. Sugano, Phys. Rev. A: At. Mol. Opt. Phys. 42 (1990) 2267.

[163] C. Yannouleas, U. Landman, R.N. Barnett, in: W. Ekardt (Ed.), Metal Clusters, Wiley, Chichester ; New York, 1999, p. 145.

[164] M. Brack, A.S. Jensen, H.C. Pauli, Strutins.Vm, C.Y. Wong, J. Damgaard, Rev. Mod. Phys. 44 (1972) 320.

[165] R.N. Barnett, U. Landman, G. Rajagopal, Phys. Rev. Lett. 67 (1991) 3058.

[166] C. Brechignac, P. Cahuzac, F. Carlier, M. Defrutos, R.N. Barnett, U. Landman, Phys. Rev. Lett. 72 (1994) 1636.

[167] P. Blaise, S.A. Blundell, C. Guet, R.R. Zope, Phys. Rev. Lett. 87 (2001) 063401.

[168] P.B. Armentrout, Annu. Rev. Phys. Chem. 52 (2001) 423.

[169] M. Schlangen, H. Schwarz, J. Catal. 284 (2011) 126.

[170] S. Yang, K.M. Ervin, J. Chem. Phys. 108 (1998) 1757.

[171] D.K. Bohme, H. Schwarz, Angew. Chem. Int. Ed. 44 (2005) 2336.

[172] V. Blagojevic, M.J.Y. Jarvis, E. Flaim, G.K. Koyanagi, V.V. Lavrov, D.K. Bohme, Angew. Chem. Int. Ed. 42 (2003) 4923.

[173] L.D. Socaciu, J. Hagen, T.M. Bernhardt, L. Woste, U. Heiz, H. Hakkinen, U.

Landman, J. Am. Chem. Soc. 125 (2003) 10437.

[174] H. Hakkinen, U. Landman, J. Am. Chem. Soc. 123 (2001) 9704.

[175] D.M. Cox, R.O. Brickman, K. Creegan, A. Kaldor, Studies of the chemical-properties of size selected metal-clusters - kinetics and saturation, Symp on Clusters and Cluster-Assembled Materials, Boston, MA, 1990, p. 43.

[176] D.M. Cox, R. Brickman, K. Creegan, A. Kaldor, Z. Phys. D: At., Mol. Clusters 19 (1991) 353.

[177] S.M. Lang, T.M. Bernhardt, R.N. Barnett, U. Landman, J. Phys. Chem. C 115 (2011) 6788.

[178] S.M. Lang, T.M. Bernhardt, R.N. Barnett, U. Landman, Angew. Chem. Int. Ed. 49 (2010) 980.

[179] M. Moseler, H. Hakkinen, U. Landman, Phys. Rev. Lett. 89 (2002) 176103.

[180] A. Sanchez, S. Abbet, U. Heiz, W.D. Schneider, H. Hakkinen, R.N. Barnett, U. Landman, J. Phys. Chem. A 103 (1999) 9573.

[181] H. Hakkinen, W. Abbet, A. Sanchez, U. Heiz, U. Landman, Angew. Chem. Int. Ed. 42 (2003) 1297.

[182] A.M. Ferrari, G. Pacchioni, J. Phys. Chem. 100 (1996) 9032.

[183] M. Kulawik, N. Nilius, H.J. Freund, Phys. Rev. Lett. 96 (2006) 036103.

[184] L. Giordano, G. Pacchioni, Phys. Chem. Chem. Phys. 8 (2006) 3335.

[185] J. Kolehmainen, H. Hakkinen, M. Manninen, Z. Phys. D: At., Mol. Clusters 40 (1997) 306.

[186] D.Y. Sun, X.G. Gong, J. Phys.: Condens. Matter 9 (1997) 10555.

[187] B. Huber, P. Koskinen, H. Hakkinen, M. Moseler, Nat. Mater. 5 (2006) 44.

[188] M. Haruta, Cattech 6 (2002) 102.

[189] D. Cunningham, S. Tsubota, N. Kamijo, M. Haruta, Res. Chem. Intermed. 19 (1993) 1.

[190] D. Ricci, A. Bongiorno, G. Pacchioni, U. Landman, Phys. Rev. Lett. 97 (2006) 036106.

[191] M. Sterrer, T. Risse, M. Heyde, H.-P. Rust, H.-J. Freund, Phys. Rev. Lett. 98 (2007) 206103.

[192] H. Gronbeck, P. Broqvist, Surf. Sci. 600 (2006) L214.

[193] C.R. Henry, Surf. Sci. 223 (1989) 519.

[194] C.R. Henry, C. Chapon, C. Duriez, J. Chem. Phys. 95 (1991) 700.

[195] M.A. Roettgen, S. Abbet, K. Judai, J.-M. Antonietti, A.S. Woerz, M. Arenz, C.R.

Henry, U. Heiz, J. Am. Chem. Soc. 129 (2007) 9635.

[196] J. Hagen, L.D. Socaciu, M. Elijazyfer, U. Heiz, T.M. Bernhardt, L. Woste, Phys. Chem. Chem. Phys. 4 (2002) 1707.

[197] J. Hagen, L.D. Socaciu, J. Le Roux, D. Popolan, T.M. Bernhardt, L. Woste, R. Mitric, H. Noack, V. Bonacic-Koutecky, J. Am. Chem. Soc. 126 (2004) 3442.

[198] D.A.H. Cunningham, W. Vogel, M. Haruta, Catal. Lett. 63 (1999) 43.

[199] M. Date, M. Haruta, J. Catal. 201 (2001) 221.

[200] M. Date, M. Okumura, S. Tsubota, M. Haruta, Angew. Chem. Int. Ed. 43 (2004) 2129.

[201] J.T. Calla, R.J. Davis, J. Catal. 241 (2006) 407.

[202] L.D. Marks, Rep. Prog. Phys. 57 (1994) 603.

[203] E. Schrodinger, Ann. Phys.-Berlin 79 (1926) 361.

[204] M. Born, R. Oppenheimer, Ann. Phys.-Berlin 84 (1927) 0457.

[205] D.R. Hartree, P. Camb Philos. Soc. 24 (1928) 89.

[206] D.R. Hartree, P. Camb Philos. Soc. 24 (1928) 111.

[207] D.R. Hartree, P. Camb Philos. Soc. 24 (1928) 426.

[208] V. Fock, Z. Physik. 61 (1930) 126.

[209] W. Pauli, Z. Physik. 31 (1925) 765.

[210] W. Pauli, Phys. Rev. 58 (1940) 716.

[211] J.C. Slater, Phys. Rev. 34 (1929) 1293.

[212] A. Szabo, N.S. Ostlund, Modern Quantum Chemistry, Dover Publications, Newyork, 1996.

[213] C. Moller, M.S. Plesset, Phys. Rev. 46 (1934) 0618.

[214] L.H. Thomas, P. Camb Philos. Soc. 23 (1927) 542.

[215] E. Fermi, Atti R. Accad. Lincei 6 (1927) 602.

[216] P.A.M. Dirac, P. Camb Philos. Soc. 26 (1930) 376.

[217] C.F.v. Weizsäcker, Z. Physik. 96 (1935) 431.

[218] P. Hohenberg, W. Kohn, Phys. Rev. B: Condens. Matter 136 (1964) B864.

[219] W. Kohn, L.J. Sham, Phys. Rev. 140 (1965) A1133.

[220] A.J. Freeman, E. Wimmer, Annu. Rev. Mater. Sci. 25 (1995) 7.

[221] D.M. Ceperley, B.J. Alder, Phys. Rev. Lett. 45 (1980) 566.

[222] L. Hedin, B.I. Lundqvist, J. Phys. C: Solid State 4 (1971) 2064.

[223] S.H. Vosko, L. Wilk, M. Nusair, Can. J. Phys. 58 (1980) 1200.

[224] J.P. Perdew, A. Zunger, Phys. Rev. B: Condens. Matter 23 (1981) 5048.

[225] L.A. Cole, J.P. Perdew, Phys. Rev. A: At. Mol. Opt. Phys. 25 (1982) 1265.

[226] J.P. Perdew, Y. Wang, Phys. Rev. B: Condens. Matter 45 (1992) 13244.

[227] D.C. Langreth, M.J. Mehl, Phys. Rev. B: Condens. Matter 28 (1983) 1809.

[228] A.D. Becke, Phys. Rev. A: At. Mol. Opt. Phys. 38 (1988) 3098.

[229] Y.K. Zhang, W.T. Yang, Phys. Rev. Lett. 80 (1998) 890.

[230] B. Hammer, L.B. Hansen, J.K. Norskov, Phys. Rev. B: Condens. Matter 59 (1999) 7413.

[231] Z.G. Wu, R.E. Cohen, Phys. Rev. B: Condens. Matter 73 (2006).

[232] J.P. Perdew, J.A. Chevary, S.H. Vosko, K.A. Jackson, M.R. Pederson, D.J. Singh, C. Fiolhais, Phys. Rev. B: Condens. Matter 46 (1992) 6671.

[233] J.P. Perdew, J.A. Chevary, S.H. Vosko, K.A. Jackson, M.R. Pederson, D.J. Singh, C. Fiolhais, Phys. Rev. B 48 (1993) 4978.

[234] J.P. Perdew, K. Burke, M. Ernzerhof, Phys. Rev. Lett. 77 (1996) 3865.

[235] J.P. Perdew, K. Burke, M. Ernzerhof, Phys. Rev. Lett. 78 (1997) 1396.

[236] J.P. Perdew, S. Kurth, A. Zupan, P. Blaha, Phys. Rev. Lett. 82 (1999) 2544.

[237] A.D. Boese, N.C. Handy, J. Chem. Phys. 116 (2002) 9559.

[238] J.M. Tao, J.P. Perdew, V.N. Staroverov, G.E. Scuseria, Phys. Rev. Lett. 91 (2003) 146401.

[239] J.P. Perdew, A. Ruzsinszky, G.I. Csonka, L.A. Constantin, J. Sun, Phys. Rev. Lett. 103 (2009) 026403.

[240] T. Van Voorhis, G.E. Scuseria, J. Chem. Phys. 109 (1998) 400.

[241] Z. Yan, D.G. Truhlar, J. Chem. Phys. 125 (2006) 194101.

[242] A.D. Becke, J. Chem. Phys. 98 (1993) 5648.

[243] C.T. Lee, W.T. Yang, R.G. Parr, Phys. Rev. B: Condens. Matter 37 (1988) 785.

[244] C. Adamo, V. Barone, J. Chem. Phys. 110 (1999) 6158.

[245] J. Heyd, G.E. Scuseria, M. Ernzerhof, J. Chem. Phys. 118 (2003) 8207.

[246] O.A. Vydrov, G.E. Scuseria, J. Chem. Phys. 125 (2006) 234109.

[247] O.A. Vydrov, J. Heyd, A.V. Krukau, G.E. Scuseria, J. Chem. Phys. 125 (2006) 074106.

[248] T. Yanai, D.P. Tew, N.C. Handy, Chem. Phys. Lett. 393 (2004) 51.

[249] J.C. Slater, Phys. Rev. 36 (1930) 0057.

[250] M.J. Frisch, G.W. Trucks, H.B. Schlegel, G.E. Scuseria, M.A. Robb, J.R. Cheeseman, V.G. Zakrzewski, J.A.M. Jr., R.E. Stratmann, J.C. Burant, S. Dapprich, J.M. Millam, A.D. Daniels, K.N. Kudin, M.C. Strain, O. Farkas, J. Tomasi, V. Barone, M. Cossi, R.

Cammi, B. Mennucci, C. Pomelli, C. Adamo, S. Clifford, J. Ochterski, G.A. Petersson, P.Y. Ayala, Q. Cui, K. Morokuma, P. Salvador, J.J. Dannenberg, D.K. Malick, A.D. Rabuck, K. Raghavachari, J.B. Foresman, J. Cioslowski, J.V. Ortiz, A.G. Baboul, B.B. Stefanov, G. Liu, A. Liashenko, P. Piskorz, I. Komaromi, R. Gomperts, R.L. Martin, D.J. Fox, T. Keith, M.A. Al-Laham, C.Y. Peng, A. Nanayakkara, M. Challacombe, P.M.W. Gill, B. Johnson, W. Chen, M.W. Wong, J.L. Andres, C. Gonzalez, M. Head-Gordon, E.S. Replogle, J.A. Pople, *Gaussian 98*. Gaussian, Inc., Pittsburgh, PA, 1998.

[251] E. Clementi, M. Yoshimine, C.C. Roothaan, Phys. Rev. 127 (1962) 1618.

[252] E. Clementi, D.L. Raimondi, J. Chem. Phys. 38 (1963) 2686.

[253] S. Huzinaga, J. Chem. Phys. 42 (1965) 1293.

[254] J.L. Whitten, J. Chem. Phys. 44 (1966) 359.

[255] W.J. Hehre, Ab initio molecular orbital theory, Wiley, New York, 1986.

[256] J. Foresman, A.E. Frisch, Exploring chemistry with electronic structure methods, Gaussian, Inc, Pittsburgh, PA, 1996.

[257] C. Kittel, Introduction to solid state physics, Wiley, Hoboken, NJ, 2005.

[258] N.W. Ashcroft, N.D. Mermin, Solid state physics, Holt, New York,, 1976.

[259] R.P. Feynman, Phys. Rev. 56 (1939) 340.

[260] H.J. Monkhorst, J.D. Pack, Phys. Rev. B: Condens. Matter 13 (1976) 5188.

[261] M.C. Payne, M.P. Teter, D.C. Allan, T.A. Arias, J.D. Joannopoulos, Rev. Mod. Phys. 64 (1992) 1045.

[262] J.C. Phillips, Phys. Rev. 112 (1958) 685.

[263] J.C. Phillips, L. Kleinman, Phys. Rev. 116 (1959) 287.

[264] M.L. Cohen, V. Heine, in: F.S. Henry Ehrenreich, T. David (Eds.), Solid state physics: advances in research and applications, Academic Press, 1970, p. 37.

[265] N.S. Mosyagin, A.V. Titov, Z. Latajka, Int. J. Quantum Chem 63 (1997) 1107.

[266] R. Car, Quant. Struct.-Act. Relat. 21 (2002) 97.

[267] P.E. Blochl, Phys. Rev. B: Condens. Matter 41 (1990) 5414.

[268] D. Vanderbilt, Phys. Rev. B: Condens. Matter 41 (1990) 7892.

[269] G. Kresse, J. Hafner, J. Phys.: Condens. Matter 6 (1994) 8245.

[270] P.E. Blochl, Phys Rev B Condens Matter 50 (1994) 17953.

[271] G. Kresse, D. Joubert, Phys. Rev. B: Condens. Matter 59 (1999) 1758.

[272] L. Kleinman, D.M. Bylander, Phys. Rev. Lett. 48 (1982) 1425.

[273] R.M. Martin, Electronic structure : basic theory and practical methods, Cambridge

University Press, Cambridge, UK ; New York, 2004.

[274] G. Kresse, J. Hafner, Phys. Rev. B: Condens. Matter 47 (1993) 558.

[275] G. Kresse, J. Hafner, Phys. Rev. B: Condens. Matter 49 (1994) 14251.

[276] G. Kresse, J. Furthmüller, Comp. Mater. Sci. 6 (1996) 15.

[277] G. Kresse, J. Furthmuller, Phys. Rev. B: Condens. Matter 54 (1996) 11169.

[278] VASP4.2 Code, http://cms.mpi.univie.ac.at/vasp/, Wien, Austria, 2008.

[279] D.D. Koelling, B.N. Harmon, J. Phys. C: Solid State 10 (1977) 3107.

[280] E.R. Davidson, J. Comp. Phys. 17 (1975) 87.

[281] M.P. Teter, M.C. Payne, D.C. Allan, Phys. Rev. B: Condens. Matter 40 (1989) 12255.

[282] D. Bylander, L. Kleinman, S. Lee, Phys. Rev. B: Condens. Matter 42 (1990) 1394.

[283] P. Pulay, Chem. Phys. Lett. 73 (1980) 393.

[284] D.M. Wood, A. Zunger, J. Phys. A: Math. Gen. 18 (1985) 1343.

[285] D.D. Johnson, Phys. Rev. B: Condens. Matter 38 (1988) 12807.

[286] U. von Barth, L. Hedin, J. Phys. C: Solid State 5 (1972) 1629.

[287] R. Armiento, A.E. Mattsson, Phys. Rev. B: Condens. Matter 72 (2005) 085108.

[288] J. Sun, M. Marsman, G.I. Csonka, A. Ruzsinszky, P. Hao, Y.-S. Kim, G. Kresse, J.P. Perdew, Phys. Rev. B: Condens. Matter 84 (2011) 035117.

[289] A.D. Becke, E.R. Johnson, J. Chem. Phys. 124 (2006) 221101.

[290] F. Tran, P. Blaha, Phys. Rev. Lett. 102 (2009) 226401.

[291] P.J. Stephens, F.J. Devlin, C.F. Chabalowski, M.J. Frisch, J. Phys. Chem. 98 (1994) 11623.

[292] J.P. Perdew, M. Emzerhof, K. Burke, J. Chem. Phys. 105 (1996) 9982.

[293] J. Paier, R. Hirschl, M. Marsman, G. Kresse, J. Chem. Phys. 122 (2005) 234102.

[294] J. Paier, M. Marsman, K. Hummer, G. Kresse, I.C. Gerber, J.G. Angyan, J. Chem. Phys. 124 (2006) 154709.

[295] J. Paier, M. Marsman, G. Kresse, J. Chem. Phys. 127 (2007) 024103.

[296] T. Oda, A. Pasquarello, R. Car, Phys. Rev. Lett. 80 (1998) 3622.

[297] D. Hobbs, G. Kresse, J. Hafner, Phys. Rev. B: Condens. Matter 62 (2000) 11556.

[298] S.L. Dudarev, G.A. Botton, S.Y. Savrasov, C.J. Humphreys, A.P. Sutton, Phys. Rev. B: Condens. Matter 57 (1998) 1505.

[299] A.I. Liechtenstein, V.I. Anisimov, J. Zaanen, Phys. Rev. B: Condens. Matter 52 (1995) R5467.

[300] S. Grimme, J. Comput. Chem. 27 (2006) 1787.

[301] S. Nose, Mol. Phys. 52 (1984) 255.

[302] S. Nose, J. Chem. Phys. 81 (1984) 511.

[303] G. Mills, H. Jonsson, G.K. Schenter, Surf. Sci. 324 (1995) 305.

[304] H. Jonsson, G. Mills, K.W. Jacobsen, in: J.B. Bruce, C. Giovanni, F.C. David (Eds.), Classical and Quantum Dynamics in Condensed Phase Simulations, World scientific, 1998, p. 385.

[305] N.D. Mermin, Phys. Rev. 137 (1965) A1441.

[306] C. Fu, K. Ho, Phys. Rev. B: Condens. Matter 28 (1983) 5480.

[307] M. Methfessel, A.T. Paxton, Phys. Rev. B: Condens. Matter 40 (1989) 3616.

[308] P.E. Blochl, O. Jepsen, O.K. Andersen, Phys. Rev. B: Condens. Matter 49 (1994) 16223.

[309] G. Vonhelden, M.T. Hsu, N. Gotts, M.T. Bowers, J. Phys. Chem. 97 (1993) 8182.

[310] M.F. Jarrold, V.A. Constant, Phys. Rev. Lett. 67 (1991) 2994.

[311] M.F. Jarrold, J.E. Bower, J. Chem. Phys. 96 (1992) 9180.

[312] X.L. Zhu, X.C. Zeng, J. Chem. Phys. 118 (2003) 3558.

[313] K. Raghavachari, J. Chem. Phys. 84 (1986) 5672.

[314] K. Raghavachari, C.M. Rohlfing, J. Chem. Phys. 89 (1988) 2219.

[315] C.M. Rohlfing, K. Raghavachari, Chem. Phys. Lett. 167 (1990) 559.

[316] K. Raghavachari, C.M. Rohlfing, J. Chem. Phys. 94 (1991) 3670.

[317] K. Raghavachari, C.M. Rohlfing, Chem. Phys. Lett. 198 (1992) 521.

[318] K.M. Ho, A.A. Shvartsburg, B.C. Pan, Z.Y. Lu, C.Z. Wang, J.G. Wacker, J.L. Fye, M.F. Jarrold, Nature 392 (1998) 582.

[319] B. Liu, Z.Y. Lu, B.C. Pan, C.Z. Wang, K.M. Ho, A.A. Shvartsburg, M.F. Jarrold, J. Chem. Phys. 109 (1998) 9401.

[320] L. Mitas, J.C. Grossman, I. Stich, J. Tobik, Phys. Rev. Lett. 84 (2000) 1479.

[321] J.M. Hunter, J.L. Fye, M.F. Jarrold, J.E. Bower, Phys. Rev. Lett. 73 (1994) 2063.

[322] S. Li, R.J. Vanzee, W. Weltner, K. Raghavachari, Chem. Phys. Lett. 243 (1995) 275.

[323] C.S. Xu, T.R. Taylor, G.R. Burton, D.M. Neumark, J. Chem. Phys. 108 (1998) 1395.

[324] E.C. Honea, A. Ogura, C.A. Murray, K. Raghavachari, W.O. Sprenger, M.F. Jarrold, W.L. Brown, Nature 366 (1993) 42.

[325] A.A. Shvartsburg, B. Liu, Z.Y. Lu, C.Z. Wang, M.F. Jarrold, K.M. Ho, Phys. Rev. Lett. 83 (1999) 2167.

[326] G.R. Burton, C.S. Xu, C.C. Arnold, D.M. Neumark, J. Chem. Phys. 104 (1996) 2757.

[327] S. Ogut, J.R. Chelikowsky, Phys. Rev. B: Condens. Matter 55 (1997) R4914.

[328] A.A. Shvartsburg, M.F. Jarrold, Phys. Rev. A: At. Mol. Opt. Phys. 60 (1999) 1235.

[329] M. Watanabe, Y. Saito, S. Nishigaki, T. Noda, Jpn. J. Appl. Phys. 1 27 (1988) 344.

[330] P.W. Deutsch, L.A. Curtiss, J.P. Blaudeau, Chem. Phys. Lett. 270 (1997) 413.

[331] W.L. Brown, R.R. Freeman, K. Raghavachari, M. Schluter, Science 235 (1987) 860.

[332] Z.Y. Lu, C.Z. Wang, K.M. Ho, Phys. Rev. B: Condens. Matter 61 (2000) 2329.

[333] E.F. Archibong, A. St-Amant, J. Chem. Phys. 109 (1998) 962.

[334] W. Qin, Q.J. Zang, W.C. Lu, C.Z. Wang, K.M. Ho, Chemical Research in Chinese Universities 27 (2011) 313.

[335] S. Yoo, X.C. Zeng, J. Chem. Phys. 124 (2006) 184309.

[336] L.Z. Zhao, W.C. Lu, W. Qin, Q.J. Zang, C.Z. Wang, K.M. Ho, Chem. Phys. Lett. 455 (2008) 225.

[337] S. Bulusu, S. Yoo, X.C. Zeng, J. Chem. Phys. 122 (2005) 164305.

[338] C. Majumder, V. Kumar, H. Mizuseki, Y. Kawazoe, Phys. Rev. B: Condens. Matter 64 (2001) 233405.

[339] Y. Saito, T. Noda, Z. Phys. D: At., Mol. Clusters 12 (1989) 225.

[340] A.A. Shvartsburg, M.F. Jarrold, Chem. Phys. Lett. 317 (2000) 615.

[341] J. Mühlbach, K. Sattler, P. Pfau, E. Recknagel, Phys. Lett. A 87 (1982) 415.

[342] Y. Saito, K. Yamauchi, K. Mihama, T. Noda, Jpn. J. Appl. Phys. 2 21 (1982) L396.

[343] K. LaiHing, R.G. Wheeler, W.L. Wilson, M.A. Duncan, J. Chem. Phys. 87 (1987) 3401.

[344] G. Gantefor, M. Gausa, K.H. Meiwesbroer, H.O. Lutz, Z. Phys. D: At., Mol. Clusters 12 (1989) 405.

[345] C. Luder, K.H. Meiwes-Broer, Chem. Phys. Lett. 294 (1998) 391.

[346] Y. Negishi, H. Kawamata, A. Nakajima, K. Kaya, J. Electron. Spectrosc. Relat. Phenom. 106 (2000) 117.

[347] R.W. Farley, P. Ziemann, A.W. Castleman, Z. Phys. D: At., Mol. Clusters 14 (1989) 353.

[348] A. Hoareau, P. Melinon, B. Cabaud, D. Rayane, B. Tribollet, M. Broyer, Chem. Phys. Lett. 143 (1988) 602.

[349] K. Balasubramanian, Chem. Rev. 90 (1990) 93.

[350] K. Balasubramanian, K.S. Pitzer, J. Chem. Phys. 78 (1983) 321.

[351] K.S. Pitzer, K. Balasubramanian, J. Phys. Chem. 86 (1982) 3068.

[352] K. Balasubramanian, D. Majumdar, J. Chem. Phys. 115 (2001) 8795.

[353] D.G. Dai, K. Balasubramanian, J. Chem. Phys. 96 (1992) 8345.

[354] D. Dai, K. Balasubramanian, J. Phys. Chem. 96 (1992) 9236.

[355] D.G. Dai, K. Balasubramanian, Chem. Phys. Lett. 271 (1997) 118.

[356] C.Y. Zhao, K. Balasubramanian, J. Chem. Phys. 116 (2002) 10287.

[357] K. Balasubramanian, J. Chem. Phys. 85 (1986) 3401.

[358] B. Wang, L.M. Molina, M.J. Lopez, A. Rubio, J.A. Alonso, M.J. Stott, Ann. Phys.-Berlin 7 (1998) 107.

[359] L.M. Molina, M.J. Ldpez, A. Rubio, L.C. BalbAs, J.A. Alonso, Adv. Quantum Chem. 33 (1998) 329.

[360] M.P. Iniguez, M.J. Lopez, J.A. Alonso, J.M. Soler, Z. Phys. D: At., Mol. Clusters 11 (1989) 163.

[361] S.K. Lai, P.J. Hsu, K.L. Wu, W.K. Liu, M. Iwamatsu, J. Chem. Phys. 117 (2002) 10715.

[362] R.P. Gupta, Phys. Rev. B: Condens. Matter 23 (1981) 6265.

[363] D.D. Stranz, R.K. Khanna, J. Chem. Phys. 74 (1981) 2116.

[364] P.J. Hay, W.R. Wadt, J. Chem. Phys. 82 (1985) 270.

[365] W.R. Wadt, P.J. Hay, J. Chem. Phys. 82 (1985) 284.

[366] P.J. Hay, W.R. Wadt, J. Chem. Phys. 82 (1985) 299.

[367] T.P. Martin, H. Schaber, J. Chem. Phys. 83 (1985) 855.

[368] B. Waldschmidt, M. Turra, R. Schaefer, Z. Phys. Chem. 221 (2007) 1569.

[369] A. Hirsch, Z. Chen, H. Jiao, Angew. Chem. 39 (2000) 3915.

[370] C. Rajesh, C. Majumder, Chem. Phys. Lett. 430 (2006) 101.

[371] V. Kumar, Y. Kawazoe, Phys. Rev. Lett. 87 (2001) 045503.

[372] C. Majumder, S.K. Kulshreshtha, Phys. Rev. B: Condens. Matter 70 (2004) 245426.

[373] S. Nigam, C. Majumder, S.K. Kulshreshtha, J. Chem. Phys. 121 (2004) 7756.

[374] C. Majumder, S.K. Kulshreshtha, Phys. Rev. B: Condens. Matter 70 (2004) 125416.

[375] K. Koyasu, M. Akutsu, M. Mitsui, A. Nakajima, J. Am. Chem. Soc. 127 (2005) 4998.

[376] H. Kawamura, V. Kumar, Y. Kawazoe, Phys. Rev. B: Condens. Matter 71 (2005) 075423.

[377] V. Kumar, T. Briere, Y. Kawazoe, Phys. Rev. B: Condens. Matter 68 (2003) 155412.

[378] V. Kumar, Y. Kawazoe, Appl. Phys. Lett. 83 (2003) 2677.

[379] V. Kumar, Y. Kawazoe, Phys. Rev. Lett. 88 (2002) 235504.

[380] V. Kumar, Y. Kawazoe, Appl. Phys. Lett. 80 (2002) 859.

[381] E.N. Esenturk, J. Fettinger, B. Eichhorn, Chem. Commun. (2005) 247.

[382] X. Zhang, G.L. Li, X.P. Xing, X. Zhao, Z.C. Tang, Z. Gao, Rapid Commun. Mass Spectrom. 15 (2001) 2399.

[383] X.P. Xing, Z.X. Tian, H.T. Liu, Z.C. Tang, Rapid Commun. Mass Spectrom. 17 (2003) 1411.

[384] E.N. Esenturk, J. Fettinger, Y.F. Lam, B. Eichhorn, Angew. Chem. Int. Ed. 43 (2004) 2132.

[385] V. Kumar, A.K. Singh, Y. Kawazoe, Nano Lett. 4 (2004) 677.

[386] S. Neukermans, E. Janssens, Z.F. Chen, R.E. Silverans, P.V. Schleyer, P. Lievens, Phys. Rev. Lett. 92 (2004) 163401.

[387] D.-L. Chen, W.Q. Tian, C.-C. Sun, Phys. Rev. A: At. Mol. Opt. Phys. 75 (2007) 013201.

[388] J.-P. Dognon, C. Clavaguera, P. Pyykko, Angew. Chem. Int. Ed. 46 (2007) 1427.

[389] V. Kumar, Y. Kawazoe, Scripta Mater. 44 (2001) 1949.

[390] H.P. Cheng, R.S. Berry, R.L. Whetten, Phys. Rev. B: Condens. Matter 43 (1991) 10647.

[391] J. Li, X. Li, H.J. Zhai, L.S. Wang, Science 299 (2003) 864.

[392] B. Waldschmidt, S. Barman, C. Rajesh, C. Majumder, G.P. Das, R. Schaefer, Phys. Rev. B: Condens. Matter 79 (2009) 045422.

[393] M.C. Daniel, D. Astruc, Chem. Rev. 104 (2004) 293.

[394] R. Sardar, A.M. Funston, P. Mulvaney, R.W. Murray, Langmuir 25 (2009) 13840.

[395] M. Haruta, Catal. Today 36 (1997) 153.

[396] M. Haruta, T. Kobayashi, H. Sano, N. Yamada, Chem. Lett. (1987) 405.

[397] G.J. Hutchings, M. Haruta, Appl. Catal., A 291 (2005) 2.

[398] M. Haruta, M. Date, Appl. Catal., A 222 (2001) 427.

[399] G.C. Bond, Catal. Today 72 (2002) 5.

[400] G.C. Bond, D.T. Thompson, Catal. Rev. 41 (1999) 319.

[401] G.J. Hutchings, J. Catal. 96 (1985) 292.

[402] B. Nkosi, M.D. Adams, N.J. Coville, G.J. Hutchings, J. Catal. 128 (1991) 378.

[403] B. Nkosi, N.J. Coville, G.J. Hutchings, M.D. Adams, J. Friedl, F.E. Wagner, J. Catal. 128 (1991) 366.

[404] T. Hayashi, K. Tanaka, M. Haruta, J. Catal. 178 (1998) 566.

[405] L. Prati, M. Rossi, J. Catal. 176 (1998) 552.

[406] A. Corma, P. Serna, Science 313 (2006) 332.

[407] M. Valden, X. Lai, D.W. Goodman, Science 281 (1998) 1647.

[408] J. Guzman, B.C. Gates, J. Am. Chem. Soc. 126 (2004) 2672.

[409] C.L. Cleveland, U. Landman, T.G. Schaaff, M.N. Shafigullin, P.W. Stephens, R.L.

Whetten, Phys. Rev. Lett. 79 (1997) 1873.

[410] H. Hakkinen, U. Landman, Phys. Rev. B: Condens. Matter 62 (2000) R2287.

[411] F. Furche, R. Ahlrichs, P. Weis, C. Jacob, S. Gilb, T. Bierweiler, M.M. Kappes, J. Chem. Phys. 117 (2002) 6982.

[412] K. Koga, H. Takeo, T. Ikeda, K. Ohshima, Phys. Rev. B: Condens. Matter 57 (1998) 4053.

[413] H. Hakkinen, M. Moseler, U. Landman, Phys. Rev. Lett. 89 (2002) 033401.

[414] B. Palpant, B. Prevel, J. Lerme, E. Cottancin, M. Pellarin, M. Treilleux, A. Perez, J.L. Vialle, M. Broyer, Phys. Rev. B: Condens. Matter 57 (1998) 1963.

[415] J.J. Zhao, X.S. Chen, G.G. Wang, Phys. Lett. A 189 (1994) 223.

[416] H. Handschuh, G. Gantefor, P.S. Bechthold, W. Eberhardt, J. Chem. Phys. 100 (1994) 7093.

[417] I.L. Garzon, A. PosadaAmarillas, Phys. Rev. B: Condens. Matter 54 (1996) 11796.

[418] J.M. Soler, M.R. Beltran, K. Michaelian, I.L. Garzon, P. Ordejon, D. Sanchez-Portal, E. Artacho, Phys. Rev. B: Condens. Matter 61 (2000) 5771.

[419] O.D. Haberlen, S.C. Chung, M. Stener, N. Rosch, J. Chem. Phys. 106 (1997) 5189.

[420] I.L. Garzon, K. Michaelian, M.R. Beltran, A. Posada-Amarillas, P. Ordejon, E. Artacho, D. Sanchez-Portal, J.M. Soler, Phys. Rev. Lett. 81 (1998) 1600.

[421] R.N. Barnett, C.L. Cleveland, H. Hakkinen, W.D. Luedtke, C. Yannouleas, U. Landman, Eur. Phys. J. D 9 (1999) 95.

[422] J.J. BelBruno, Heteroat. Chem 9 (1998) 651.

[423] N.T. Wilson, R.L. Johnston, Eur. Phys. J. D 12 (2000) 161.

[424] T.X. Li, S.Y. Yin, Y.L. Ji, B.L. Wang, G.H. Wang, J.J. Zhao, Phys. Lett. A 267 (2000) 403.

[425] T.G. Schaaff, M.N. Shafigullin, J.T. Khoury, I. Vezmar, R.L. Whetten, W.G. Cullen, P.N. First, C. GutierrezWing, J. Ascensio, M.J. JoseYacaman, J. Phys. Chem. B 101 (1997) 7885.

[426] P. Weis, T. Bierweiler, S. Gilb, M.M. Kappes, Chem. Phys. Lett. 355 (2002) 355.

[427] G. Dietrich, S. Kruckeberg, K. Lutzenkirchen, L. Schweikhard, C. Walther, J. Chem. Phys. 112 (2000) 752.

[428] H. Hakkinen, B. Yoon, U. Landman, X. Li, H.J. Zhai, L.S. Wang, J. Phys. Chem. A 107 (2003) 6168.

[429] H. Gronbeck, W. Andreoni, Chem. Phys. 262 (2000) 1.

[430] S. Gilb, P. Weis, F. Furche, R. Ahlrichs, M.M. Kappes, J. Chem. Phys. 116 (2002)

4094.
[431] J.M. Gottfried, K.J. Schmidt, S.L.M. Schroeder, K. Christmann, Surf. Sci. 511 (2002) 65.
[432] B. Yoon, H. Hakkinen, U. Landman, J. Phys. Chem. A 107 (2003) 4066.
[433] X.L. Ding, Z.Y. Li, J.L. Yang, J.G. Hou, Q.S. Zhu, J. Chem. Phys. 120 (2004) 9594.
[434] T.H. Lee, K.M. Ervin, J. Phys. Chem. 98 (1994) 10023.
[435] B.E. Salisbury, W.T. Wallace, R.L. Whetten, Chem. Phys. 262 (2000) 131.
[436] D. Stolcic, M. Fischer, G. Gantefor, Y.D. Kim, Q. Sun, P. Jena, J. Am. Chem. Soc. 125 (2003) 2848.
[437] Y.D. Kim, M. Fischer, G. Gantefor, Chem. Phys. Lett. 377 (2003) 170.
[438] W. Huang, H.-J. Zhai, L.-S. Wang, J. Am. Chem. Soc. 132 (2010) 4344.
[439] K. Koszinowski, D. Schroder, H. Schwarz, Chemphyschem 4 (2003) 1233.
[440] B.R. Sahu, G. Maofa, L. Kleinman, Phys. Rev. B: Condens. Matter 67 (2003) 115420.
[441] S. Neukermans, E. Janssens, H. Tanaka, R.E. Silverans, P. Lievens, Phys. Rev. Lett. 90 (2003) 033401.
[442] D.W. Yuan, Y. Wang, Z. Zeng, J. Chem. Phys. 122 (2005) 114310.
[443] E. Janssens, H. Tanaka, S. Neukermans, R.E. Silverans, P. Lievens, Phys. Rev. B: Condens. Matter 69 (2004) 085402.
[444] E. Janssens, H. Tanaka, S. Neukermans, R.E. Silverans, P. Lievens, New J. Phys. 5 (2003) 46.
[445] W. Bouwen, F. Vanhoutte, F. Despa, S. Bouckaert, S. Neukermans, L.T. Kuhn, H. Weidele, P. Lievens, R.E. Silverans, Chem. Phys. Lett. 314 (1999) 227.
[446] H. Tanaka, S. Neukermans, E. Janssens, R.E. Silverans, P. Lievens, J. Am. Chem. Soc. 125 (2003) 2862.
[447] H. Tanaka, S. Neukermans, E. Janssens, R.E. Silverans, P. Lievens, J. Chem. Phys. 119 (2003) 7115.
[448] L. Gagliardi, J. Am. Chem. Soc. 125 (2003) 7504.
[449] B. Kiran, X. Li, H.J. Zhai, L.F. Cui, L.S. Wang, Angew. Chem. Int. Ed. 43 (2004) 2125.
[450] X. Li, B. Kiran, L.F. Cui, L.S. Wang, Phys. Rev. Lett. 95 (2005) 253401.
[451] M.-X. Chen, X.H. Yan, J. Chem. Phys. 128 (2008) 174305.
[452] P. Pyykko, N. Runeberg, Angew. Chem. Int. Ed. 41 (2002) 2174.
[453] P. Pyykko, J. Organomet. Chem. 691 (2006) 4336.
[454] J. Autschbach, B.A. Hess, M.P. Johansson, J. Neugebauer, M. Patzschke, P. Pyykko,

M. Reiher, D. Sundholm, Phys. Chem. Chem. Phys. 6 (2004) 11.

[455] X. Li, B. Kiran, J. Li, H.J. Zhai, L.S. Wang, Angew. Chem. Int. Ed. 41 (2002) 4786.

[456] Y. Gao, S. Bulusu, X.C. Zeng, J. Am. Chem. Soc. 127 (2005) 15680.

[457] Y. Gao, S. Bulusu, X.C. Zeng, Chemphyschem 7 (2006) 2275.

[458] Y. Gao, N. Shao, S. Bulusu, X.C. Zeng, J. Phys. Chem. C 112 (2008) 8234.

[459] L.M. Molina, B. Hammer, J. Catal. 233 (2005) 399.

[460] F.R. Negreiros, L. Sementa, G. Barcaro, S. Vajda, E. Apra, A. Fortunelli, ACS Catal. 2 (2012) 1860.

[461] L.M. Molina, M.D. Rasmussen, B. Hammer, J. Chem. Phys. 120 (2004) 7673.

[462] N. Lopez, J.K. Norskov, J. Am. Chem. Soc. 124 (2002) 11262.

[463] I.N. Remediakis, N. Lopez, J.K. Norskov, Angew. Chem. Int. Ed. 44 (2005) 1824.

[464] I.N. Remediakis, N. Lopez, J.K. Norskov, Appl. Catal., A 291 (2005) 13.

[465] T.V.W. Janssens, B.S. Clausen, B. Hvolbaek, H. Falsig, C.H. Christensen, T. Bligaard, J.K. Norskov, Top. Catal. 44 (2007) 15.

[466] Z.P. Liu, P. Hu, A. Alavi, J. Am. Chem. Soc. 124 (2002) 14770.

[467] Z.P. Liu, X.Q. Gong, J. Kohanoff, C. Sanchez, P. Hu, Phys. Rev. Lett. 91 (2003) 266102.

[468] L.M. Liu, B. McAllister, H.Q. Ye, P. Hu, J. Am. Chem. Soc. 128 (2006) 4017.

[469] S. Chretien, H. Metiu, Catal. Lett. 107 (2006) 143.

[470] V. Shapovalov, H. Metiu, J. Catal. 245 (2007) 205.

[471] P. Schwerdtfeger, Angew. Chem. Int. Ed. 42 (2003) 1892.

[472] B. Yoon, H. Hakkinen, U. Landman, A.S. Worz, J.M. Antonietti, S. Abbet, K. Judai, U. Heiz, Science 307 (2005) 403.

[473] Q.M.S. Rong, F.M. Liu, X.Y. Li, Y.F. Zhao, X.G. Jing, Chem. Pap. 61 (2007) 308.

[474] M. Heinebrodt, N. Malinowski, F. Tast, W. Branz, I.M.L. Billas, T.P. Martin, J. Chem. Phys. 110 (1999) 9915.

[475] C. Majumder, A.K. Kandalam, P. Jena, Phys. Rev. B: Condens. Matter 74 (2006) 205437.

[476] C. Majumder, S.K. Kulshreshtha, Phys. Rev. B: Condens. Matter 73 (2006) 155427.

[477] Y.-R. Luo, Comprehensive handbook of chemical bond energies, CRC Press, Boca Raton, 2007.

[478] K.E. Shuler, J. Chem. Phys. 21 (1953) 624.

[479] R. Burgert, H. Schnoeckel, A. Grubisic, X. Li, S.T. Stokes, K.H. Bowen, G.F. Gantefor, B. Kiran, P. Jena, Science 319 (2008) 438.

[480] S. Chretien, H. Metiu, J. Chem. Phys. 129 (2008) 074705.

[481] F. Pittaway, L.O. Paz-Borbon, R.L. Johnston, H. Arslan, R. Ferrando, C. Mottet, G. Barcaro, A. Fortunelli, J. Phys. Chem. C 113 (2009) 9141.

[482] C.N. Ramachandran, F.Y. Naumkin, J. Phys. Chem. A 117 (2013) 6803.

[483] G. Barcaro, M. Broyer, N. Durante, A. Fortunelli, M. Stener, J. Phys. Chem. C 115 (2011) 24085.

[484] B.D. Yu, M. Scheffler, Phys. Rev. B: Condens. Matter 56 (1997) R15569.

[485] H. Shi, C. Stampfl, Phys. Rev. B: Condens. Matter 76 (2007) 075327.

[486] W.R. Tyson, W.A. Miller, Surf. Sci. 62 (1977) 267.

[487] F.R.d. Boer, Cohesion in metals : transition metal alloys, Elsevier Scientific Pub. Co., New York, N.Y., U.S.A., 1988.

[488] V. Kumar, K. Esfarjani, in: Y. Kawazoe, T. Kondow, K. Ohno (Eds.), Clusters and Nanomaterials, Springer Berlin Heidelberg, 2002, p. 9.

[489] G. Rossi, A. Rapallo, C. Mottet, A. Fortunelli, F. Baletto, R. Ferrando, Phys. Rev. Lett. 93 (2004) 105503.

[490] D.W. Goodman, Chem. Rev. 95 (1995) 523.

[491] B.C. Gates, Chem. Rev. 95 (1995) 511.

[492] R.J. Lad, Surf. Rev. Lett. 2 (1995) 109.

[493] A.M. Azad, S.A. Akbar, S.G. Mhaisalkar, L.D. Birkefeld, K.S. Goto, J. Electrochem. Soc. 139 (1992) 3690.

[494] U. Kirner, K.D. Schierbaum, W. Gopel, B. Leibold, N. Nicoloso, W. Weppner, D. Fischer, W.F. Chu, Sensors and Actuators B-Chemical 1 (1990) 103.

[495] B.C. Gates, L. Guczi, H. Knözinger, Metal clusters in catalysis, Elsevier, New York, NY, U.S.A., 1986.

[496] R.M. Lambert, G. Pacchioni (Ed.)^(Eds.), Chemisorption and reactivity on supported clusters and thin films : towards an understanding of microscopic processes in catalysis. Kluwer Academic Publishers, Dordrecht ; Boston, 1997.

[497] M. Haruta, Gold Bulletin 37 (2004) 27.

[498] A. Bongiorno, U. Landman, Phys. Rev. Lett. 95 (2005) 106102.

[499] L. Cheng, C. Yin, F. Mehmood, B. Liu, J. Greeley, S. Lee, B. Lee, S. Seifert, R.E. Winans, D. Teschner, R. Schloegl, S. Vajda, L.A. Curtiss, ACS Catal. 4 (2014) 32.

[500] L.M. Molina, S. Lee, K. Sell, G. Barcaro, A. Fortunelli, B. Lee, S. Seifert, R.E. Winans, J.W. Elam, M.J. Pellin, I. Barke, V. von Oeynhausen, Y. Lei, R.J. Meyer, J.A. Alonso, A.F. Rodriguez, A. Kleibert, S. Giorgio, C.R. Henry, K.-H. Meiwes-

Broer, S. Vajda, Catal. Today 160 (2011) 116.

[501] Y. Lei, F. Mehmood, S. Lee, J. Greeley, B. Lee, S. Seifert, R.E. Winans, J.W. Elam, R.J. Meyer, P.C. Redfern, D. Teschner, R. Schlogl, M.J. Pellin, L.A. Curtiss, S. Vajda, Science 328 (2010) 224.

[502] G. Barcaro, A. Fortunelli, J. Phys. Chem. C 111 (2007) 11384.

[503] G. Barcaro, L. Sementa, F.R. Negreiros, R. Ferrando, A. Fortunelli, Nano Lett. 11 (2011) 5542.

[504] S. Surnev, A. Fortunelli, F.P. Netzer, Chem. Rev. 113 (2013) 4314.

[505] R. Ferrando, G. Barcaro, A. Fortunelli, Phys. Rev. B: Condens. Matter 83 (2011) 045418.

[506] N.C. Hernandez, J.F. Sanz, J. Phys. Chem. B 106 (2002) 11495.

[507] N.C. Hernandez, J.F. Sanz, Appl. Surf. Sci. 238 (2004) 228.

[508] N.C. Hernandez, J. Graciani, A. Marquez, J.F. Sanz, Surf. Sci. 575 (2005) 189.

[509] J.R.B. Gomes, F. Illas, N.C. Hernandez, J.F. Sanz, A. Wander, N.M. Harrison, J. Chem. Phys. 116 (2002) 1684.

[510] V.V. Rivanenkov, V.A. Nasluzov, A.M. Shor, K.M. Neyman, N. Rosch, Surf. Sci. 525 (2003) 173.

[511] N.C. Hernandez, A. Marquez, J.F. Sanz, J.R.B. Gomes, F. Illas, J. Phys. Chem. B 108 (2004) 15671.

[512] Z. Lodziana, J.K. Norskov, J. Chem. Phys. 115 (2001) 11261.

[513] R. Yang, A.P. Rendell, J. Phys. Chem. B 110 (2006) 9608.

[514] R. Meyer, J. Lockemeyer, R. Yeates, M. Lemanski, D. Reinalda, M. Neurock, Chem. Phys. Lett. 449 (2007) 155.

[515] R. Meyer, Q. Ge, J. Lockemeyer, R. Yeates, M. Lemanski, D. Reinalda, M. Neurock, Surf. Sci. 601 (2007) 134.

[516] A. Chatterjee, S. Niwa, F. Mizukami, J. Mol. Graphics Modell. 23 (2005) 447.

[517] L. Xiao, W.F. Schneider, Surf. Sci. 602 (2008) 3445.

[518] N.C. Hernandez, J.F. Sanz, J. Phys. Chem. B 105 (2001) 12111.

[519] J.R.B. Gomes, Z. Lodziana, F. Illas, J. Phys. Chem. B 107 (2003) 6411.

[520] C. Zhou, J. Wu, T.J.D. Kumar, N. Balakrishnan, R.C. Forrey, H. Cheng, J. Phys. Chem. C 111 (2007) 13786.

[521] S. Nigam, C. Majumder, Langmuir 26 (2010) 18776.

[522] S. Nigam, C. Majumder, J. Phys. Chem. C 116 (2012) 2863.

[523] L.M. Molina, B. Hammer, Phys. Rev. Lett. 90 (2003) 206102.

[524] L.M. Molina, B. Hammer, Phys. Rev. B: Condens. Matter 69 (2004) 155424.

[525] G. Pacchioni, Phys. Chem. Chem. Phys. 15 (2013) 1737.

[526] G. Pacchioni, L. Giordano, M. Baistrocchi, Phys. Rev. Lett. 94 (2005) 226104.

[527] K. Honkala, H. Hakkinen, J. Phys. Chem. C 111 (2007) 4319.

[528] P. Frondelius, H. Hakkinen, K. Honkala, Phys. Rev. B: Condens. Matter 76 (2007) 073406.

[529] P. Frondelius, H. Hakkinen, K. Honkala, New J. Phys. 9 (2007) 339.

[530] V.A. Nasluzov, T.V. Shulimovich, A.M. Shor, V.I. Bukhtiyarov, N. Rösch, Phys. Status Solidi B 247 (2010) 1023.

[531] P. Thompson, D.E. Cox, J.B. Hastings, J. Appl. Crystallogr. 20 (1987) 79.

[532] B. Holm, R. Ahuja, Y. Yourdshahyan, B. Johansson, B.I. Lundqvist, Phys. Rev. B: Condens. Matter 59 (1999) 12777.

[533] R.H. French, J. Am. Ceram. Soc. 73 (1990) 477.

[534] G. Kresse, J. Furthmuller, VASP the Guide. Available from http://cms.mip.univie.ac.at/VASP.

[535] C. Verdozzi, D.R. Jennison, P.A. Schultz, M.P. Sears, Phys. Rev. Lett. 82 (1999) 799.

[536] A. Wander, B. Searle, N.M. Harrison, Surf. Sci. 458 (2000) 25.

[537] C. Sousa, F. Illas, G. Pacchioni, J. Chem. Phys. 99 (1993) 6818.

[538] J. Carrasco, J.R.B. Gomes, F. Illas, Phys. Rev. B: Condens. Matter 69 (2004) 064116.

[539] C. Ruberto, Y. Yourdshahyan, B.I. Lundqvist, Phys. Rev. B: Condens. Matter 67 (2003) 195412.

[540] P.K. Jain, Struct. Chem. 16 (2005) 421.

[541] A. Deka, R.C. Deka, Journal of Molecular Structure-Theochem 870 (2008) 83.

[542] B. Assadollahzadeh, P. Schwerdtfeger, J. Chem. Phys. 131 (2009) 064306.

[543] E.M. Fernandez, L.C. Balbas, Phys. Status Solidi A 203 (2006) 1277.

[544] S. Lee, C.Y. Fan, T.P. Wu, S.L. Anderson, J. Phys. Chem. B 109 (2005) 11340.

[545] N. Nilius, M.V. Ganduglia-Pirovano, V. Brazdova, M. Kulawik, J. Sauer, H.J. Freund, Phys. Rev. B: Condens. Matter 81 (2010) 045422.

[546] N. Nilius, M.V. Ganduglia-Pirovano, V. Brazdova, M. Kulawik, J. Sauer, H.J. Freund, Phys. Rev. Lett. 100 (2008) 096802.

[547] T. Ito, G.N. Patwari, M. Arakawa, A. Terasaki, J. Phys. Chem. A 118 (2014) 8293.

[548] D. Manzoor, S. Krishnamurty, S. Pal, J. Phys. Chem. C 118 (2014) 7501.

[549] X.-N. Li, Z. Yuan, S.-G. He, J. Am. Chem. Soc. 136 (2014) 3617.

[550] A. Lyalin, A. Nakayama, K. Uosaki, T. Taketsugu, J. Phys. Chem. C 117 (2013)

21359.

[551] F.R. Negreiros, E. Apra, G. Barcaro, L. Sementa, S. Vajda, A. Fortunelli, Nanoscale 4 (2012) 1208.

List of Publications

1. Rajesh, C.; Majumder, C.; Rajan, M. G. R.; Kulshreshtha, S. K., Isomers of small Pb_n clusters (n=2-15): Geometric and electronic structures based on ab initio molecular dynamics simulations. *Phys. Rev. B: Condens. Matter* 2005, *72* (23), 235411.

2. Rajesh, C.; Majumder, C., Energy level reordering and stability of MPb_{12} clusters: An interplay between geometry and electronic structure. *Chem. Phys. Lett.* 2006**,** *430* (1-3), 101-107.

3. Rajesh, C.; Majumder, C., Atomic and electronic structures of neutral and charged Pb_n clusters (n=2-15): Theoretical investigation based on density functional theory. *J. Chem. Phys.* 2007, *126* (24), 244704.

4. Rajesh, C.; Majumder, C., Structure and electronic properties of Pb_nM (M=C, Al, In, Mg, Sr, Ba, and Pb; n=8, 10, 12, and 14) clusters: Theoretical investigations based on first principles calculations. *J. Chem. Phys.* 2008, *128* (2), 024308.

5. Barman, S.; Rajesh, C.; Das, G. P.; Majumder, C., Structural and electronic properties of $Sn_{n-1}Pb$ and $Pb_{n-1}Sn$ clusters: a theoretical investigation through first principles calculations. *Eur. Phys. J. D* 2009, *55* (3), 613-625.

6. Waldschmidt, B.; Barman, S.; Rajesh, C.; Majumder, C.; Das, G. P.; Schaefer, R., Energetics and fragmentation of single-doped tin and lead clusters. *Phys. Rev. B: Condens. Matter* 2009, *79* (4), 045422.

7. Rajesh, C.; Majumder, C.; Mizuseki, H.; Kawazoe, Y., A theoretical study on the interaction of aromatic amino acids with graphene and single walled carbon nanotube. *J. Chem. Phys.* 2009, *130* (12) 124911.

8.. Rajesh, C.; Majumder, C., Oxidation of Al doped Au clusters: A first principles study. *J. Chem. Phys.* 2009, *130* (23), 234309.

9. Rajesh, C.; Nigam, S.; Majumder, C., The structural and electronic properties of Au

clusters on the α-Al_2O_3(0001) surface: a first principles study. *Phys. Chem. Chem. Phys.* **2014**. DOI 10.1039/C4CP02137A